UNIVERSITY OF OXFORD

DEPARTMENT OF ENGINEERING SCIENCE

Surfactant Adsorption and Marangoni Flow in Liquid Jets

A thesis submitted in partial fulfilment of the requirements for
the degree of Doctor of Philosophy

by

Michael Weiß

Hertford College

Hilary Term 2004

Abstract

This thesis is concerned with the interfacial behaviour of surfactant solutions on short time scales. A gravity-driven laminar liquid jet is used to create a rapidly expanding liquid surface, which exposes the surfactant solution to highly non-equilibrium surface conditions. This expansion causes the surface tension to differ locally from its equilibrium value, generating a (Marangoni) shear stress that acts on the jet surface and retards the surface acceleration.

A boundary-layer treatment of the flow very near the nozzle shows that the cube-root dependence of the axial surface velocity on the distance travelled is altered through the adsorption of surfactant.

A numerical model of the surfactant adsorption process in the jet has been developed within the framework of the computational fluid dynamics (CFD) program FIDAP. Complemented by the major results from the boundary-layer treatment—the Marangoni stress at the detachment point does not exceed the shear stress inside the nozzle and the surface concentration at that point is finite—a hybrid CFD model is presented. The hybrid CFD model is extended to incorporate the effects of micelle disintegration. This model extension assumes one micelle species, and the break-down of micelles is modelled using kinetic expressions.

Results from the hybrid CFD model are computed for sub-micellar C_{16}TAB and C_{14}TAB, and for C_{16}TAB in the presence of micelles. The computed results are validated with experimental data.

Acknowledgements

I would like to express my gratitude to a number of important people for their help and company during my time at Oxford.

First, I would like to thank my supervisor, Prof. Richard C. Darton. Without his guidance, this work would not have been possible, and he has always been an invaluable source of motivation at difficult times. Second, I would like to thank my co-supervisor, Dr. Colin D. Bain of the Physical and Theoretical Chemistry Laboratory (PTCL) at Oxford, for his continuous support throughout my research at Oxford. I thank both Richard and Colin for making the jet project a rewarding and fun project to work on.

I am indebted to Drs. Turgut Battal and Dimitrina Valkovska of Colin's research group at PTCL. I thank Turgut for the excellent collaboration on the jet project and Dimitrina for her assistance with some of the modelling aspects, and for providing the equilibrium isotherms. I also thank Daniel Colegate, who recently joined the jet project at PTCL, for his pleasant company in the past few months.

I gratefully acknowledge financial support from the Engineering and Physical Science Research Council (EPSRC).

I had great pleasure in spending the past four years in the very relaxing and stimulating environment of the Hertford College Middle Common Room, and I thank its members for their friendship and company.

Finally, I thank my parents for their support and encouragement not only during my time at Oxford, but throughout my academic education.

Contents

List of Figures

List of Tables

List of Symbols

Dimensionless Groups

$\mathrm{Ca} = \mu\bar{u}_0/\sigma$ Capillary number

$\mathrm{E} = \widehat{N}\mathcal{R}T\Gamma_{sat}/(\mu\bar{u}_0)$ Elasticity number

$\mathrm{Fr} = \bar{u}_0^2/(2R_0 g)$ Froude number

$\mathrm{Ma} = \left|\mathrm{Ca}^{-1} - \mathrm{Ca}_0{}^{-1}\right|$ Marangoni number

$\mathrm{Pe} = \mathrm{ReSc}/2 = R_0\bar{u}_0/D$ Péclet number

$\mathrm{Re} = 2R_0\rho\bar{u}_0/\mu$ Reynolds number

$\mathrm{Sc} = \mu/(\rho D)$ Schmidt number

$\mathrm{St} = 4R_0^4\rho g/(\mu\bar{u}_0)$ Stokes number

$\mathrm{We} = \mathrm{ReCa} = 2R_0\rho\bar{u}_0^2/\sigma$ Weber number

Latin Symbols

ℓ	Transition length scale, see Equation (5.44)	m
$\mathbf{n}$	Normal vector, see Equation (3.36)	m
$\mathbf{u}$	Velocity vector, see Equation (3.36)	m s^{-1}
$\mathcal{A}$	Dimensionless constant, see Equation (4.47)	
$\mathcal{C}$	Downstream solution fit parameter, see Equation (4.58)	
$\mathcal{F}$	Relative deviation factor, see Equation (6.3)	
$\mathcal{K}$	Dimensionless fit parameter, see Equation (2.16)	
$\mathcal{L}$	Dimensionless length of mesh edge/boundary, see Equation (5.15)	
$\mathcal{N}$	Dimensionless integral parameter, see Equation (2.12)	

$\mathcal{P}$	Mesh interval length ratio, see Equation (5.15)	
$\mathcal{R}$	Universal gas constant	8.314 J mol^{-1} K^{-1}
$\mathcal{T}$	Time, see Equation (1.2)	s
$\mathcal{X}$	Downstream solution fit parameter, see Equation (5.49)	
$\mathcal{Y}$	Downstream solution fit parameter, see Equation (5.50)	
$\overline{u}$	Mean jet velocity	m s^{-1}
$\widehat{A}$	Dummy parameter, see Equation (2.35)	s^{-1}
$\widehat{B}$	Dummy parameter, see Equation (2.35)	m^{-1} s^{-1}
$\widehat{N}$	Ionic number, see Equation (4.35)	
$\widehat{s}$	Arc length of a surface element, see Equation (3.17)	
$\widehat{u}$	Time-smoothed axial velocity component, see Equation (2.31)	m s^{-1}
$\widetilde{p}$	Width of micelle species spectrum, page 13	
A	Cross-sectional area of the jet, see Equation (2.21)	m^2
a	Dummy variable, see Equation (2.36)	m s^{-1}
a_i	Activity of species i, see Equation (1.19)	mol m^{-3}
b	Dummy parameter, see Equation (2.36)	s^{-1}
c	Molar concentration	mol m^{-3}
D	Coefficient of diffusivity	m^2 s^{-1}
d	Number of mesh intervals, see Equation (5.15)	
F	Total axial force, see Equation (2.30)	N
f	Functional dependence of u_s on z, see Equation (4.22)	m s^{-1}
G	Weight of liquid column, see Equation (2.30)	N
g	Gravitational acceleration	9.81 m s^{-2}
H	Reservoir liquid height, see Equation (7.2)	m
h	Monomer boundary layer thickness, page 133	m
i	Aggregation number, page 13	

j	Molar flux, see Equation (1.9)	mol m^{-2} s^{-1}
K	Equilibrium constant, see Equation (5.29)	mol^{1-N} m^{3N-3}
k	Langmuir constant, see Equation (5.21)	mol m^{-3}
k_{ads}	Adsorption rate parameter, see Equation (1.10)	m s^{-1}
k_{des}	Desorption rate parameter, see Equation (1.10)	s^{-1}
k_d	Micelle disintegration rate constant, see Equation (5.28)	s^{-1}
k_f	Micelle formation rate constant, see Equation (5.28)	mol^{1-N} m^{3N-3} s^{-1}
L	Transition length scale, see Equation (5.45)	m
l	Nozzle length, see Equation (7.6)	m
M	Molecular weight	kg mol^{-1}
m	Downstream solution fit parameter, see Equation (4.58)	
N	Mean aggregation number, page 13	
n	Normal coordinate	m
p	Pressure	Pa
Q	Mass flow rate, see Equation (2.33)	g s^{-1}
q	Mass flux, see Equation (4.27)	kg m^{-2} s^{-1}
R	Jet radius	m
r	Radial coordinate	m
R_c	Parameter of curvature, see Equation (3.14)	m^{-1}
r_m	Micelle radius, see Equation (6.2)	Å
$r_s = h(z)$	Jet radius, see Equation (3.17)	m
S	Surfactant molecule, see Equation (5.28)	
s	General source/sink term, see Equation (5.1)	kg m^{-3} s^{-1}
T	Temperature	K
t	Tangential coordinate	m
U	Axial core velocity of the jet, see Equation (2.35)	m s^{-1}

u	Axial velocity component	$\mathrm{m\ s^{-1}}$
v	Radial velocity component	$\mathrm{m\ s^{-1}}$
W	Normalised dimensionless concentration, see Equation (4.78)	
w	Mass fraction, see Equation (4.21)	
x	Mesh grading parameter, see Equation (5.15)	
y	Transverse coordinate in boundary layer	m
z	Axial coordinate	m
	Greek Symbols	
α	Surface-slip factor, see Equation (4.7)	
Δ	Downstream surface velocity off-set value, see Equation (4.42)	
δ	Radial distance of edge of boundary layer, see Equation (2.36)	m
ϵ	Relative error estimate, see Equation (4.63)	
Γ	Surface concentration/coverage	$\mathrm{mol\ m^{-2}}$
γ	Dummy variable, see Equation (1.6)	s
κ	Dimensionless constant, see Equation (4.43)	
λ	Length of the region of detachment, see Equation (4.56)	m
μ	Dynamic viscosity	$\mathrm{kg\ m^{-1}\ s^{-1}}$
μ_i	Chemical potential of species i, see Equation (1.19)	$\mathrm{J\ mol^{-1}}$
ν	Kinematic viscosity	$\mathrm{m^2\ s^{-1}}$
Ω	Surface area element, see Equation (1.1)	$\mathrm{m^2}$
$\bar{\rho}$	Coefficient of ellipticity, page 205	
ϕ	Dimensionless constant, see Equation (2.29)	
Ψ	Dimensionless parameter, see Equation (4.79)	
ψ	Substitution parameter, see Equation (A.2)	
ρ	Density	$\mathrm{kg\ m^{-3}}$
σ	Surface tension	$\mathrm{N\ m^{-1}}$

τ	Stress component	$\mathrm{N\ m^{-2}}$
θ	Contact angle, see Equation (3.34)	°
ε	Thickness of hydrodynamic boundary layer, see Equation (2.36)	m
φ	Dimensionless constant, see Equation (2.29)	
$\widetilde{\Delta}$	Downstream surface concentration off-set value, see Equation (4.50)	
ξ_1	Integration constant, see Equation (A.7)	
ξ_2	Integration constant, see Equation (A.8)	
ζ	Substitution parameter, see Equation (A.9)	

Subscripts

0	Nozzle exit/point of detachment
ads	Adsorption
$conv$	Convection
des	Desorption
$diff$	Diffusion
eff	Effective diffusivity
$pseudo$	Pseudo-diffusivity
sat	Saturation
$\max$	Maximum
θ	Circumferential direction/component
a	Ambient
b	Bulk
d	Disintegration
e	Hydrodynamic entry length
f	Formation
jk	Components of the stress tensor
m	Micelles

n	Normal direction/component
r	Radial direction/component/position
s	Surface
T	Total concentration
t	Tangential direction/component
w	Water
z	Axial direction/component/position
cmc	Critical micelle concentration
	Superscripts
$*$	Dimensionless variables
$+$	Cation
$-$	Anion (counter-ion)
0	Standard

Chapter 1

Introduction

Surfactants constitute an important group of chemical products, not only in terms of quantity, but also in view of the great variety of application areas in households and commerce, in industry, and in agriculture. Recent figures show that the annual world production—of which surfactants in detergent products account for 15 to 25%, thus making the household detergent and personal care market the largest single usage of surfactants—approaches 11 million tons, and about half of the quantity is the share of Western Europe and America [1–3].

With more than 500 trade names, surfactants are used in nearly 100 types of industries and have some four thousand different applications. Among the major surfactant consumers are such industries as mining, mineral and oil processing, metal working, textile, construction (additives to concrete and asphalt), transportation (oils, lubricants, lubricating cooling liquids), polymer materials, lacquer and paint manufacturing, pharmaceutical, food, perfumes, printing, water treatment, and many others [4, 5].

Virtually all industrial applications of surfactants are dynamic processes, involving expanding and compressing interfaces on varying time scales, away from the state of equilibrium. For example, when applying thin coats of a liquid as a spray, as in car-painting, droplets need to merge quickly and smoothly at the surface of the wet film. Emulsions and foams, on the other hand, are sustained by inhibiting or slowing the coalescence of droplets or bubbles. The interaction of interfacial fluid dynamics and surfactant adsorption is central to these processes.

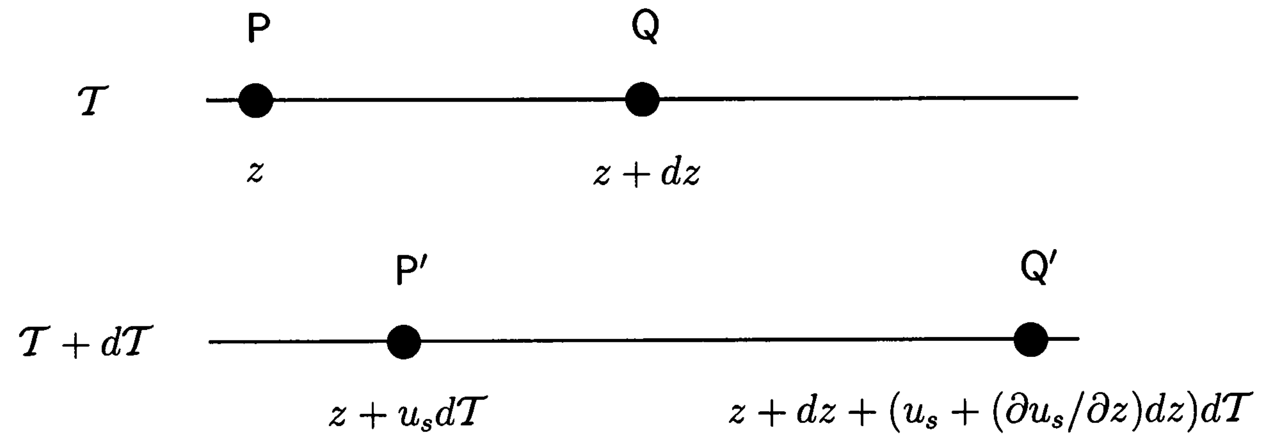

Figure 1.1: Scheme of an area deformation of a surface element $\overline{\mathsf{PQ}}$, where z is the coordinate parallel to the surface.

1.1 Dynamics of Surfaces

1.1.1 Surface Expansion and Surface Dilatation

Let us consider a surface element, which is deformed in the direction parallel to the surface only (see Figure 1.1). At time $\mathcal{T}$, the surface element is defined by point P at z, and point Q at $z + dz$. At time $\mathcal{T} + d\mathcal{T}$, this surface element is deformed, so that P becomes P′, and Q becomes Q′, and in such a way that $\overline{\mathsf{PQ}} \neq \overline{\mathsf{P'Q'}}$. The surface element is stretched if $\overline{\mathsf{PQ}} < \overline{\mathsf{P'Q'}}$, which is shown in Figure 1.1, and compressed if $\overline{\mathsf{PQ}} > \overline{\mathsf{P'Q'}}$. If $\overline{\mathsf{PQ}} = \overline{\mathsf{P'Q'}}$, no surface deformation takes place. Referring to the situation sketched in Figure 1.1, point P′ is located at $z + u_s d\mathcal{T}$, where u_s is the velocity along the surface. The location of point Q′ is at $z + dz + (u_s + (\partial u_s/\partial z)dz)d\mathcal{T}$.

The relative area deformation, $d\Omega/\Omega$, where Ω is the area of the surface element when no deformation takes place, can be obtained from [6,7]

$$\frac{d\Omega}{\Omega} = \frac{\overline{\mathsf{P'Q'}} - \overline{\mathsf{PQ}}}{\overline{\mathsf{PQ}}} = \frac{\partial u_s}{\partial z} d\mathcal{T}. \tag{1.1}$$

With $d\Omega/\Omega = d\ln\Omega$, we easily find

$$\frac{d\ln\Omega}{d\mathcal{T}} = \frac{\partial u_s}{\partial z}. \tag{1.2}$$

In Equation (1.2), the term $d\ln\Omega/d\mathcal{T}$ is referred to as the rate of surface dilatation, and $\partial u_s/\partial z$ is known as the rate of surface expansion. Thus, a velocity gradient along the surface corresponds to a surface dilatation and vice versa.

1.1.2 The Concept of Surface Age

In a system that is at rest, the age of the surface is a well-defined and perfectly meaningful quantity. The surface is "born" at $\mathcal{T} = 0$, and at a time $\mathcal{T} > 0$ has reached an age that equals exactly $\mathcal{T}$. Since the surface is at rest, all surface elements have the same surface age.

The age of a surface is still well-defined and meaningful in a flowing system that moves at a constant velocity throughout. As an example, we consider the (theoretical) case of a liquid jet that leaves the nozzle with plug flow. Fluid particles in the bulk and the surface move at the same velocity everywhere in the jet, and hence $u_s = \overline{u}$, where $\overline{u}$ is the constant velocity of the jet. On leaving the nozzle at $z = 0$, a fluid element on the surface is "born" at $\mathcal{T} = 0$. This surface element travels downstream and at $z > 0$, in the absence of gravity, has reached an age of $\mathcal{T} = z/\overline{u}$. Since $du_s/dz = d\ln\Omega/d\mathcal{T} = 0$, from Equation (1.2) and neglecting jet contraction, the size of the surface element does not change, and it is composed of the same fluid particles as at the point of creation ($z = 0$). In this case, the surface age of a flowing system, in which the surface expansion rate is zero, corresponds to that of a system at rest.

We now consider the (real) case of a liquid jet that leaves the nozzle with a steady flow profile. Along the nozzle wall, up to the point of emergence of liquid from the nozzle, the velocity is zero due to the no-slip condition. This constraint is removed as the liquid leaves the nozzle. The fluid elements in the surface experience an acceleration, $du_s/dz > 0$, in an attempt to equalise the velocity deficit between the layers in the bulk and the surface of the jet. The surface is thus stretched to accommodate the local increase in velocity, $d\ln\Omega/d\mathcal{T} > 0$, and the surface element at a downstream position z does not contain the same fluid particles as at the point of surface creation at $z = 0$. The concept of surface age is therefore not meaningful in a flow with local variations in surface velocity, since the state of the surface at some point $z > 0$ is determined by the entire history of the surface from the point of creation at $z = 0$ onwards.

Several researchers, however, have given definitions of the age of continually expanding jet surfaces. These works were conducted in relation to dynamic surface tension studies in jet flows (see Section 1.7.2) for (*i*) reasons of comparability with other dynamic measurement methods (see for example the works of Miller *et al.* [8] and Noskov [9] for a detailed review of dynamic measurement methods), and (*ii*) to facilitate the application of time-dependent adsorption

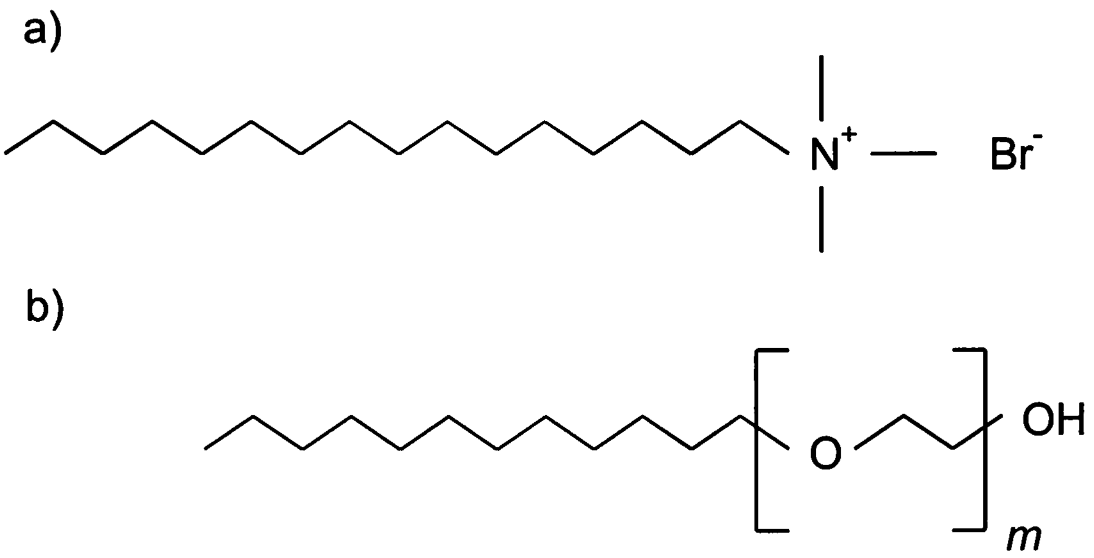

Figure 1.2: The chemical structure of cationic C_{16}TAB (a) and non-ionic $C_{12}E_m$ (b).

models (see Section 1.3).

From Equation (1.2), Hansen [7] derived his defintion of the average surface age of an expanding jet surface,

$$\mathcal{T} = \frac{z}{u_s(z)}, \tag{1.3}$$

which was often used to assign an "age" to elements of the surface (see Section 1.7.2). Other definitions of the age of the surface of a liquid jet were given by Harper [10] and Davies and Makepeace [11].

1.2 Chemistry of Surfactants

Surfactant molecules are amphipathic, which means that the molecule consists of two parts—one which is highly soluble (hydrophilic) in an aqueous medium, and one which is insoluble (hydrophobic) [12]. Two main groups of surfactants may be distinguished—ionic (including anionic, cationic, and ampholytic) and non-ionic. Ionic surfactants possess a hydrophilic head group such as $-OSO_3^-$ (anionic SDS) or $-N^+(CH_3)_3$ (cationic CTAB). The chemical structure of the cationic surfactant C_{16}TAB (hexadecyltrimethylammonium bromide, $C_{19}H_{42}N^+Br^-$), the surfactant mostly studied in this thesis, is shown in Figure 1.2. Cationic surfactants play an important role as antiseptic agents in cosmetics, as general fungicides and germicides, and as disinfectants [4, 13]. Other examples of the use of cationic surfactants are as textile auxiliaries, fabric softener, and hair conditioners [3]. With ampholytic surfactants, the nature of the ionised group depends on pH. An important class of non-ionics, which is widely used as detergents, emulsifiers, and dispersants [4, 14], are alkyl poly(ethylene glycol) ethers, $CH_3(CH_2)_{n-1}(OCH_2CH_2)_mOH$ or C_nE_m for short. The chemical structure of $C_{12}E_m$ is shown in Figure 1.2.

1.3 Action of Surfactants

Surface-active surfactant molecules, or monomers, may adsorb at the surface, but they may also aggregate in micelles, if the bulk concentration exceeds some critical value (see Section 1.3.4). Both monomers and micelles constitute the surfactant inventory. The mechanisms by which surfactant moves into and out of the surface and through which micelles affect that movement are portrayed in Figure 1.3.

Expansion of the surface reduces the concentration of surfactant at the surface. In this case, monomers diffuse towards the surface in order to 're-fill' the empty sites at the surface. On the other hand, compression of the surface leads to the emission of monomers, and surfactants diffuse away from the surface towards the bulk.

In the bulk, micelles and monomers are in equilibrium. If this state of equilibrium is upset by the expansion or compression of the surface, which results in movement of the monomer population within the surfactant inventory, then micelles give up or incorporate monomers in order to re-establish the state of equilibrium. Micelles thus act as local reservoirs within the liquid.

1.3.1 Diffusion-Controlled Adsorption

The simplest possible model assumes local equilibrium between the surface and the bulk, that is, monomers adsorb (or desorb) instantaneously at (or from) the surface, and diffusion to (or from) the surface is the time-limiting transport step. Such models are referred to as diffusion-controlled adsorption models.

Ward and Tordai [16] developed a general theory of diffusion of solute molecules to a surface at rest. Comparison of experimental data with this theory indicates whether diffusion is a complete explanation of the time-variation of sur-

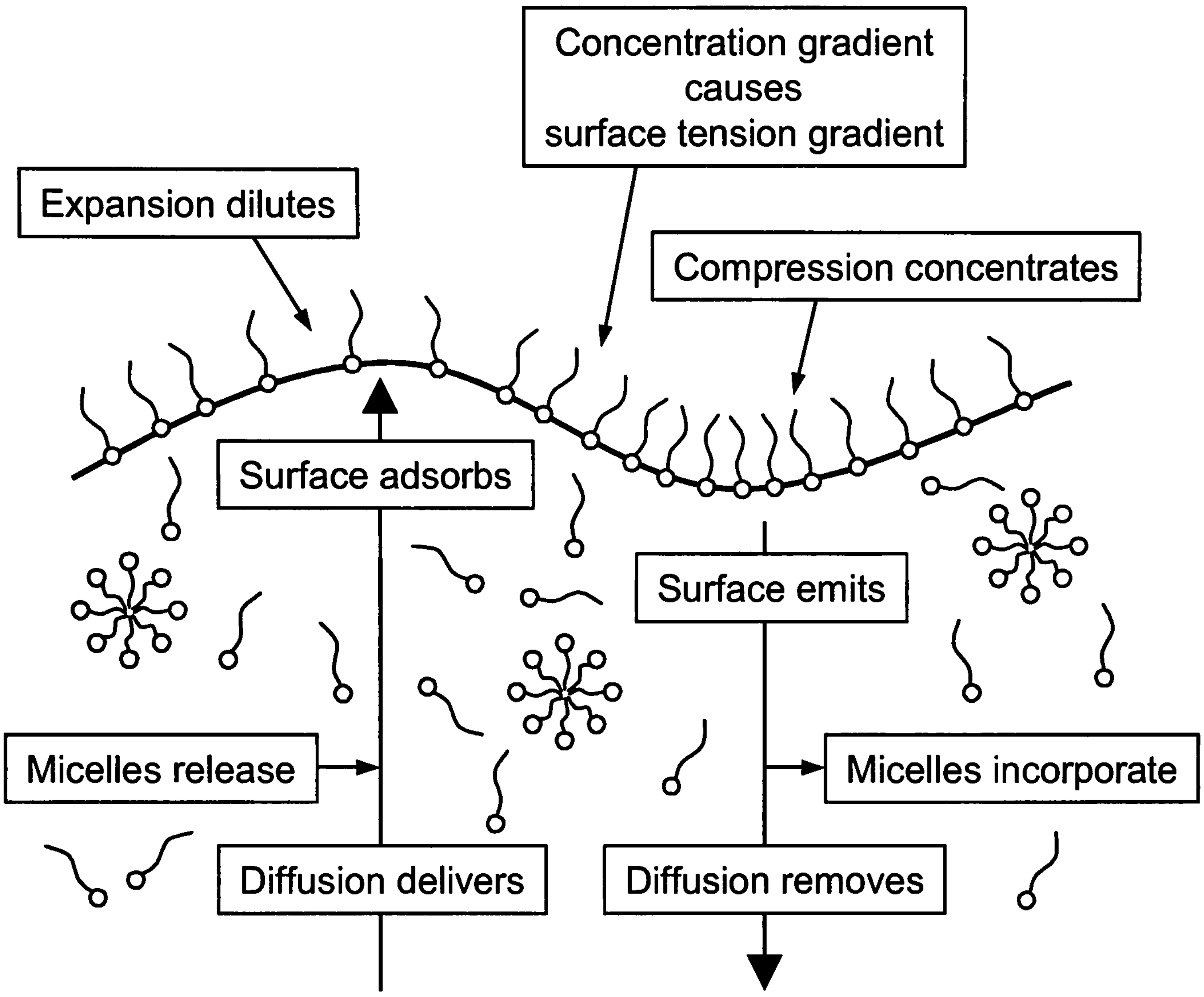

Figure 1.3: Surfactant action at and near a free surface, adapted from the work of Schunk [15].

face tension or whether some additional effects must be sought. Their analysis is based on the one-dimensional diffusion equation,

$$\frac{\partial c}{\partial \mathcal{T}} = D\frac{\partial^2 c}{\partial y^2}, \tag{1.4}$$

where c is the molar bulk concentration, D is the coefficient of diffusivity, and y is the coordinate perpendicular to the surface. This bulk conservation equation, together with the conservation of mass at the surface,

$$\frac{d\Gamma}{d\mathcal{T}} = D\left(\frac{\partial c}{\partial y}\right)_{y=0}, \tag{1.5}$$

the boundary condition $c = c_b$ as $y \to \infty$, where c_b is the bulk concentration, and the initial condition of a clean surface ($\Gamma = 0$ at $\mathcal{T} = 0$) gives what became widely known as the Ward and Tordai equation, namely,

$$\Gamma = 2\sqrt{\frac{D}{\pi}}\left\{ c_b\sqrt{\mathcal{T}} - \int_0^{\sqrt{\mathcal{T}}} c_s\left(\mathcal{T}-\gamma\right) d\sqrt{\gamma} \right\}, \tag{1.6}$$

in which $c_s = c(y = 0)$ is the sub-surface concentration, and γ is a dummy variable.

An equilibrium adsorption isotherm is used to relate the surface concentration Γ (per unit area) to the sub-surface concentration c_s (per unit volume). The sub-surface may be taken as an imaginary plane, a few molecular diameters below the surface [17]. The simplest non-linear isotherm is that of Langmuir [18],

$$\frac{\Gamma}{\Gamma_{sat}} = \frac{c_s}{k + c_s}, \tag{1.7}$$

which is used in this thesis to describe the local equilibrium at the surface, but other, more sophisticated non-linear isotherms are sometimes encountered [19–21]. A collection of the adsorption equilibrium parameters of the Langmuir isotherm, Γ_{sat} and k, for various surfactants is given by Chang and Franses [22]. An overview of the most frequently used adsorption isotherms may be found in the work of Danov *et al.* [23, p. 309]. Exact solutions to the Ward and Tordai equation can only be found for linear adsorption isotherms. The use of non-linear isotherms generally requires the application of numerical techniques [24].

Equations (1.6) and (1.7) were for example solved by Miller and Ziller [25, 26], and Hansen presented a solution to this system of equations, in which he included the effect of evaporation of solute [27]. Rampazzo gave a solution to Equation (1.6) for the more sophisticated Frumkin isotherm [28].

For Equation (1.6) to be applicable to flowing systems, a surface age must be contrived. In the case of liquid jets, a number of researchers have employed Hansen's definition of surface age, given by Equation (1.3), to do this (see Section 1.7.2).

A more convenient (and more precise) way of modelling the adsorption at surfaces that are in motion, which does not make use of the concept of surface age, is by locally balancing diffusion to the surface with convection and diffusion in the surface, that is, in terms of a local tangential, t, and normal, n, coordinate system,

$$\frac{\partial \Gamma}{\partial \mathcal{T}} + \frac{\partial}{\partial t}\left(u_t \Gamma\right) + D_s \frac{\partial^2 \Gamma}{\partial t^2} = D\frac{\partial c_s}{\partial n}, \tag{1.8}$$

where u_t is the velocity tangent to the surface, and D_s is the surface diffusion coefficient. At steady state, Equation (1.8) can be simplified since $\partial\Gamma/\partial\mathcal{T} = 0$. Furthermore, the contribution of surface diffusion can often be neglected, as will be shown in Section 4.2. A discussion of Equation (1.8) may be found in the works of Levich [29, p. 393], Krotov and Rusanov [30, p. 37], and Joos [6, p. 144].

In the case of diffusion-controlled adsorption, Equation (1.8) is used together with an appropriate equilibrium isotherm, such as the Langmuir isotherm. The bulk concentration field is obtained by solving the convection-diffusion conservation equation for the surfactant species. In addition, Equation (1.8) requires the fluid motion at the surface to be known.

This modelling approach is used in this thesis, and has been applied to various flow systems before. For example, van Voorst Vader *et al.* [31] modelled surfactant adsorption in a Langmuir trough using Equation (1.8). The same method was applied in the surfactant mass transfer model of the overflowing cylinder experiment [32,33], which was previously modelled numerically by Schunk [15], who also predicted surfactant adsorption in slide coating using this approach [34]. Ghadiali *et al.* [35] presented a numerical model of surfactant adsorption at the interface of a semi-infinite bubble progressing in a capillary tube, which uses Equation (1.8). Cerro and Whitaker [36] used this model in their theoretical study on the hydrodynamic development of thin films in the presence of surfactant.

1.3.2 Mixed Diffusion-Kinetic Adsorption

If the adsorption or desorption rate at the surface is slow or comparable to the diffusion rate, then Γ is not necessarily at local equilibrium with c_s. This situation is often termed "mixed diffusion-kinetic adsorption" [8,17], but the terminology "barrier-limiting adsorption" [37] and "adsorption-limiting mechanism" [38] is also used. The adsorbing and desorbing molar fluxes of monomers to and from the surface, j_{ads} and j_{des}, respectively, which determine the change in surface concentration at the surface, are then related by [17,39]

$$\frac{d\Gamma(\mathcal{T})}{d\mathcal{T}} = j_{ads} - j_{des}. \tag{1.9}$$

Following a procedure put forward by Borwankar and Wasan [40], one assumes that the adsorption flux is a function of both c_s and Γ, $j_{ads} = j_{ads}(c_s, \Gamma)$, whereas the desorption flux depends solely on Γ, $j_{des} = j_{des}(\Gamma)$. For example, a kinetic expression, which is consistent with the Langmuir isotherm at equilibrium, is the Langmuir-Hinshelwood equation [9,22],

$$\frac{d\Gamma(\mathcal{T})}{d\mathcal{T}} = k_{ads}c_s(\mathcal{T})\left(1 - \frac{\Gamma}{\Gamma_{sat}}\right) - k_{des}\Gamma(\mathcal{T}), \tag{1.10}$$

where k_{ads} and k_{des} are the adsorption and desorption rate parameters. For $\mathcal{T} \to \infty$, where $d\Gamma/d\mathcal{T} \to 0$, Equation (1.10) reduces to Equation (1.7), and we find the relation

$$k = \frac{k_{des}}{k_{ads}}\Gamma_{sat}. \tag{1.11}$$

Kinetic relations such as Equation (1.10) are applicable whenever the adsorption process is not controlled purely by diffusion, that is, whenever adsorption at the surface is hindered by a so-called "adsorption barrier". Although this provides a means to make a statement of the time scale of adsorption from the sub-surface to the surface—through the adsorption and desorption rate parameters—it does not yield any information about the nature of the adsorption barrier. The term adsorption barrier thus serves as a catchall to incorporate any of or all the factors that affect adsorption, such as molecule orientation, the availability of empty sites in the surface, or the existence of potential energy barriers [39].

Liggieri and co-workers [41,42] proposed a general model to describe adsorption kinetics, which takes into account an interfacial potential barrier. By employing two activation energies—one as a pre-requisite for molecules to adsorb, and the other for the desorption of adsorbed molecules—an effective diffusion coefficient was established, which gave a variation on the Ward and Tordai equation to account for a potential adsorption barrier. Similarly, the contribution of molecular orientation during the process of adsorption was taken into account [43].

Andelman and co-workers have proposed a general model that relies on a free-energy formulation, which describes both the diffusive transport of surfactant from the bulk to the surface and the kinetics taking place at the surface itself [44–47]. This model addresses the drawbacks of conventional models, (*i*) the use of an external closure relation between surface concentration and sub-surface concentration that does not uniquely arise from the model itself, (*ii*) the dynamic surface tension relies on an equilibrium equation of state, and assumes that it also holds out of equilibrium, (*iii*) extensions to describe more complicated systems, such as ionic surfactants, are not easily performed.

Treating the bulk sub-system as an ideal, dilute solution, the contributions of the finite molecular size of the surfactant molecules and their interactions were taken into account near the interface. In this way, the variation of surface tension with respect to the local surfactant volume fraction yielded the excess in chemical potential at a distance from the surface.

From equilibrium considerations, Andelman and co-workers recovered the Frumkin equilibrium isotherm—which, when molecular interactions are neglected, reduces to Langmuir's equilibrium isotherm—and the corresponding equilibrium equation of state. Away from equilibrium, using the ordinary diffusion equation (in terms of volume fractions) and a discretised form of the mass balance at the surface, the authors obtained a relation between the surface and sub-surface volume fractions that gives a slight variation on the classical Ward and Tordai equation, as a result of the discretisation near the surface. The closure relation between surface concentration and sub-surface concentration, which governs the kinetics at the surface, relates the change in surface concentration with time to the change in chemical potential between surface and sub-surface across the sub-surface layer.

1.3.3 Electric Double Layer

Ionic surfactants, such as C_{16}TAB (see Figure 1.2), dissociate when dissolved in water. In the case of cationic C_{16}TAB, a 1:1 electrolyte, the surfactant molecule dissociates into the positively charged surface-active ion (cation), and the negatively charged bromide ion (anion or counter-ion). The solution as a whole is electroneutral, that is, each cation matches one counter-ion. During adsorption, however, the surface acquires a charge, which inhibits the adsorption of other ions of the same charge, as depicted schematically in Figure 1.4. Adsorption will only continue to occur if the molecule has a strong affinity to the surface, and if the surface charge is screened by ions of the opposite charge close to the surface [48]. In the case of C_{16}TAB, the surface-active cations produce the positive surface charge, and the bromide counter-ions concentrate near the surface, resulting in an electric double layer (EDL).

The concentration of the counter-ions decreases gradually with increasing distance from the surface, until the bulk concentration is reached. Similarly, the non-adsorbed cations are repelled from the surface, which results in a low concentration near the surface that increases with increasing distance from the

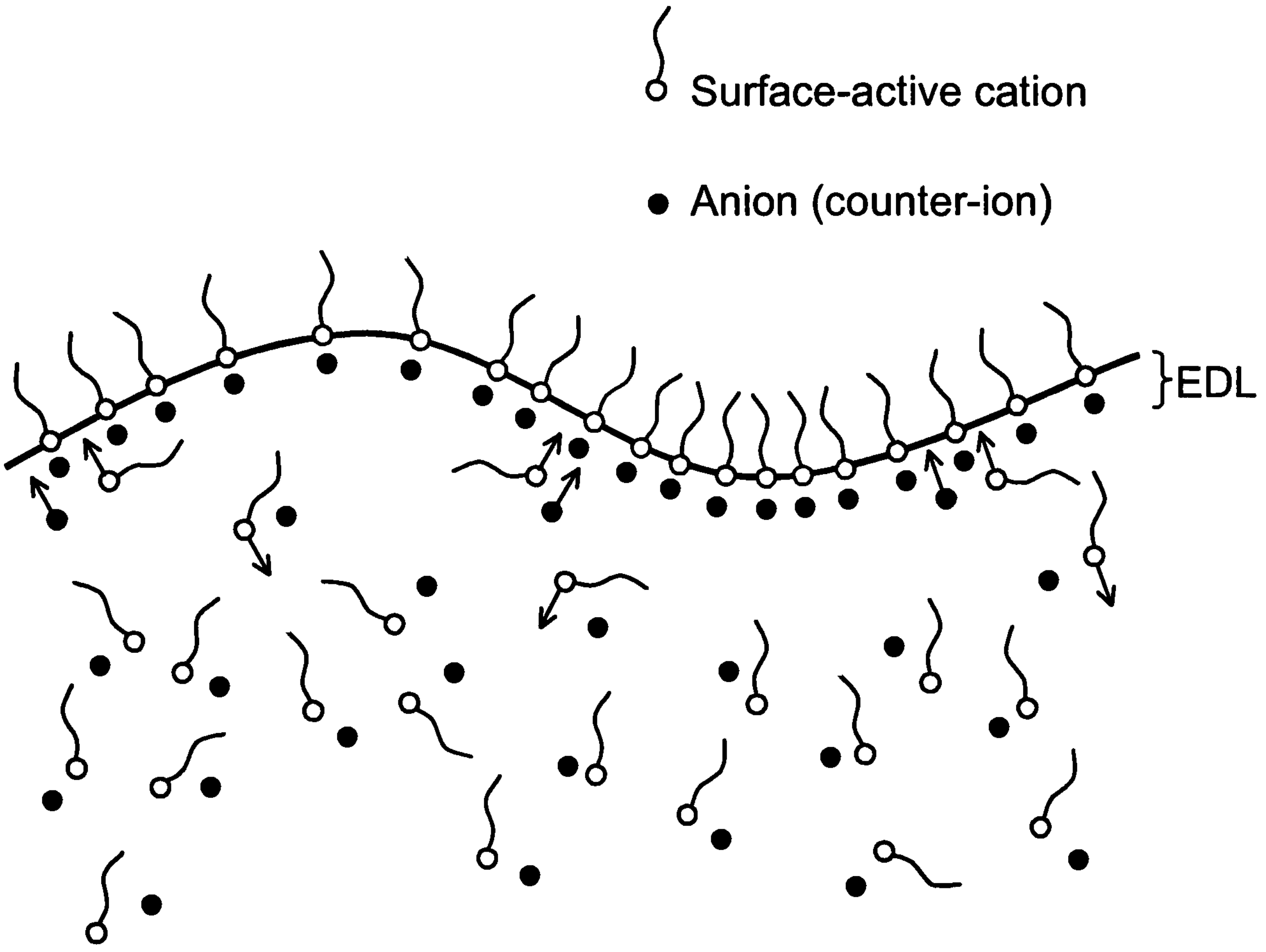

Figure 1.4: Schematic of the transport of cationic surfactant to a surface.

surface, until the corresponding bulk value is reached. The cations very near the surface adsorb, leading to a net transport of surfactant ions to the surface. However, the surfactant ions diffusing within the EDL must overcome the electrostatic repulsion from the surface. Hence, the rate of transport of an ionic surfactant to the surface must be slower than that of an equivalent non-ionic surfactant [49].

Modelling efforts are generally based on the Nernst-Planck diffusion-migration (NPDM) equation—an extension of the diffusion equation used by Ward and Tordai—for each of the ionic species, interfacial mass balances, which relate the surfactant and counter-ion adsorption to their fluxes from the bulk, and the Poisson equation to relate the electrical potential to the ionic distribution [49–51]. The NPDM equations and the interfacial mass balances have been extended to account for convective motion at the steadily expanding surface of an overflowing cylinder [50]. The transport of ionic surfactant to a surface is thus a more general case of the analysis performed by Ward and Tordai for uncharged adsorbing species. Some of the modelling work accounts for the presence of an additional

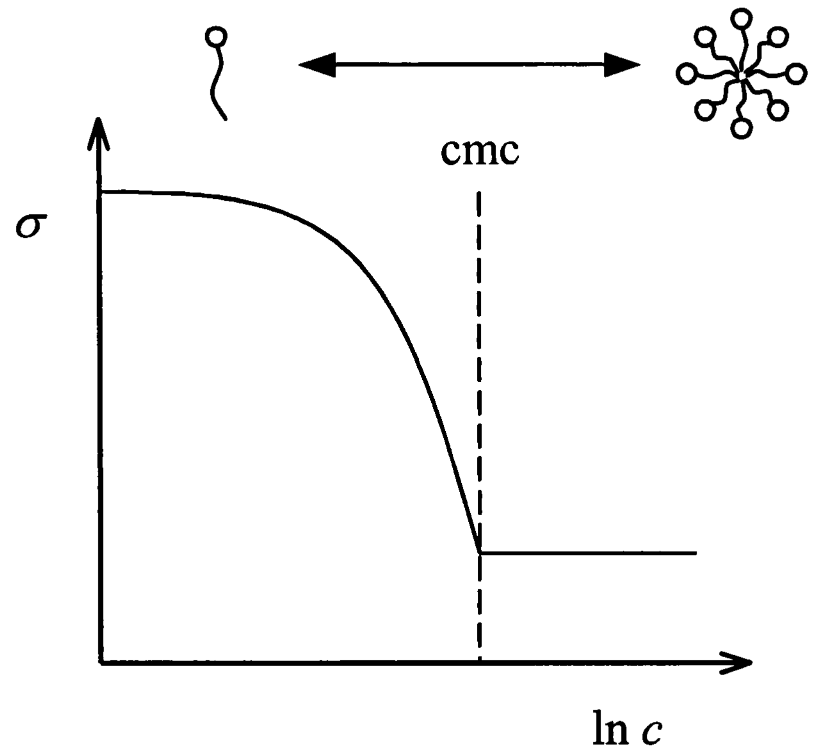

Figure 1.5: Surface tension, σ, as a function of solution concentration, c, typical of an aqueous surfactant solution.

background electrolyte [49, 52, 53].

In this thesis, although we exclusively model the adsorption behaviour of cationic C_{14}TAB and C_{16}TAB, we employ effective ionic diffusivities (see Equation (6.1)) and the presence of counter-ions at the surface is considered in the equation of state (see Equation (5.23)). This allows us to neglect the ions and treat the diffusion and adsorption process as equivalent to that of non-ionic surfactant species.

1.3.4 Micelles

The surface tension of a dilute solution of surfactant, when plotted as a function of the solution concentration, shows a more or less sharp break at a certain concentration (see Figure 1.5). This phenomenon is attributed to the formation of aggregates of surfactant molecules, called micelles, whose contribution to the physical properties of the system is different from that of individual molecules. The solution concentration at which the formation of micelles occurs is called the critical micelle concentration (cmc). Micelles can be made up of 50 to 150 or more molecules, and they may adopt various forms, including spheres and cylinders, and disk-like and lamellar shapes [12].

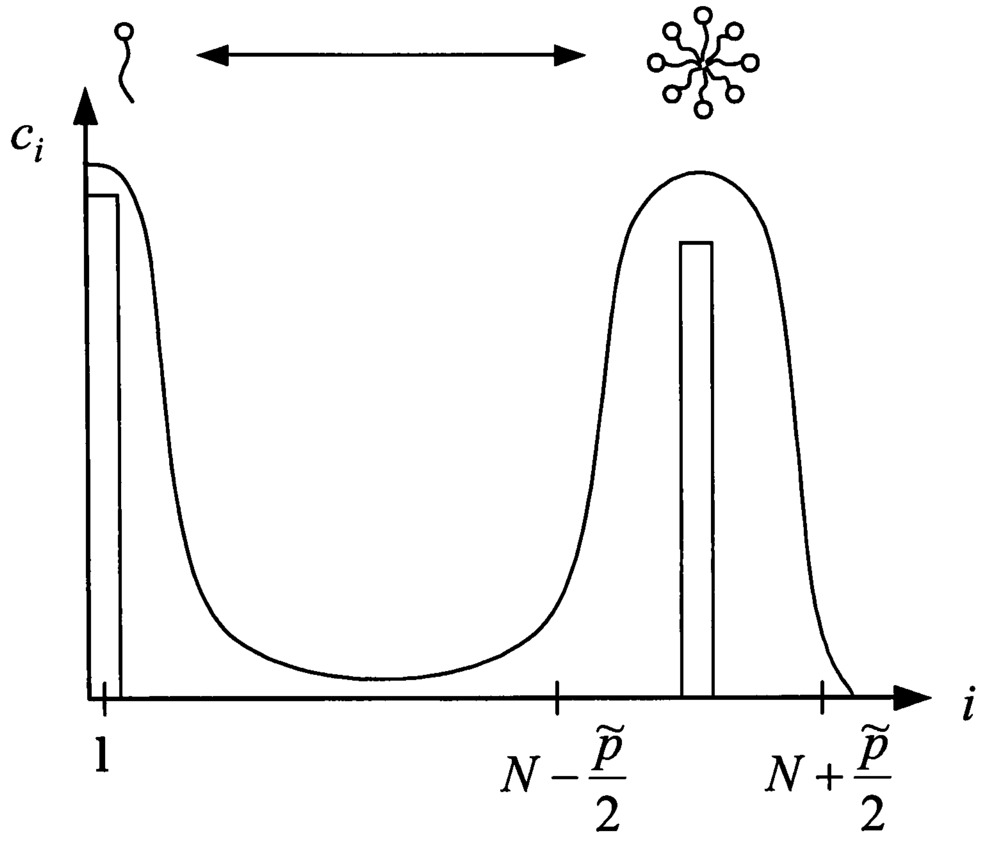

Figure 1.6: Micelle-monomer surfactant inventory.

The formation of micelles is usually understood as a series of reaction steps that lead to the micelle species, as described by Aniansson *et al.*, involving formation and dissociation rate constants at each step [54]. Two surfactant monomers react to form a dimer, which finds another monomer to form a trimer, and so forth, until the first stable micelle species is formed. Stable micelles are also formed through coalescence of smaller agglomerates. A range of stable micelle species is generally assumed (see Figure 1.6), spanning from the "floor" to the "ceiling", that is, from $N-\frac{\tilde{p}}{2} \leqslant i \leqslant N+\frac{\tilde{p}}{2}$, where i is the aggregation number, which specifies the number of monomers that form a micelle species, $\tilde{p}$ defines the width of the spectrum of micelle species, and N is the mean aggregation number [55–58].

The process of micellisation is governed by two time scales—one that describes the release (or take-up) of single monomers by the micelles, and one that relates to the complete dissociation (or formation) of the micelles—usually referred to as the fast and the slow process. The time scale of the slow process may be $\sim$ 100 times longer than that of the fast one [23]. However, the relaxation times may show large variations, depending upon the chemical nature of the surfactant polar head, electrolyte concentration, and on the molecular weight of the surfactant. For example, the characteristic time of the slow process for amphiphilic block copolymers, with a molecular weight that is a factor 10^3 larger than that of $C_{16}TAB$, can exceed 10 h, and that for a fast process can reach several minutes. On the other hand, for a surfactant with a short hydrocarbon chain (heptylammonium chloride), the relaxation time of the fast process can be less than 0.1 μs [58]. The fast process affects the mean aggregation number, whereas the slow process adjusts the concentration of micelles [59].

Bidner *et al.* presented a model that accounts for both relaxation times, but considers only monomers and the region where proper micelles exist, that is, the intermediate state where $1 < i < N - \frac{\widetilde{p}}{2}$, is not taken into account [60]. This model was used by Schunk [15] to predict adsorption from micellar solutions in an overflowing cylinder. He considered three micellar species, that is, $\widetilde{p} = 2$.

The simplest model of micellar aggregation, which considers only the relaxation time of the slow process, assumes that N monomers S form one micelle S_m (given by the bars at $i = 1$ and $i = N$ in Figure 1.6),

$$N \cdot S \underset{k_d}{\overset{k_f}{\rightleftharpoons}} S_m, \tag{1.12}$$

where k_f and k_d are the rate constants of the formation and disintegration of the micelles, respectively. We note here that the formation of a micelle in one reaction step is highly improbable, as it requires the simultaneous collision of a large number of monomers [61].

The equilibrium between monomers and micelles in the bulk is described by

$$K = \frac{k_f}{k_d} = \frac{c_{m,b}}{c_{\text{cmc}}^N}, \tag{1.13}$$

where K is the equilibrium constant. The concentration of micelles in the bulk, $c_{m,b}$, is obtained from the mass balance of the whole surfactant inventory,

$$c_T = c_{\text{cmc}} + N c_{m,b}, \tag{1.14}$$

where c_T is the total concentration and c_{cmc} is the concentration of monomers in the bulk at the cmc.

Applying the principle of mass action to the reaction mechanism (1.12), we find

$$-\frac{1}{N}\frac{dc}{dT} = k_f c^N - k_d c_m, \tag{1.15}$$

or

$$\frac{dc}{d\mathcal{T}} = N\left(k_d c_m - k_f c^N\right) \tag{1.16}$$

for the monomers. Similarly, we find

$$\frac{dc_m}{d\mathcal{T}} = k_f c^N - k_d c_m \tag{1.17}$$

for the micelles.

This simple aggregation model was employed by Miller [62], Danov *et al.* [63], and very recently by Breward and Howell [64]. We use this model in this thesis to study the effect of dissociation of micelles on the adsorption in the jet.

1.4 Surface Thermodynamics at Equilibrium

The Gibbs adsorption equation, at constant temperature and pressure, is given as [6]

$$d\sigma = -\sum_i \Gamma_i d\mu_i, \tag{1.18}$$

where $d\sigma$ is the change in surface tension, Γ_i is the surface concentration of component i, and $d\mu_i$ is the change in chemical potential of the adsorbed species i. At equilibrium, we can write

$$\mu_i = \mu_i^0(p,T) + \mathcal{R}T \ln a_i, \tag{1.19}$$

and hence

$$d\mu_i = \mathcal{R}T d\ln a_i, \tag{1.20}$$

where $\mu_i^0(p,T)$ is the standard chemical potential of species i, which depends on pressure and temperature, $\mathcal{R}$ is the universal gas constant, and a_i is the activity of species i in the bulk. The Gibbs equation becomes

$$d\sigma = -\mathcal{R}T \sum_i \Gamma_i d\ln a_i. \tag{1.21}$$

Let us now consider a system containing water (species 1) and surfactant (species 2), then, from Equation (1.21),

$$d\sigma = -\mathcal{R}T\left(\Gamma_1 \frac{da_1}{a_1} + \Gamma_2 \frac{da_2}{a_2}\right). \tag{1.22}$$

Using the Gibbs convention, the location of the plane dividing the liquid and the gas phase is chosen such that $\Gamma_1 = 0$, which gives

$$d\sigma = -\mathcal{R}T\Gamma d\ln a \approx -\mathcal{R}T\Gamma d\ln c_b, \tag{1.23}$$

where we have dropped the subscripts for the surfactant species, and assumed the case of an ideal dilute solution, that is, $a \approx c_b$.

For an ionic surfactant, we have the adsorption of two kinds of ions. The Gibbs equation is then written as

$$d\sigma = -\mathcal{R}T\left(\Gamma^+ d\ln c_b^+ + \Gamma^- d\ln c_b^-\right).$$

The surface concentration of the cations is given by Γ^+, and Γ^- is that of the counter-ions. Analogously, c_b^+ and c_b^- are the bulk concentrations of cations and counter-ions. With $c_b^+ = c_b^- = c_b$ and $\Gamma^+ = \Gamma^- = \Gamma$, the requirement of electro-neutrality in the bulk and at the surface, we find

$$\Gamma = -\frac{1}{2\mathcal{R}T}\frac{d\sigma}{d\ln c_b}, \tag{1.24}$$

or

$$-\frac{d\sigma}{dc_b} = \frac{2\mathcal{R}T\Gamma}{c_b}. \tag{1.25}$$

Equation (1.24) applies to a 1:1 electrolyte, such as $C_{16}TAB$.

The Gibbs equation relates the adsorption with the surface tension and the bulk concentration. As it is a thermodynamic expression, it is always correct. However, it stands as a differential expression, and it does not tell us the surface tension (or surface concentration) as a function of the bulk concentration. We require a somewhat more explicit equation, a surface equation of state, that is, but this equation does not have the same rigor and is not always correct [6].

For dilute solutions, the interactions between solute molecules are negligible, and Henry's law is obeyed. In this case, the variation of surface tension with bulk concentration, c_b, is linear [48], and we can approximate

$$-\frac{d\sigma}{dc_b} \approx \frac{\sigma_w - \sigma}{c_b} \tag{1.26}$$

where σ_w is the surface tension of the pure solvent, which we assume to be water. From Equations (1.25) and (1.26), we find a surface equation of state,

$$\sigma = \sigma_w - 2\mathcal{R}T\Gamma, \tag{1.27}$$

which applies to dilute solutions of 1:1 electrolytes in water.

The linear dependence of surface tension on concentration breaks down at higher bulk concentrations. Combining the Langmuir equilibrium isotherm, Equation (1.7), with the Gibbs equation gives the Frumkin equation [6, 65],

$$\sigma = \sigma_w + 2\mathcal{R}T\Gamma_{sat} \ln\left(1 - \frac{\Gamma}{\Gamma_{sat}}\right), \tag{1.28}$$

which in terms of bulk concentrations is known as the Szyszkowski equation [66],

$$\sigma = \sigma_w + 2\mathcal{R}T\Gamma_{sat} \ln\left(1 - \frac{c_b}{k + c_b}\right), \tag{1.29}$$

which was first found empirically in 1908.

1.5 Marangoni Flow

1.5.1 The Phenomenon

Variation of surface tension along a free surface in a liquid-gas system gives rise to tangential shear stress, $\partial\sigma/\partial t$, acting on this boundary. The presence of this shear stress must be accompanied by convective motion, $\partial u_t/\partial n$, so that

$$\frac{\partial \sigma}{\partial t} = \mu \frac{\partial u_t}{\partial n}, \tag{1.30}$$

where u_t is the velocity tangential to the surface. This situation is depicted in Figure 1.7 for the case of a surface containing surfactant solution (see also Figure 1.3).

If this surface, which was initially at rest, experiences expansion and compression, the composition of this surface is altered, being locally depleted in surfactant where expansion occurred and locally enriched in surfactant where compression took place. From the surface equation of state, Equations (1.27) or (1.28), we see that local variations in surface composition result in local variations in surface tension. As a consequence, surface motion inevitably arises in the system. The motion of liquid induced by tangential gradients of surface tension is called Marangoni flow [67–69].

This phenomenon was first reported in 1871 by Marangoni [70]. He had observed that a drop of olive oil placed on a water surface spread out spontaneously.

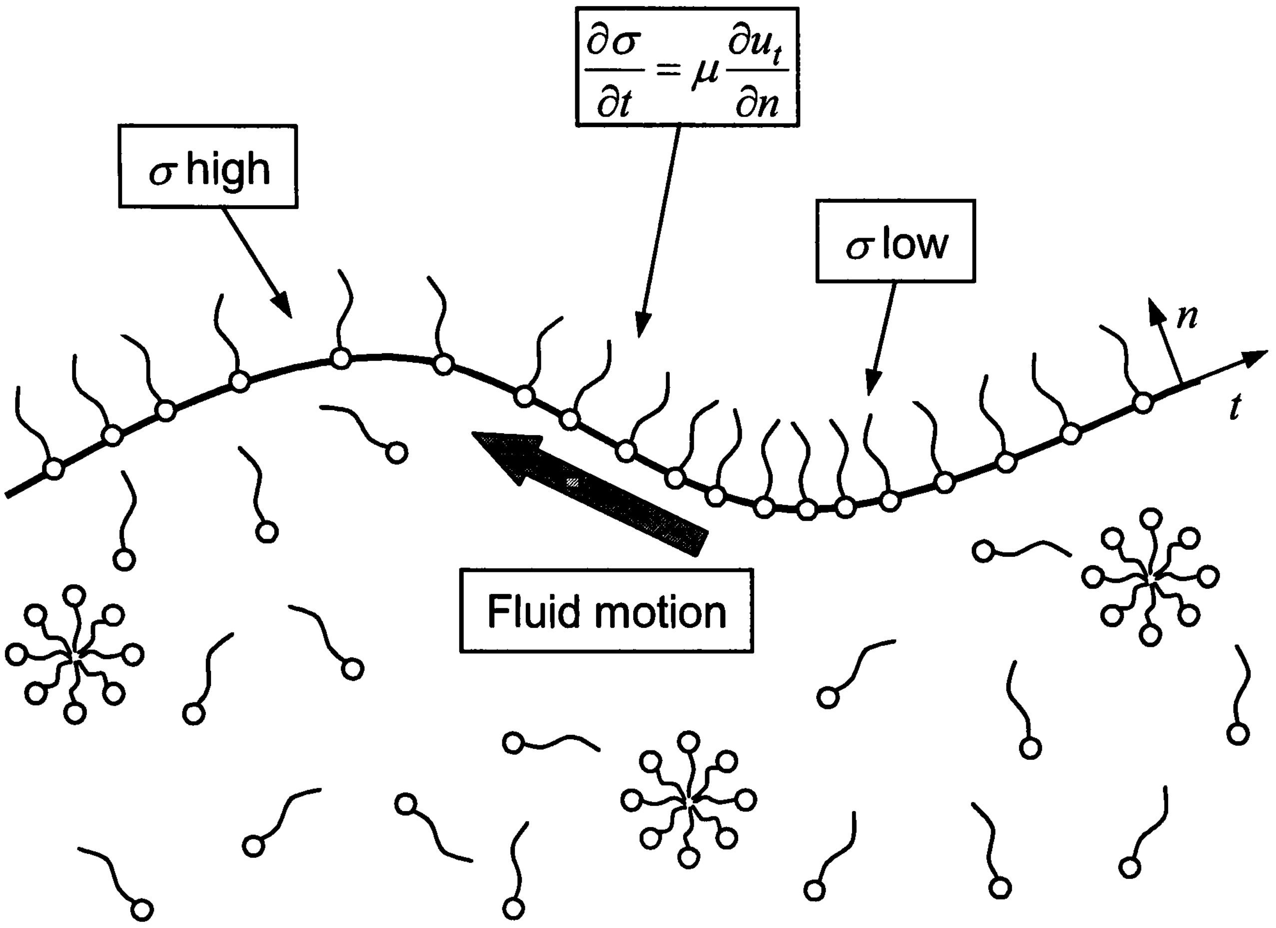

Figure 1.7: Marangoni stress acting on a surface as a consequence of local variations in surface concentration.

He explained this phenomenon in terms of the surface tension acting at the oil-water contact line, oil having a lower surface tension than water. Marangoni observed that

> *"... the spreading of the drops usually happened so quickly that one was not able to observe the advancement of this phenomenon in conventional containers, and only the final result became apparent. I therefore conducted my experiments in a mighty water basin (the great basin of the Tuilerien in Paris), which has a diameter of approximately 70 metres. I threw an oil-soaked sponge into the basin and noticed that a circular line had formed around the sponge, which was the border of the spreading oil. This border advanced rapidly ..."*

Surface tension gradients can be caused by local variations in composition, but also by local variations in temperature, along a free surface [71,72]. In 1900, Bénard [73, 74] investigated a fluid, with a free surface, heated from below in a dish, and noticed a rather regular cellular pattern of hexagonal convection cells.

Figure 1.8: Evaporation of alcohol in a wine glass creating a Marangoni stress that causes the wine to climb to the top of the thin film, where it accumulates in a band that grows until becoming gravitationally unstable and releasing the "tears of wine". Photograph by J.W.M. Bush, Fluid Dynamics Group, MIT, Cambridge, Massachusetts, USA [76].

Rayleigh [75] explained this in 1916 in terms of a buoyancy driven instability. However, in buoyancy driven convection the expected pattern would be a striped pattern of convection rolls, rather than the cellular pattern observed by Bénard. The convection observed by Bénard is now understood to be driven by temperature dependent surface tension forces rather than by buoyancy. Nevertheless, the striped or roll cell pattern formed in buoyancy driven convection is today referred to as Rayleigh-Bénard convection.

The "tears" that form in a wine glass are another classical example (see Figure 1.8). In the meniscus, where the wine meets the glass, evaporation of the alcohol leads to a surface tension gradient that draws liquid up the side of the glass. Gravity eventually wins and the wine returns to the glass in the form of tears [77].

A droplet settling under gravity in a surfactant solution falls more slowly than a droplet settling in a surfactant-free solution. Surfactant adsorbs on the drop interface and reduces the surface tension. Surface convection sweeps adsorbed surfactant towards the rear of the droplet, where it accumulates, further reducing the surface tension there. The interface pulls from this low-tension region towards the leading stagnation point, exerting a Marangoni stress, which increases the drag resisting the flow, thereby retarding the terminal velocity [78–81]. Carbon dioxide bubbles in champagne, for example, rise more slowly than in pure water, because the liquid phase contains dissolved organic molecules, such as proteins, which act as surfactants. Beer, on the other hand, contains about 30 times more surfactants than champagne, and so CO_2 bubbles in beer move far more slowly than those in champagne. There is also less dissolved gas in beer, so bubbles grow and ascend at a more leisurely pace [82].

Recent advances in the field of microscopic flows have shown that active tuning of surface tension effects can be used to drive small-scale flows [83,84].

1.5.2 Marangoni Flow in Liquid Jets

In a liquid jet, whether horizontal or vertical, fresh surface is created very rapidly at the point of emergence of liquid from the capillary tube or nozzle. The surface concentration in this region of the jet flow will consequently be low, which gives a high surface tension. Further downstream, where the rate of surface expansion approaches zero in the absence of gravity, the surface will approach a state of equilibrium. The surface tension approaches that of a surfactant solution in equilibrium (see Figure 1.9). In the presence of gravity, although the surface experiences continuous expansion, the downstream surface concentration will still be high, thus giving a low surface tension. The Marangoni stress will thus oppose the inertia of the jet flow, and retardation of the surface velocity is expected.

Davies and Makepeace, using different nozzle types, showed that the relative reduction in surface velocity, u_s, is greatest near the nozzle [11]. A reduction in surface velocity of up to 24% compared with u_s for the laminar jet of pure water at Re = 1820 was measured by means of high-speed flash cine photography. A reduction in surface velocity was also observed under fully turbulent flow conditions.

Jobert and Leblond employed laser Doppler velocimetry (LDV) to measure

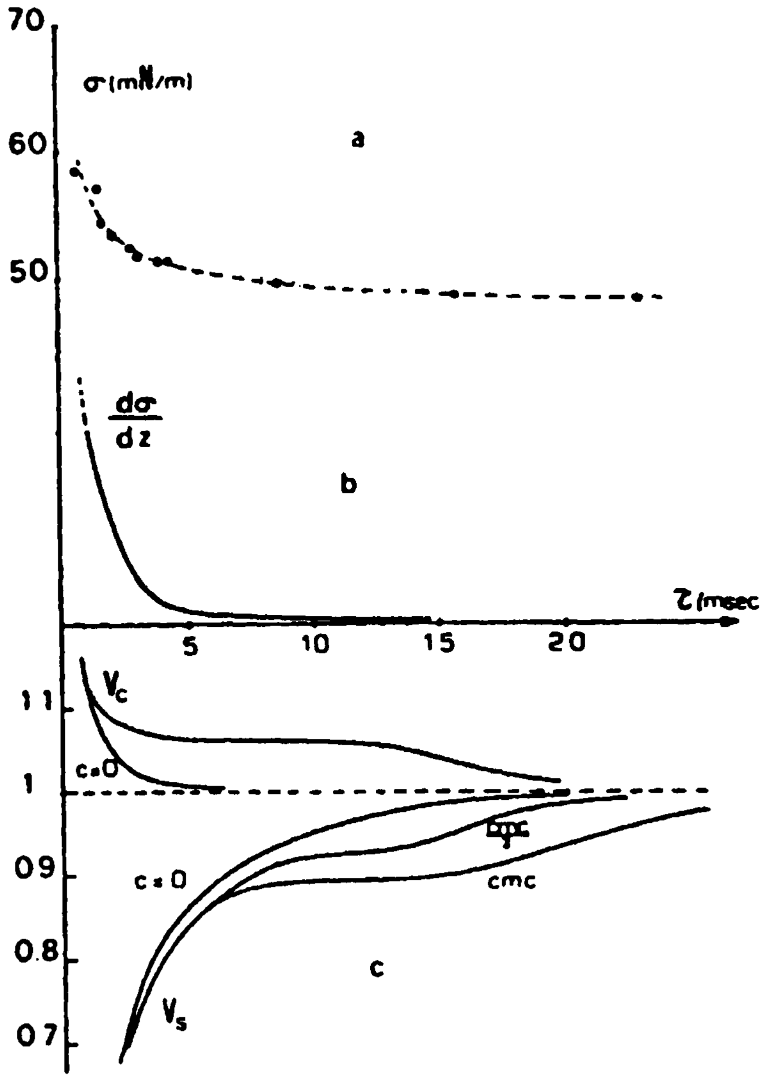

Figure 1.9: Normalised core, V_c, and surface, V_s, velocities over mean surface age, τ, for pure water and two concentrations (cmc and 0.5 × cmc) of SDS, graphs (c), according to Jobert and Leblond [85]. Graphs (a) and (b) show surface tension and Marangoni stress, respectively, as a function of surface age.

Marangoni stresses in liquid jets at Reynolds numbers of $2340 \leqslant Re \leqslant 3060$ [85]. This technique was previously used by Sato *et al.* to measure the velocity profiles in low Reynolds number liquid jets [86]. Jobert and Leblond observed the slow-down in surface velocity when aqueous sodium dodecyl sulfate (SDS) solution was used at two different concentrations (see Figure 1.9).

In a more recent work, Gonzáles-Mendizabal *et al.* applied LDV to liquid jets at Reynolds numbers of $300 \leqslant Re \leqslant 1000$ [87]. Various surfactant mixtures were used to study the effect of surface tension on the fluid mechanics of liquid jets. Unfortunately, dynamic surface tension behaviour was not considered at all, and Marangoni flows were not observed since velocities in the surface layer of the jet were not measured.

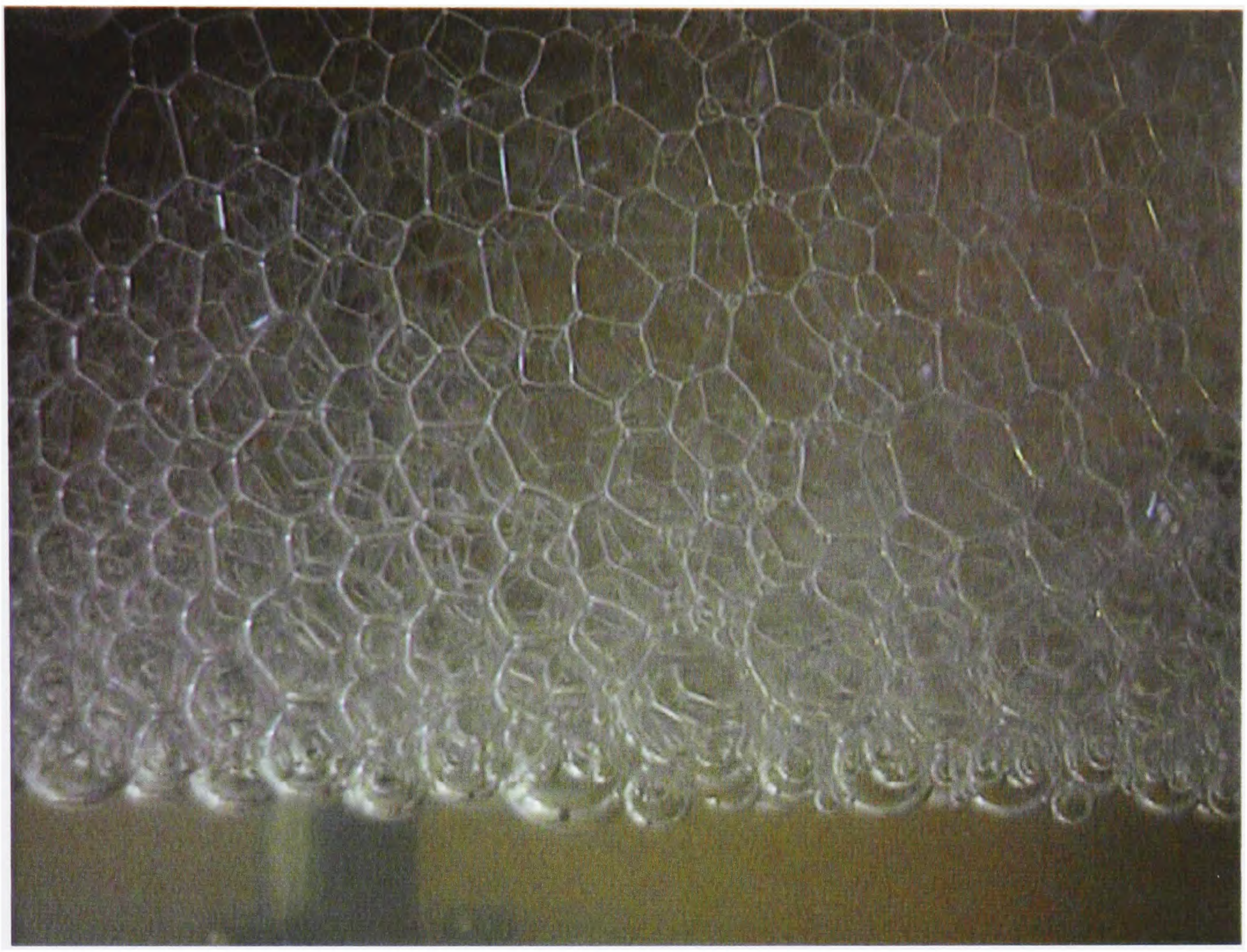

Figure 1.10: Photograph of foam in the riser of a multi-stage foam fractionation column. This method, which employs successive steps of foam fractionation and collapse, can be used to purify proteins, for example, or biosurfactants, or to recover substances extracted by surfactant [93].

1.6 Applications

1.6.1 Foams

During drainage in a foam, film thinning occurs, as shown in Figure 1.10, where the foam becomes increasingly dry with increasing foam height. In the thin part of the film, the surface concentration of the surface-active solute falls with a resulting rise in the local surface tension. A surface force acts towards the region of high surface tension, which causes a counter surface flow of liquid that opposes film drainage and restores the film [88–90]. Foam in surfactant solutions is thus remarkably stable, as the surface tension forces promote a regular structure, and surfactant adsorption prevents coalescence.

Foaming in fractionation and absorption columns can drastically lower capacity and lead to premature flooding, liquid carryover, and solvent losses. In packed columns, foaming can also lead to poor distributor and re-distributor action. Although the factors which lead to film stabilisation, and hence foaming, are well understood qualitatively, prediction of their quantitative importance in practical situations is difficult. Past experience is usually used to identify troublesome foaming systems, sometimes supplemented by foaming tests. Having identified the potential foaming problem, it is usually dealt with by derating the design of the tray and the downcomer. If, for example, foaming occurs unexpectedly in an existing column, it is usual to use antifoaming agents [90–92].

In recent years, advances have been made to gain a better understanding of the physics of foams. Visible light tomography has been used to resolve aqueous three-dimensional foam Plateau borders, and experimental studies were carried out in small-scale columns to investigate the effect of surfactant concentration on the foamability of aqueous solutions by Darton and co-workers [94,95]. Tuinier *et al.* showed that there exists a maximum foamability at a certain surfactant concentration [96], which was also demonstrated by Darton and Sun [95]. In recent years, extensive mathematical modelling of the drainage of foams was carried out by Breward and Howell [97–100] and by Koehler, Stone, and Hilgenfeldt [101–106], and their respective co-workers.

In fractionation columns, foams are clearly unwanted. But there are numerous examples, where aqueous foams are carefully engineered to perform specific tasks, such as fire fighting, dust suppression, and crop treatment, and they were even tested for their ability to lessen the violence of explosions [107]. Foam flows are used in the oil and gas industry, where the transport of particulates in well drilling and clean-out operations benefits from the highly viscous nature of foams [108]. By means of surfactants and other additives, such as alcohols, proteins, and polymers, many familiar products (including shampoo, shaving cream, and beer) are engineered to provide a controlled amount of foaming. The life time of the foamy head on a glass of beer, for example, follows an exponential decay law [109].

1.6.2 Coating

In industrial coating processes, one or several liquid layers are deposited onto a solid substrate, often a flexible web, and are subsequently dried, chilled, or

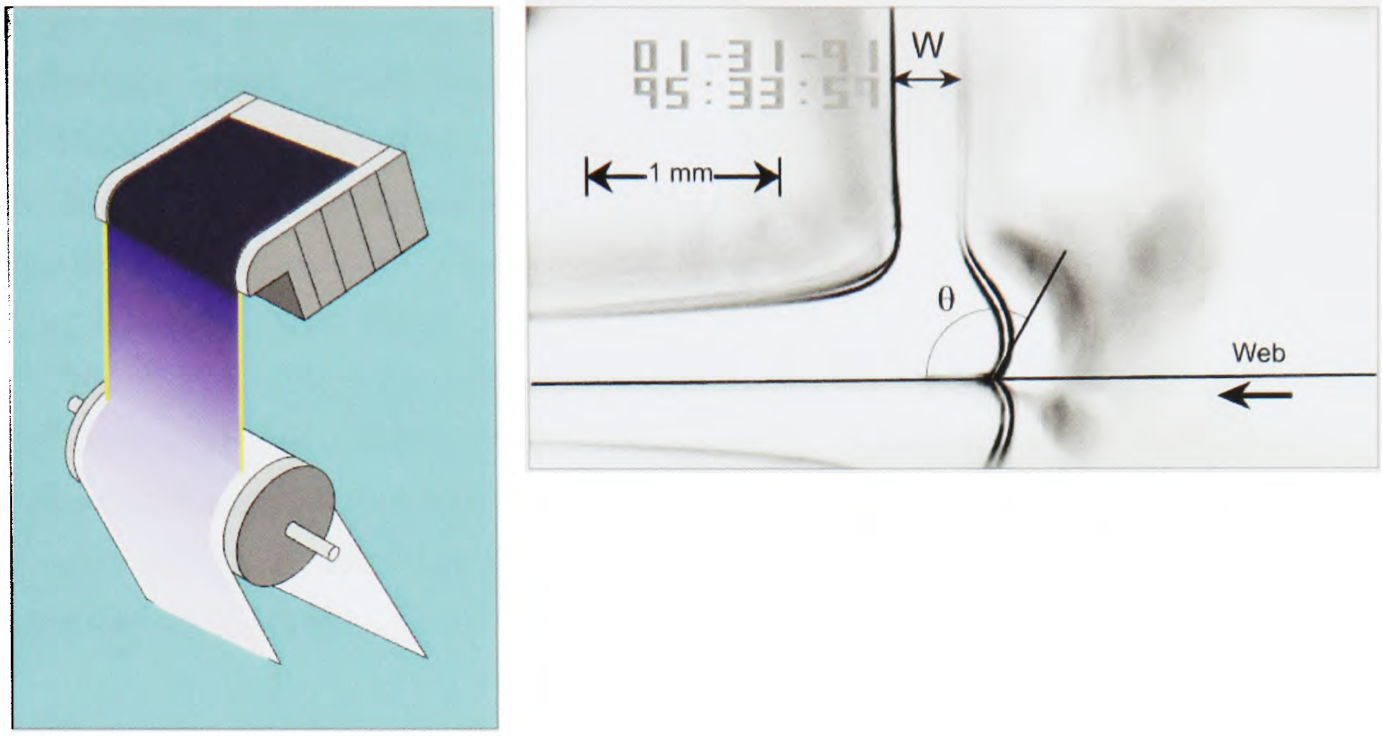

Figure 1.11: Schematic of a curtain coater (left) and a photographic image from visualisation experiments (right) showing details of the flow where the curtain (width W) strikes the web [114]. The dynamic contact angle at the wetting line is θ, the inner line is the bubble trace, and the outer line is a reflection. Both images by Kodak European R & D, Harrow, Middlesex, UK.

cured to form solid films that serve specific functions. At the heart of the coating process lies the displacement of a gas previously in contact with the substrate by a liquid film. The wet thickness of the coated films is typically of the order 1 to 100 μm or more [110, 111].

Curtain coating is often used when thin liquid layers are to be applied to substrate material at very high speeds [112]. The essence of this coating method is that the liquid impinges onto the substrate as a two-dimensional jet. In this context, the word "curtain" means a vertical sheet of liquid, accelerated by free fall (see Figure 1.11).

Coating, in general, is essentially a process of dynamic wetting [113]. In the curtain coater, as the wetting line moves, a dynamic contact angle is observed, which increases with speed (see Figure 1.11). At sufficiently high displacement speeds, when the dynamic contact angle approaches 180°, wetting failure occurs, and air is entrained between the liquid and the substrate. Air entrainment thus limits the coating speed [115, 116].

In the manufacture of photographic film, multiple layers of light-sensitive silver halide crystals and dye-forming chemicals in gelatine are coated onto a substrate (web), which typically moves at 3 to 6 m s^{-1} or more. Near the wetting line, strain rates are well in excess of 10^4 s^{-1} [117]. The influence of surfactants present in the upper layers of the emulsion is extremely important in the coating process. They prevent curtain break-up and ensure uniformity of the thin, stretching layers.

Schunk and Scriven modelled surfactant-generated dynamic surface tension behaviour in slide coating numerically [15,34]. A theoretical analysis of surface-stress-driven thin-layer flow was presented by Schwartz, in which a non-uniformly heated substrate is used to generate Marangoni stresses on the surface of a liquid coating layer [118].

1.7 Studying Flows

1.7.1 Overflowing Cylinder

In an overflowing cylinder (OFC), fluid flows up through the central cylinder and out over the rim into the outer cylinder. At the surface, the fluid flows from the central stagnation point to the outer rim, thereby producing an expanding interface that is readily accessible from the top for surface measurements, as shown in Figure 1.12. The use of this principle to generate clean surfaces can be traced back more than 100 years, when, in 1892, Wilhelm Conrad Röntgen proposed a method of obtaining fresh liquid surfaces, which uses an overflowing funnel [119].

In recent years, the OFC was subject to intensive experimental investigation, using a suite of non-invasive, laser-based measurement techniques to study the fluid mechanics, dynamic surface tension, and surfactant adsorption in the apparatus [32,48,120–123]. Dynamic surface tensions of aqueous solutions of C_{16}TAB were deduced from surface light scattering and ellipsometry measurements [121]. Measurements of the coefficient of ellipticity, which corresponds to surface concentration, showed that the adsorption of C_{16}TAB varies quadratically with radial distance from the centre of the cylinder surface [122]. Neutron reflection measurements were conducted, which serve to convert measured ellipticity to surface concentration [123]. The radial surface velocity in the OFC varies approximately linearly with radial distance from the stagnation point,

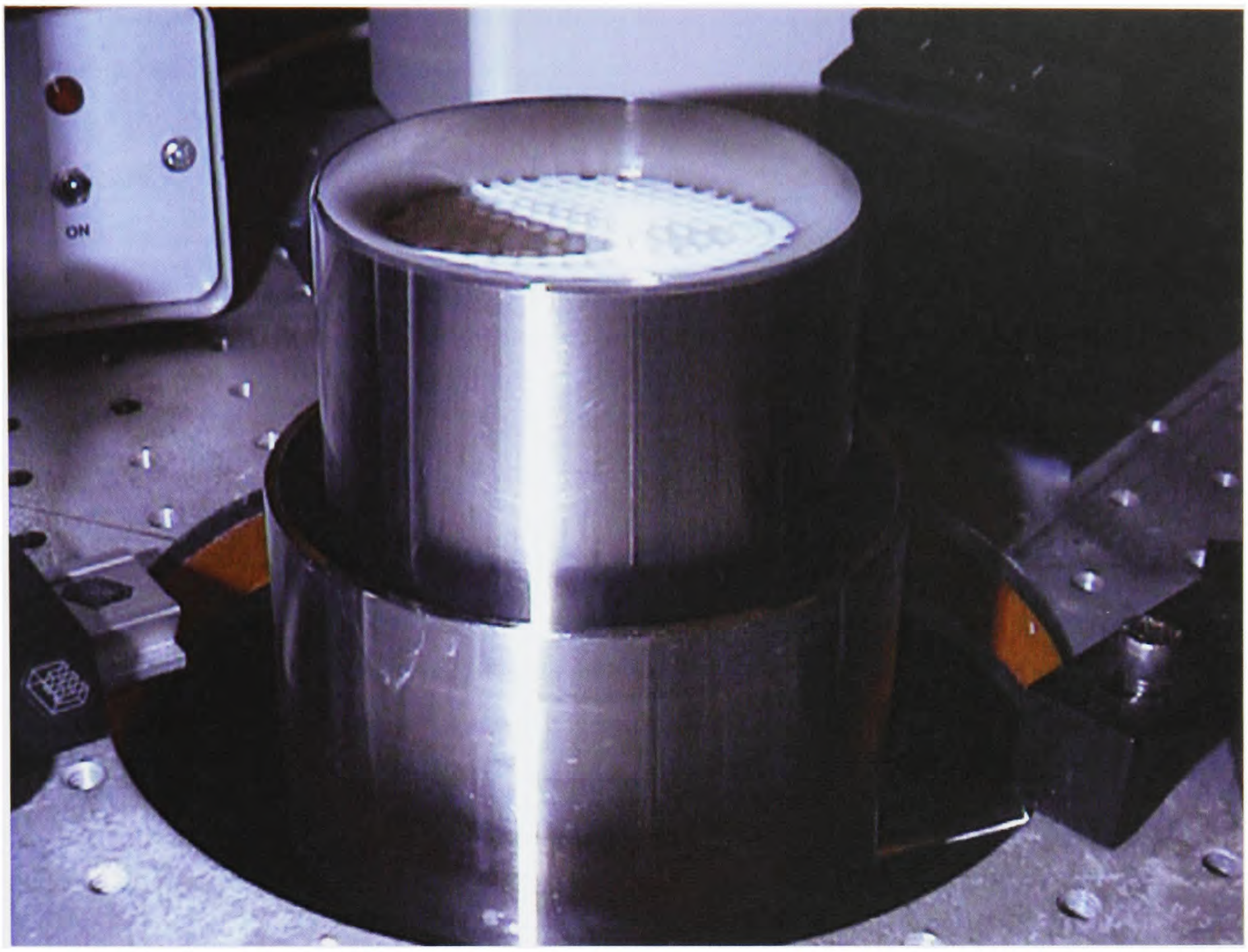

Figure 1.12: Photograph of an overflowing cylinder (OFC). A liquid surface is formed in a cylinder that brims over when liquid is pumped into it from below. The surface is almost flat, and is easily accessible from above for measurements.

as measurements of the fluid mechanics with laser Doppler velocimetry (LDV) showed. The adsorption of surfactant generates a shear stress at the surface that accelerates the surface flow. At bulk concentrations near the cmc, the radial surface velocity is increased by about an order of magnitude [32].

The LDV measurements show that the rate of surface expansion at and near the centre of the OFC surface is constant, but varies with bulk concentration. This experimental value was used in the modelling work on the mass transport of C_{16}TAB in the OFC, assuming diffusion-controlled adsorption [32,33]. The experimental data were found to be in good agreement with the diffusion-controlled model, except for very low concentrations. Later, an extension of the model was suggested that resolves the indeterminacy of the previous modelling work, which had required the use of one parameter from the experiment. Within this extended model, the surface concentration at the stagnation point was chosen such that it reaches exactly zero at the outer rim of the OFC [124]. The ionic character of C_{16}TAB, which had been neglected in the earlier modelling work, was accounted for recently through consideration of the electric double layer [52]. The same work contains a first attempt to model micellar break-down kinetics in an OFC, assuming infinitely fast micellar break-down kinetics of one micelle species. This approach was extended to account for finite micellar break-down rates [64].

1.7.2 Liquid Jets

Jet Figures

The study of the free flow of liquid attracted the interest of philosophers, scientists, and engineers several hundred years ago when Sir Isaac Newton, in his 17th-century *Principia*, determined the motion of water flowing out of a cylindrical vessel through a hole in the bottom [125, p. 733]. Newton observed that the free downward flow of water was a consequence

> "... *of their gravity, and that in falling these parts form a cataract or column of water* ..."

About two centuries later, in 1834, Savart published his studies on the shape and behaviour of liquid jets that issued from a circular orifice in the flat bottom of a cylindrical container [126]. Savart, who extended his studies to include horizontal and even upwards pointing jets, observed two distinct sections of the jet flow—a clear and calm upper part and a cloudy and restless lower part, in which the jet appeared to exhibit oscillating behaviour. Savart soon came to realise that the apparent periodical swelling and contracting of the jet surface in the downstream section was in fact the result of a succession of droplets of different sizes, separated by empty spaces, which gave the jet its cloudy appearance.

Plateau formed a connection between his work on the equilibrium figures of liquids, published in 1851, and Savart's observations on the disintegration of liquid jets [127]. He studied the equilibrium figures of olive oil, which he added to a mixture of alcohol and water that gave the same density as the olive oil in order to eliminate the effects of gravity. The oil that he added to the alcohol/water mixture took on the shape of spheres, and with the aid of wire frame constructions, Plateau was able to produce other equilibrium figures, such as cubes, prisms, and cylinders. Referring to the observations that he made with cylindrical figures, Plateau wrote that

> "*... the properties of the liquid cylinders give a complete explanation of the behaviour of the liquid veins that issue from circular orifices ...*"

Two wire rings were used to form the end bases of an olive oil cylinder within the alcohol/water phase. Plateau stated that molecular attraction forces in the liquid and between the liquid and the wire rings determined the surface shape of the equilibrium figure. Cylindrical equilibrium figures were produced up to a value of 3.0 for the ratio of length to diameter. At a value of 3.6 for the ratio of length to diameter, the cylinders disintegrated into a row of equally-sized spheres, which had their centres on the axis of the cylinder. Smaller spheres of varying size, also on the cylinder axis, were found between the larger spheres.

During the disintegration of the cylinder, Plateau first noticed successive swelling and contracting of the cylinder surface at locations that were equally apart from each other, giving a wave-like pattern. This swelling and contracting became more pronounced with an increase in the ratio of length to diameter. The liquid then retreated from the contracted parts of the cylinder, so that thin cylindrical threads were formed, which experienced the same type of transformation that previously happened to the cylinder, that is, two contracted parts and one swollen part were formed. These newly formed thin cylindrical threads were separated by a swelling of the centre again, and so forth. Eventually, when all thin parts ruptured, the afore-mentioned rotationally symmetric pattern of spheres emerged.

The transformation from a liquid cylinder to a liquid sphere was described by Plateau as the transformation from one equilibrium figure to another. The phenomenon of transformation into isolated spheres applied to any liquid figure that leaves its own state of equilibrium.

Plateau concluded that the axially symmetric jet must disintegrate into isolated axially symmetric spheres, because its ratio of length to diameter becomes too large. Plateau also states that the transformation cannot happen abruptly, but is a continuous process, which begins at the orifice exit. He concludes that the transformation mechanism is the same as in his experiments, which explains the different sizes of droplets that were observed by Savart.

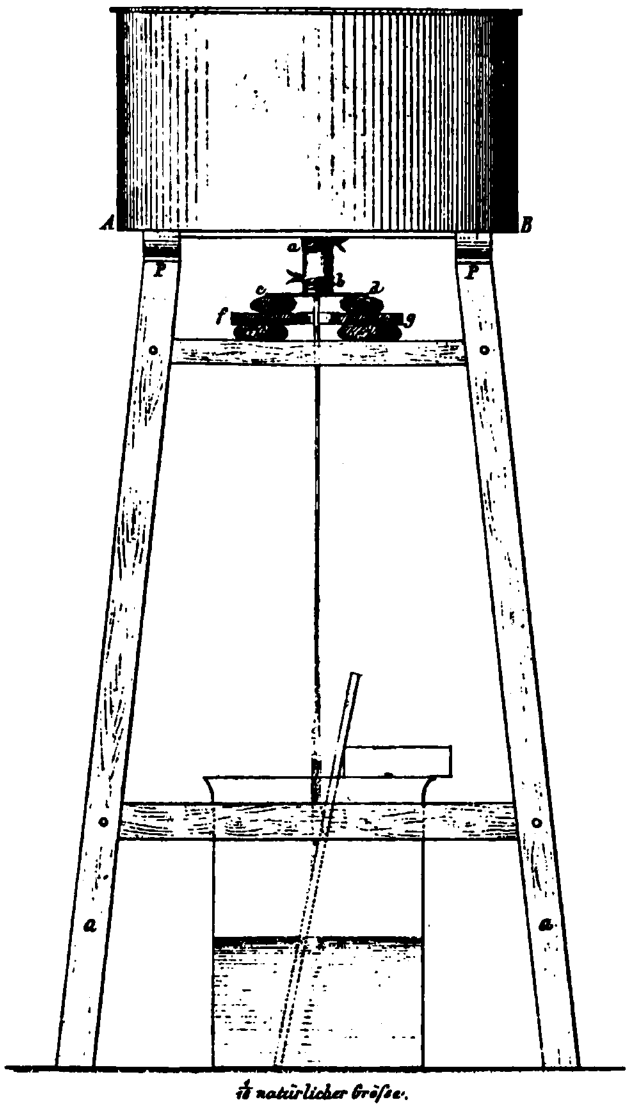

Figure 1.13: Construction of Magnus' jet apparatus [131]. The reservoir had a height of 0.4 m and a diameter of 0.8 m and was mounted on a wooden frame, which was 1.75 m in height. The bottom of the reservoir was equipped with a brass plate that had a circular hole of 5 cm in diameter, which facilitated the use of inserts with orifices of different shape to carry out the investigation.

Hagen, in response to Plateau's experimental work on the stability of cylindrical equilibrium figures,[1] gave a theoretical value of 2.8248 for the ratio of the length and the diameter of the cylinder, at which the transformation into droplets occurs [128]. Plateau, in a response to Hagen's publication, disagreed with Hagen's theoretical treatment, and gave a value of exactly $\pi = 3.1416$ for the stability criterion of the cylinder, which is in line with his experimental observations [129].

---

[1] Note that Hagen referred to Plateau's earlier publications in the 16th and 23rd volume of the *Mém. de l'acad. de Bruxelles.*

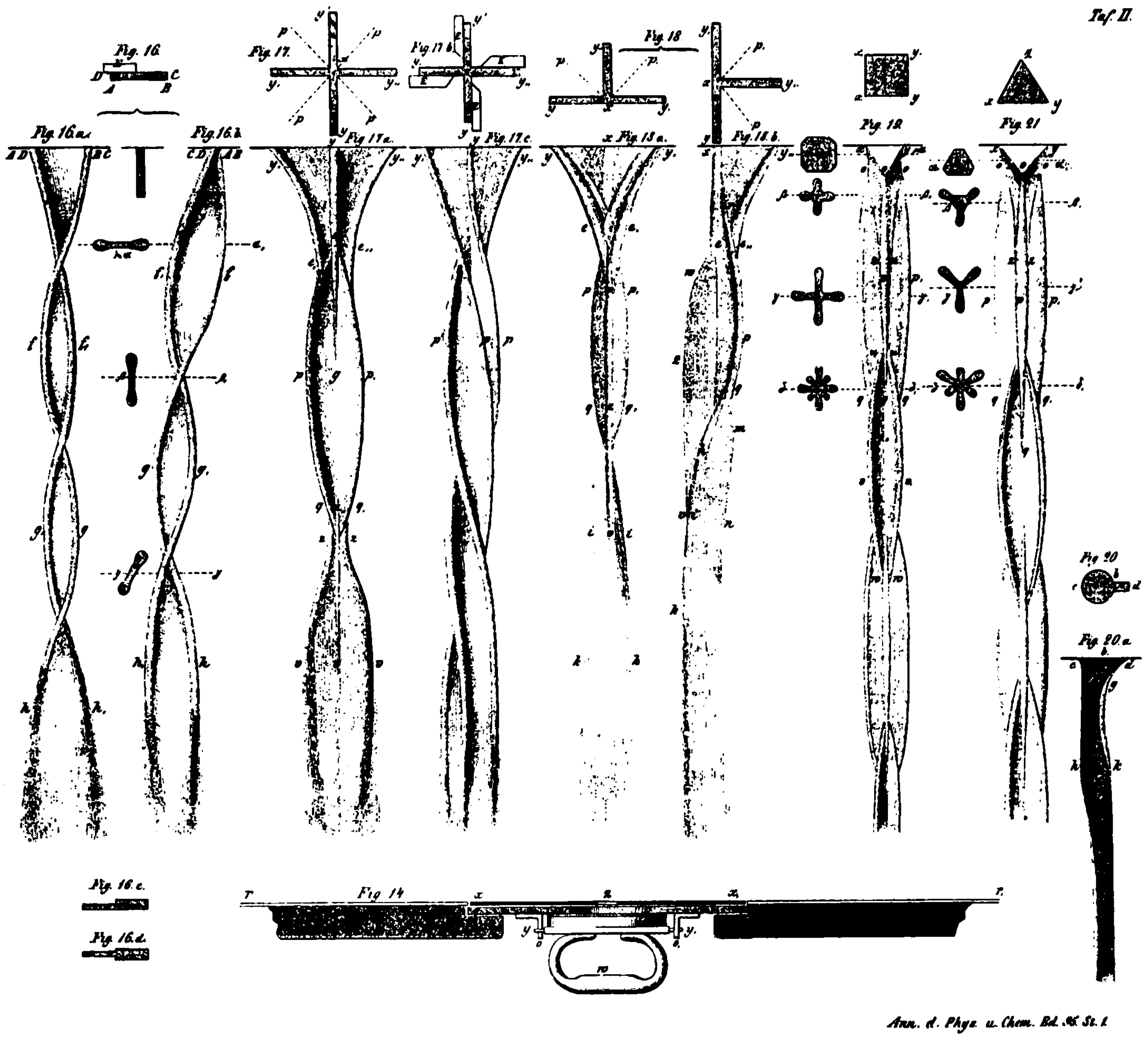

Figure 1.14: Magnus' recordings of the surface shapes of jets produced from non-circular orifices [130].

Magnus' extensive *Hydraulic Investigations* were published in 1855 and 1859, in which he studied the shape of water jets that issued vertically from non-circular and circular orifices and tubes [130, 131]. Some of his elaboratively produced drawings are shown in Figures 1.13 to 1.15. Magnus was careful to control the flow of the liquid inside the reservoir, above the orifice, which was placed in the centre of the bottom of the reservoir, and also to reduce external vibrations that would influence the flow of the free water jet. He varied the water pressure in the reservoir and found that with increasing pressure, the distance from one knot to the next had increased. Another parameter in his study was the flow of water to the orifice inside the reservoir. Placing small obstacles near the orifice inside the reservoir, he observed that this caused the free stream of water to deviate from its usual vertical direction of flow and, in some cases, resulted in a twisted shape of the jets.

When used with circular orifices, Magnus' jet apparatus apparently produced continuous water streams of significant length. He reports that with

> "... *an orifice of 12 mm in diameter and a pressure height of 0.25 m, I obtained a stream of water that ran perfectly smooth and without any swellings 2.5 m vertically downwards.*"[2]

In agreement with Savart's observations, Magnus confirms that the diameter of the water streams is reduced very quickly at the orifice and continues to decrease due to the increase in velocity that is caused by gravitational acceleration.

The Oscillating Jet Method

Researchers such as Savart, Plateau, and Magnus had thus laid the foundations for the use of liquid jets for dynamic surface tension studies. Based on the observations made by these researchers—a steady liquid jet issued from a non-circular orifice oscillates around its equilibrium circular section—Lord Rayleigh gave the first mathematical description of what became known as the Oscillating Jet Method (OJM) in 1879 [132].

Lord Rayleigh was very much inspired by the work of Bidone,[3] who gave an experimental account of the shape of a free stream of water issuing from an elliptical orifice. With respect to Magnus' view on the cause of the repeated expansion and contraction of the water stream—the action of what Magnus termed cohesion forces—Lord Rayleigh stated that it is doubtful whether Magnus had a clear idea upon the subject. Here, Lord Rayleigh attributes the first true explanation of this phenomenon to Buff, who referred the phenomenon distinctly to the capillary force, as he reported in a letter to Magnus, which was published in 1857 [133]. Lord Rayleigh wrote that

> "*Under the operation of this force the fluid behaves as if enclosed in an envelope of constant tension, and the recurrent form of the jet*

---

[2] Since Magnus' jet apparatus had a reported height of only 1.75 m, suitable modifications to the apparatus were probably performed to allow for such jet lengths.

[3] "*Expériences sur la Forme et sur la Direction des Veines et des Courans d'Eau lancés par diverses Ouvertures.*" by George Bidone.

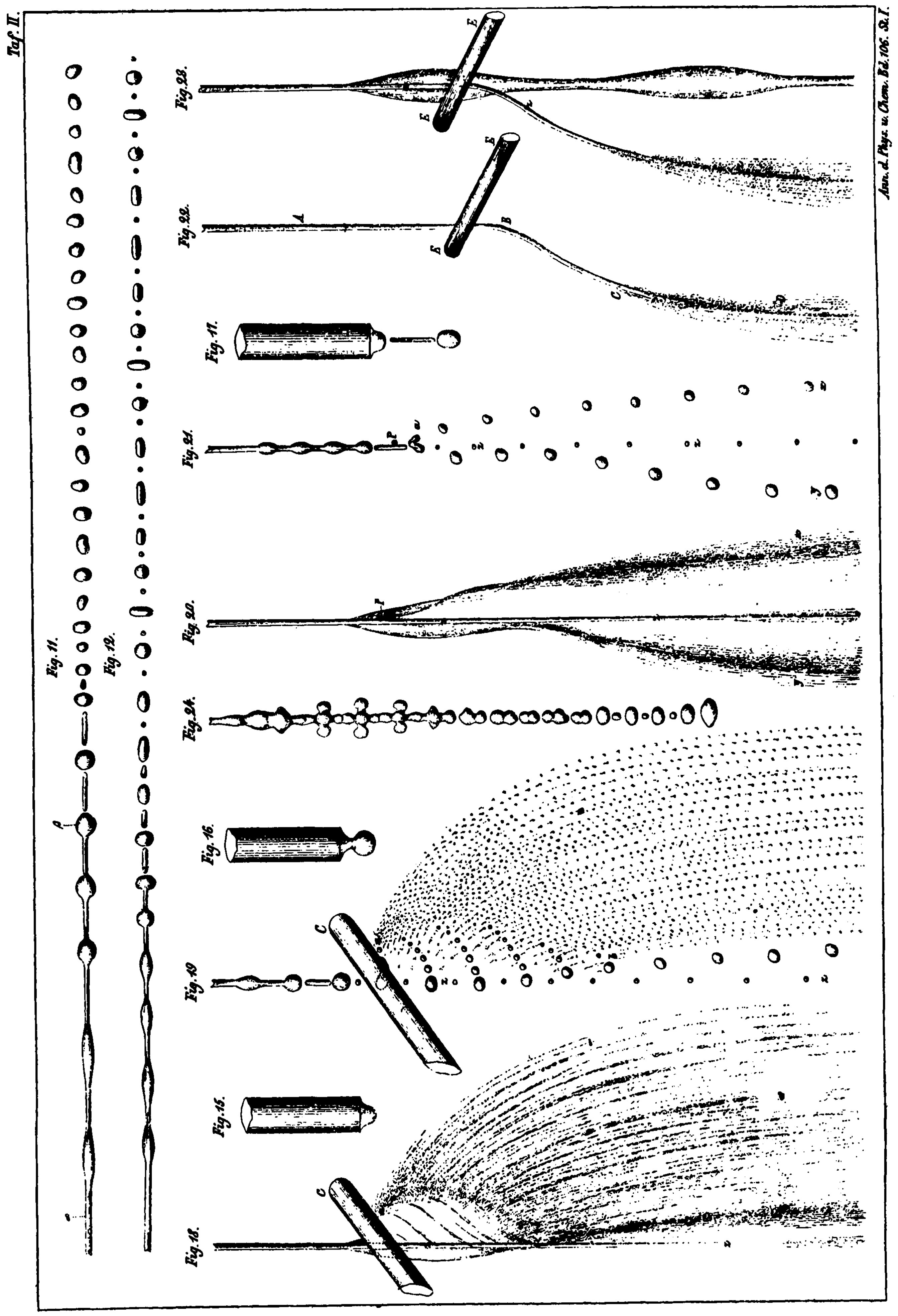

Figure 1.15: Magnus' recordings of the surface shapes and disintegration of jets issuing from circular orifices [131].

> *is due to vibrations of the fluid column about the circular figure of equilibrium, superposed upon the general progressive motion. Since the phase of vibration depends upon the time elapsed, it is always the same at the same point in space, and thus the motion is steady in the hydrodynamical sense, and the boundary of the jet is a fixed surface."*

It was noted that the wave length of the recurrent figure is directly proportional to the velocity of the jet in the orifice, that is, to the square root of the head of water, as reported before by Magnus. This law of proportionality, however, only holds when the vibrations are infinitely small, and it breaks down at higher pressures.

An expected augmentation of wave length caused by the acceleration of vertical jets due to the action of gravity was not observed. Lord Rayleigh argues that most of this augmentation is compensated by a change in the frequency of vibration due to the attenuation (contraction), which is the necessary concomitant of the increased velocity.

What is very important is that the value of the wave length, other parameters being the same, depends upon the nature of the fluid. Lord Rayleigh observed that

> *"... methylated alcohol gave a wave length about twice as great as tap water. This is a consequence of the smaller capillarity."*

When the wave length is considerable in comparison with the diameter of the jet, the vibrations about the circular form take place practically in two dimensions, which simplified the mathematical treatment greatly. In his paper of 1879, Lord Rayleigh confined himself to this two-dimensional treatment of the oscillating jet. The theory of the more general case, which Lord Rayleigh derived and in which there is no limitation upon the magnitude of the diameter, was used and extended later by Pedersen [135] and Bohr [137, 138].

By means of considerations of dimensions, for a given orifice shape, Lord Rayleigh inquired into the nature of the dependence of the wave length upon the surface tension, the liquid density, the cross-sectional area, and the pressure under which the jet escapes. Although this dimensional treatment accounted for the contraction of the jet, the flow was assumed to be frictionless,[4] so that

---

[4] This assumption was also made in Lord Rayleigh's development of the more general theory, in which there is no restriction upon the ratio of wave length to aperture diameter.

the jet velocity was taken to be constant across the jet. Measurements of the corresponding wavelength, the pressure head, and the cross-section of the jet, together with the density of the liquid afford the necessary parameters for the calculation of the surface tension.

In his work of 1879, the experiments reported were designed to illustrate the theory rather than to prove its quantitative application. About a decade later, Lord Rayleigh used his previously published theory of oscillating jets to study the surface tension of aqueous soap (oleate of soda) solutions and alcohol/water mixtures on liquid surfaces less than 10 ms old [134].[5] Figure 1.16 shows Lord Rayleigh's experimental jet apparatus.

Different soap concentrations were used, and the wave lengths were longer than for water, approaching the pure water value with a decrease in concentration. No difference could be detected between the first and the second wave length.

By 1907, Lord Rayleigh's OJM had found little use—Meyer[6] [136] reported its use to measure the surface tension of mercury at a freshly formed surface in 1898—which, as Pedersen explains, was connected with the difficulties in the exact determination of the wave length and the cross-section of the jet [135]. Pedersen's work was therefore primarily concerned with the elaboration of adequate methods to measure these parameters of the oscillating jet flow with high accuracy. Using the more general form of Lord Rayleigh's theory, Pedersen pointed out that neglecting the wave-damping effect of the viscosity is not satisfactory in practice, and he included a correction term for small viscosities. This viscosity correction, however, was later found to be incorrect by Bohr [137].

Amongst the many improvements that Pedersen contributed to the experimental aspects of the OJM was the design of a continuous jet apparatus. To decouple the pressure head, which determines the velocity of the jet, from the speed of the water supply from the tap, he employed Röntgen's method of the overflowing funnel [119]. A similar experimental arrangement was used by Bohr [137].

Further refinement of Lord Rayleigh's OJM was presented by Bohr in his treatment of the oscillating jet flow, which was published very shortly after

---

[5] The surface age is given as the quotient of distance travelled on the surface of the horizontal jet and jet velocity. We remember that Lord Rayleigh's theory assumes constant jet velocities across the stream.

[6] Meyer references Piccard's study of 1890, in which Lord Rayleigh's OJM appears to have been used for measuring the surface tension of mercury at newly created surfaces as well.

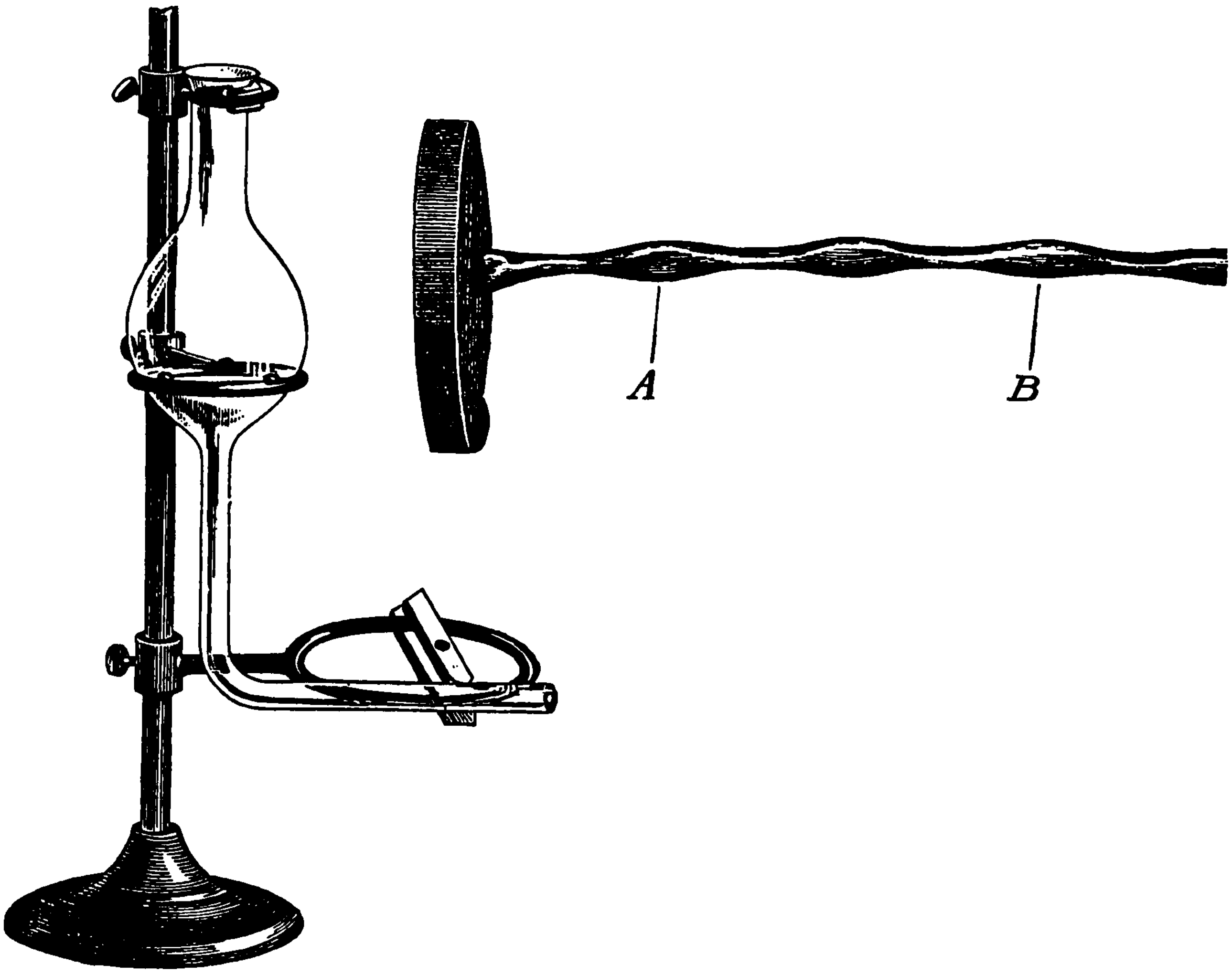

Figure 1.16: Lord Rayleigh's horizontal jet apparatus and an engraving from a photograph of a water jet [134]. The reservoir was an ordinary flask, 8 cm in diameter, to which was attached a tube of 1 cm in diameter, bent at a right angle. The elliptical aperture was rather fine, about 2 by 1 mm, and was perforated in thin sheet brass, attached to the tube by cement. The distance between the points A and B corresponds to two wave lengths.

Pedersen's work [137, 138]. Based on the equations of motion and the equation of continuity, Bohr carried out a hydrodynamical analysis of the oscillating jet flow, in which the viscosity was retained. In this way, Bohr derived a viscosity correction. As another refinement to Lord Rayleigh's OJM, Bohr also considers the effect of the inertia of the surrounding air on the wave length. More important, however, are Bohr's remarks on the development of the velocity profile in the jet. Stating that in the jets produced in the experiments, the velocity is greater in the middle of the jet than close to the surface, Bohr attempted to get an idea of the rate at which the velocity-differences between the bulk and the surface of the jet would be extinguished by the viscosity of the liquid. Considering a circular fluid-cylinder, in which each part moves with a velocity parallel to the axis of the cylinder, Bohr finds a coarse estimate of the rate of decay of exiting Poiseuille flows.[7] Bohr used this estimate to establish the distance from the exit of the drawn-out glass tube, at which the velocity deficit between the surface and the bulk is small.

Addison set out to design a simple laboratory apparatus, which would make the OJM a standard laboratory tool to measure dynamic surface tension of low-viscosity liquids [139–142]. This meant that the rather large liquid hold-up, that was inherent to the designs by Pedersen and Bohr, had to be reduced, whilst retaining the continuous operation of the apparatus. Ensuring that the flow rates were large enough for the wave length to be at least equal to, but mostly larger than the jet diameter, Addison used Lord Rayleigh's simple OJM for two-dimensional oscillations, where the wave length varies directly with the flow rate. The first few wave lengths near the capillary tube orifice were ignored, because they represented the period necessary for the establishment of fluid equilibrium.

Using a plate orifice, Addison applied Lord Rayleigh's OJM to vertical jets, for which he gave a method that enables the vertical wave length at any position to be converted to the corresponding horizontal jet value, thus enabling the methods used for the horizontal jets to be applied to vertical jets also.

The dynamic surface tension behaviour of aqueous solutions of alcohol, at varying bulk concentrations, was studied by Addison along the length of the jet. The waves in an oscillating jet lengthened as adsorption at the surface proceeded and reached a constant value only when the adsorption was completed.

An extension of Bohr's OJM for vertical jets was proposed by Hansen *et al.* [143], who also derived a method for determining the dependence of the axial surface velocity on the axial distance near the orifice. This method was used by Defay and Pétré to correct surface tension data of pure liquids that were obtained by applying Bohr's OJM [144].

Rideal and Sutherland [145] obtained dynamic surface tension data of aqueous solutions of alcohol by means of Bohr's horizontal OJM. The authors found that the results depended strongly on the type of orifice used and estimated the boundary-layer growth within the jet using an analogy with the flow behind an infinitely thin plate.[8] Then, from a simplified solution of the mass transport

---

[7] See also Equation (3.49) in Section 3.6.3.

[8] The same analogy was used by Scriven and Pigford [160, 161], as outlined in Section 2.3.

problem, Rideal and Sutherland found that diffusion to the surface alone did not predict the experimental surface concentration data, which were deduced from the measured surface tension data using a Szyszkowski-type equation of state.[9] The authors assumed that this discrepancy was due to the existence of hindrance to molecules entering the surface. However, the calculations put forward by Rideal and Sutherland assume that the diffusion and flow processes do not interact, and the authors point out that this assumption is most certainly incorrect.

The effects of surface tension gradients brought on by expansion and contraction of the surface of an oscillating jet was studied by Quinn and Saville, who developed a theory, which is based on a description of small amplitude deformations of a viscous cylinder [146]. It was found that these gradients are large enough to severely disguise measurements made with oscillating jets.

Thomas and Potter [147] applied Bohr's horizontal OJM to measure the dynamic surface tension of water and aqueous surfactant solutions using a range of different orifice tubes and over a surface age range from 0.6 to 75 ms.[10] The surface tension values obtained from the first few measured waves showed a strong dependence on the type of orifice tube used, indicating that the orifice tubes did not conform with the Bohr equation. By fixing the position of the orifice tube and standardising with water, a relative method was developed for determining dynamic surface tensions that were independent of the tubes used and of the flow rate. An orifice and flow rate correction method similar to that used by Thomas and Potter was employed by Defay and Hommelen [148].

Kochurova and Rusanov [149] applied Bohr's OJM to vertical jets of water to measure the dynamic surface tension of water for surface ages of 0.7 to 8.0 ms. The surface age was determined by dividing the axial distance from the orifice with the axial surface velocity at that point, as defined by Hansen [7]. The axial surface velocity was inferred from the method given by Hansen *et al.* [143]. Kochurova and Rusanov argued that for surface ages of less than 3 ms, the dynamic surface tension of water is higher than the equilibrium value.

Similar findings were reported by Thomas and Potter [147]. Employing a diaphragm-type elliptical orifice that was coated with paraffin to make it non-

---

[9] See Equation (1.29) in Section 1.4.

[10] The surface age was given by the quotient of the distance between the orifice and the midpoint of the wave and the mean velocity of the jet, which was calculated from the measured flow rate and the measured cross-sectional area at that distance.

wetting to water, and using Bohr's OJM on a vertical jet, Caskey and Barlage's measurements showed that for surface ages greater than 4 ms, the dynamic surface tension of water was independent of exposure time and flow rate and agreed closely with the equilibrium value [150].

Other Methods Involving Liquid Jets

The generation of second harmonic light from the surface of a water jet (2 mm in diameter and with a constant velocity of 1.8 m s^{-1} everywhere) was used to study the dynamics of the adsorption of *p*-nitrophenol by Castro *et al.* [151]. The distance from the nozzle tip to the laser spot was varied from 1 to 40 mm, which corresponded to times of 0.55 to 22 ms. Experimental data, which show low surface concentrations near the nozzle, were reported for bulk concentrations of 10, 33, and 67 mM. The kinetics of adsorption were found to be consistent with a kinetic Langmuir-Hinshelwood model, as given in Equation (1.10).

Kochurova and Rusanov [152, 153] reported in their work that the measurement of the surface electric potential of anionic, cationic, and non-ionic surfactants in aqueous solution—a method that was first used by Posner and Alexander [154–156] on horizontal jets, and for which Noskov [9] gave a detailed review—can be used to investigate the adsorption mechanisms of surfactants. The change in surface potential along a vertical liquid jet was measured with respect to some constant reference surface potential. The authors derived a correlation between the changes in the dynamic surface tension and the surface potential. They concluded that if this correlation is linear, then the adsorption process is diffusion-controlled. Deviation from the linear dependence shows that an adsorption barrier is present. Aqueous solutions of C_{16}TAB at two different concentrations (0.28 and 0.56 mol m^{-3}) were used. The linear dependence was shown in the case of the lower concentration. The correlation deviated from the linear dependence in the case of the higher concentration.

In a second method, the surface potentials of aqueous solutions of hexanoic acid ($C_6H_{12}O_2$) and heptanoic acid ($C_7H_{14}O_2$) were measured. The data obtained were transferred into time-dependent surface coverage—the surface age was estimated using Hansen's [7] approximation—by use of an equilibrium isotherm. Ward and Tordai's [16] diffusion equation was extended to account for the velocity profile inside the jet and used to calculate the time dependence of the surface coverage for two acids. The same procedure was carried out for an aqueous solution of heptanol. In the case of the acids, the calculated surface coverage was higher than the measured surface coverage, which led the authors to the conclusion that an adsorption barrier exists. The agreement between calculated and experimentally obtained values was very good in the case of the alcohol, so that no barrier seemed to be present in that case.

In a precursor to the present work, Hutchison *et al.* used ellipsometry to study the adsorption kinetics of aqueous C_{16}TAB solutions in a horizontal liquid jet [157]. Assuming constant jet velocity throughout, the surface coverage was studied on the 1 to 20 ms time-scale. A simple analysis of the adsorption data yielded satisfactory agreement with Ward and Tordai's [16] equation for diffusion-controlled adsorption.

Recently, Marmottant *et al.* reported an indirect method, in which a liquid jet is used to produce an expanding circular liquid sheet by directing it onto a small disk [158]. The diameter of the sheet depends on the amount of surfactant diluted in the system. The apparatus enabled the authors to measure dynamic surface tensions on the 10 to 100 ms time-scale, and to observe Marangoni flow. In the surfactant experiments, octanol and an industrial detergent, for which the exact composition was unknown, were used. The use of Ward and Tordai's [16] diffusion equation confirmed diffusion-controlled adsorption.

Absorption and Diffusion Studies

The short times of exposure of liquid to gas achievable in liquid jets led to the utilisation of this technique in the study of the mechanisms of gas absorption and diffusion studies [159–164]. Cullen and Davidson [159] made an interesting observation when their vertical water jet was contaminated with a surface-active agent (Teepol). A stagnant film developed from the jet-collecting reservoir at the bottom towards the point of jet emergence. Its height varied with the velocity of the jet, being smaller for higher velocities, and was independent of the Teepol concentration, provided it was greater than a mass fraction of 2×10^{-3}. Cullen and Davidson believed this end effect to be a free surface energy phenomenon. Any surface-active material in the jet or take-off tube would tend to collect at the relatively stagnant horizontal surface of the take-off tube and form a film of low surface tension. The jet would have a higher surface tension and in an attempt to minimise the energy, the lower surface tension film would tend to spread upwards over the whole jet. This tendency was resisted by the shear stress between the surface film and the jet, and a balance was established between the two effects. Such phenomena were also observed by Addison and Elliott [165]. Recently, Awati and Howes studied surfactant-induced stationary modes on cylindrical water jets that strike an obstacle placed in the stream path [166].

1.8 Background

The collaboration in this study is based on a previous project, which dealt with the study of surfactant adsorption in an OFC, as outlined in Section 1.7.1. In this study, the adsorption kinetics of surfactants in a steady laminar liquid jet at a high Reynolds number were studied experimentally, as well as numerically and analytically. This thesis focusses on the theoretical study. The same laser-based surface analysis techniques that were already employed in the OFC project—laser Doppler velocimetry (LDV) and ellipsometry—were applied in the experimental part of the investigation, which was conducted in the Physical and Theoretical Chemistry Laboratory at the University of Oxford. A proof-of-principle experiment showed the applicability of these techniques to laminar jets [157]. The development of the numerical and analytical model of the adsorption process in the jet flow was carried out in the Department of Engineering Science at the University of Oxford.

1.9 Objectives

The overall objective of the study presented in this thesis was the investigation of surfactant adsorption and dynamic surface tension behaviour (Marangoni flow) at expanding surfaces. The specific aims of this study were

- to design an experimental apparatus for a vertical and laminar liquid jet which allows the investigation of surfactant adsorption and dynamic surface tension behaviour using non-invasive laser-based techniques (LDV and ellipsometry) for surface ages in the 1 to 100 ms timescale,
- to develop a mathematical model, within the framework of a Computational Fluid Dynamics (CFD) programme, of the liquid jet incorporating diffusion-controlled surfactant adsorption in the absence and presence of micelles and Marangoni flow,

- to validate the mathematical model by means of the experimental data,
- to identify engineering applications for the techniques developed in this work.

The mathematical model of the adsorption process in the jet flow was developed using the CFD code FIDAP, one of FLUENT's general-purpose finite-element CFD solvers. Although sophisticated, commercially available CFD programmes, such as FIDAP, are capable of predicting Marangoni flows that arise from *applied* surface tension gradients, these programmes are currently not directly capable of modelling Marangoni flows that arise from the adsorption of surfactant, and there is no "off-the-shelf" CFD solution to free-surface flow problems involving the adsorption of surfactant available.

In a recent article on the current status and the potential of CFD for designing process equipment, Joshi and Ranade gave their perspective on the developments needed for overcoming current limitations [167]. The authors point out that providing non-invasive, spatially, and temporally resolved measurements of single-phase and multi-phase systems are important for verifying the applicability of the existing and new physical models. Furthermore, close communication between experimentalists and those developing numerical models and methods is essential. Capturing small-scale features of the interface, and the computation of gradients at the interface are among the limitations of current models, according to Joshi and Ranade. Development is needed to overcome these limitations, and the authors single out the development of physical models that describe the influence of surface tension on transport rates.

We sought to make significant contributions in both fields—through the application of non-invasive measurement techniques and through the development of mathematical modelling techniques—in the form of a close collaboration of experimentalists and model developers here at Oxford. This collaboration formed the underlying basis of this project, and ensured the immediate validation of the modelling work with experimental results and vice versa.

The ultimate objective of this programme is to apply the techniques that we developed to engineering applications, such as coating flows and foams. In this context, the modelling techniques will be of prime importance, because most of these engineering applications are rather complex, and the use of experimental techniques to study interfacial behaviour is virtually impossible. Before we make attempts to model dynamic surface tension behaviour in such complex systems, however, we need a clear understanding of the underlying physico-chemical mechanisms. Studying flow systems such as the jet flow or the overflowing cylinder allows us to gain this understanding.

1.10 Outline of Thesis

The asymptotic behaviour of laminar jet flows of a pure liquid in both the downstream region and in the nozzle exit region is studied in Chapter 2. We derive the final ratio of contraction in horizontal jets at high Reynolds numbers through conservation of mass and momentum, and we investigate the effect of gravity on the downstream jet flow in vertical jets using the energy principle. A boundary-layer treatment of the jet flow at the nozzle exit is used to find the cube-root dependence of the axial surface velocity on the axial jet coordinate. The relevant literature is discussed.

In Chapter 3, we outline the CFD model of horizontal and vertical laminar jets of a pure liquid. We present the set of flow-governing field equations and the boundary conditions, and we detail the flow geometry and the discretisation of the computational flow domain. A short overview of the work in the literature on creeping jet flows in the absence and presence of gravity is given. Computed results for horizontal water jets at high Reynolds numbers from the CFD model are discussed next, where the effects of the flow parameters are investigated separately. This study is followed by a comparison of computed results for vertical jets with experiments. Relevant literature on the numerical computation of the hydrodynamics of vertical jet flows is presented. Chapter 3 concludes with an investigation of the effect of wetting of the nozzle tip on the fluid mechanics of the jet flow.

A theoretical analysis of surfactant adsorption in the water jet is performed in Chapter 4. The boundary-layer treatment presented in Chapter 2 is extended to include the surfactant-generated surface shear (Marangoni) stress. This shear stress is then determined from a simplified solution of the coupled mass-transfer problem in the absence and presence of micelles.

Chapter 5 details the CFD model of surfactant adsorption in the jet flow. The field equations that govern the diffusion and convection of surfactant monomers and micelles are presented, and meshing requirements that arise from the added complexity of the coupled mass-transfer problem are discussed. The boundary conditions for both monomers and micelles are detailed. The thermodynamical relationships, which connect surface concentration and surface tension with the bulk concentration, are presented. The equilibrium between monomers and micelles is discussed, and the source terms in the convection-diffusion equations for monomers and micelles are expressed through micelle-monomer kinetics. Chapter 5 closes with the presentation of the hybrid CFD model, in which we implement the two major consequences of our theoretical model from Chapter 4—the maximum Marangoni stress at the nozzle exit and the finite surface concentration at that point—into the CFD model.

Computed results for the surface concentration, surface tension, and surface velocity that were obtained from the hybrid CFD model are discussed in Chapter 6. These results are compared with experimental data, for the cationic surfactants C_{16}TAB, below and above the cmc, and for C_{14}TAB below the cmc.

The experimental investigation is briefly portrayed in Chapter 7. Finally, Chapter 8 presents the conclusions, and Chapter 9 suggests future developments for the project. The Appendix contains GAMBIT and FIDAP journal file listings of the CFD models, listings of Fortran user-subroutines, and a collection of experimental data.

Chapter 2

Asymptotic Behaviour of Jet Flows

2.1 Final Ratio of Contraction in Horizontal Jets

In 1955, Harmon performed a simple analysis for a steady laminar liquid jet, which issues horizontally from a circular nozzle [168]. Neglecting the effect of gravity and drag forces acting on the free surface of the jet and the effects of surface tension and viscous dissipation, he applied the equation of continuity of jet mass and conservation of momentum in the axial direction to calculate the ratio of jet contraction.

At the nozzle exit ($z = 0$), the mean nozzle exit velocity is $\overline{u}_0$, and the jet radius equals the radius of the nozzle, R_0 (see Figure 2.1). The liquid leaves the nozzle with a parabolic velocity profile, which is given by

$$u(r, z = 0) = 2\overline{u}_0 \left(1 - \left(\frac{r}{R_0}\right)^2\right). \tag{2.1}$$

Inside the nozzle, the flow is constrained by the no-slip condition at the nozzle wall, which exerts a shear stress on the liquid. The constraint of the nozzle wall is removed when the liquid leaves the nozzle, and the velocity profile is then free to relax. During the relaxation of the velocity profile between the nozzle exit and a downstream position z, the shear stress within the jet disappears completely, and the velocity profile of the jet must gradually become uniform.

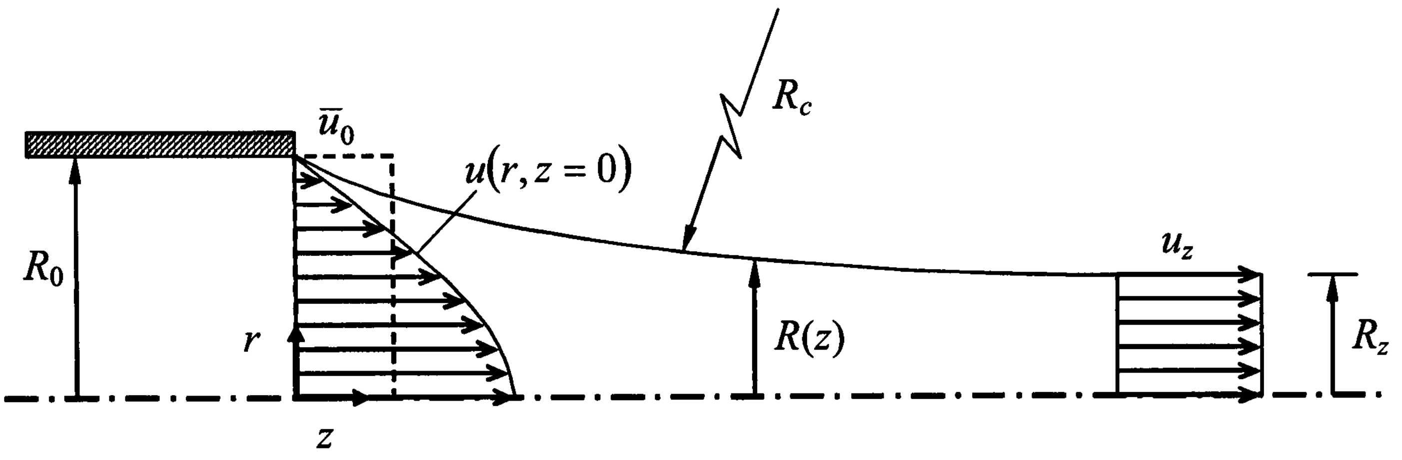

Figure 2.1: Horizontal laminar liquid jet. R_0, nozzle radius; $\overline{u}_0$, mean nozzle exit velocity; $u(r,z=0)$, parabolic nozzle exit velocity profile; r, radial jet coordinate; z, axial jet coordinate; $R(z)$, free surface position; R_c, curvature parameter (see also Equation (3.14) and Figure 3.1 in Section 3.2.1); u_z, downstream jet velocity; R_z, downstream surface position.

At this downstream position z, the uniform jet velocity is u_z and the jet radius is R_z, as indicated in Figure 2.1. The continuity equation between the nozzle exit and this downstream point is then given as

$$4\overline{u}_0 \int_0^{R_0} \left(1 - \left(\frac{r}{R_0}\right)^2\right) r dr = R_z^2 u_z, \tag{2.2}$$

which has the solution

$$\left(\frac{R_0}{R_z}\right)^2 = \frac{u_z}{\overline{u}_0}. \tag{2.3}$$

The formulation of momentum conservation in the axial direction yields

$$8\overline{u}_0^2 \int_0^{R_0} \left(1 - \left(\frac{r}{R_0}\right)^2\right)^2 r dr = R_z^2 u_z^2, \tag{2.4}$$

and has the solution

$$\frac{2}{\sqrt{3}} \frac{R_0}{R_z} = \frac{u_z}{\overline{u}_0}. \tag{2.5}$$

Combining Equations (2.3) and (2.5) gives the ratio of jet contraction,

$$R_z^* = \frac{R_z}{R_0} = \frac{\sqrt{3}}{2} = 0.866. \tag{2.6}$$

The ratio of the velocities, from Equation (2.3), is then

$$u_z^* = \frac{u_z}{\overline{u}_0} = \frac{4}{3}. \tag{2.7}$$

Several authors confirmed Harmon's result for different Newtonian liquids in their experimental work on jet contraction of horizontal liquid jets [169, 170, 172]. However, the predicted value in Equation (2.6) for R_z^* is observed only for Reynolds numbers of $\mathrm{Re} > 150$. For Reynolds numbers smaller than 100 the ratio increases, and for $\mathrm{Re} < 16$ swelling behaviour of the jet is observed, that is, $R_z^* > 1.0$ [173, 174].

The Reynolds number, Re, in the jet flow is based on the geometry of the nozzle (inner diameter $2R_0$) and the mean nozzle exit velocity, $\bar{u}_0$, and is defined as

$$\mathrm{Re} \equiv \frac{2R_0\rho\bar{u}_0}{\mu} = \frac{2R_0\bar{u}_0}{\nu}. \tag{2.8}$$

It relates inertia forces to viscous forces. In this thesis, we assume that the jet flow is laminar for $\mathrm{Re} \leqslant 2000$, which is the usual laminarity criterion for a pipe flow.

In the 1960's, Middleman and Gavis [170, 171] completed the axial momentum balance in Equation (2.4), in which surface tension forces as well as the axial component of the stress tensor were not considered. After some confusion about the correct incorporation of surface tension, the completed axial momentum balance, applied to a section of a steady state, horizontal jet at the tube exit and to a section at a point far downstream was formulated by Gavis [175] as

$$2\pi \int_0^{R_0} \left[\rho u^2 - \tau_{zz}\right]_0 r dr - 2\pi \int_0^{R_z} \left[\rho u^2 - \tau_{zz}\right]_z r dr = 2\pi\sigma \left(R_0 - R_z\right). \tag{2.9}$$

The first term on the left-hand side of Equation (2.9) represents the rate of flow of momentum into the section at the tube exit. The stress $(\tau_{zz})_0$, consisting of the hydrostatic pressure caused by surface tension and an axial stress arising because of the relaxation of the velocity profile from parabolic to flat, which begins at the nozzle exit, is given by

$$(\tau_{zz})_0 = -\frac{\sigma}{R_0} + 2\mu\left(\frac{\partial u}{\partial z}\right)_0. \tag{2.10}$$

The second term on the left-hand side of Equation (2.9) denotes the rate of flow of momentum out of the downstream section. There is no axial velocity gradient, and $(\tau_{zz})_z$, containing only the surface hydrostatic pressure, is given by

$$(\tau_{zz})_z = -\frac{\sigma}{R_z}. \tag{2.11}$$

The term $2\pi\sigma R_0$ on the right-hand side of Equation (2.9) represents an interfacial force between the liquid and the solid material of the nozzle, which holds the jet to the nozzle at its exit. The term $2\pi\sigma R_z$ describes a force on the jet at the downstream section, exerted at its surface by liquid further downstream.

The integration of the first integral in Equation (2.9) cannot be performed completely without explicit knowledge of the decaying velocity profile $(\partial u/\partial z)_0$ of the jet at that point. Middleman [176], for example, approximated the decaying velocity profile within a horizontal jet using a fourth-order polynomial in the radial coordinate, with coefficients that were functions of the axial coordinate. Using Equations (2.1) and (2.3), this part of the integral is denoted by the parameter $\mathcal{N}$ in the dimensionless solution of Equation (2.9), which is

$$R_z^{*-2} = \frac{4}{3} - \frac{8\mathcal{N}}{\text{Re}} + \frac{2\left(R_z^* - 1\right)}{\text{We}^2}. \tag{2.12}$$

In Equation (2.12), the Weber number, We, is defined as the product of Capillary number, Ca, and Reynolds number, Re, and is given by

$$\text{We} \equiv \text{Re}\,\text{Ca} = \frac{2R_0\rho\bar{u}_0^2}{\sigma}. \tag{2.13}$$

It compares inertia forces to surface tension forces. The Capillary number, Ca, compares viscous forces to surface tension forces and is defined as

$$\text{Ca} \equiv \frac{\mu\bar{u}_0}{\sigma}. \tag{2.14}$$

Equation (2.12) indicates that R_z^* is a function of both Re and We. The dependence upon Re is large or small depending upon the form of $\mathcal{N}$. If both Re and We are large, so that viscous forces as well as surface tension forces can be neglected, Equation (2.12) reduces to Equation (2.6), Harmon's result. When the jet expands, surface tension reduces the expansion; when the jet contracts, it reduces the contraction. If there is no change in diameter ($R_z^* = 1$) caused by other forces, surface tension will not itself cause any change.

Gavis [175] gave a semi-empirical equation for R_z^* that is the result of a fit of Equation (2.12) to the experimental data of Middleman and Gavis [170]. It reads

$$R_z^* = 1.10 - 0.23\exp\left(-\frac{60}{\text{Re}^{3/2}}\right). \tag{2.15}$$

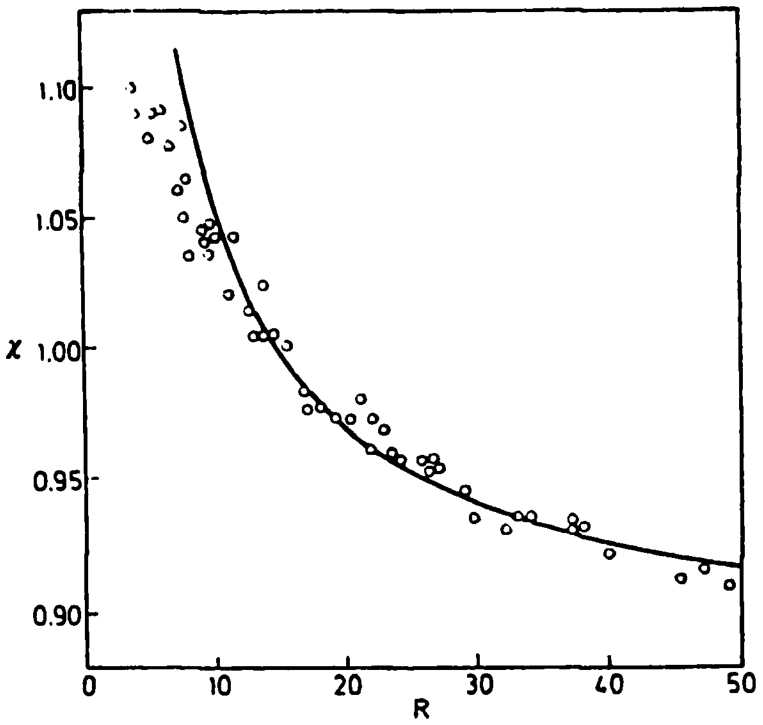

Figure 2.2: Contraction ratio experiments of Goren and Wronski [169] (open circles) in comparison with Joseph's Equation (2.16) (solid line). Figure 2 in Joseph's original paper [177]. $\chi = R^* = R/R_0$ as a function of the Reynolds number, here given by Joseph as R.

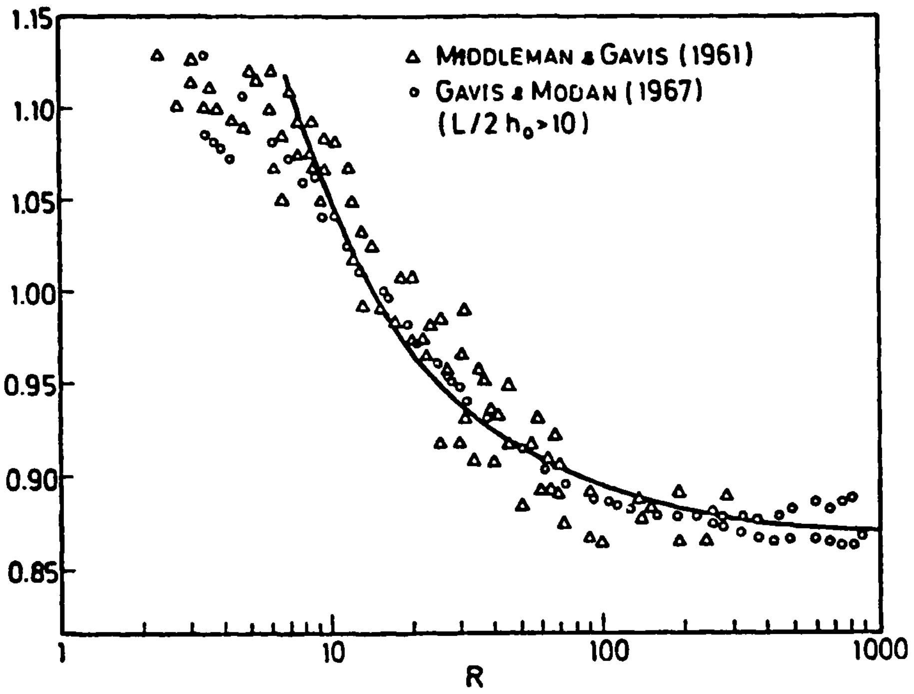

Figure 2.3: Contraction ratio experiments of Middleman and Gavis [170] (open triangles), and Gavis and Modan [173] (open circles) in comparison with Joseph's Equation (2.16) (solid line). Figure 3 in Joseph's original paper [177]. $\chi = R^* = R/R_0$ as a function of the Reynolds number, here given by Joseph as R.

Joseph [177] performed a momentum analysis on high Reynolds number jets in the absence of gravity, in which he considered surface tension. He gave the final rate of contraction as

$$R_z^{*-2} = \frac{4}{3} - \frac{\mathcal{K}}{\mathrm{Re}^{2/3}}, \tag{2.16}$$

where $\mathcal{K} = 1.97$ is supposed to be a weak function of Re and was chosen to fit one point of the experimental data of Goren and Wronski [169] when $R_z^* = 1.0$ and Re = 14.4. Equation (2.16) was found to be in good agreement with all experimental data of Goren and Wronski [169] (see Figure 2.2), and Middleman and Gavis [170] and Gavis and Modan [173] (see Figure 2.3) for Re > 10. As Re $\rightarrow \infty$, Equation (2.16) reduces to Harmon's result.

2.2 Action of Gravity on the Downstream Position of Vertical Jets

If gravity is present, no steady-state jet contraction is achieved. The velocity continuously increases due to the constant acceleration of the jet fluid, and conservation of mass requires that the jet continues to contract. Gravity also causes the velocity profile within the jet to relax at a much later stage than in the case of the horizontal jet. Neglecting the effects of viscosity (velocity profile rearrangement within the jet) and surface tension (pressure varying with jet radius), and ignoring the velocity profile at the nozzle exit, the Bernoulli equation takes on the form

$$\overline{u}_0^2 = u_z^2 - 2gz, \tag{2.17}$$

where z is the distance from the exit of the nozzle, which is positive in the direction of flow, $\overline{u}_0$ is again the mean nozzle exit velocity, g is the gravitational acceleration, and u_z is the uniform downstream jet velocity. Note that we have introduced a slight simplification at this stage of our derivation, since in a vertical jet flow, in the presence of gravity, the velocity profile does in fact not fully relax as a result of the constant acceleration. However, the inequality in the jet velocity far downstream of the nozzle is small, and as before, we assume that a uniform velocity profile u_z is reached at a downstream position z. Combining Equation (2.17) with the equation of continuity (2.3) gives an equation for the jet radius as a function of the jet length, which can be written as

$$R_z = R_0 \left(1 + \frac{2g}{\overline{u}_0^2} z\right)^{-1/4}. \tag{2.18}$$

Introducing the dimensionless variables $R_z = R_z^* R_0$ and $z = z^* R_0$ gives

$$R_z^* = \left(1 + \frac{2R_0 g}{\overline{u}_0^2} z^*\right)^{-1/4} = \left(1 + \frac{z^*}{\mathrm{Fr}}\right)^{-1/4}. \tag{2.19}$$

The Froude number,

$$\mathrm{Fr} \equiv \frac{\overline{u}_0^2}{2R_0 g}, \tag{2.20}$$

relates inertia forces to gravitational forces.

Equation (2.19) discounts the nozzle exit velocity profile. To take this into account, the Bernoulli equation takes on the form

$$\frac{\int_0^{A_0} (u(r, z = 0))^2 \, dA}{\int_0^{A_0} dA} = u_z^2 - 2gz, \tag{2.21}$$

where $u(r, z = 0)$ is given in Equation (2.1), and with $dA = 2\pi r dr$ we can write

$$\frac{\int_0^{R_0} \left[2\overline{u}_0 \left(1 - (r/R_0)^2\right)\right]^2 r dr}{\int_0^{R_0} r dr} = u_z^2 - 2gz. \tag{2.22}$$

The continuity equation (2.3) is used again to replace u_z^2, and the solution of Equation (2.22) is

$$R_z = R_0 \left(\frac{4}{3} + \frac{2g}{\overline{u}_0^2} z\right)^{-1/4}, \tag{2.23}$$

which in dimensionless form reads

$$R_z^* = \left(\frac{4}{3} + \frac{z^*}{\mathrm{Fr}}\right)^{-1/4}. \tag{2.24}$$

Equation (2.24) is used in our numerical model of the jet flow to estimate the contact angle at the outlet of the computational flow domain (see Section 3.4.4).

We note that both Equations (2.19) and (2.24) give R_z^* as a function of the axial jet coordinate z^*, which enables us to predict the shape of the jet flow over the whole length of the jet. The Bernoulli equation, however, requires a uniform downstream velocity u_z, and a nearly relaxed velocity profile can only be found at a relatively large distance from the nozzle exit. We can thus expect a reasonably accurate prediction of R_z^* from Equations (2.19) and (2.24) only at the downstream jet position, sufficiently far away from the nozzle exit. Both equations show the same asymptotic behaviour for large values of z^*, in which case we have that $R_z^* \approx (z^*/\mathrm{Fr})^{-1/4}$ if $z^*/\mathrm{Fr} \gg 1$ or 4/3, respectively. For $z^* \to \infty$, we have that $R_z^* \to 0$. At the nozzle exit, the jet radius equals the radius of the nozzle, so that $R_z^* = 1.0$ at $z^* = 0$. This value is correctly obtained from Equation (2.19). From Equation (2.24), we get $R_z^*(z^* = 0) = (4/3)^{-1/4} = 0.9306$. Equation (2.24) thus underpredicts the jet radius at the nozzle exit. The predictions of R_z^* as a function of z^* that are obtained from Equations (2.19) and (2.24) are compared with the CFD calculations of a vertical jet flow in Section 3.6.3.

In the derivation of Equations (2.19) and (2.24) we have assumed that the gravitational energy finds its equivalent in an increase of the kinetic energy of the jet flow (Bernoulli's law). The influence of surface tension on the shape of the jet has not been accounted for, and instead we have studied a continuum of liquid, which assumes the shape of a jet drawn-down under the action of gravity.

The surface of the jet flow, however, is continuously renewed with liquid that leaves the nozzle. Each mass of liquid that leaves the nozzle forms a fresh surface. Surface tension opposes the formation of fresh surface, and not all the gravitational energy is thus utilised to increase the kinetic energy of the jet flow. A proportion of it must balance the capillary energy that opposes the formation of surface.

Scheuermann seems to have been among the first scientists to account for the incomplete conversion of gravitational energy caused by surface tension [179]. He published his studies on the shape and the disintegration of falling liquid jets in a paper of 1919, in which he derived an extension to Equation (2.19) that is based on the energy principle. Discounting the loss of energy through viscous dissipation—the velocity profile relaxation within the jet flow, that is—he performed an energy balance on a differential volume segment of the jet flow.

The solution of this energy balance is an implicit equation for R_z as a function of z,

$$z = \frac{\overline{u}_0^2}{2g}\left[\left(\frac{R_0}{R_z}\right)^4 - 1\right] + \frac{2\sigma}{\rho g R_0}\left[\frac{R_0}{R_z} - 1\right]. \tag{2.25}$$

An incorrect version of this relation was used by Addison and Elliott [165] to determine the surface tension from the dimensions of a vertical liquid jet.[11]

We introduce the dimensionless variables $R_z = R_z^* R_0$ and $z = z^* R_0$ into Equation (2.25) as before and obtain

$$z^* = \mathrm{Fr}\left[R_z^{*^{-4}} - 1\right] + \frac{8\,\mathrm{Fr}}{\mathrm{Ca}\,\mathrm{Re}}\left[R_z^{*^{-1}} - 1\right]. \tag{2.26}$$

The quotient Re / Fr is also called the Stokes number,

$$\mathrm{St} \equiv \frac{\mathrm{Re}}{\mathrm{Fr}} = \frac{4R_0^4 \rho g}{\mu \overline{u}_0}, \tag{2.27}$$

which compares gravitational forces to viscous forces. In Equation (2.26), the first term on the right-hand side is the implicit form of Equation (2.19). The second term on the right-hand side of Equation (2.26) is the surface tension contribution, which leads to the prediction of larger values for R_z^* than those predicted by Equation (2.19) for the same value of z^*. For $\sigma = 0$, or Ca → ∞, we obtain Equation (2.19). Scheuermann also reports that Equation (2.19) was used by Weisbach to predict the shape of vertical liquid jets in as early as 1855.

Adding Scheuermann's surface tension contribution to Equation (2.24) gives

$$z^* = \mathrm{Fr}\left[R_z^{*^{-4}} - \frac{4}{3}\right] + \frac{8\,\mathrm{Fr}}{\mathrm{Ca}\,\mathrm{Re}}\left[R_z^{*^{-1}} - 1\right], \tag{2.28}$$

in which the first term on the right-hand side is the implicit form of Equation (2.24). The prediction of R_z^* as a function of z^* that is obtained from Equation (2.28) is compared with the CFD calculations of a vertical jet flow in Section 3.6.3.

Using the equations of motion for an inviscid and steady jet flow in conjunction with the differential and integral form of the equation of continuity, and neglecting the weak dependence of the jet radius on the jet length and assuming that the axial velocity is a function of the jet length only, Equation (2.26) was derived much later by Anno [180].[12]

---

[11] Equation (2) in the original reference. Instead of $2\sigma(\rho g R_0)^{-1}$, the quotient σg^{-1} was used in the surface tension contribution term, which is dimensionally not consistent. This was (unintentionally) corrected by the authors through the introduction of an empirical factor.

[12] Note that Anno's version of Equation (2.26) contains a factor 4 Fr / (Re Ca) instead of 8 Fr / (Re Ca).

The shape of vertical laminar jets and the total axial force exerted on the liquid at the point of emergence from the nozzle were investigated by Adachi *et al.* [181] for circular jets and by Adachi [182] for plane jets. For a circular jet, the authors proposed the equation

$$z^* = \mathrm{Fr}\left[R_z^{*^{-4}} - \varphi\right] + \mathrm{Fr}\left\{\frac{2}{\mathrm{We}} + \left[\left(\frac{2}{\mathrm{We}}\right)^2 + \frac{24}{\mathrm{Re}\,\mathrm{Fr}}\right]^{1/2}\right\}\left[R_z^{*^{-1}} - \phi\right] \qquad (2.29)$$

to compute R_z^*, in which φ and ϕ are adjustable constants. For Re → ∞ and $\varphi = \phi = 1$, Equation (2.29) reduces to Anno's version of Equation (2.26). The shape of the jet, R_z^*, was measured photographically, and φ and ϕ were chosen to give a best fit of Equation (2.29) to the experimental data.

A macroscopic axial force balance for a suspending jet filament,

$$F_0 = F_z + G_z, \qquad (2.30)$$

was employed to check on the consistency of the measured jet shape. In Equation (2.30), $F_0 = F(z = 0)$ is the total axial force exerted on the upper end of the suspending filament, $F_z = F(z)$ is the total axial force acting on the filament at a downstream position z, and $G_z = G(z)$ is the weight of the suspending filament from its upper end ($z = 0$) to z. Equation (2.30) describes an integral invariant—both F_z and G_z vary with z, but their sum must be constant along the vertical axis z. F_z and G_z depend on z through R_z. F_z and G_z were calculated using these measured data of R_z and were required to satisfy the invariance criterion. F_0 was measured directly with an electric weighing device. The consistency between the two kinds of experimental data on the axial force F_0 and the jet shape R_z was checked using Equation (2.30), that is, the values for F_0 were directly measured and F_z and G_z were calculated from the measured R_z data.

Scheuermann compared Equation (2.19) and the more sophisticated Equation (2.26) with his photographic measurements of the shape of vertical water jets. In his experiments, he employed brass nozzles of 15 to 30 cm length and used nozzle radii of 4.53 to 7.89 mm. The jets were fully turbulent, with Reynolds numbers in the range of $6456 \leqslant \mathrm{Re} \leqslant 12436$. Figure 2.4 shows one set of his experimental data at a Reynolds number of $\mathrm{Re} = 6456$ in comparison with values that are calculated using Equations (2.19) and (2.26).

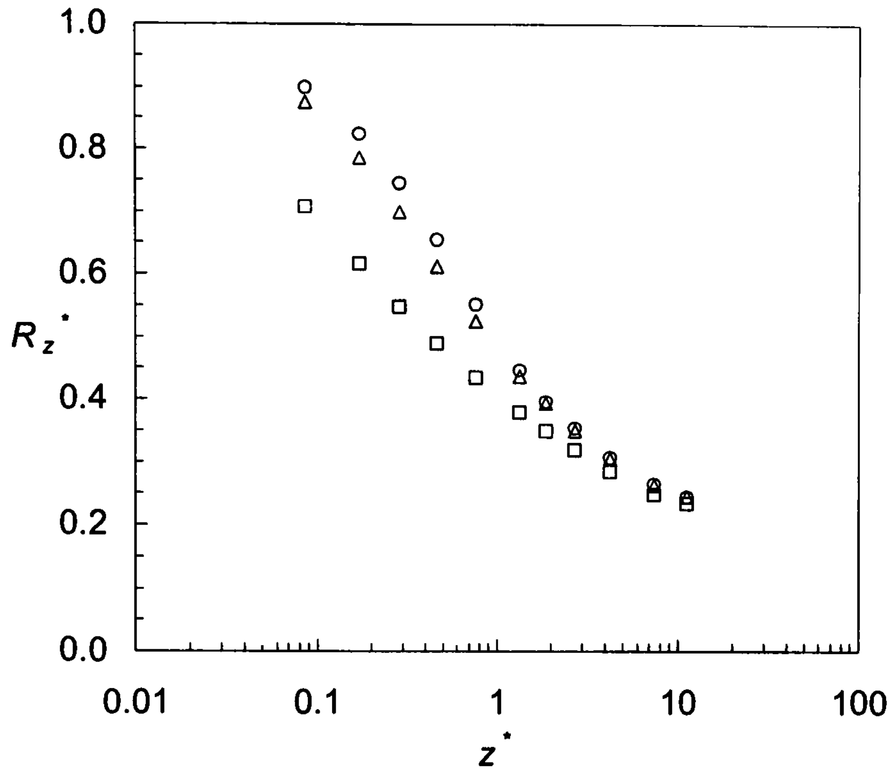

Figure 2.4: Contraction ratio, R_z^*, as a function of the jet length, z^*, in a turbulent vertical water jet according to Scheuermann [179]. $\overline{u}_0 = 0.56$ m s^{-1}, $R_0 = 5.72$ mm, Re = 6456, Ca = 0.0076, and Fr = 2.837. The open circles are the experimental data of Scheuermann, the open squares are Equation (2.19), and the open triangles are Equation (2.26).

We can see from Figure 2.4 that for larger values of z^*, both Equation (2.19) and Equation (2.26) approximate the experimental data well, indicating that the surface tension contribution at large z^* and at this high Reynolds number is negligibly small. Near the point of surface formation, Equation (2.26) follows the pattern of the experimental data more closely than the simpler Equation (2.19). The contribution of surface tension has the effect of increasing the ratio of contraction, R_z^*, relative to the values obtained from Equation (2.19).

Interestingly, Equation (2.26) shows good agreement with the experimental data near the nozzle despite the fact that it does not take the shape of the velocity profile at the nozzle exit into account. We remember that it assumes a flat profile that has the value $\overline{u}_0$, and that the flow conditions in Scheuermann's experiments were those of fully developed turbulent flow. In a fully developed laminar pipe flow (Poiseuille flow), which we consider mostly in this thesis, the velocity profile is that given by Equation (2.1), and the maximum velocity (in the centre of the pipe) is twice the value of the mean velocity, $\overline{u}_0$. In a fully developed turbulent pipe flow, however, the velocity profile is given by the empirical equation

$$\widehat{u}\,(r, z = 0) = \widehat{u}_{\max}\left(1 - \frac{r}{R_0}\right)^{1/7} , \qquad (2.31)$$

where $\widehat{u}$ and $\widehat{u}_{\max}$ are time-smoothed quantities [190, p. 155]. In the case of fully developed turbulent flow, the maximum velocity is 1.25 times the mean velocity. If we use Equation (2.31) in Equation (2.21) to account for the velocity profile of a fully developed turbulent flow at the nozzle exit, we arrive at

$$R_z^* = \left(1.063 + \frac{z^*}{\mathrm{Fr}}\right)^{-1/4} \approx \left(1 + \frac{z^*}{\mathrm{Fr}}\right)^{-1/4} . \qquad (2.32)$$

The assumptions that have been made in the derivation of Equations (2.19) and (2.26) are thus more closely met than in the case of fully developed laminar flow.

Optical measurements of the shape of vertical water jets were reported by von Lang in 1878 [183]. He used a glass tube with an inner diameter of 1.08 cm and an outer diameter of 1.44 cm, which had a length of 8 cm. The shape of the end of the glass tube was described as "*... not flat but intentionally irregularly serrated.*" The reason for this deliberate action is, however, not disclosed to the reader.

Von Lang was probably the first scientist to construct a continuous jet apparatus. This achievement was made possible through the use of newly built domestic water supplies in 19th-century Vienna. The glass tube was connected directly to the water supply by means of a flexible rubber tube, and the flow rate was controlled by the tap. To minimise the effect of external vibrations from the floor on the water jet, von Lang attached the apparatus to the wall of the room. His experimental set-up allowed the jet to reach a maximum length of 130 cm, a length at which the jet hit a wooden board and the liquid was collected in a reservoir. As he reports, perfectly smooth and continuous water jets were produced at a suitable flow rate, provided the pressure in the water supply system remained at the normal value, which, as it seems, was frequently not the case.

Von Lang measured the jet radius R for varying mass flow rates at different axial positions z. The jet velocity was taken to be constant throughout the jet at each downstream position, and measurements were carried to within 5 cm of the glass tube. The mean nozzle exit velocities ranged from 2.4 to 39.5 cm s^{-1}, which resulted in Reynolds numbers of 260 to about 4270. Thus both laminar and turbulent flow conditions were encountered.

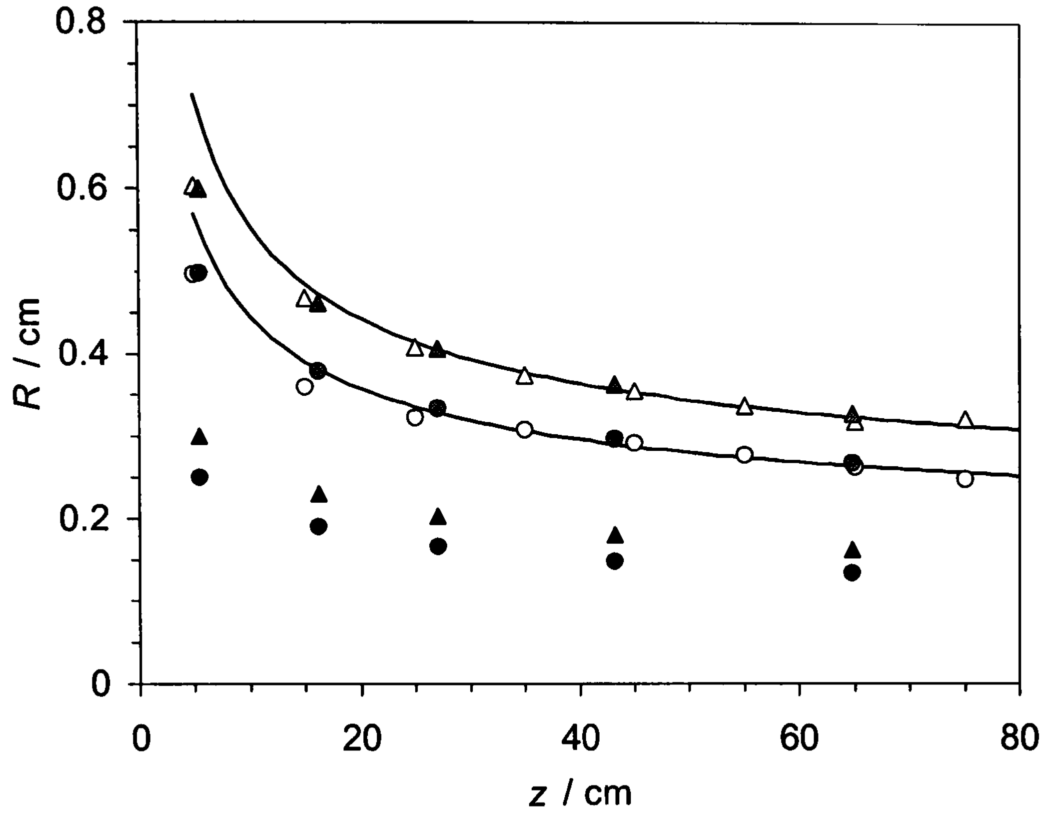

Figure 2.5: Free-surface position, R, of vertical water jets as a function of the axial downstream distance, z, at Re = 2358 (circles) and Re = 3537 (triangles). The open symbols are the experimental data of von Lang [183], the black symbols are computed using Equation (2.26), and the grey symbols are obtained from Equation (2.34). The solid lines are computed using Equation (2.33).

Some of von Lang's experimental data,[13] at flow rates of $Q = 20$ and 30 g s^{-1}, are plotted in Figure 2.5 (open symbols). These flow rates correspond to Reynolds numbers of 2358 and 3537, respectively. Von Lang gave an empirical equation for R, which is also plotted in Figure 2.5 (solid lines), that was fitted to the experimental data at the two flow rates for $z \geqslant 35$ cm. It is given by

$$R = 0.09246 + 0.002709Q + (0.42748 + 0.025918Q)\frac{1}{\sqrt{z}}, \qquad (2.33)$$

where Q is the mass flow rate in [g s^{-1}], z is the axial distance from the nozzle orifice in [cm], and R is the jet radius in [cm]. Figure 2.5 shows that Equation (2.26) does not reproduce von Lang's experimental data (black symbols). A comparison of von Lang's experimental data for $R(z)$ with the values that are obtained from Equation (2.26) shows that the latter are lower by a factor of 2.

---

[13] The experimental data at $z = 5$, 15, and 25 cm in Figure 2.5 were obtained through linear interpolation from von Lang's original data, which he published in tabular form.

If we implement this factor in Equation (2.26), we obtain

$$z^* = \mathrm{Fr}\left[16 R_z^{*^{-4}} - 1\right] + \frac{8\,\mathrm{Fr}}{\mathrm{Ca\,Re}}\left[2 R_z^{*^{-1}} - 1\right]. \tag{2.34}$$

Equation (2.34) can reproduce von Lang's experimental data very accurately (grey symbols in Figure 2.5). There is, however, no physical justification for the use of Equation (2.34) instead of Equation (2.26), and we are lacking an explanation for the discrepancy between von Lang's experimental data and the values that are calculated using Equation (2.26).

In 1906, Trouton reported a method for the measurement of the slope of the surface of a falling column of liquid, in which a beam of light from a horizontal slit and lens is allowed to fall on the liquid column and is reflected into a telescope, which is pointed upwards to receive the reflected light [184]. The tangent of half the angle between the incident and reflected beams gave the slope of the surface. He applied this method to a highly viscous mixture of pitch and tar that descended under its own weight through a circular hole in the bottom of a wide tin vessel. He also measured the shape of the surface of the same system, in some cases by means of a cathetometer telescope, in other cases by casting the shadow of the column from a distant source of light on a long vertical sheet of paper placed close to the column, and then tracing out the shadow with a pencil. It was found possible to fit an equilateral hyperbola of the form $R\,(z + 1.8) = 1.85$ to these measured data.

2.3 Boundary Layer Development at the Nozzle Exit: The Cube-Root Dependence

At the nozzle exit, the velocity profile is that of fully developed laminar flow, with the usual no-slip condition at the wall. This no-slip condition is immediately relaxed when the fluid leaves the tube. In the absence of any surface shear (no surfactant present) a region of zero vorticity appears at the surface of the jet, and as the fluid travels downwards, the zero-vorticity region diffuses towards the centre of the jet, eventually equalising the velocity across the jet. In fact, the relaxation of shear is the major effect in the boundary layer development. Initially, however, this region is very thin, and we will consider its initial growth when its thickness, ε, is much less than the radius of the nozzle, R_0, or of the jet, R (see Figure 2.6).

Near to the jet nozzle, the effect of gravity may be neglected. Fluid in the zero-vorticity layer is accelerated by the adjacent layer of faster moving fluid. The parabolic profile at the nozzle exit ($z = 0$) is

$$U(y) = \widehat{A}y + \widehat{B}y^2, \tag{2.35}$$

where $\widehat{A} = 4\overline{u}_0 R_0^{-1}$ and $\widehat{B} = -2\overline{u}_0 R_0^{-2}$. At a distance z from the nozzle exit the depth of the zero-vorticity layer, measured from the line $y = 0$, is $\delta = R_0 - R + \varepsilon$. Note that the actual thickness of the layer, ε, is less than δ. If we let the velocity in the zero-vorticity layer be

$$u(y) = a + b\{y - (\delta - \varepsilon)\}, \tag{2.36}$$

then a is the surface velocity, u_s, and b is zero since there is no shear stress at the surface and so $\partial u/\partial y = 0$ throughout the layer (see dashed boundary layer velocity profile in Figure 2.6). We set the condition that the velocity be continuous at the edge of the layer, so that $U(\delta) = u(\delta)$, which gives $\widehat{A}\delta + \widehat{B}\delta^2 = a$. Substituting for $\widehat{A}$, $\widehat{B}$, and a shows that the surface velocity is

$$u_s = 4\overline{u}_0 \left(\frac{\delta}{R_0} - \frac{\delta^2}{2R_0^2} \right), \tag{2.37}$$

and since $\delta \ll R_0$,

$$u_s = \frac{4\overline{u}_0 \delta}{R_0}. \tag{2.38}$$

The thickness of the layer, ε, at a distance z can be found by continuity, since

$$\int_0^\delta U(y)dy = \int_{\delta-\varepsilon}^\delta u(y)dy, \tag{2.39}$$

from which $\widehat{A}\delta^2/2 + \widehat{B}\delta^3/3 = a\varepsilon$, and

$$\varepsilon = \frac{2\overline{u}_0 R_0}{u_s} \left(\frac{\delta^2}{R_0^2} - \frac{\delta^3}{3R_0^3} \right), \tag{2.40}$$

and since $\delta \ll R_0$,

$$\varepsilon = \frac{2\overline{u}_0 \delta^2}{u_s R_0} = \frac{\delta}{2}. \tag{2.41}$$

The thickness of the vorticity-free layer is just half the distance δ.

The fluid streamlines which leave the nozzle between $y = 0$ and $y = \delta$, at the distance z are found between $y = \delta/2$ and $y = \delta$. The rate of gain of momentum

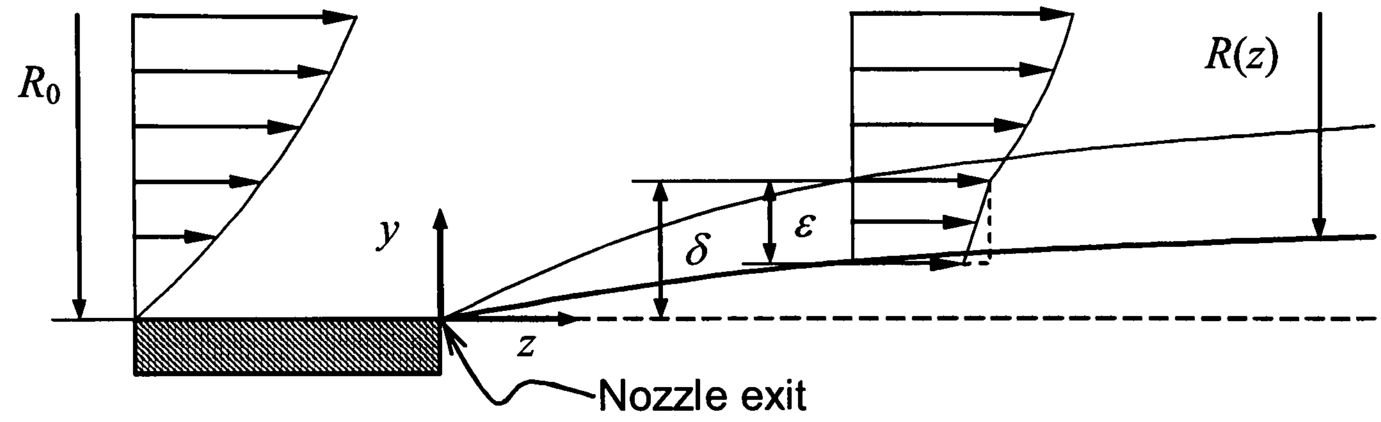

Figure 2.6: Development of the hydrodynamic boundary layer at the nozzle exit. R_0, nozzle radius; $R(z)$, jet radius; ε, thickness of boundary layer (with contraction); δ, radial distance of edge of boundary layer from nozzle wall; z, axial jet coordinate; y, cartesian transverse coordinate in the boundary layer. A dashed line shows the boundary layer velocity profile in the absence of surfactant $(\partial u/\partial y = 0)$, and a solid line the boundary layer velocity profile in the presence of surfactant $(\partial u/\partial y \neq 0)$.

by fluid in this layer is equal to the force acting. For unit width, assuming the depth of the layer is small compared with the jet radius, the rate of momentum gain is

$$\rho \int_0^\delta U(y)\left\{u\left(\frac{y+\delta}{2}\right) - U(y)\right\} dy = \mu\left(\frac{\partial U}{\partial y}\right)_{y=\delta} z. \tag{2.42}$$

Neglecting terms in δ^3 and higher powers of δ, from Equation (2.42) we obtain $\widehat{A}a\delta^2 = 2\nu(A + 2\widehat{B}\delta)z$, so that $a = 2\nu(\delta^{-2} + 2\widehat{B}\widehat{A}^{-1}\delta^{-1})z$. From the parabolic profile we have $2\widehat{B}\widehat{A}^{-1} = -R_0^{-1}$, so the surface velocity, $u_s = a$, is given by

$$u_s = \frac{2\nu z}{\delta^2}\left(1 - \frac{\delta}{R_0}\right), \tag{2.43}$$

and since $\delta \ll R_0$,

$$u_s = \frac{2\nu z}{\delta^2}. \tag{2.44}$$

Combining Equations (2.38) and (2.44) gives

$$u_s = \left(\frac{32\overline{u}_0^2 \nu z}{R_0^2}\right)^{1/3}, \tag{2.45}$$

$$\delta = \left(\frac{R_0 \nu z}{2\overline{u}_0}\right)^{1/3}, \tag{2.46}$$

and

$$\varepsilon = \frac{1}{2}\left(\frac{R_0 \nu z}{2\overline{u}_0}\right)^{1/3} . \tag{2.47}$$

The relative narrowing of the jet due to acceleration of the surface layer is given by

$$\frac{R(z)}{R_0} = \frac{R_0 - (\delta - \varepsilon)}{R_0} = 1 - \frac{1}{2}\left(\frac{\nu z}{2R_0^2 \overline{u}_0}\right)^{1/3} . \tag{2.48}$$

Introducing the dimensionless variables $u_s = u_s^* \overline{u}_0$ and $z = z^* R_0$ into Equation (2.45) leads to

$$u_s^* = 4\left(\frac{z^*}{\mathrm{Re}}\right)^{1/3} . \tag{2.49}$$

Similarly, a dimensionless expression for the relative narrowing of the jet,

$$R^* = \frac{R}{R_0} = 1 - 0.5\left(\frac{z^*}{\mathrm{Re}}\right)^{1/3} , \tag{2.50}$$

can be derived.

There is thus a singularity at the point $(z = 0, y = 0)$, where the surface expansion rate, du_s/dz, becomes infinite. This is a consequence of the step change in the surface shear condition at this point.

The cube-root dependence of u_s and R on z was found by other authors before. In the late 1950's, Scriven and Pigford [160, 161], in the course of their investigation of CO_2 absorbtion into freely falling laminar liquid jets, assumed a uniform velocity profile in the core of the jet (short nozzles were used and hence no fully developed laminar flow was achieved at the nozzle exit), whereas an annular boundary layer existed outside the core of the jet in which the velocity was reduced, in consequence of the viscous effects close to the nozzle wall. A cubic equation was employed to represent the velocity distribution within this annular boundary layer. Mass and momentum balances between the nozzle exit plane and a downstream position that corresponds to a fully relaxed velocity profile in the jet yielded an approximate expression for the boundary layer thickness as a function of the measured jet radius. The authors concluded from the smallness of the boundary layer at the nozzle exit—only one tenth of the nozzle radius—that the core velocity of the jet remained unchanged by momentum exchange with the boundary layer. Assuming that the rate of change of jet diameter is negligibly small, and neglecting gravitational acceleration, the problem of analysing the velocity distribution in the neighbourhood of the jet surface became identical with the problem of calculating the velocity distribution in a laminar wake behind an infinitely thin, flat plate oriented parallel to the direction of flow. This analogy was pointed out earlier by Rideal and Sutherland [145]. The surface velocity near the nozzle exit was described by a cube-root dependence (at leading order) on the axial distance.

In 1966, Goren [185] studied the development of the boundary layer accompanying the formation of a free surface from a two-dimensional horizontal uniform shear flow that was taken to be of infinite extent in both directions. Neglecting surface tension forces, his analysis shows that both the surface velocity and surface position vary as the cube root of the distance downstream. Goren's results are applicable to newly formed capillary jets for small axial distances, provided the interaction of the bounday layer with the core region of the jet, where the initial velocity profile is not one of uniform shear, is negligible. For a jet of average velocity $\overline{u}_0$, issuing from a long needle of radius R_0 with parabolic flow, Goren gave the equation for the surface velocity, $u_s^* = u_s/\overline{u}_0$, as

$$u_s^* = 5.07\left(\frac{z^*}{\mathrm{Re}}\right)^{1/3}, \tag{2.51}$$

and for the jet contraction, $R^* = R/R_0$, as

$$R^* = 1 - 0.703\left(\frac{z^*}{\mathrm{Re}}\right)^{1/3}. \tag{2.52}$$

In the same year, Goren and Wronski [169] reported measurements of the radius of horizontal capillary jets as a function of the axial distance. For the highest Reynolds number under consideration (Re $\approx$ 200) the measurements confirmed the cube root dependence on the axial distance, but the observed coefficient was lower than the predicted one by about a factor of 2. The authors concluded that this discrepancy is either due to the relatively small Reynolds number or to the interaction of the peripheral boundary layer with the core of the jet fluid. Goren and Wronski suggested that their boundary layer approach should be tested against data obtained from jet flows at higher Reynolds numbers ($1000 \leqslant \mathrm{Re} \leqslant 2000$) to verify its validity.

Only two years later, Tillett [186] also applied boundary-layer analysis to a horizontal liquid jet emerging from a two-dimensional channel at high Reynolds number, but he assumed that the flow inside the channel has the basic Poiseuille profile. Ignoring the effects of surface tension, Tillett did not confine modifications to the basic profile to the boundary layer. Instead, he drived solutions

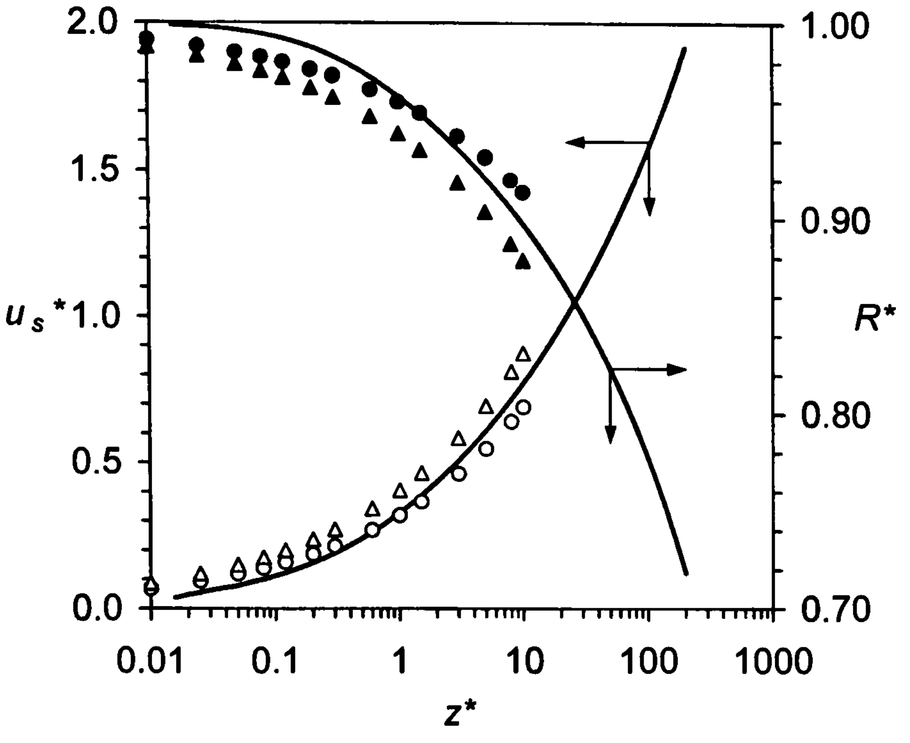

Figure 2.7: Surface velocity, $u_s^* = u_s/\overline{u}_0$, and free-surface position, $R^* = R/R_0$, of the water jet as a function of the jet length, $z^* = z/R_0$. $\mathrm{Re} = 1950$, $\mathrm{Ca}^{-1} = 58.9$, and $(2\,\mathrm{Fr})^{-1} = 0.00507$. The lines are the numerical solution computed from the CFD model that is described in Chapter 3. The open and closed circles are given by Equations (2.49) and (2.50), respectively. Goren's theoretical results, Equations (2.51) and (2.52), are the open and closed triangles, respectively.

for the 'inner' (boundary layer) region and the 'outer' (core) region of the jet flow, which he matched. It emerged, however, from his solution that Goren's assumption is fully justified—for moderate downstream distances, the interaction between the boundary layer and the core of the jet flow can be neglected. Tillett confirmed Goren's solution for the channel flow (the cube-root dependence), but he did not apply his derivations to the case of an axisymmetric jet leaving a circular pipe.

We have plotted Equations (2.49) and (2.50) for a jet of water at a high Reynolds number of Re = 1950 in Figure 2.7. The results from the boundary-layer treatment are compared with computations of $u_s^*(z^*)$ and $R^*(z^*)$ in a vertical water jet at the same Reynolds number, which were obtained from the CFD model outlined in Chapter 3. The same numerical $u_s^*(z^*)$ and $R^*(z^*)$ profiles are compared with experimental data in Figures 3.32 and 3.33. Also shown in Figure 2.7 is the theoretical solution found by Goren, Equations (2.51) and (2.52).

At larger values of z^*, our boundary-layer theory under-predicts the surface velocity and the contraction in the jet, whereas Goren's theory over-predicts both variables. As the distance from the nozzle exit grows ($z^* > 10$), both theories strongly under-predict both the surface velocity and the contraction of the jet. At these larger distances from the point of emergence of liquid from the nozzle, gravity dominates the fluid mechanics of the jet, which is not accounted for in either of the theories. At small z^*, both theories over-predict the surface velocity and contraction of the jet. The very rapid acceleration of fluid particles in the surface close to the nozzle exit is evident. This acceleration results in very high surface expansion rates, du_s^*/dz^*, near the nozzle exit, which provide the driving force for the diffusion of surfactant to the surface, as will be discussed in Chapter 4.

The cube-root dependence in the case of a jet of a pure liquid is thus a well-established result. We go on to investigate how the presence of surfactant at the jet surface affects the boundary layer development in the jet flow, particularly at the nozzle exit, in Section 4.1.

The negligibly small interaction between the velocity profile in the boundary layer and the velocity profile in the core of the jet also justifies the assumption that fully developed laminar flow exists at the channel/nozzle exit in the high Reynolds number limit. This assumption is otherwise inadequate as pointed out by Middleman [187], who commented on the fact that the vorticity associated with the axial deformation of the liquid at the nozzle exit can diffuse upstream and affect the velocity profile within the nozzle, just upstream from the nozzle exit. Fisher *et al.* [188] and Dutta and Ryan [189] showed the upstream diffusion of vorticity in the course of their numerical investigations of creeping jet flows ($\mathrm{Re} \approx 0$). Brun and Lienhard [178], in the course of their experimental and theoretical work on horizontal oil jets, confirmed the assumption of parabolic flow at the nozzle exit at $\mathrm{Re} = 280$. The authors calculated velocity profiles in the jet from stagnation pressures, which were measured with a traversing probe. Bulging of the jet surface that was caused by the probe did not allow for accurate measurements very near the surface. The apparatus, however, did allow for measurements to be made within the nozzle exit plane. A comparison of the velocity distribution that was calculated from the measured stagnation pressures with the theoretical Poiseuille profile revealed an average deviation of only 1.8%.

Chapter 3

Computational Fluid Dynamics Model of the Jet Flow

The methods presented in the previous chapter allow us to estimate the asymptotic behaviour of a laminar liquid jet at the downstream position and at the nozzle exit. In order to calculate the velocity distribution within the jet and hence to investigate the velocity profile relaxation process and the jet contraction as a function of the jet length, one has to solve the equations of motion.

An exact analytic solution of the Navier-Stokes equations for an axisymmetric flow of an isothermal Newtonian fluid issuing from a capillary of uniform circular cross section is not available, and solutions are generally obtained numerically. The complexity is not only due to the presence of the inertia terms that reflect the dynamics of the exit region, but also because the exit flow is a free-boundary flow, one for which the interface of the free jet, the bounding surface of the flow, is itself unknown and must be found as part of the solution.

In this work, FIDAP, one of FLUENT's general-purpose Computational Fluid Dynamics (CFD) solvers that employs a finite-element method to discretise the governing set of partial differential equations, is used to obtain a numerical solution of the flow field of the jet.

3.1 The Governing Field Equations

For an axisymmetric steady flow with constant viscosity, μ, and density, ρ, the Navier-Stokes equations in cylindrical polar coordinates (r, z) can be written as [190, p. 85]

$$\rho\left(v\frac{\partial u}{\partial r}+u\frac{\partial u}{\partial z}\right)=-\frac{\partial p}{\partial z}+\mu\left(\frac{1}{r}\frac{\partial}{\partial r}\left(r\frac{\partial u}{\partial r}\right)+\frac{\partial^2 u}{\partial z^2}\right)+\rho g \tag{3.1}$$

in the axial direction (z-component), and

$$\rho\left(v\frac{\partial v}{\partial r}+u\frac{\partial v}{\partial z}\right)=-\frac{\partial p}{\partial r}+\mu\left(\frac{\partial}{\partial r}\left(\frac{1}{r}\frac{\partial}{\partial r}(rv)\right)+\frac{\partial^2 v}{\partial z^2}\right) \tag{3.2}$$

for the r-component in the radial direction. In a free-surface flow, it is more convenient to use the stress formulation of the Navier-Stokes equations, that is,

$$\rho\left(v\frac{\partial u}{\partial r}+u\frac{\partial u}{\partial z}\right)=-\frac{\partial p}{\partial z}+\left(\frac{1}{r}\frac{\partial}{\partial r}(r\tau_{rz})+\frac{\partial \tau_{zz}}{\partial z}\right)+\rho g \tag{3.3}$$

in the axial direction (z-component), and

$$\rho\left(v\frac{\partial v}{\partial r}+u\frac{\partial v}{\partial z}\right)=-\frac{\partial p}{\partial r}+\left(\frac{1}{r}\frac{\partial}{\partial r}(r\tau_{rr})+\frac{\partial \tau_{rz}}{\partial z}\right) \tag{3.4}$$

in the radial direction (r-component). Formulated in terms of the stresses, τ_{jk}, the normal and tangential stress boundary conditions at the surface, which are presented in Section 3.4.5, Equations (3.38) and (3.43), then act as direct boundary conditions to the equations of motion.

The equation of continuity completes the set of governing equations, that is

$$\frac{1}{r}\frac{\partial}{\partial r}(rv)+\frac{\partial u}{\partial z}=0. \tag{3.5}$$

In order to non-dimensionalise Equations (3.1) and (3.2), and the equation of continuity (3.5), we select the nozzle radius, R_0, as the characteristic length scale of the jet and the mean nozzle exit velocity, $\overline{u}_0$, as the characteristic jet velocity. These two characterisitc flow parameters are used to obtain a set of dimensionless variables,

$$u=u^*\overline{u}_0,\ v=v^*\overline{u}_0,\ z=z^*R_0,\ r=r^*R_0,\ p=p^*\left(\rho\overline{u}_0^2\right). \tag{3.6}$$

The dimensionless variabless defined in (3.6) are introduced into the Equations (3.1), (3.2), and (3.5), which leads to a set of dimensionless field equations, which can be written as

$$\frac{\mathrm{Re}}{2}\left(v^*\frac{\partial u^*}{\partial r^*}+u^*\frac{\partial u^*}{\partial z^*}\right)=-\frac{\partial p^{**}}{\partial z^*}+\left(\frac{1}{r^*}\frac{\partial}{\partial r^*}\left(r^*\frac{\partial u^*}{\partial r^*}\right)+\frac{\partial^2 u^*}{\partial z^{*2}}\right)+\frac{\mathrm{Re}}{4\,\mathrm{Fr}}, \tag{3.7}$$

$$\frac{\mathrm{Re}}{2}\left(v^*\frac{\partial v^*}{\partial r^*}+u^*\frac{\partial v^*}{\partial z^*}\right)=-\frac{\partial p^{**}}{\partial r^*}+\left(\frac{\partial}{\partial r^*}\left(\frac{1}{r^*}\frac{\partial}{\partial r^*}(r^*v^*)\right)+\frac{\partial^2 v^*}{\partial z^{*2}}\right), \tag{3.8}$$

and

$$\frac{1}{r^*}\frac{\partial}{\partial r^*}(r^*v^*)+\frac{\partial u^*}{\partial z^*}=0. \tag{3.9}$$

The pressure, p^{**}, is defined as

$$p^{**}=\frac{\mathrm{Re}}{2}p^*. \tag{3.10}$$

Two dimensionless parameters are obtained from the dimensionless Navier-Stokes equations—the Reynolds number, Re, and the Froude number, Fr, which are defined in Equations (2.8) and (2.20), respectively.

The stress components in the stress formulation of the Navier-Stokes equations are non-dimensionalised according to

$$\tau_{jk}=\tau^*_{jk}(\rho\bar{u}_0^2), \tag{3.11}$$

and together with the set of dimensionless variables defined in (3.6) leads to the dimensionless version of the stress formulation of the Navier-Stokes equations, namely

$$\left(v^*\frac{\partial u^*}{\partial r^*}+u^*\frac{\partial u^*}{\partial z^*}\right)=-\frac{\partial p^*}{\partial z^*}+\left(\frac{1}{r^*}\frac{\partial}{\partial r^*}(r^*\tau^*_{rz})+\frac{\partial \tau^*_{zz}}{\partial z^*}\right)+\frac{1}{2\,\mathrm{Fr}}, \tag{3.12}$$

and

$$\left(v^*\frac{\partial v^*}{\partial r^*}+u^*\frac{\partial v^*}{\partial z^*}\right)=-\frac{\partial p^*}{\partial r^*}+\left(\frac{1}{r^*}\frac{\partial}{\partial r^*}(r^*\tau^*_{rr})+\frac{\partial \tau^*_{rz}}{\partial z^*}\right). \tag{3.13}$$

3.2 Geometry of the Jet Surface

3.2.1 Parameter of Curvature

The curvature parameter, R_c, of an axisymmetric free surface (see also Figure 2.1) is defined as [187]

$$2R_c=\frac{1}{R_{zr}}+\frac{1}{R_{n\theta}}. \tag{3.14}$$

The two radii R_{zr} and $R_{n\theta}$, which are depicted in Figure 3.1, are the principal radii of curvature of the surface. The radius of the axisymmetric surface, in the cylindrical coordinate system, is $r_s = h(z)$. At any point on the surface the curvature of the surface in the z, r-plane may be described by the radius R_{zr}. The second principal radius of curvature is not $r_s = h(z)$, the radius of the cross-section of the surface in the r, θ-plane, because $r_s = h(z)$ is not normal to the surface. The second principal radius of curvature is $R_{n\theta}$, a radius connecting the axis of symmetry with the point on the surface, such that the line $R_{n\theta}$ is normal to the surface.

From the geometry shown in Figure 3.1 we can find

$$R_{n\theta} = \widehat{s}h, \tag{3.15}$$

and

$$R_{zr} = \frac{\widehat{s}^3}{-d^2h/dz^2} = \frac{\widehat{s}^3}{-h''}, \tag{3.16}$$

where

$$\widehat{s} \equiv \left(1 + h'^2\right)^{1/2} \tag{3.17}$$

is the arc length of an element of the axi-symmetric surface. We can replace the principal radii of curvature in Equation (3.14) with Equations (3.15) and (3.16) and we obtain

$$2R_c = -\frac{h''}{\widehat{s}^3} + \frac{1}{\widehat{s}h}. \tag{3.18}$$

Substituting for $\widehat{s}$ then gives an equation for the curvature parameter, which reads

$$2R_c = -\frac{hh'' + (1 + h'^2)}{h\,(1 + h'^2)^{3/2}}. \tag{3.19}$$

3.2.2 Local Normal and Tangential Coordinate System

The components of the normal vector, n_r and n_z, in the cylindrical coordinate system are

$$n_r = \left(1 + h'^2\right)^{-1/2}, \tag{3.20}$$

and

$$n_z = -h'\left(1 + h'^2\right)^{-1/2}, \tag{3.21}$$

where $h' = dh/dz$. The tangential and normal unit vectors are related by

$$|t_z| = |n_r| \text{ and } |t_r| = |n_z|. \tag{3.22}$$

From these definitions follows that

$$v_s = h'u_s$$

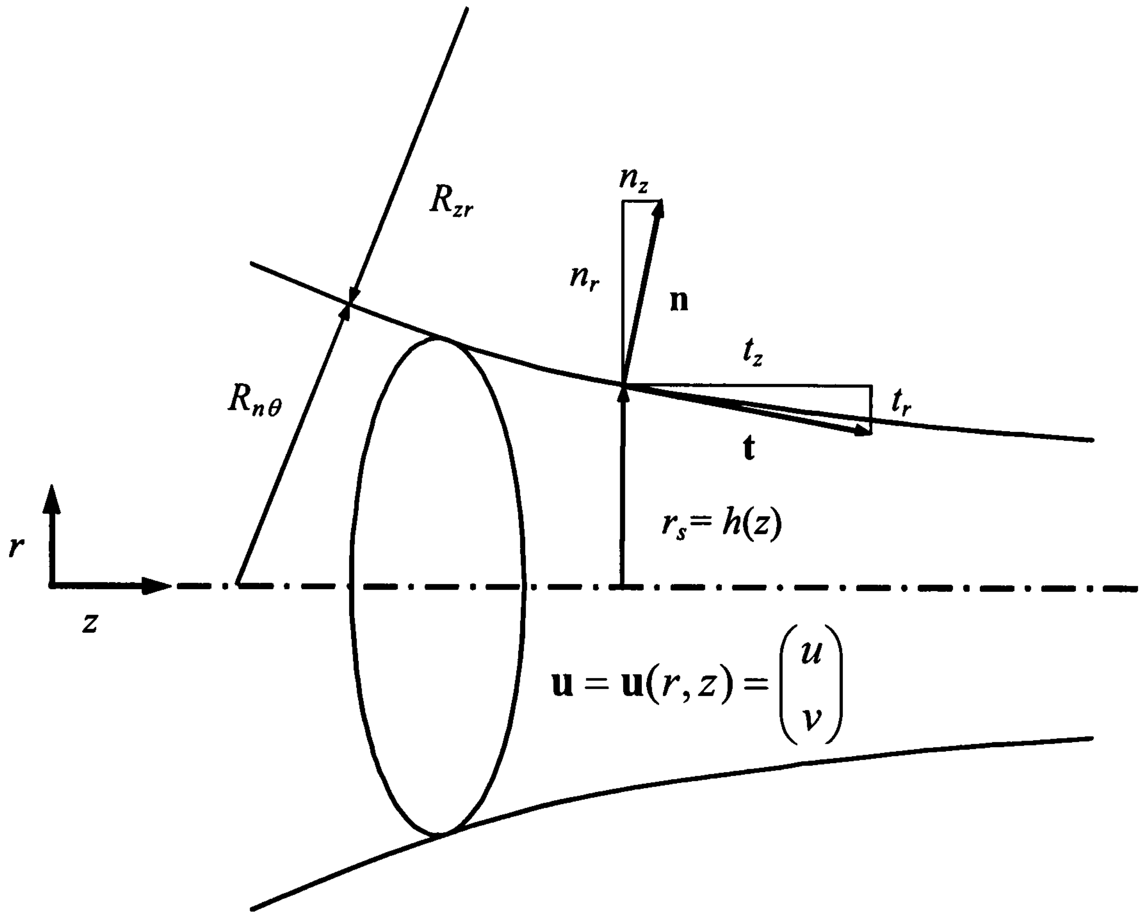

Figure 3.1: Surface geometry of the jet flow.

along $r_s = h(z)$. Therefore, if h' is small, the curvature of the jet surface may be neglected and $v_s \approx 0$.

3.3 Computational Domain and Meshing

The three-dimensional liquid jet is reduced to the axisymmetric case, that is, only the radial coordinate, r, the radial velocity component, v, the axial coordinate, z, and the axial velocity component, u, are considered. The origin of the cylindrical coordinate system is located where the centre line of the jet (the symmetry line) intersects the nozzle exit plane. Gravity, if considered in the flow problem, points in the positive axial direction, as shown in Figure 3.2.

A short part of the long capillary nozzle is included in the model, and at the inlet, some distance upstream of the nozzle exit, a parabolic flow profile is assumed, which results from the flow in the long capillary nozzle. The liquid emerges from the nozzle and the free liquid jet develops, once the shear stress at the nozzle wall vanishes. For the high Reynolds numbers under consideration

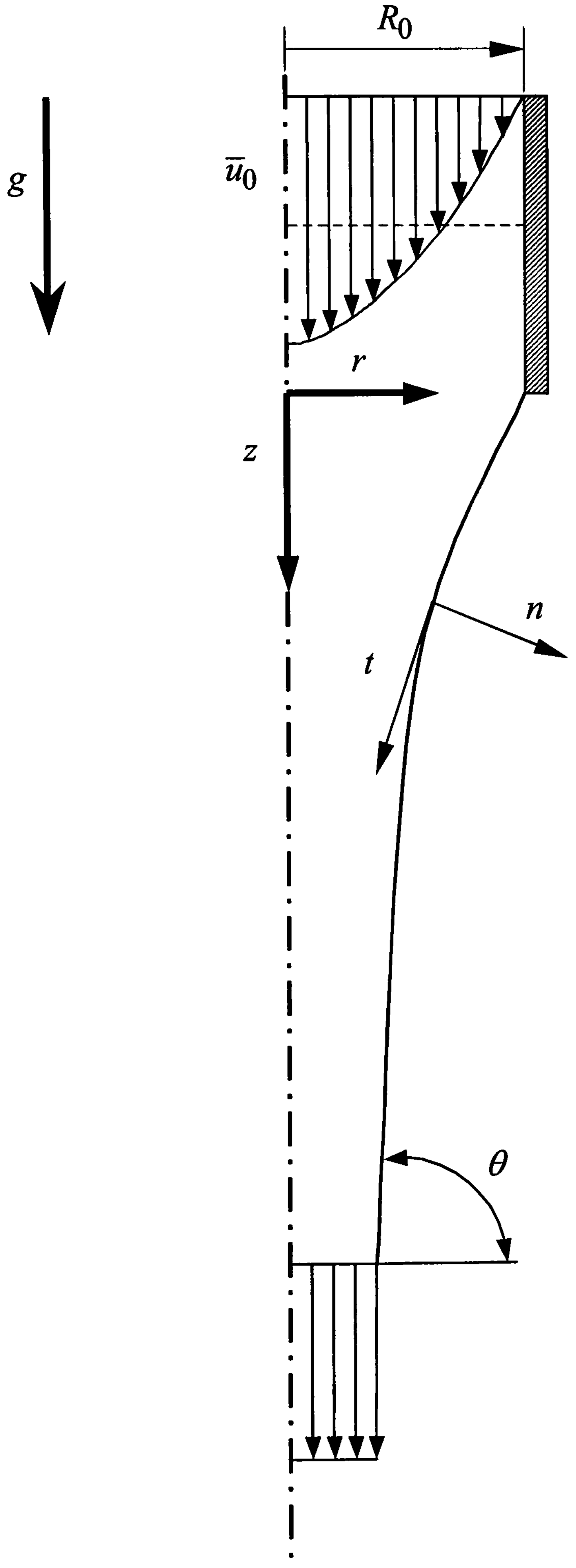

Figure 3.2: Axisymmetric model of the jet flow.

in this work, the jet contracts, which is depicted in Figure 3.2.

The jet emerges into a gas phase, usually air at atmospheric pressure and room temperature. This surrounding air phase is neglected in the model and treated as a vacuum. This means that the pressure of the adjacent phase is set equal to zero and it only exerts a pressure on the free surface of the jet due to the surface tension. Since the jet surface is curved, the pressure at the surface of the jet cannot be uniform. The flow region of the jet model ends at a downstream position sufficiently far away from the nozzle exit region, so that the appropriate boundary conditions can be applied at that position.

The dimensionless flow geometry of the axi-symmetric jet flow consists of a set of three contiguous rectangles, as shown in the upper sketch in Figure 3.3. The vertical lines (the radius of the jet) are of length unity, and the total length of the jet flow region in the case of a pure liquid is 200 length units, that is, for a nozzle radius of $R_0 = 1.0$ mm, the length of the free jet in the model is 200 mm.

The nozzle part of the flow geometry, the far-left rectangle, has a length of 3 length units. The vertical line on the left is the nozzle inlet, or simply "inlet", and the top vertical line is the nozzle wall, or simply "wall". The rectangle in the centre of the flow geometry and the far-right rectangle form the flow region of the free jet flow. The horizontal top lines of these two rectangles are the "free-surface" boundaries. The far-right vertical line represents the "outlet" of the jet flow geometry. The horizontal bottom lines of all three rectangles coincide with the axis of "symmetry". The two inner vertical lines are part of the "fluid" region. These lines are drawn for a special meshing purpose, which is indicated in Figure 3.3 by the three arrows that point towards the nozzle rim, where the free surface starts to develop. The boundary condition in this region of the jet flow changes from a no-slip condition at the nozzle wall to a condition of full slip at the free surface. This results in a rapid velocity increase at the point of emergence of liquid from the nozzle, which is associated with steep velocity gradients that require a dense mesh for the computation in this region. Therefore, a coarse-to-fine grading in the direction of the arrows is applied on the three lines that point towards this critical point.

The mesh configuration, that is, the number of elements and the grading that is applied to the distribution of elements along the edges of the flow geometry, is shown in the lower drawing in Figure 3.3. The number code refers to the

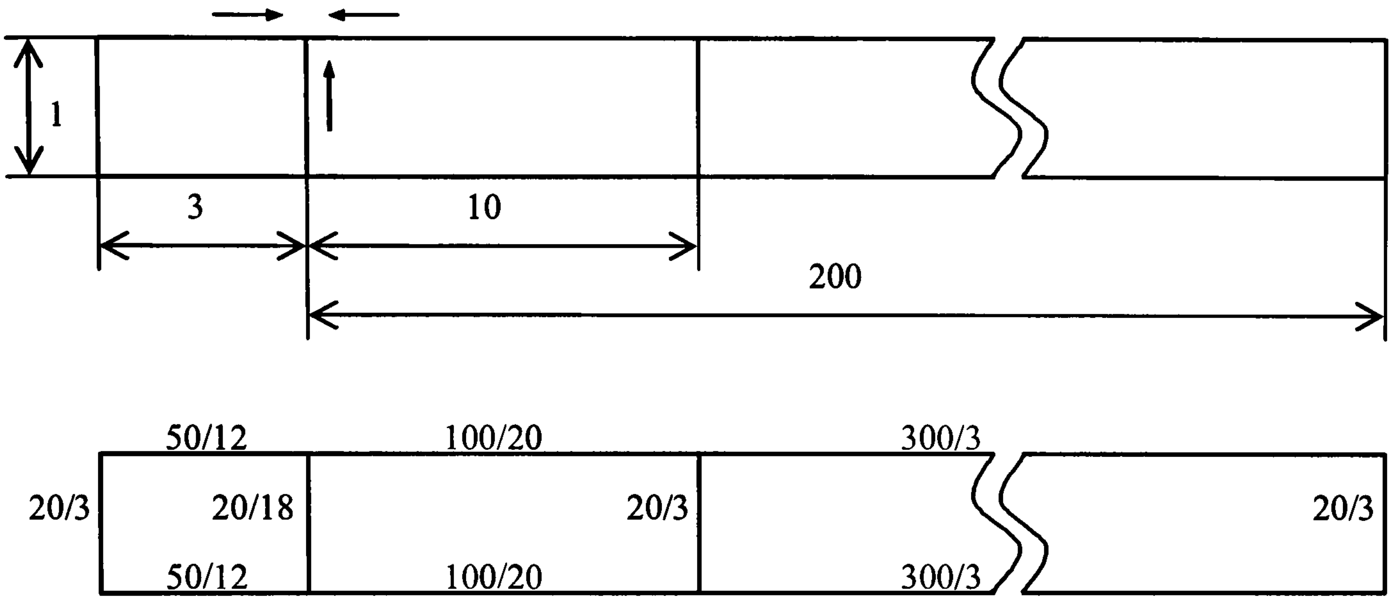

Figure 3.3: Flow geometry (upper drawing) and mesh configuration (lower drawing) of the axi-symmetric model of a pure liquid jet (not to scale).

number of nodal intervals on the relevant edge and the spacing ratio between the first and the last node on this particular edge. For example, 20/3 refers to 20 intervals along the edge, the interval between the last two nodes on this particular edge being only 1/3 of the interval of the first two nodes on this edge. The total numbers of elements in the mesh configuration shown in Figure 3.3 is 9000, which resulted in average computation times of not more than 5 minutes for the water jet on a Windows 2000 PC with 512 Mb RAM and a 1.0 GHz processor.

The mesh was created using FLUENT's mesh generator GAMBIT (see Appendix B.1). A section of the mesh, which matches the configuration shown in Figure 3.3, is displayed in Figure 3.4. The relatively simple geometry permits the use of a regular type of mesh. The horizontal line in Figure 3.4 shows the initial position of the free surface before deformation. The position of the surface is adjusted to its required position during the computation by moving the nodes of the mesh in and below the surface vertically downwards along the so-called spines. The fully-coupled Newton-Raphson iteration scheme updates the position of the free surface at each iteration step to satisfy the kinematic condition on the surface, Equation (3.37).

The position of the node at the nozzle exit, which is part of the nozzle wall and the free surface, is fixed at $z^* = 0$ and $R^* = 1.0$. The shape of the free surface is then determined by the stress balance and the kinematic condition on

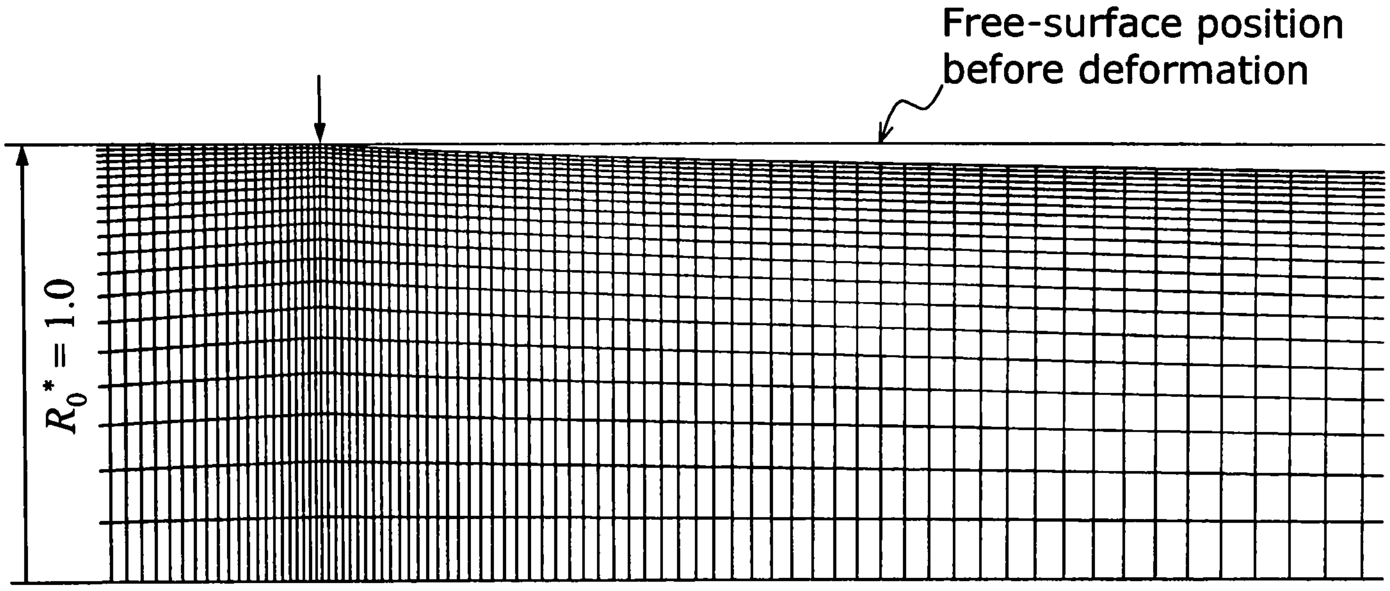

Figure 3.4: Regular mesh of the water jet in the nozzle region. The nozzle exit ($z = 0, r = R_0$) is marked by the arrow. The nozzle radius is $R_0 = 0.79$ mm and the length of the mesh section shown is about 3 times the nozzle radius. The flow conditions are Re = 1550, $\mathrm{Ca}^{-1} = 74.3$, and $(2\,\mathrm{Fr})^{-1} = 0.00807$.

the surface. At the outlet, the contact angle, θ, defines the direction of surface movement.

The mesh that is displayed in Figure 3.4 has been used in all computations of the water jet. The results obtained were found to be of sufficient accuracy and insensitive to further refinement of the mesh.

3.4 Boundary Conditions

3.4.1 Inlet Section

Poiseuille flow is assumed at the inlet of the flow domain, that is

$$u(r) = 2\overline{u}_0 \left(1 - \left(\frac{r}{R_0}\right)^2\right), \quad v = 0 \text{ for } (r, z < 0). \tag{3.23}$$

Using the dimensionless variables defined in (3.6), we can write this boundary condition as

$$u^*(r^*) = 2\left(1 - r^{*2}\right), \quad v^* = 0 \text{ for } r^*, z^* < 0. \tag{3.24}$$

3.4.2 Nozzle Wall

At the nozzle wall, the usual no-slip condition,

$$u, v = 0 \text{ for } r = R_0, z \leqslant 0, \tag{3.25}$$

is applied, which in its dimensionless form reads

$$u^*, v^* = 0 \text{ for } r^* = 1.0, z^* \leqslant 0. \tag{3.26}$$

3.4.3 Symmetry Line

Along the centre line of the jet flow, the symmetry conditions

$$v = 0, \ \frac{\partial u}{\partial r} = 0 \text{ for } r = 0, z \tag{3.27}$$

are employed. In their dimensionless form, these boundary conditions are

$$v^* = 0, \frac{\partial u^*}{\partial r^*} \text{ for } r^* = 0, z^*. \tag{3.28}$$

3.4.4 Downstream Position

Horizontal Jet Flows

For horizontal jets, it is generally accepted that a radially uniform axial velocity distribution and a final jet diameter are approached asymptotically as the distance from the jet nozzle is increased (see Section 2.1), that is,

$$\theta\,(r = R_z) = \frac{\pi}{2}, v = 0 \text{ for } z \gg 0, \tag{3.29}$$

or

$$\theta\,(r^* = R_z^*) = \frac{\pi}{2}, v^* = 0 \text{ for } z^* \gg 0. \tag{3.30}$$

Vertical Jet Flows

A vertical jet continues to contract due to the action of gravity and does not reach a final diameter (see Section 2.2). It is presumed that, for a long enough jet, the inertia term will eventually grow so that it overwhelms viscous forces and balances the gravitational term, thus leading to a free-fall velocity field [191]. This requires that $\theta < \pi/2$. Applying Bernoulli's law and the equation of continuity, and accounting for the parabolic velocity profile at the nozzle exit yields an expression for the free-surface position of the jet, R_z, as a function of the axial jet coordinate, z. We have derived this expression in Section 2.2 in Equation (2.23). Differentiation of this equation with respect to z yields an expression for the change of the axial surface position in a vertical jet,

$$\frac{dR_z}{dz} = -\frac{g}{2R_0\overline{u}_0^2}\left(\frac{4}{3} + \frac{2g}{\overline{u}_0^2}z\right)^{-5/4}. \tag{3.31}$$

We can thus obtain a value for the contact angle, θ, at the outlet of the jet flow domain. It reads

$$\theta(z \gg 0, r = R_z) = \frac{\pi}{2} - \arctan\left(\frac{dR_z}{dz}\right). \tag{3.32}$$

Continuous contraction of the jet results in a velocity profile that is not exactly uniform in the radial direction. The symmetry condition requires $v(r = 0) = 0$, but v increases with increasing r, reaching its maximum value at the surface ($r = R_z$). This maximum value may be expressed in terms of the contact angle, θ, and the axial jet velocity component, u, to give

$$v(z \gg 0, r = R_z) = u \tan\left(\frac{\pi}{2} - \theta\right) \approx u\left(\frac{\pi}{2} - \theta\right). \tag{3.33}$$

The smallness of $(\pi/2 - \theta)$, which is of order 10^{-4}, leads to very small values for $v(z \gg 0, r = R_z)$. However, downstream boundary conditions formulated by requiring that all velocity gradients vanish result in an inconsistent flow field for a vertical jet. Therefore, only the contact angle, $\theta(z \gg 0, r = R_z)$, is applied as a downstream boundary condition. In its dimensionless form, this boundary condition reads

$$\theta(z^* \gg 0, r^* = R_z^*) = \frac{\pi}{2} - \arctan\left\{-\frac{1}{4\,\mathrm{Fr}}\left(\frac{4}{3} + \frac{z^*}{\mathrm{Fr}}\right)^{-5/4}\right\}. \tag{3.34}$$

The curvature in the azimuthal direction and the non-zero surface tension value dictate that the pressure at the common node between the free surface and the outlet is non-zero. If there is no boundary condition specified on the normal component of velocity at the outlet, which is the case, the so-called stress-free natural boundary condition is applied in FIDAP, which is

$$-p + 2\mu\frac{\partial u_n}{\partial n} = 0, \tag{3.35}$$

where p is the pressure, μ is the viscosity, u_n is the normal component of velocity, and n is the normal to the outlet. Note that in the jet flow geometry, the direction of the normal at the outlet of the flow domain is identical with the axial direction of flow. If the flow is fully developed (or nearly fully developed) at the outlet (making the derivative $\partial u_n/\partial n$ zero, or nearly zero) or if the viscous contribution is small, then Equation (3.35) effectively makes the pressure zero at the outlet, which conflicts with the non-zero pressure at the outlet node caused by the curvature and the non-zero surface tension value. Removing the pressure term from Equation (3.35) resolves this conflict.

3.4.5 Free Surface of the Jet

Kinematic Condition

A kinematic condition is used to update the changing position of the free surface of the jet, as it links surface position and surface velocity, and is the assertion that fluid does not cross the free surface. This implies that

$$\mathbf{u} \cdot \mathbf{n} = vn_r + un_z = 0 \tag{3.36}$$

along the free surface. In Equation (3.36), $\mathbf{u} \cdot \mathbf{n}$ is the normal velocity at the surface that has the radial component vn_r and the axial component un_z. The normal velocity is made dimensionless in the usual way, which gives

$$v^* n_r^* + u^* n_z^* = 0. \tag{3.37}$$

Equation (3.37) is not a true boundary condition to the equations of motion. Rather, it is a distinguished condition that can be treated as an additional equation for the location of the unknown position of the free surface.

Normal and Tangential Stress Conditions

Two stress boundary conditions, normal and tangential to the free surface, act as true boundary conditions to the equations of motion [192]. The normal stress condition

$$\tau_n = (2\sigma R_c - p_a) \tag{3.38}$$

accounts for the varying pressure along the jet axis due to the curvature of the jet surface using the Young-Laplace equation. In Equation (3.38), σ is the coefficient of surface tension, R_c is the curvature parameter, and p_a is the ambient pressure of the gas surrounding the liquid jet. The dimensionless form of Equation (3.38) is

$$\tau_n^{**} = \frac{2R_c^*}{\mathrm{Ca}} - p_a^{**}, \tag{3.39}$$

in which the dimensionless normal stress component, τ_n^{**}, is defined as

$$\tau_n^{**} = \frac{\mathrm{Re}}{2}\tau_n^* = \frac{\mathrm{Re}}{2}\frac{\tau_n}{\rho \overline{u}_0^2}, \tag{3.40}$$

and the dimensionless curvature parameter of the jet, R_c^*, is given as

$$R_c^* = R_0 R_c. \tag{3.41}$$

Equation (3.39) provides the third dimensionless parameter of the jet flow—the Capillary number, Ca, which is defined in Equation (2.14). The dimensionless ambient pressure in Equation (3.39), p_a^{**}, is defined as

$$p_a^{**} = \frac{\mathrm{Re}}{2}p_a^* = \frac{\mathrm{Re}}{2}\frac{p_a}{\rho \overline{u}_0^2}. \tag{3.42}$$

In the numerical computations presented in this thesis, we have set $p_a = 0$. The tangential stress condition is given by

$$\tau_t = \frac{\partial \sigma}{\partial t} = \mu \frac{\partial u_t}{\partial n}. \tag{3.43}$$

Equation (3.43) represents a balance between viscous traction and the Marangoni (shear) stress due to a gradient in the surface tension. In the case of a jet of a pure liquid, where the surface tension is constant, the tangential stress condition is zero due to $\partial\sigma/\partial t = 0$, which results in $\partial u_t/\partial n = 0$. The adsorption of surfactant, which causes the surface tension to vary locally along the jet surface, that is, $\partial\sigma/\partial t \neq 0$, renders this boundary condition active and thus alters the fluid mechanics of the jet flow (Marangoni effect). The dimensionless form of Equation (3.43) is

$$\tau_t^{**} = \frac{\partial}{\partial t^*}\left(\frac{1}{\mathrm{Ca}}\right) = \frac{\partial u_t^*}{\partial n^*}, \tag{3.44}$$

in which the dimensionless tangential stress component, τ_t^{**}, is made dimensionless in an analogous way to the normal stress component, τ_n^{**} (see Equation (3.40)). The dimensionless tangential velocity component, u_t^*, is scaled using $\overline{u}_0$, and the dimensionless tangential coordinate, t^*, is made dimensionless using R_0.

3.5 Creeping Jet Flows: Die-Swell

3.5.1 Die-Swell in the Absence of Gravity

A finite-difference technique was described by Horsfall in 1973 to predict the shape of a die-swell of a Newtonian liquid emerging from a capillary at zero Reynolds number [197]. The terms on the left-hand side of the Navier-Stokes equations (3.7) and (3.8) are then equal to zero. Horsfall formulated the Navier-Stokes equations and the boundary conditions in terms of the stream function, and neglected the effect of surface tension on the flow. Parabolic flow was assumed upstream of the capillary exit, a no-slip condition was applied at the capillary wall, and a fully relaxed velocity profile formed the downstream boundary condition. In Horsfall's numerical procedure, an arbitrary boundary shape was chosen and the stress tangential to the surface was made zero. The stress distribution normal to the surface was calculated and the boundary shape was adjusted so as to minimise the normal stress. Horsfall expressed doubts about the accuracy of his finite-difference technique in representing the discontinuity at the capillary exit, where the tangential stress is finite at the wall and zero at the free surface. The die-swell of a Newtonian liquid at very low shear rates was found experimentally to be 13.5% [169, 170]; Horsfall's simulations predicted a die-swell of only 6.3%.

Only one year later, Nickell *et al.* [198] carried out their own experiments and concluded that for $\mathrm{Ca}^{-1} \ll 1$, the effect of surface tension on the expansion of the jet was negligible, which was also shown by Middleman and Gavis [170, 171] and Goren and Wronski [185]. The experiments of Nickell *et al.* have shown that for very low Reynolds numbers, $\mathrm{Re} \leqslant 1$, the viscous forces completely dominate the flow problem, which is in agreement with Horsfall's model. The finite-element program AXFINR, a system of Fortran routines, was used to discretise the governing set of equations. Normal stress, shear stress and normal velocity were required to be zero simultaneously on the free surface. The die-swell of a Newtonian liquid for the limiting case of zero Reynolds number was calculated to be about 13%, which is in very good agreement with the experimentally found value. The dominant feature in their calculations was the stress singularity at the exit lip of the die. The shear stress along the tube wall changes from its Poiseuille flow value to larger magnitudes as the tube exit is approached, indicating that Poiseuille flow does not persist up to the nozzle exit at very low

Reynolds numbers.

3.5.2 Die-Swell in the Presence of Gravity

Dutta and Ryan employed a finite-difference method to compute the die-swell of Newtonian liquids [189]. Their numerical technique includes both surface tension and gravitational forces. The set of boundary conditions includes Poiseuille flow a little upstream from the nozzle exit, uniform flow at the far downstream position, and a no-slip condition at the nozzle wall. The tangential stress at the free surface was set equal to zero and the normal stress component was balanced by the tractions due to surface tension forces and the pressure exerted on the surface by the surrounding medium. A kinematic condition related the surface movement to the surface velocity components.

Neglecting gravity and surface tension and applying very small Reynolds numbers led to a predicted die-swell of 12%, which is reasonably close to the experimental value of 13.5%. As before in the work of Nickell *et al.*, the results in Dutta and Ryan's work showed that the flow is not fully developed at the nozzle exit, because of the absence of inertia forces due to the very small Reynolds numbers, which allowed the vorticity generated at the nozzle tip to diffuse both downstream and upstream from the exit plane.

The results show that Middleman's [187] doubts regarding the assumption of fully developed laminar flow at the nozzle exit are legitimate in the case of creeping Newtonian flow ($\mathrm{Re} \approx 0$) when inertia forces can be neglected. Fisher *et al.* [188] observed the same phenomenon in their numerical predictions of low Reynolds number jet flows. We have raised this issue in Section 2.3, where we demonstrated, as a result of a boundary-layer treatment at high Reynolds numbers, that the exchange of momentum between the boundary layer and the core of the jet is negligible, and Poiseuille flow thus exists at the nozzle exit. The authors mentioned above have shown that this simplification is not valid at low Reynolds numbers.

Dutta and Ryan stated that gravitational forces dominate the viscous forces at $\mathrm{St} > 0.5$, leading to contraction of the jet and acceleration of the fluid. The presence of surface tension had an inhibiting effect on the swelling behaviour of the jet. If both surface tension and gravity are considered, the contribution of gravity in reducing die-swell is significantly greater.

Trang and Yeow investigated the role of gravitational forces in extrudate swell experimentally and numerically for Re < 0.02 [199]. The jet swelled immediately after leaving the nozzle. As the jet travelled vertically downwards the 'stretching' effect of gravity reduced its diameter. The observed behaviour depended on the magnitude of gravitational body force compared to viscous force in the elongated jet (the Stokes number, St). The theoretical investigation performed by Trang and Yeow can be described as a hybrid technique since both a numerical as well as an analytical solution were obtained. The flow field was divided into two parts to avoid difficulties in the free surface iteration scheme; the extrudate swell region close to the nozzle and the fully developed flow region further downstream of the nozzle exit. The flow in the first region was treated as being fully two-dimensional and a finite-element method was applied using the program AXFINR to solve the governing equations. In the second part the axial velocity was assumed to be independent of the radial coordinate, and a simple analytical solution was obtained. The two solutions were then matched.

3.6 High Reynolds number Liquid Jets in the Absence and Presence of Gravity

In this section, we study the behaviour of jet flows of pure liquids (mostly water) in the absence and presence of gravity. We introduce the convention that a horizontal jet refers to a jet in the absence of gravity, while a vertical jet refers to a jet in the presence of gravity. First, in the absence of gravity, we vary the values for the mean nozzle exit velocity, $\overline{u}_0$, and the nozzle radius, R_0, which results in different combinations of Reynolds numbers, Re, and Capillary numbers, Ca (see Table 3.2). We also wish to establish the flow conditions under which Harmon's results, Equations (2.6) and (2.7), are obtained. Next, we investigate the effect of surface tension on the surface velocity and the jet contraction of a horizontal jet, that is, we effectively compare a horizontal jet of water with a jet of liquid that has a lower surface tension than that of water under the same flow conditions.

Gravity is introduced in the following section, in which the hydrodynamics of a horizontal and a vertical water jet are compared. Here, we compare the numerical simulations with the theoretical equations that were derived from the conservation of energy (Bernoulli equation) in Section 2.2. We also discuss

Table 3.1: Physical properties of water at T = 293 K used in the numerical computations.

ρ / kg m^{-3}	1000
μ / kg m^{-1} s^{-1}	0.001
σ / 10^{-3} N m^{-1}	72.8

the modelling work of Brun and Lienhard [178], Duda and Vrentas [195], and Georgiou *et al.* [202] on vertical liquid jets at mostly high Reynolds numbers.

In the following section, we study the fluid mechanics of a vertical jet when the nozzle exit velocity profile is not that of Poiseuille flow, which is the case when short nozzles are used. Then, we compare the CFD simulations to measurements of the fluid mechanics of vertical water jets. Finally, we include wetting at the nozzle exit in the CFD model, which causes a toroidal flow to occur near the nozzle exit that leads to stagnating flow at the jet surface.

3.6.1 Effect of Mean Nozzle Exit Velocity and Nozzle Radius

The liquid jet reaches a final state if gravitational acceleration is not present in the flow problem (see Section 2.1). Once the velocity profile within the jet is fully relaxed and the jet has a uniform velocity throughout, the free-surface position as well as the jet velocity remains constant. The Reynolds number, Re, and the Capillary number, Ca, are the parameters of the horizontal jet. In this section, using our CFD model, we wish to establish the flow conditions under which Harmon's [168] results for the horizontal water jet, Equations (2.6) and (2.7), are valid. The properties of water at T = 293 K are given in Table 3.1 and are kept constant in all computations.

The Reynolds number and the Capillary number, which are defined in Equations (2.8) and (2.14), respectively, change through variations of the mean nozzle exit velocity, $\overline{u}_0$, and the nozzle radius, R_0. Table 3.2 shows the combinations of $\overline{u}_0$ and R_0 that have been chosen to achieve the desired values of Re and Ca^{-1}.

For a low Reynolds number of Re = 500, Figures 3.5 and 3.6, the velocity profile relaxes rapidly and a final state is reached well within the limits of the computational flow domain, which extends to a downstream distance of $z^* = 200$.

In Figure 3.5, a constant surface velocity of about $u_s^* = 1.20$ and a constant jet contraction of $R^* = 0.916$ is reached at a jet length of approximately $z^* = 80.0$. In Figure 3.6, where the surface tension parameter Ca^{-1} has a lower value at the same Reynolds number, the jet shows a higher degree of contraction. At about the same downstream distance from the nozzle, a constant surface velocity of about $u_s^* = 1.25$ and a constant jet contraction of $R^* = 0.89$ is calculated, which is nearer to Harmon's values.

At $\mathrm{Re} = 500$, the CFD simulation predicts a lower jet contraction than Harmon's result. Consequently, due to continuity, the predicted value of the final jet velocity is also lower. This discrepancy has its origin in the neglected effects of surface tension and viscous dissipation on the shape of the jet in Harmon's work. Harmon assumed that the kinetic energy of the jet at the nozzle exit is fully used to redistribute the velocity profile within the jet towards a uniform jet velocity, and no energy loss due to dissipation occurs. Harmon's result can therefore be regarded as a theoretical maximum for the jet contraction ratio of a horizontal liquid jet.

The velocity profile of the jet relaxes less rapidly if the Reynolds number is increased. Figures 3.7 to 3.9 show the jet shape and the surface velocity for $\mathrm{Re} = 1000$ and $\mathrm{Re} = 2000$, respectively. At $\mathrm{Re} = 1000$, depending on the choice of $\overline{u}_0$ and R_0, the surface tension parameter, Ca^{-1}, takes on two different values. Only one combination of $\overline{u}_0$ and R_0 is studied at $\mathrm{Re} = 2000$.

For $\mathrm{Re} = 1000$, a virtually uniform jet velocity is reached at the outflow of the computational flow domain. Almost the same final values for u_s^* and R^* are predicted in both Figures 3.7 and 3.8, which indicates that surface tension forces become less important with increasing Reynolds number. The agreement with Harmon's values is better with an increase in Re.

Table 3.2: Flow parameters of the horizontal jet.

Figures	Re	Ca^{-1}	$\overline{u}_0$ / m s^{-1}	R_0 / mm
3.5	500	291.2	0.25	1.0
3.6	500	72.8	1.0	0.25
3.7	1000	145.6	0.5	1.0
3.8	1000	72.8	1.0	0.5
3.9 and 3.10	2000	72.8	1.0	1.0

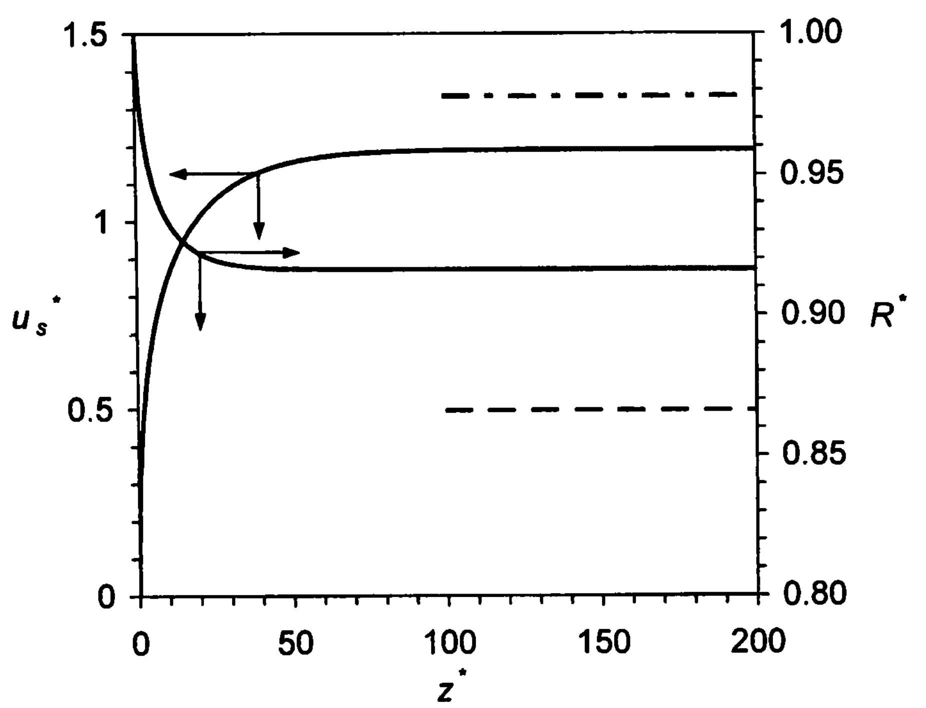

Figure 3.5: Axial surface velocity, $u_s^* = u_s/\overline{u}_0$, and free-surface position, $R^* = R/R_0$, as a function of the axial jet coordinate, $z^* = z/R_0$, in a horizontal water jet. Re = 500, $\mathrm{Ca}^{-1} = 291.2$, $\overline{u}_0 = 0.25$ m s^{-1}, $R_0 = 1.0$ mm. The plot shows Harmon's results for the final surface position (dashed line) and velocity (semi-dashed line) in a horizontal jet, Equations (2.6) and (2.7), respectively.

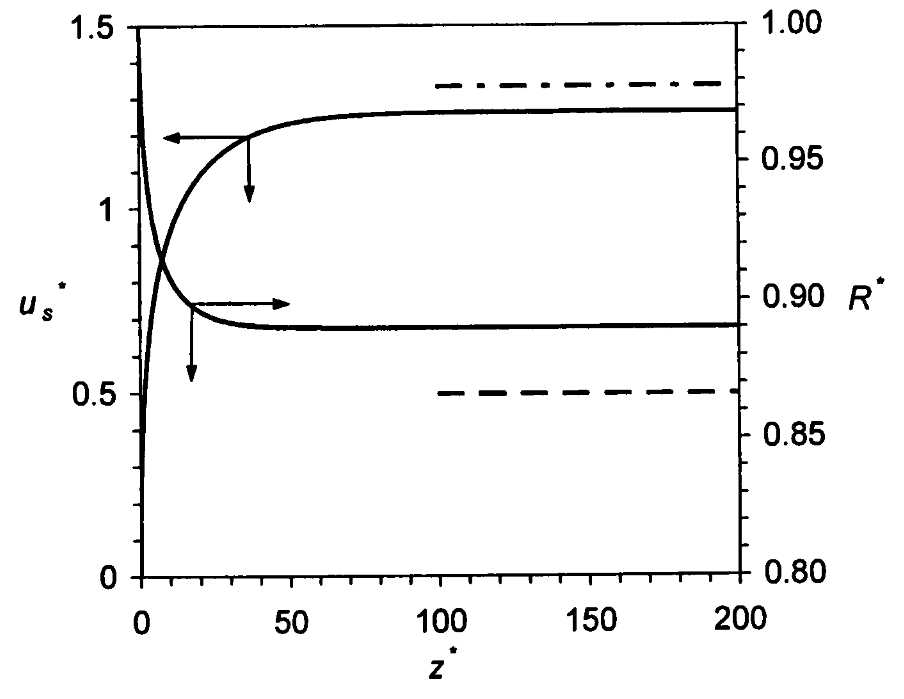

Figure 3.6: Axial surface velocity, $u_s^* = u_s/\overline{u}_0$, and free-surface position, $R^* = R/R_0$, as a function of the axial jet coordinate, $z^* = z/R_0$, in a horizontal water jet. Re = 500, $\mathrm{Ca}^{-1} = 72.8$, $\overline{u}_0 = 1.0$ m s^{-1}, $R_0 = 0.25$ mm. The plot shows Harmon's results for the final surface position (dashed line) and velocity (semi-dashed line) in a horizontal jet, Equations (2.6) and (2.7), respectively.

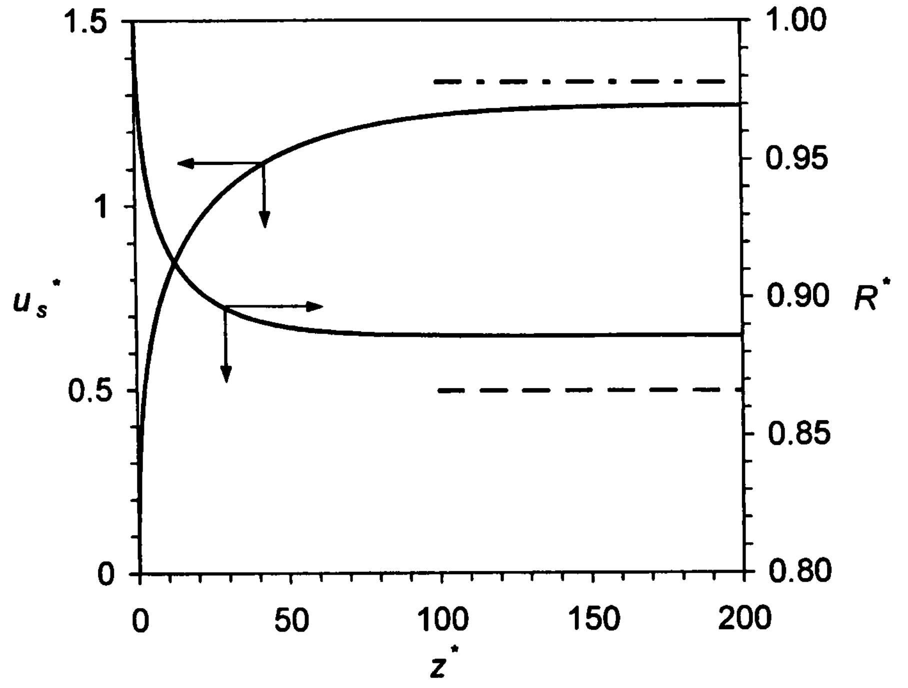

Figure 3.7: Axial surface velocity, $u_s^* = u_s/\overline{u}_0$, and free-surface position, $R^* = R/R_0$, as a function of the axial jet coordinate, $z^* = z/R_0$, in a horizontal water jet. Re = 1000, $\text{Ca}^{-1} = 145.6$, $\overline{u}_0 = 0.5$ m s^{-1}, $R_0 = 1.0$ mm. The plot shows Harmon's results for the final surface position (dashed line) and velocity (semi-dashed line) in a horizontal jet, Equations (2.6) and (2.7), respectively.

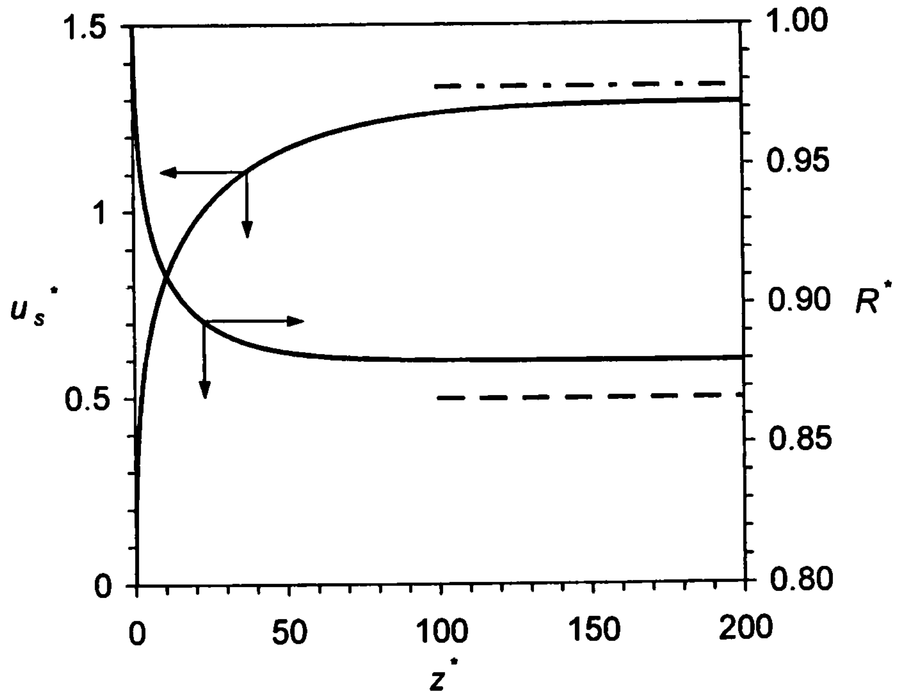

Figure 3.8: Axial surface velocity, $u_s^* = u_s/\overline{u}_0$, and free-surface position, $R^* = R/R_0$, as a function of the axial jet coordinate, $z^* = z/R_0$, in a horizontal water jet. Re = 1000, $\text{Ca}^{-1} = 72.8$, $\overline{u}_0 = 1.0$ m s^{-1}, $R_0 = 0.5$ mm. The plot shows Harmon's results for the final surface position (dashed line) and velocity (semi-dashed line) in a horizontal jet, Equations (2.6) and (2.7), respectively.

The length of the jet model does not suffice to show fully relaxed velocity profiles if Re is further increased to a value of 2000, as no uniform jet velocity is predicted (see Figure 3.9). The inertia forces dominate both the viscous forces and the surface tension forces in high Reynolds number jet flows. However, long jet lengths are needed to achieve the theoretical values.

Axial jet velocity profiles at various jet lengths are given in Figure 3.10 to illustrate the relatively slow velocity profile relaxation at the high Reynolds number of $\mathrm{Re} = 2000$. The graphs show clearly that Harmon's theoretical values are approached at very large distances from the nozzle.

The finite-element program AXFINR was used by Omodei to model axisymmetric Newtonian jets of incompressible viscous fluid [200, 201]. A range of Reynolds numbers between 10^{-4} and 1000 was covered and surface tension effects were considered as well. Zero pressure was applied in the invsicid fluid surrounding the jet, a fully developed Poiseuille flow was assumed at a little distance upstream of the nozzle exit and a uniform velocity profile was employed at the downstream position. The normal stress on the jet surface was imposed in the direction of the outward normal to that boundary and the shear stress was set equal to zero.

The authors attributed any divergence tendency for the range of values of Re and Ca^{-1} to the free surface configuration rather than the non-linear inertia terms, since rapid convergence was achieved whenever the free surface was kept fixed. The iterative process soon became divergent as the ratio Ca^{-1} increased. The iteration scheme for the free surface was therefore modified to regain convergence for a large range of Ca^{-1}, so that the change in the free surface position was not too large. Two mesh configurations were used. For $\mathrm{Re} \leqslant 36$ a mesh with a length of 17 nozzle radii units was found to be sufficient. For $36 \leqslant \mathrm{Re} \leqslant 1000$ the length was increased up to 300 nozzle radii units to ensure that a uniform velocity profile was attained.

As the surface tension parameter Ca^{-1} became significantly larger than unity, oscillations in the curvature of the free surface became an increasingly significant feature of the surface profiles. These oscillations were regarded as a property of the numerical solution and apparently caused severe problems in the limiting range of conditions. Refining the mesh increased these spatial oscillations in amplitude, which was supposed to be due to the surface tension boundary conditions since they were derived from the curvature of the surface.

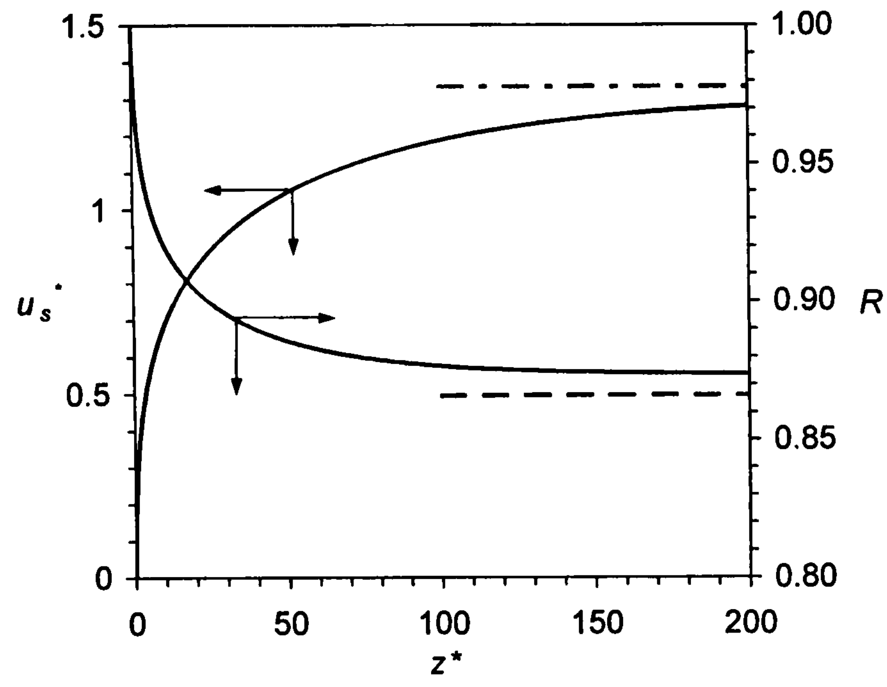

Figure 3.9: Axial surface velocity, $u_s^* = u_s/\overline{u}_0$, and free-surface position, $R^* = R/R_0$, as a function of the axial jet coordinate, $z^* = z/R_0$, in a horizontal water jet. Re = 2000, $\mathrm{Ca}^{-1} = 72.8$, $\overline{u}_0 = 1.0$ m s^{-1}, $R_0 = 1.0$ mm. The plot shows Harmon's results for the final surface position (dashed line) and velocity (semi-dashed line) in a horizontal jet, Equations (2.6) and (2.7), respectively.

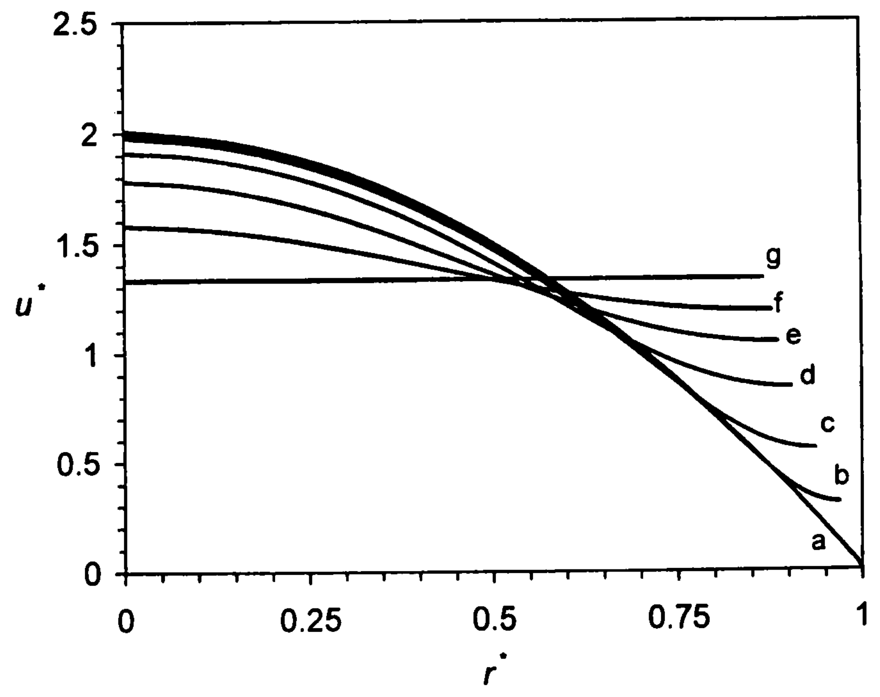

Figure 3.10: Axial velocity profiles, $u^*(r^*) = u(r)/\overline{u}_0$, in a horizontal water jet at different downstream positions, z^*. Re = 2000, $\mathrm{Ca}^{-1} = 72.8$, $\overline{u}_0 = 1.0$ m s^{-1}, $R_0 = 1.0$ mm. $z^* = 0$ (a), $z^* = 1.0$ (b), $z^* = 5.0$ (c), $z^* = 20.0$ (d), $z^* = 50.0$ (e), $z^* = 100.0$ (f), and Harmon's result, Equation (2.7), (g).

3.6.2 Effect of Surface Tension

The effect of surface tension on the fluid mechanics of a horizontal liquid jet is shown in Figures 3.11 and 3.12 for a high and a low Reynolds number of Re = 2000 and 500, respectively. The mean nozzle exit velocity is kept constant at $\overline{u}_0 = 1.0$ m s^{-1}, and we achieve a reduction in Re through a change in the nozzle radius from $R_0 = 1.0$ mm to $R_0 = 0.25$ mm. The desired variation of the surface tension parameter, Ca^{-1}, is thus solely based on a variation in surface tension, σ. The free-surface position, $R^*(z^*)$, and the axial surface velocity, $u_s^*(z^*)$, are calulated for Ca$^{-1} = 72.8$ and Ca$^{-1} = 30$ at each Reynolds number.

As can be seen from Figure 3.11, surface tension forces have only a minor effect on the fluid mechanics of the liquid jet if the Reynolds number is high, which emerged already in the previous section. The surface velocity curves for Ca$^{-1} = 72.8$ and Ca$^{-1} = 30.0$ in Figure 3.11 fall together, and nearly no alteration of the jet flow occurs. The effect of surface tension on the jet flow is more significant if the Reynolds number is lower, as shown in Figure 3.12. Lowering the value of the surface tension parameter causes the jet to contract more, thereby increasing the surface velocity of the jet due to continuity of mass flow.

In the presence of surfactant, the surface tension parameter is not uniform along the jet length, but varies along the jet surface. The shear stress condition (3.44), which is zero in the absence of surface-active material, becomes active. We then have, in addition to the stress acting normally on the jet surface, a second force acting tangentially on the jet surface. The computed and measured data presented in Chapter 4 show how this tangential (Marangoni) shear stress leads to alteration of the jet flow in the high Reynolds number flow regime.

3.6.3 Effect of Gravity

The effect of gravitational acceleration on the jet flow is discussed in this section. Gravity acts in the positive axial direction and further accelerates the jet flow (see Figure 3.2). A comparison between the jet flow with and without gravity for Re = 2000 and Ca$^{-1} = 72.8$ is given in Figures 3.13 and 3.14.

Jet contraction, $R^*(z^*)$, and surface velocity, $u_s^*(z^*)$, of the jet in the presence and absence of gravity are given in Figure 3.13. The surface velocity of the jet is significantly increased at the far downstream position due to the presence of

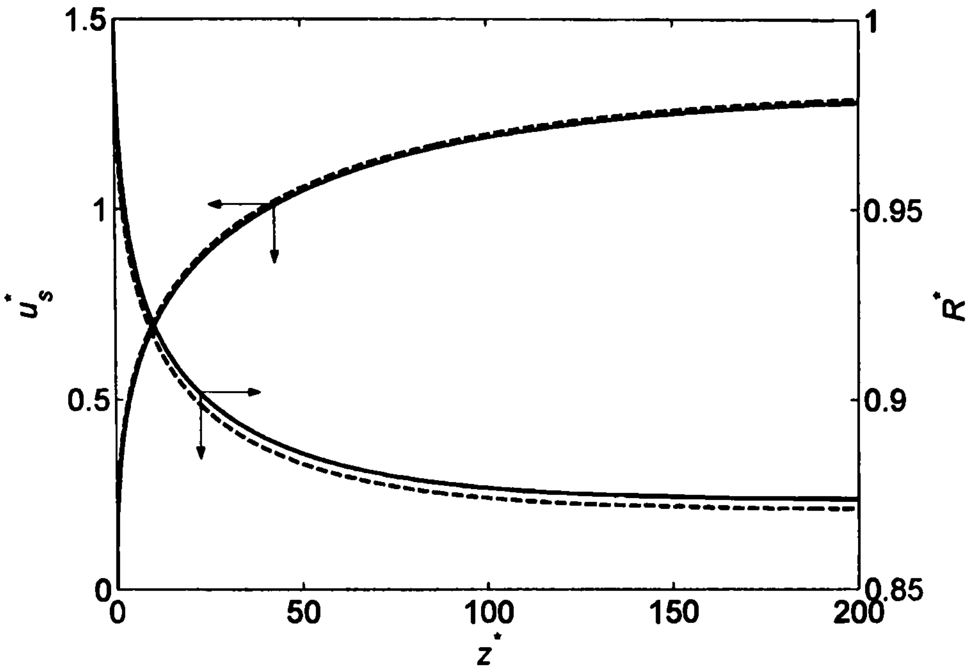

Figure 3.11: Effect of surface tension on the axial surface velocity, $u_s^* = u_s/\overline{u}_0$, and free-surface position, $R^* = R/R_0$, in a horizontal jet as a function of the axial jet coordinate, z^*. Re = 2000, $\mathrm{Ca}^{-1} = 72.8$ (solid lines) and 30.0 (dashed lines), $\overline{u}_0 = 1.0$ m s^{-1}, $R_0 = 1.0$ mm.

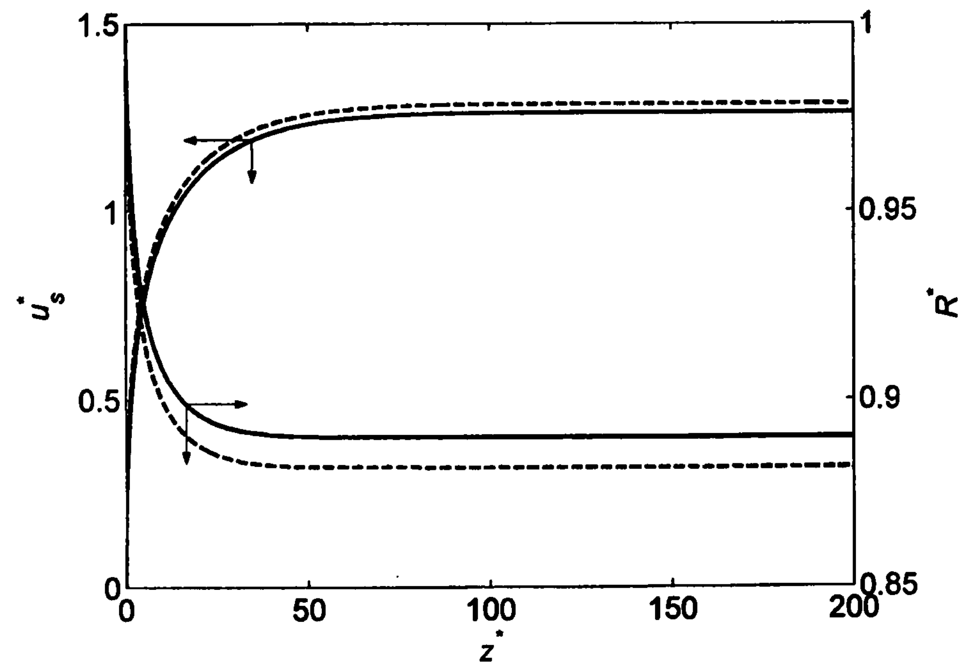

Figure 3.12: Effect of surface tension on the axial surface velocity, $u_s^* = u_s/\overline{u}_0$, and free-surface position, $R^* = R/R_0$, in a horizontal jet as a function of the axial jet coordinate, z^*. Re = 500, $\mathrm{Ca}^{-1} = 72.8$ (solid lines) and 30.0 (dashed lines), $\overline{u}_0 = 1.0$ m s^{-1}, $R_0 = 0.25$ mm.

gravity. The effect of gravity on the jet contraction is equally obvious. It is clearly visible that no final values for the surface velocity and the free-surface position are reached (which we discussed in Section 2.2). Near the point of emergence of liquid from the nozzle, we see that the impact of gravity is less strong. In this region of the jet, the relaxation of the velocity profile within the hydrodynamic boundary layer is the dominating effect that causes the velocity at the surface to increase rapidly, as demonstrated in Section 2.3.

The velocity profile rearrangement with and without gravity for the same flow parameters as in Figure 3.13 is shown in Figure 3.14, where velocity profiles, $u^*(r^*)$, are given at various downstream positions, z^*. It is evident from both graphs that non-uniform velocity profiles persist for significant jet lengths. The presence of gravity not only leads to higher surface velocities but it also accelerates the fluid particles in the core of the jet.

In the flow region close to the nozzle ($z^* \leqslant 5.0$, curves (a) and (b) in Figure 3.14), gravitational forces hardly affect the jet flow. Within the hydrodynamic boundary layer, the removal of the no-slip condition at the nozzle wall causes the fluid particles in the surface to experience a rapid acceleration, which is accompanied by a rearrangement of the velocity profile in the fluid layers adjacent to the surface. This process of velocity profile rearrangement within the boundary layer near the point of detachment is determined by viscous forces. We note that the velocity profiles near the point of detachment from the nozzle in both graphs deviate from the Poiseuille profile only in the (small) region of the hydrodynamic boundary layer. We made use of this behaviour in our boundary-layer treatment in Section 2.3.

Reynolds number, Re = 2000, and Froude number, Fr = 51, are significantly higher than unity, indicating that the inertia forces dominate both viscous forces as well as gravitational forces in the core of the jet flow in the nozzle exit region. The role of the surface tension forces can be estimated from the order of magnitude of the Weber number, We, the product of Re and Ca, which is defined in Equation (2.13). For our parameters, we obtain $\mathrm{We} = 25 > 1$, which shows that the inertia forces also dominate the surface tension forces in the flow region close to the nozzle exit. We had already shown in the two previous sections that at sufficiently high Reynolds numbers, the surface tension forces have only a minor impact on the hydrodynamics of the jet. Gravitational forces eventually dominate the jet flow at the far downstream position, where the velocity profiles

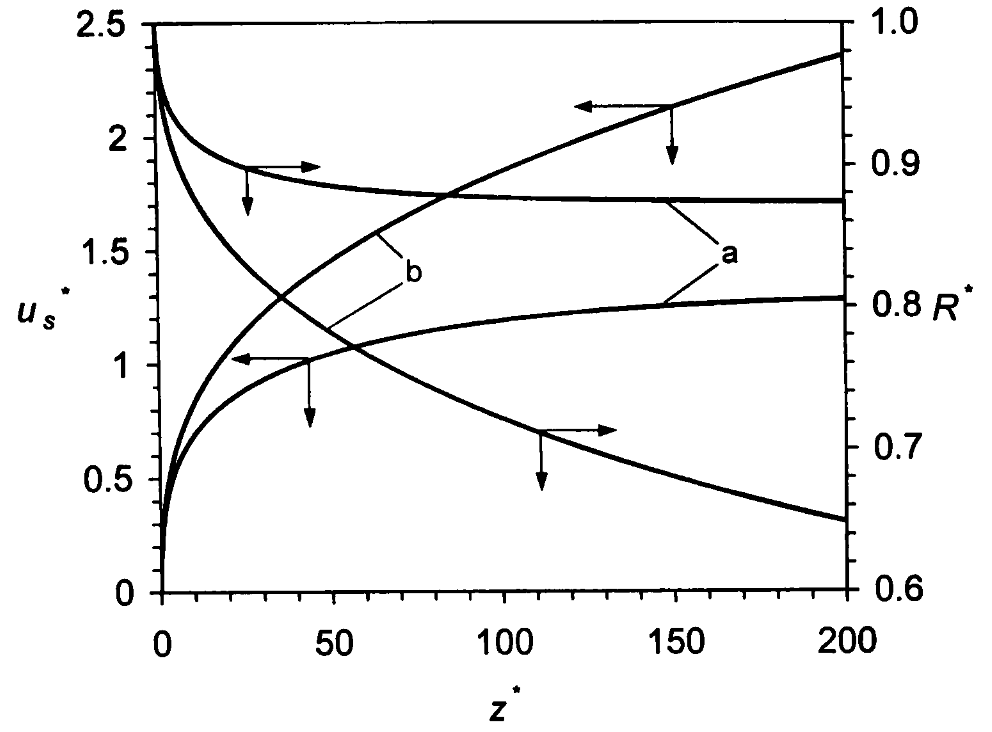

Figure 3.13: Effect of gravity on the shape of the jet, $R^* = R/R_0$, and the axial surface velocity, $u_s^* = u_s/\overline{u}_0$, as a function of the axial jet coordinate, $z^* = z/R_0$. Re = 2000, $\text{Ca}^{-1} = 72.8$, $(2\,\text{Fr})^{-1} = 0$ (a), $(2\,\text{Fr})^{-1} = 0.00981$ (b), $\overline{u}_0 = 1.0$ m s^{-1}, $R_0 = 1.0$ mm.

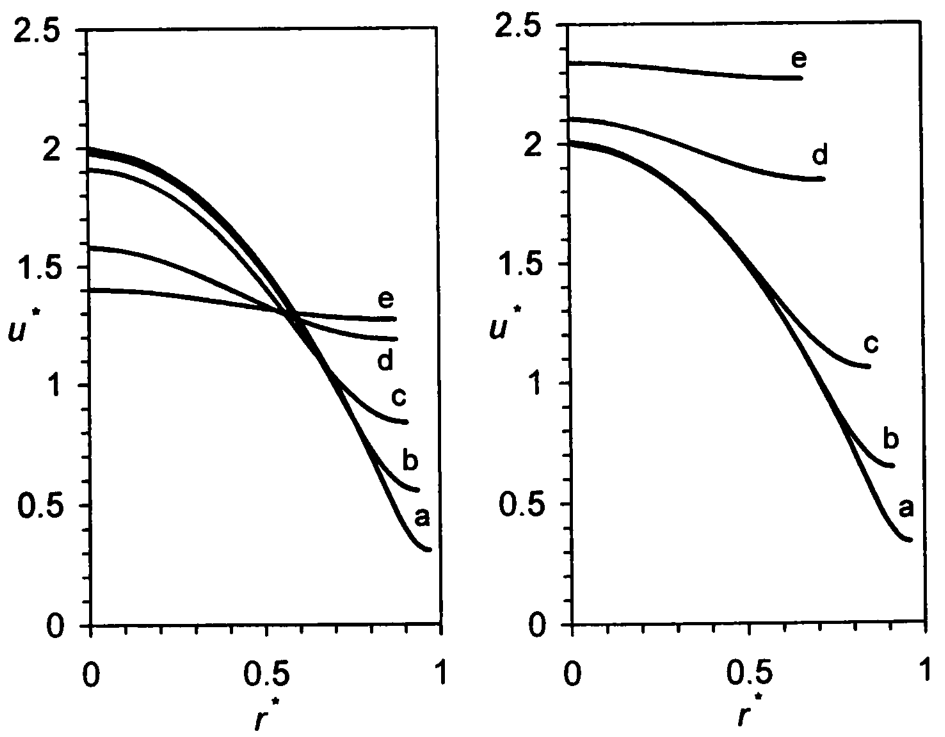

Figure 3.14: Effect of gravity on velocity profile relaxation in the jet, $u^*(r^*) = u(r)/\overline{u}_0$, at different downstream positions, $z^* = z/R_0 = 1$ (a), 5 (b), 20 (c), 100 (d), and 180 (e). Re = 2000, $\text{Ca}^{-1} = 72.8$, $(2\,\text{Fr})^{-1} = 0$ (left graph), $(2\,\text{Fr})^{-1} = 0.00981$ (right graph), $\overline{u}_0 = 1.0$ m s^{-1}, $R_0 = 1.0$ mm.

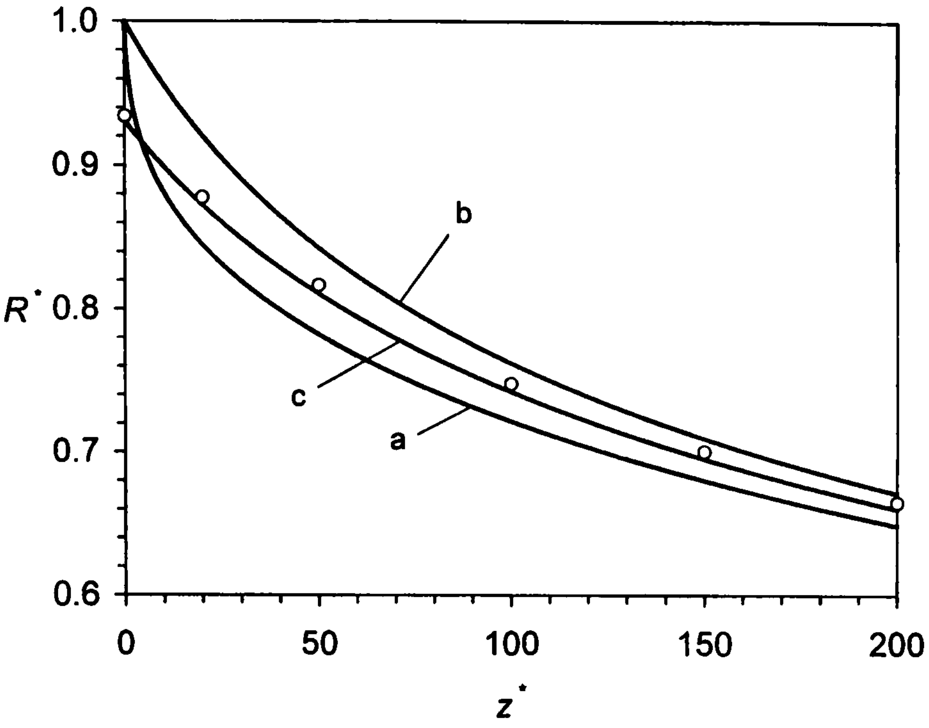

Figure 3.15: Free-surface position, $R^* = R/R_0$, of a water jet in the presence of gravity as a function of the axial jet coordinate, $z^* = z/R_0$. Re = 2000, $\mathrm{Ca}^{-1} = 72.8$, $(2\,\mathrm{Fr})^{-1} = 0.00981$, $\overline{u}_0 = 1.0$ m s^{-1}, $R_0 = 1.0$ mm. CFD model (a), Equation (2.19) (b), Equation (2.24) (c), Equation (2.28) (open circles).

become increasingly relaxed.

Figure 3.15 shows a comparison of the jet contraction, $R^*(z^*)$, from the CFD calculation, curve (a), with some of the analytical expressions that we derived using energy conservation of the jet flow in the presence of gravity in Section 2.2. Curve (b) and (c) are calculated using Equations (2.19) and (2.24), respectively. Equation (2.19) assumes that the velocity is uniform everywhere in the jet, and Equation (2.24) accounts for the parabolic nozzle exit velocity profile. As mentioned earlier, the effects of viscosity (velocity profile rearrangement within the jet) and surface tension (pressure varying with jet radius) are not considered in both Equations (2.19) and (2.24), resulting in the deviation from the numerical result near the nozzle exit. With increasingly relaxed velocity profiles, both approximations approach the numerical solution. The jet then shows the behaviour of a freely falling body in the field of gravity. In Figure 3.15, we also calculated some values for $R^*(z^*)$ using Equation (2.28), which is an extension of Equation (2.24) that accounts for the surface tension contribution within the energy balance. The surface tension contribution is negligibly small at this high Reynolds number, and Equation (2.28) does not lead to better agreement with the CFD computation.

In 1968, Brun and Lienhard [178] and Lienhard [193] developed an approximate method for solving the equations of motion, which they applied to free exiting Poiseuille flows. The dimensionless variables

$$u^* = \frac{u}{\overline{u}_0},\ v^* = \frac{v}{\overline{u}_0}\,\mathrm{Re},\ z^* = \frac{z}{R_0}\frac{1}{\mathrm{Re}},\ r^* = \frac{r}{R_0},\ p^* = \frac{p}{\rho\overline{u}_0^2} \tag{3.45}$$

were introduced and the equations of motion could then be written as[14,15]

$$v^*\frac{\partial u^*}{\partial r^*} + u^*\frac{\partial u^*}{\partial z^*} = -\frac{dp^*}{dz^*} + \frac{1}{r^*}\frac{\partial}{\partial r^*}\left(r^*\frac{\partial u^*}{\partial r^*}\right) + \frac{\mathrm{Re}}{\mathrm{Fr}} \tag{3.46}$$

in the axial direction, and

$$\frac{\partial u^*}{\partial z^*} = -\frac{1}{r^*}\frac{\partial}{\partial r^*}\left(r^*v^*\right) \tag{3.47}$$

in the radial direction. The pressure gradient $\partial p^*/\partial r^*$ is set to zero. The equations of motion were simplified by eliminating the transverse component of velocity, v^*, using a linearised approximation for the inertia terms [194], that is,

$$v^*\frac{\partial u^*}{\partial r^*} + u^*\frac{\partial u^*}{\partial z^*} \simeq \mathcal{O}(0)\frac{\partial u^*}{\partial r^*} + \mathcal{O}\left(1\right)\frac{\partial u^*}{\partial z^*}. \tag{3.48}$$

The resulting momentum equation in the axial direction is then

$$\frac{\partial u^*}{\partial z^*} = -\frac{dp^*}{dz^*} + \frac{1}{r^*}\frac{\partial}{\partial r^*}\left(r^*\frac{\partial u^*}{\partial r^*}\right) + \frac{\mathrm{Re}}{\mathrm{Fr}}. \tag{3.49}$$

This full approximation of the convective acceleration was used by Bohr [137] to obtain a coarse estimate of the rate of velocity decay of exiting Poiseuille flows. Combining Equations (3.49) and (3.47) provided an approximation for the transverse velocity component,

$$v^* = -\frac{\partial u^*}{\partial r^*} + \frac{r^*}{2}\left(\frac{dp^*}{dz^*} - \frac{\mathrm{Re}}{\mathrm{Fr}}\right). \tag{3.50}$$

Equation (3.50) was used to simplify Equation (3.46), which led to a second-order equation in the single dependent variable u^*,

$$u^*\frac{\partial u^*}{\partial z^*} - \left(\frac{\partial u^*}{\partial r^*}\right)^2 = \frac{1}{r^*}\frac{\partial}{\partial r^*}\left(r^*\frac{\partial u^*}{\partial r^*}\right) - \left(\frac{dp^*}{dz^*} - \frac{\mathrm{Re}}{\mathrm{Fr}}\right)\left(1 + \frac{r^*}{2}\frac{\partial u^*}{\partial r^*}\right). \tag{3.51}$$

---

[14] Note that Lienhard did not consider the viscous terms $\partial^2 u^*/\partial z^{*2}$ in the axial direction and $\partial^2 v^*/\partial z^{*2}$ in the radial direction.

[15] Lienhard used the nozzle radius, R_0, instead of the nozzle diameter, $2R_0$, to define the Reynolds number, Re.

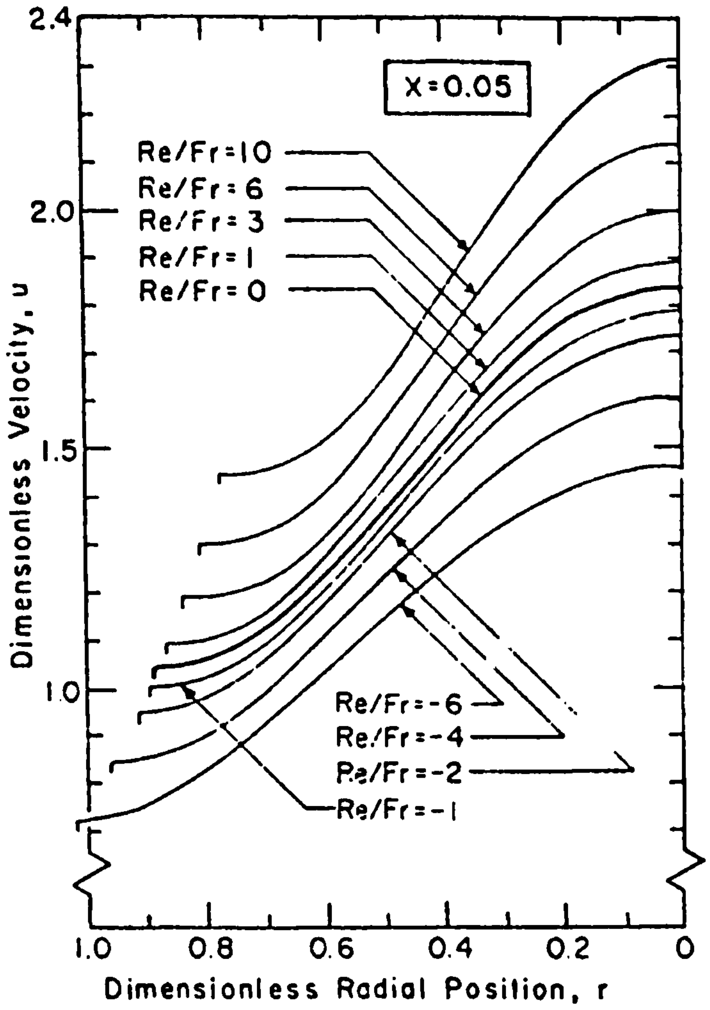

Figure 3.16: Axial velocity profiles according to Lienhard's [193] model in a vertical jet at a downstream distance of 0.05 × R_0. Negative values for Re / Fr correspond to upwards pointing jets.

The boundary conditions include symmetry conditions on the centre line of the jet, a no-shear condition on the free surface of the jet,[16] and a parabolic velocity profile at the nozzle exit. The position of the free-surface boundary is determined by requiring mass and momentum to be conserved across each cross-section.

The model is valid for $50 \leqslant \mathrm{Re} \leqslant 1050$ and for $\mathrm{We} \geqslant 100$. In these regions of the parameters Re and We, viscous and surface tension effects are negligibly small.

Equation (3.51) was solved numerically. Brun and Lienhard obtained jet velocity profiles at various jet lengths and for different combinations of Re, Fr, and We numbers. Figure 3.16 shows the effect of gravity on the velocity profile in the jet at $z^* = 0.05$ for various combinations of Re / Fr.

Only one year earlier, Duda and Vrentas published their model of a laminar

---

[16] Note that the curvature of the jet surface was not considered.

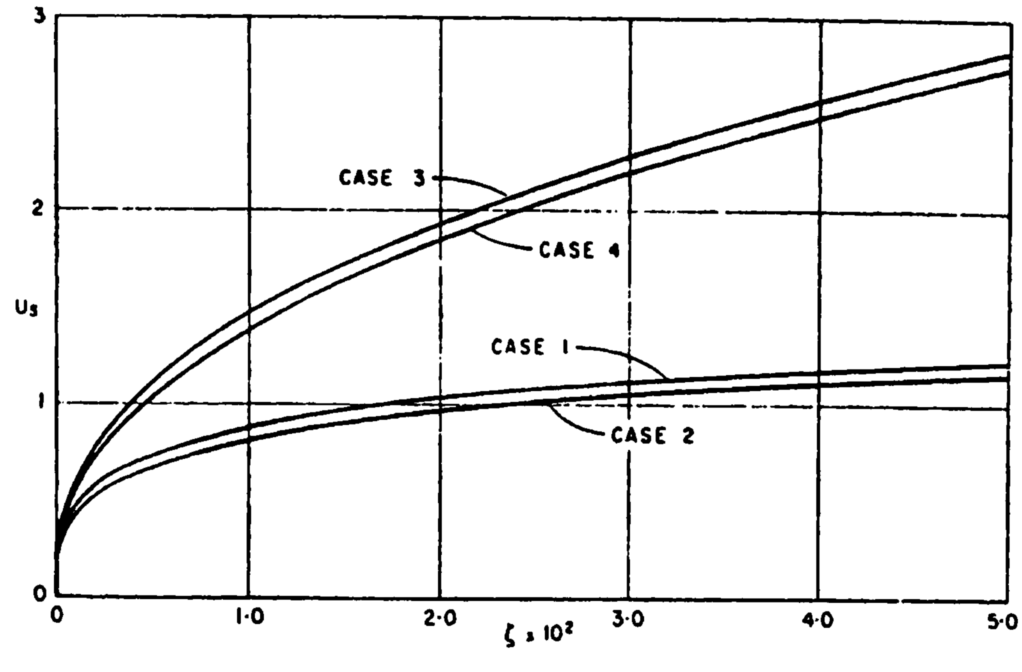

Figure 3.17: Surface velocity, u_s, which is normalised using $\overline{u}_0$, as a function of the dimensionless jet length, $\zeta = z^* / \mathrm{Re}$, according to Duda and Vrentas [195]. $\mathrm{Re} / \mathrm{Fr} = 0$, $\mathrm{We} = \infty$ (Case 1); $\mathrm{Re} / \mathrm{Fr} = 0$, $\mathrm{We} = 5.0$ (Case 2); $\mathrm{Re} / \mathrm{Fr} = 128.6$, $\mathrm{We} = \infty$ (Case 3); $\mathrm{Re} / \mathrm{Fr} = 128.6$, $\mathrm{We} = 5.4$ (Case 4).

liquid jet [195]. They overcame the difficulties created by the free boundary by the development of a coordinate system, symbolically referred to as the Protean coordinate system, whose coordinate lines change shape in a manner determined by the change of jet dimensions. Fundamental to the formation of this new coordinate system was the use of the stream function as the independent variable. Since fluid does not cross lines of constant stream function, the surface of the jet was uniquely defined in the Protean coordinate system.

The complete equations and boundary conditions, which describe the flow of an axi-symmetrical Newtonian jet in an inviscid medium that issues from a long pipe, were formulated in the Protean coordinate system. These general equations were simplified by a boundary-layer analysis for flow at high Reynolds numbers [196, p. 200]. A finite-difference scheme was used to obtain numerical solutions for several cases.

Solutions were given for four different sets of conditions. Case 1 represents the flow of a horizontal jet, surface tension effects being excluded and case 2 represents a horizontal jet with a Weber number that is characteristic of water jets. Cases 3 and 4 represent vertical jets under the influence of gravity, surface tension effects not being considered in case 3. Case 4 is the same jet with surface forces typical of water jets. Figure 3.17 shows the calculated surface velocities for all four cases. A comparison with the surface velocity curves in Figure 3.13, which are obtained from the CFD model described in this thesis, confirms the characteristic features of high Reynolds number jets. These features are that (*i*) the surface liquid experiences rapid acceleration at small axial distances from the nozzle exit, and the effect of gravity in this region of the jet flow is negligibly small; (*ii*) in the absence of gravity, the jet reaches a final state at large axial distances from the nozzle exit; (*iii*) if gravity is present, no final state is reached, and the jet assumes the behaviour of a freely-falling body in the field of gravity for large axial distances from the nozzle exit.

Figure 3.18 shows the velocity profiles of case 1 (right graph) and case 4 (left graph). The jet must travel relatively long distances in both cases before uniform jet velocities are approached. The presence of gravity leads to more contraction of the jet and to higher jet velocities. The computation from the CFD model, Figure 3.14, shows the same solution features.

The jet behaviour of flows at higher Reynolds numbers, $0 \leqslant \mathrm{Re} \leqslant 2000$, and Capillary numbers ranging from $10^{-5} \leqslant \mathrm{Ca} \leqslant 10^{5}$ was investigated by Georgiou *et al.* [202]. A Newtonian iteration scheme was used, in which the free surface profile was computed simultaneously with the velocities and pressures, and the mesh was updated at each iteration step. The boundary conditions applied were the same as in the works of Dutta and Ryan [189] and Omodei [201], which matches those outlined in Section 3.4. In their results surface tension had the already well-known effect of reducing either expansion or contraction. Oscillations, as previously reported by Omodei [201], did not seem to occur at the free surface when the value for the surface tension parameter was increased. If the outflow plane was sufficiently far downstream, gravity could be included without problems. However, these simulations were carried out at Reynolds numbers below 2.

Georgiou *et al.* [202] chose the values of the length of the nozzle section and the length of the free-surface section such that the solution was insensitive to increments to these two lengths. The nozzle length was kept at $4 \times R_0$, which was found to be adequate for all Re and St, whereas the length of the free-surface section had to be increased as Re and St increased. For zero St, $25 \times R_0$ was sufficient for $\mathrm{Re} \leqslant 20$, $100 \times R_0$ was adequate for $\mathrm{Re} \leqslant 200$, and $500 \times R_0$ for $\mathrm{Re} \leqslant 2000$. For non-zero St, the length of the free-surface section had to

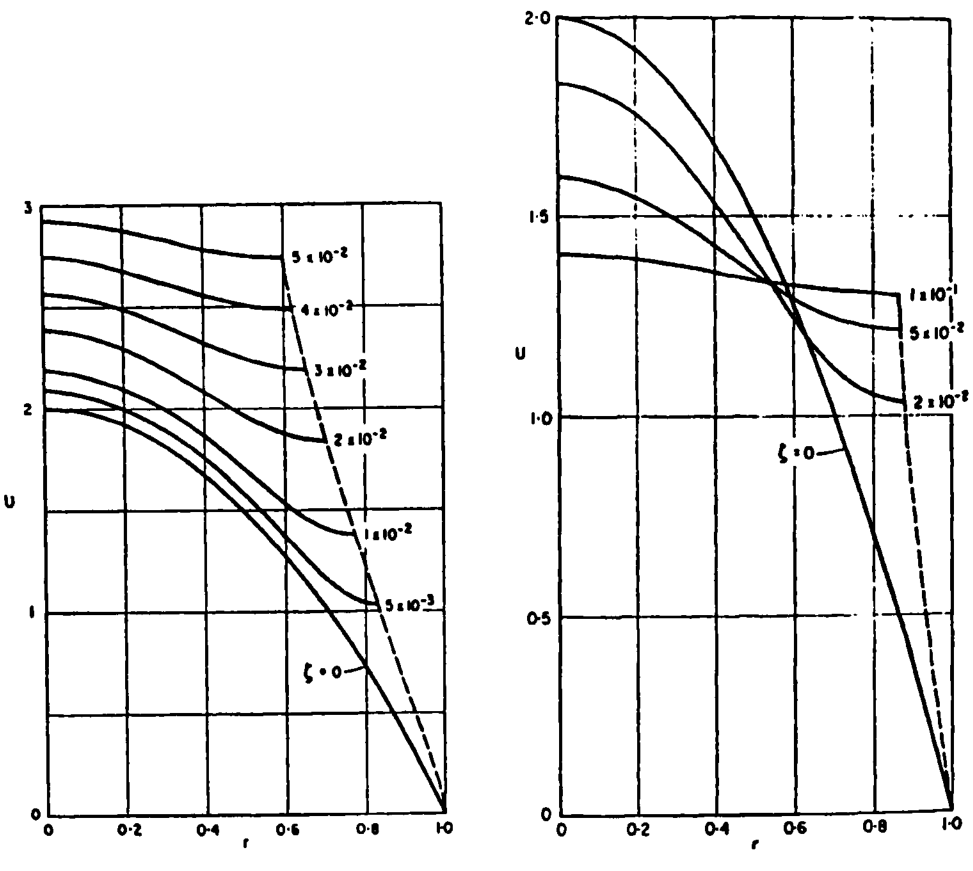

Figure 3.18: Axial velocity distributions, where u is normalised using $\overline{u}_0$ and r is normalised using R_0, according to Duda and Vrentas [195] at different downstream positions, $\zeta = z^*/\mathrm{Re}$. $\mathrm{Re}/\mathrm{Fr} = 0$, $\mathrm{We} = \infty$ (right graph); $\mathrm{Re}/\mathrm{Fr} = 128.6$, $\mathrm{We} = 5.4$ (left graph).

be increased further. The number of elements in their mesh ranged from 150 to 222.

Two works have been reported in which not only the hydrodynamics of laminar liquid jets but also heat transfer were calculated by Chacha *et al.* [203], and by Mitrovic and Ricoeur [204, 205].

Chacha *et al.* focused on the study of the mechanical and thermal behaviour of a high-temperature gravity-driven Newtonian jet using a finite-difference method based on the coordinate transformation and boundary layer approximations proposed by Duda and Vrentas [195]. Reynolds numbers of less than 1000 were considered. Surface velocity and temperature distribution on the jet were not linked via a shear stress condition, although a considerable decrease in surface temperature on moving away from the nozzle exit was observed, which would have given rise to an increase in surface tension (Marangoni effect acting in the downstream direction and hence accelerating the movement of the jet

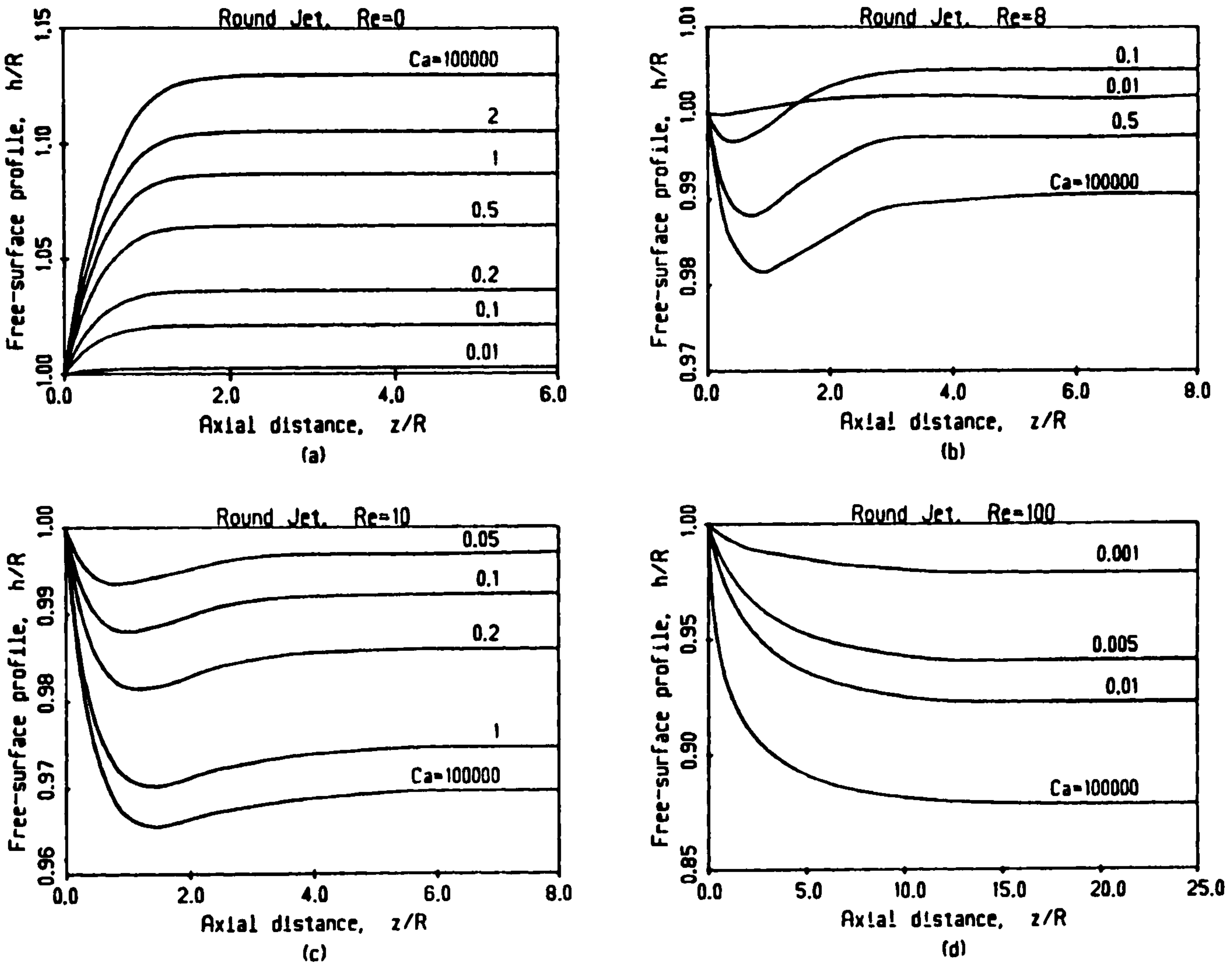

Figure 3.19: Free-surface profiles of horizontal water jets predicted by Georgiou *et al.* [202] for various Reynolds and Capillary numbers.

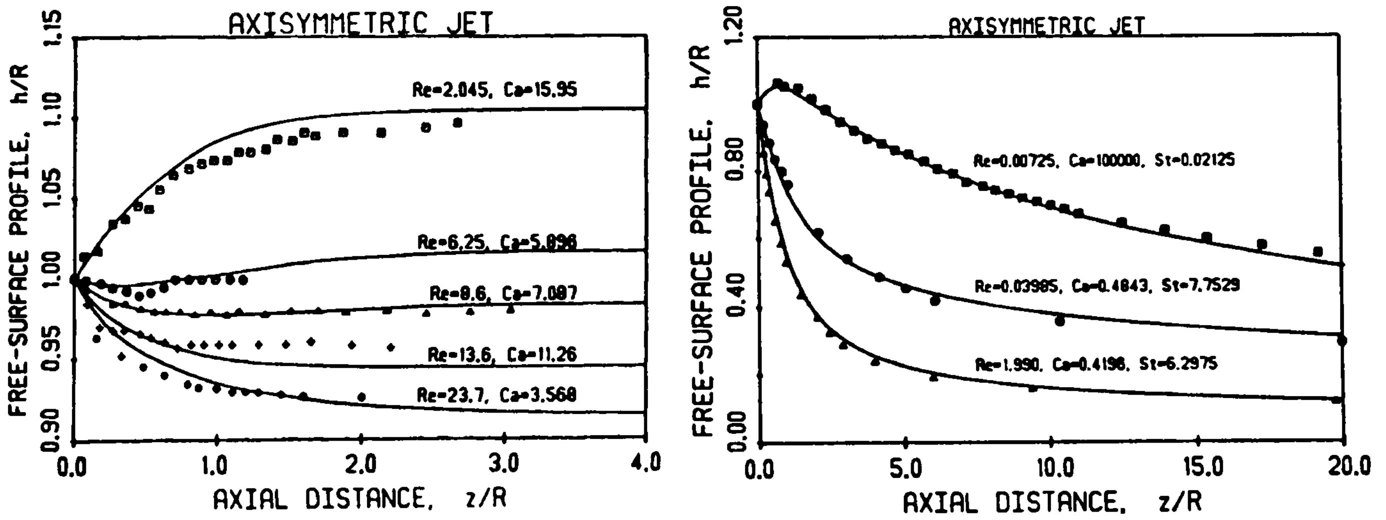

Figure 3.20: Free-surface profiles of horizontal and vertical water jets predicted by Georgiou *et al.* [202] for various Reynolds, Capillary and Stokes numbers.

surface).

Condensation heating of capillary jets was studied by Mitrovic and Ricoeur. The motivation for their investigation originated with vapour condensation on horizontal tubes. The phenomenon of velocity profile relaxation in the case studied occurs from the outer jet surface towards the centre of the jet, where a no-slip condition at the tube wall prescribes the initial motion of the liquid. An initial velocity maximum is found at the jet surface. The axial velocity in the centre of the jet increases with vertical distance from the tube so that the velocity profile becomes increasingly flat. Due to the complexity of the flow problem a simplified physical model was proposed, in which a homogeneous initial velocity as well as a constant temperature was assumed at the origin of a circular jet. The liquid jet was surrounded by saturated vapour and saturation temperature, which was higher than the initial jet temperature, was assumed at the jet surface. Also, a shear stress acting at the interface between jet and the moving vapour phase was considered. The equations of motion were simplified using boundary layer theory and the set of governing equations was then solved using a finite-difference scheme. The numerical results showed that the axial velocity decreased towards the jet surface, which was due to the interfacial shear stress, which increased with increasing jet length.

A model that simulates an optical fiber-forming process involving momentum, heat and mass transfer was presented by Tsai and Lui [206]. The finite-element method was used in their work. The nodes in the mesh were moved by means of the spine method. A two-component system was modelled in which one component diffused to the jet surface where it evaporated. The mathematical model developed describes the fiber-forming process before polymerisation starts. The effects of inertia forces, surface tension, viscous heating and friction on the jet surface were not considered in the numerical calculations.

Very recently, Chauhan *et al.* have investigated the stability of low Reynolds number[17] vertical jets of FC40 fluorocarbon oil [207]. The pressure-driven jets issued from thin needles (R_0 = 0.275 mm), which were sufficiently long for

---

[17] Chauhan *et al.* defined the Reynolds number as

$$\mathrm{Re} = \frac{2R_0\rho\bar{u}_0}{\sqrt{3}\mu},$$

where $4\bar{u}_0/3$ is the mean jet velocity at a downstream distance that corresponds to a ratio of jet contraction of $\sqrt{3}R_0/2$.

Poiseuille flow to exist at the needle exit. The authors report that at a Reynolds number[18] of $\mathrm{Re} = 70.3$, the (undisturbed) jet contracts quickly, reaching a value of $0.866 \times R_0$ (Harmon's result, Equation (2.6)) for the jet radius within only two needle diameters' distance from the needle exit ($z^* = 4$). Figure 3.21 shows some of the authors' experimental data[19] in comparison with computed values from our CFD calculation at $\mathrm{Re} = 70.3$, $\mathrm{Ca}^{-1} = 10.47$, and $(2\,\mathrm{Fr})^{-1} = 0.02919$. In the CFD calculation, R^* reaches a contraction ratio of 0.866 at a downstream distance of about $z^* = 10$, which corresponds to five nozzle diameters.

The authors further claim that on reaching the downstream point at which $R^* = 0.866$, the exchange of momentum has effectively equalised the deficit in velocity between the surface and the bulk of the jet, and further contraction beyond this point is solely due to gravitational acceleration of the liquid. Figure 3.22 shows various velocity profiles, $u^*(r^*)$, that are computed using the CFD model. Evidently, a significant velocity deficit exists between the bulk and the surface of the jet at $z^* = 4$. At a downstream distance of 10 nozzle radii, the velocity in the jet is nearly uniform throughout.

3.6.4 Effect of Nozzle Exit Velocity Profile

The velocity profile in the nozzle exit plane of a laminar liquid jet depends on the Reynolds number, the nozzle diameter, and on the length of the nozzle [222]. If the nozzle length is around 100 times the nozzle diameter or longer, one can assume a fully developed laminar flow profile in the nozzle exit plane for high Reynolds numbers up to 2000. Such a velocity profile was applied in all the simulations presented so far. If the nozzle is shorter, the nozzle exit velocity profile may not be fully developed, that is, the velocity profile tends towards that of a plug flow with a uniform velocity, the shorter the nozzle (for constant Re and R_0).

For very small nozzle diameters (< 1.0 mm), a fully developed laminar flow might not be achievable in a gravity-driven jet flow due to the high pressure loss associated with the flow in thin and long capillaries. If such small nozzles are to be used in a gravity-driven jet flow, shorter nozzles may have to be chosen in order to remain in the high Reynolds number flow regime. It is of interest

---

[18] This value of Re is calculated using Equation (2.8), in which Re is based on the nozzle diameter, $2R_0$, and the mean nozzle exit velocity, $\overline{u}_0$.

[19] The values were read off the original Figure 3 in the work of Chauhan *et al.*

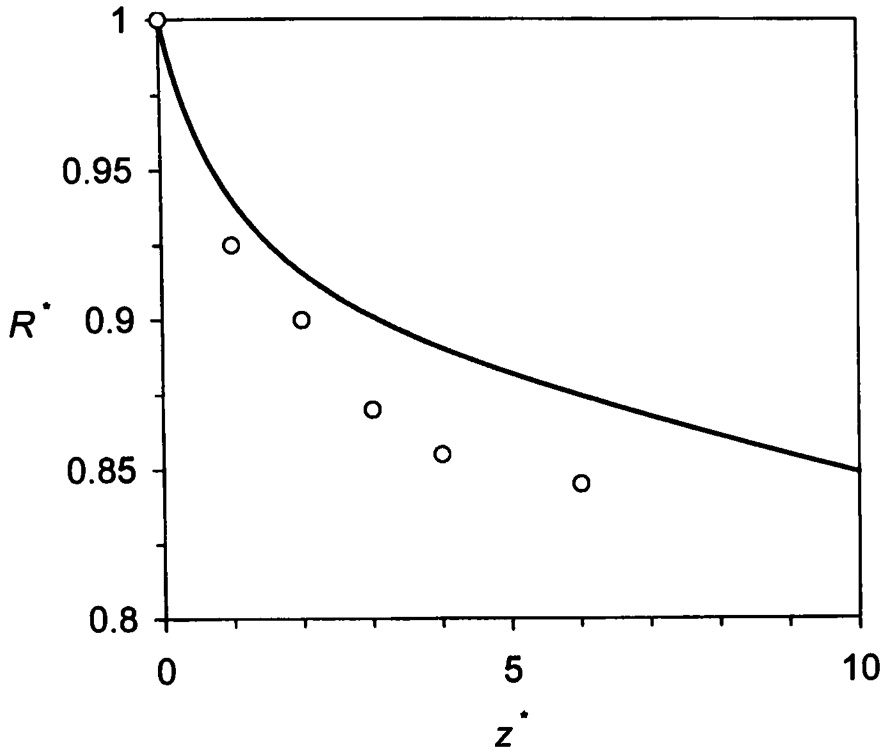

Figure 3.21: Free-surface position, $R^*(z^*)$, in a vertical jet of FC40 fluorocarbon oil at Re = 70.3, $\mathrm{Ca}^{-1} = 10.47$, and $(2\,\mathrm{Fr})^{-1} = 0.02919$. Experimental data of Chauhan *et al.* [207] (open circles) in comparison with the CFD calculation (solid line).

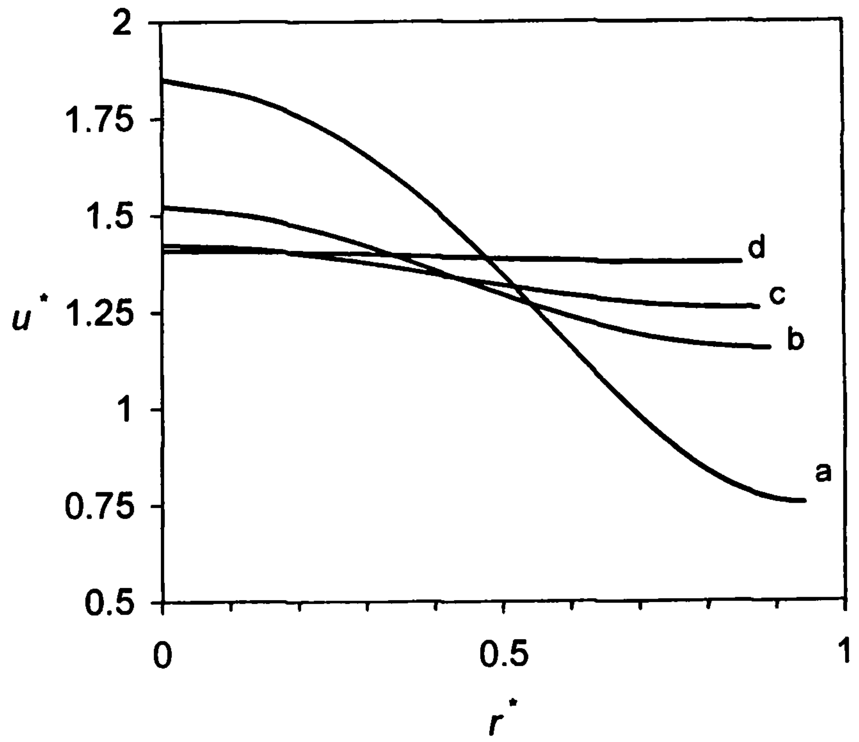

Figure 3.22: Velocity profiles, $u^*(r^*)$, in a vertical jet of FC40 fluorocarbon oil at $z^* = 1.0$ (a), 4.0 (b), 6.0 (c), and 10.0 (d). Re = 70.3, $\mathrm{Ca}^{-1} = 10.47$, and $(2\,\mathrm{Fr})^{-1} = 0.02919$.

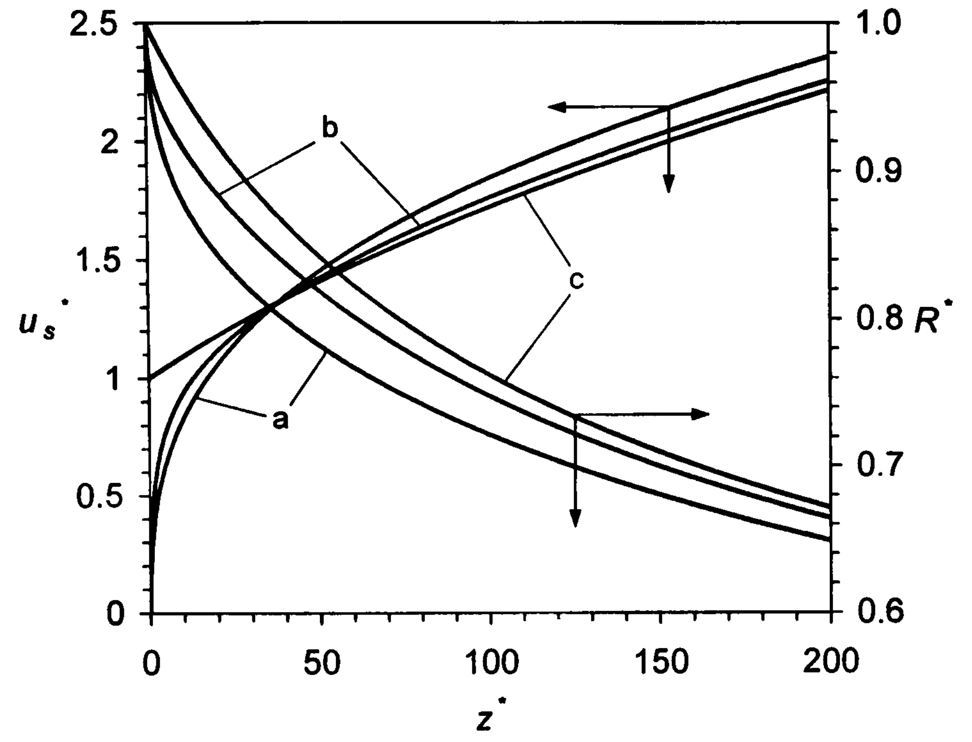

Figure 3.23: Effect of nozzle exit velocity profile on the jet radius, $R^* = R/R_0$, and axial surface velocity, $u_s^* = u_s/\overline{u}_0$, at Re = 2000, $\mathrm{Ca}^{-1} = 72.8$, $(2\,\mathrm{Fr})^{-1} = 0.00981$, $\overline{u}_0 = 1.0$ m s^{-1}, $R_0 = 1.0$ mm. Parabolic profile (a), 8th-order polynomial (b), and Equation (2.19) (c).

to investigate the effect on the hydrodynamics of the free liquid jet if the flow profile at the nozzle exit is not that of a fully developed laminar flow. This effect is shown in Figure 3.23.

The boundary condition at the nozzle inlet, the parabolic velocity profile, given in Equation (3.24), is substituted by an 8th-order polynomial,

$$u^*(r^*) = u^*_{\max}\left(1 - r^{*^8}\right), v^* = 0. \qquad (3.52)$$

For the same dimensionless mean nozzle exit velocity as in the case of the parabolic flow profile, a lower maximum velocity of the flow profile, $u^*_{\max}$, was calculated using

$$\overline{u}_0^* = 1.0 = 2u^*_{\max}\int_0^1 \left(1 - r^{*^8}\right) r^* dr^* \Rightarrow u^*_{\max} = 1.25. \qquad (3.53)$$

For the parabolic flow profile, the maximum velocity is exactly twice the mean nozzle exit velocity, and only found on the symmetry axis. Equation (3.52) describes a velocity profile for which velocities close to the maximum velocity are found at some distance towards the free surface of the jet. We use Equation (3.52) to simulate a liquid jet that issues from a nozzle much shorter than 100 times the nozzle diameter. The flow parameters are again $\mathrm{Re} = 2000$, $\mathrm{Ca}^{-1} = 72.8$, and $(2\,\mathrm{Fr})^{-1} = 0.00981$. Figure 3.23 shows the surface velocity, $u_s^*(z^*)$, and the jet contraction, $R^*(z^*)$, for the parabolic nozzle exit velocity profile, curves (a), and for the 8th-order polynomial, curves (b). Equation (2.19) was used to produce the third set of curves (c).

Two extreme flow conditions at the nozzle exit can be encountered—a fully developed laminar flow (parabolic velocity profile) and a plug flow (constant velocity throughout the fluid). The 8th-order polynomial, Equation (3.52), provides flow conditions at the nozzle exit, which approximate plug flow. In the (theoretical) case of constant velocity throughout the jet at the nozzle exit and in the presence of gravity, the jet would show the behaviour described by Equation (2.19). Curves (b) in Figure 3.23 show the tendency towards this ideal behaviour. These results confirm that the highest degree of jet contraction is reached with a fully developed laminar flow profile.

Attempts have been made to realise jet flows that show nearly ideal behaviour by means of appropriate nozzle design. The advantage is obvious, since it simplifies the theoretical treatment of the fluid mechanics of the jet greatly. For example, Cullen and Davidson investigated the absorption of carbon dioxide into a jet of water issuing under gravity [159]. An apparatus was designed to produce a jet that was meant to have a uniform velocity across every section of the jet. Such velocity profiles were achieved by means of an orifice plate fixed in a circular tube, which had a diameter that was six times that of the orifice. Only one year later, Scriven and Pigford also investigated the absorption of CO_2 into freely-falling laminar water jets [160]. Very short nozzles were employed to achieve a nearly plug flow at the nozzle exit.

3.6.5 Comparison of CFD Model with Experiments

Figures 3.24 to 3.33 show measured velocities of vertical water jets in comparison with CFD calculations, which were carried out using the numerical model of the jet flow outlined above. Table 3.3 summarises the flow parameters that were employed in the experiments and CFD calculations.

Mean values of the nozzle exit velocity, $\overline{u}_0$, were calculated from measured flow rates. The inner diameter of the nozzle used in the experiments was $2R_0 =$

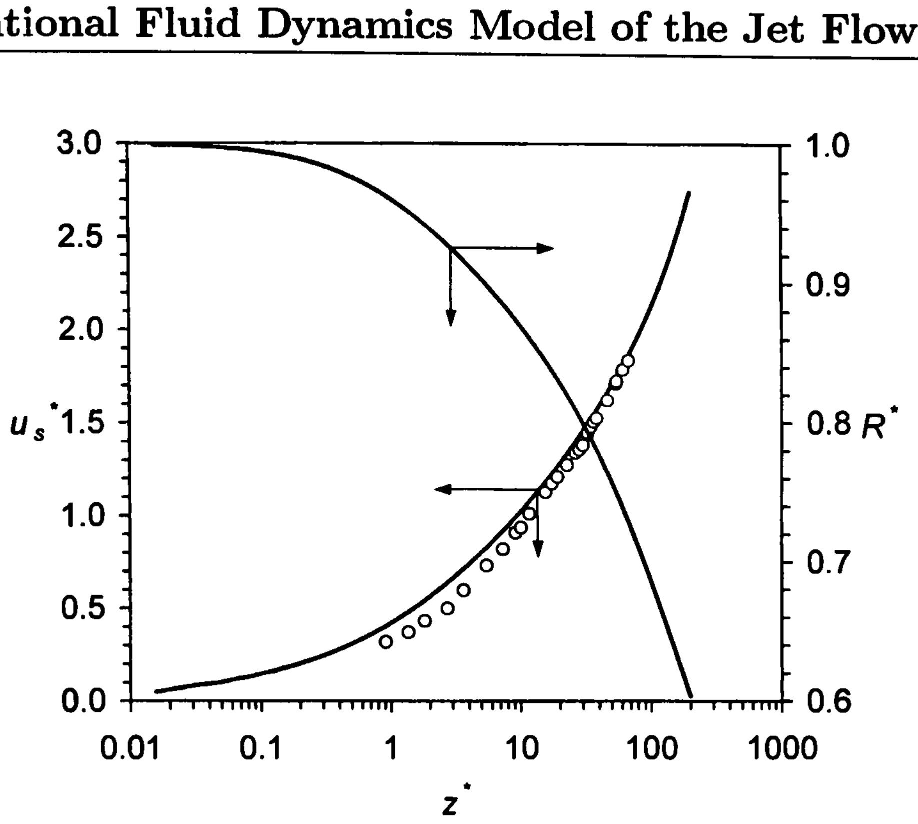

Figure 3.24: Axial surface velocity, $u_s^* = u_s/\overline{u}_0$, and free-surface position, $R^* = R/R_0$, in a vertical water jet as a function of the axial jet coordinate, $z^* = z/R_0$. Comparison of experimental data with CFD calculations. Re = 640, $\mathrm{Ca}^{-1} = 125.1$, $(2\,\mathrm{Fr})^{-1} = 0.01590$, $\overline{u}_0 = 0.58$ m s^{-1}, $R_0 = 0.55$ mm.

1.58 mm at Re = 1280, 1550, and 1950. At the lowest Reynolds number, Re = 640, the nozzle diameter was $2R_0 = 1.1$ mm. Different nozzle exit velocities were achieved through adjustment of the liquid head in the liquid reservoir to which the long nozzle was attached. The experimental data were obtained by means of laser Doppler velocimetry (LDV). An overview of the experimental work is given in Chapter 7 and is published in [208]. Appendix C.1 contains a FIDAP journal file of the jet flow in the presence of gravity at Re = 1550.

The experimental apparatus does not allow the measurement of the axial

Table 3.3: Flow parameters of the vertical water jets studied in the experimental investigation.

Figure	Re	Ca^{-1}	$(2\,\mathrm{Fr})^{-1}$	θ / °	$\overline{u}_0$ / m s^{-1}	R_0 / mm
3.24 and 3.25	640	125.1	0.01590	89.964	0.58	0.55
3.26 to 3.28	1280	90.0	0.01184	89.964	0.81	0.79
3.29 to 3.31	1550	74.3	0.00807	89.965	0.98	0.79
3.32 and 3.33	1950	58.9	0.00507	89.968	1.24	0.79

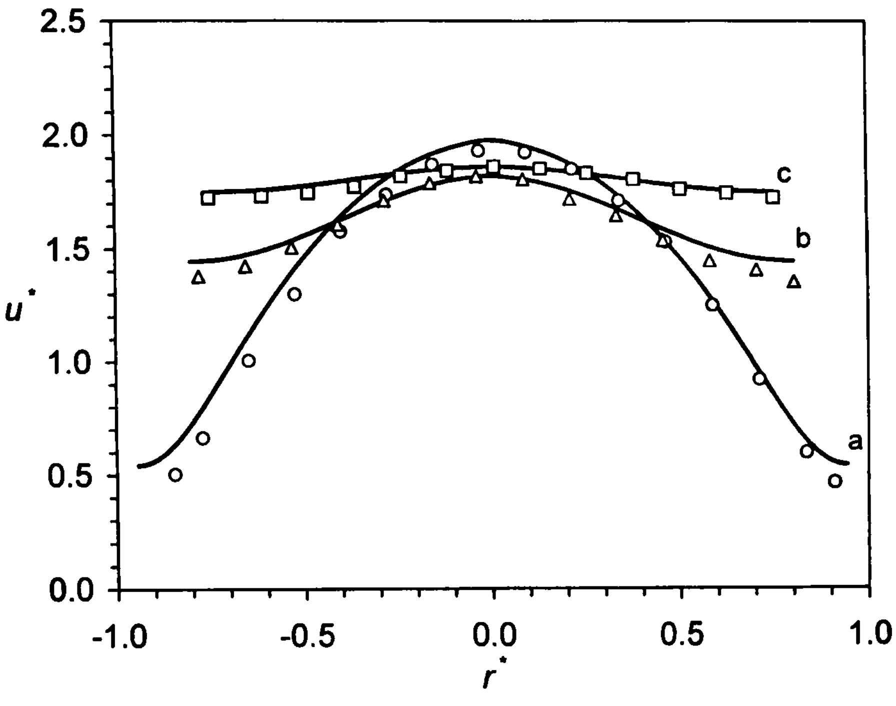

Figure 3.25: Axial velocity profiles, $u^*(r^*) = u(r)/\overline{u}_0$, in a vertical water jet at different downstream positions $z^* = z/R_0 = 1.8$ (a, circles), 29.1 (b, triangles), and 54.6 (c, squares). Comparison of experimental data (symbols) with CFD calculations (solid lines). $\mathrm{Re} = 640$, $\mathrm{Ca}^{-1} = 125.1$, $(2\,\mathrm{Fr})^{-1} = 0.01590$, $\overline{u}_0 = 0.58$ m s^{-1}, $R_0 = 0.55$ mm.

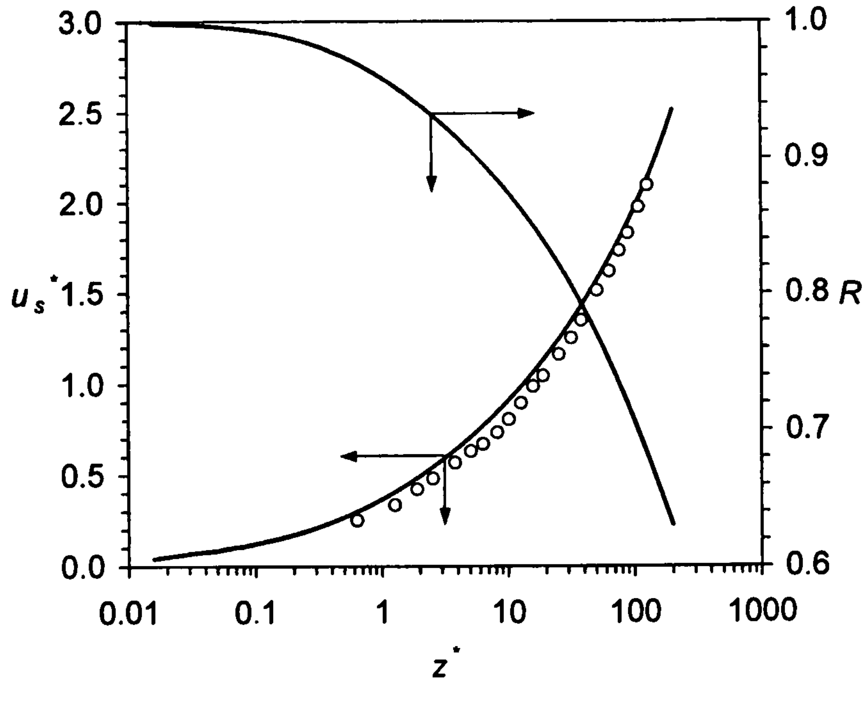

Figure 3.26: Axial surface velocity, $u_s^* = u_s/\overline{u}_0$, and free-surface position, $R^* = R/R_0$, in a vertical water jet as a function of the axial jet coordinate, $z^* = z/R_0$. Comparison of experimental data with CFD calculations. $\mathrm{Re} = 1280$, $\mathrm{Ca}^{-1} = 90.0$, $(2\,\mathrm{Fr})^{-1} = 0.01184$, $\overline{u}_0 = 0.81$ m s^{-1}, $R_0 = 0.79$ mm.

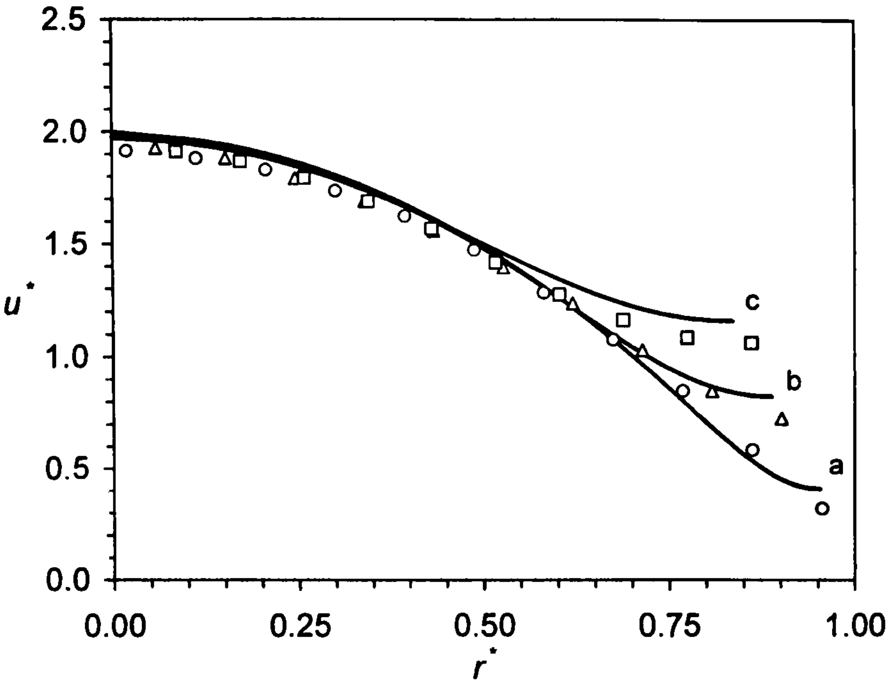

Figure 3.27: Axial velocity profiles, $u^*(r^*) = u(r)/\overline{u}_0$, in a vertical water jet at different downstream positions $z^* = z/R_0 = 1.3$ (a, circles), 7.6 (b, triangles), and 20.3 (c, squares). Comparison of experimental data (symbols) with CFD calculations (solid lines). $\mathrm{Re} = 1280$, $\mathrm{Ca}^{-1} = 90.0$, $(2\,\mathrm{Fr})^{-1} = 0.01184$, $\overline{u}_0 = 0.81$ m s^{-1}, $R_0 = 0.79$ mm.

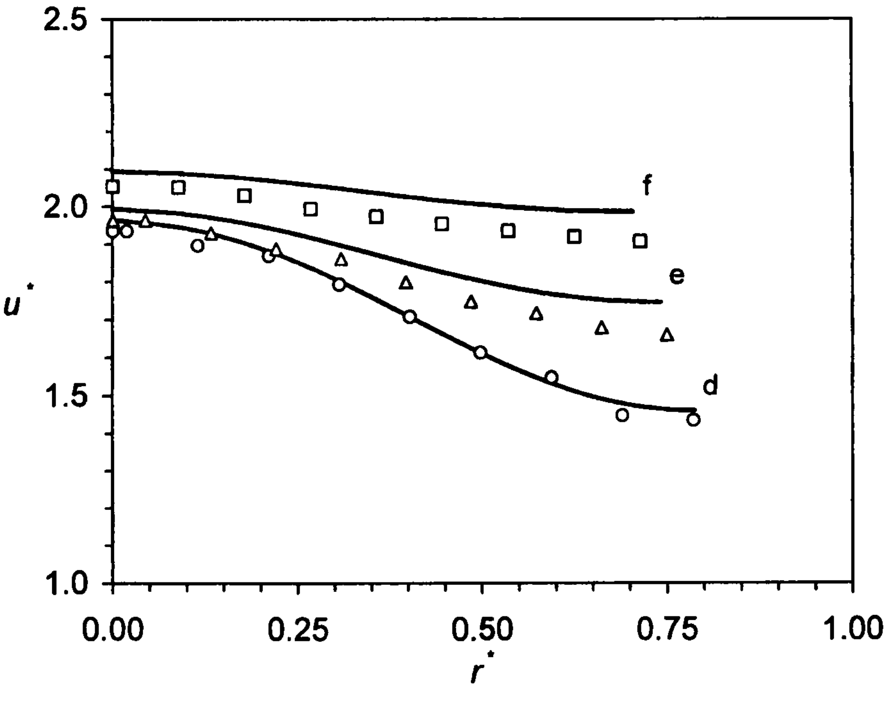

Figure 3.28: Axial velocity profiles, $u^*(r^*) = u(r)/\overline{u}_0$, in a vertical water jet at different downstream positions $z^* = z/R_0 = 40.5$ (d, circles), 69.6 (e, triangles), and 102.5 (f, squares). Comparison of experimental data (symbols) with CFD calculations (solid lines). $\mathrm{Re} = 1280$, $\mathrm{Ca}^{-1} = 90.0$, $(2\,\mathrm{Fr})^{-1} = 0.01184$, $\overline{u}_0 = 0.81$ m s^{-1}, $R_0 = 0.79$ mm.

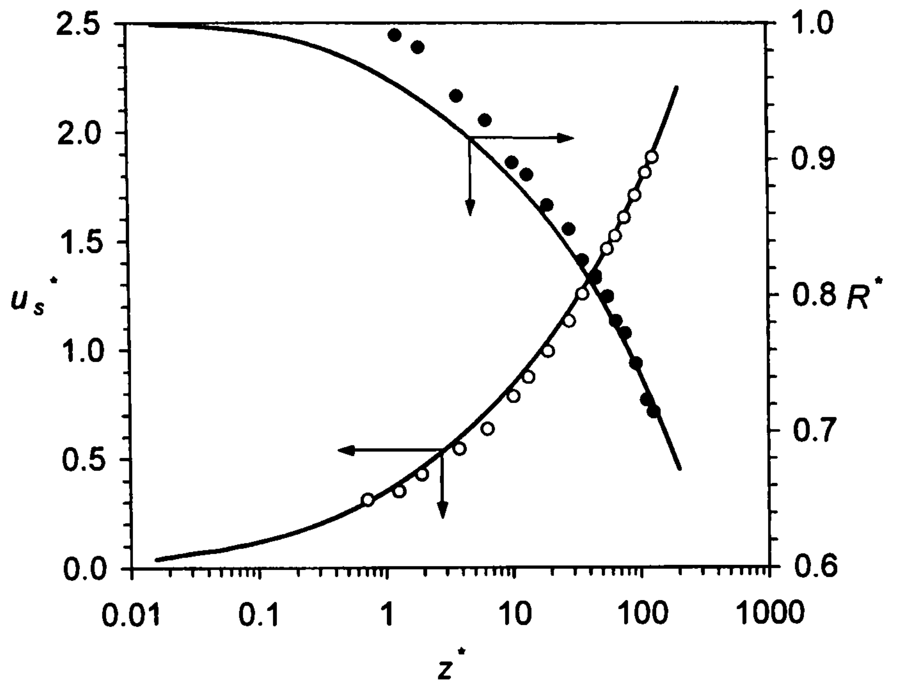

Figure 3.29: Axial surface velocity, $u_s^* = u_s/\overline{u}_0$, and free-surface position, $R^* = R/R_0$, in a vertical water jet as a function of the axial jet coordinate, $z^* = z/R_0$. Comparison of experimental data with CFD calculations. $\mathrm{Re} = 1550$, $\mathrm{Ca}^{-1} = 74.3$, $(2\,\mathrm{Fr})^{-1} = 0.00807$, $\overline{u}_0 = 0.98$ m s^{-1}, $R_0 = 0.79$ mm.

jet velocity profile at the point of detachment ($z = 0$), and these values are therefore not available. However, velocity profiles as close as 1.0 mm to the nozzle could be obtained in this set-up, and velocity profiles at this downstream position are given at Re = 640, 1280, and 1550. The close agreement of the measured velocity distributions and CFD simulation at this short downstream distance from the nozzle suggests that the liquid flow is at least very nearly fully developed on leaving the nozzle. Surface velocities could be measured as close as 200 μm to the point of detachment.

Velocity profiles were measured throughout the jet at Re = 640 (Figure 3.25) and 1550 (Figures 3.30 and 3.31). There is excellent agreement between the CFD simulation and the measured flow field for the half of the jet nearest to the lasers ($r^* > 0$). The agreement between experiment and modelling in the part of the jet furthest from the point of entry of the laser beams ($r^* < 0$) is not quite as good as a result of distortions in the probe beams caused by reflections in the cylindrical jet.[20] Measured velocity profiles in the half of the jet nearest to the lasers are also provided at Re = 1280 (Figures 3.27 and 3.28)

---

[20] A correction is applied, to allow for this optical distortion, but inevitably the experimental error is somewhat increased.

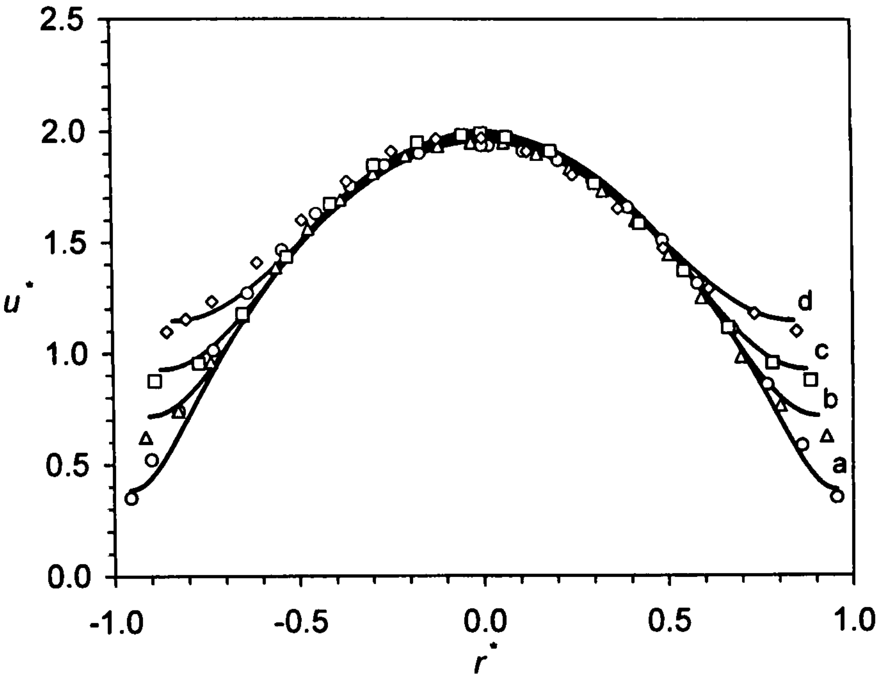

Figure 3.30: Axial velocity profiles, $u^*(r^*) = u(r)/\bar{u}_0$, in a vertical water jet at different downstream positions $z^* = z/R_0 = 1.3$ (a, circles), 6.3 (b, triangles), 13.3 (c, squares), and 25.3 (d, diamonds). Comparison of experimental data (symbols) with CFD calculations (solid lines). Re = 1550, $\mathrm{Ca}^{-1} = 74.3$, $(2\,\mathrm{Fr})^{-1} = 0.00807$, $\bar{u}_0 = 0.98$ m s^{-1}, $R_0 = 0.79$ mm.

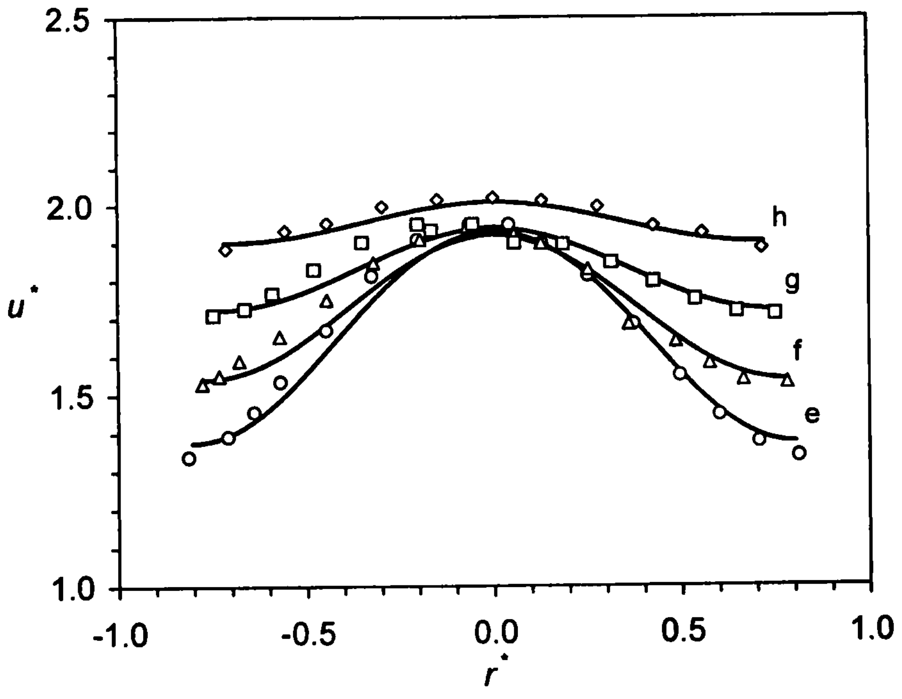

Figure 3.31: Axial velocity profiles, $u^*(r^*) = u(r)/\bar{u}_0$, in a vertical water jet at different downstream positions $z^* = z/R_0 = 44.9$ (e, circles), 64.6 (f, triangles), 92.4 (g, squares), and 126.6 (h, diamonds). Comparison of experimental data (symbols) with CFD calculations (solid lines). Re = 1550, $\mathrm{Ca}^{-1} = 74.3$, $(2\,\mathrm{Fr})^{-1} = 0.00807$, $\bar{u}_0 = 0.98$ m s^{-1}, $R_0 = 0.79$ mm.

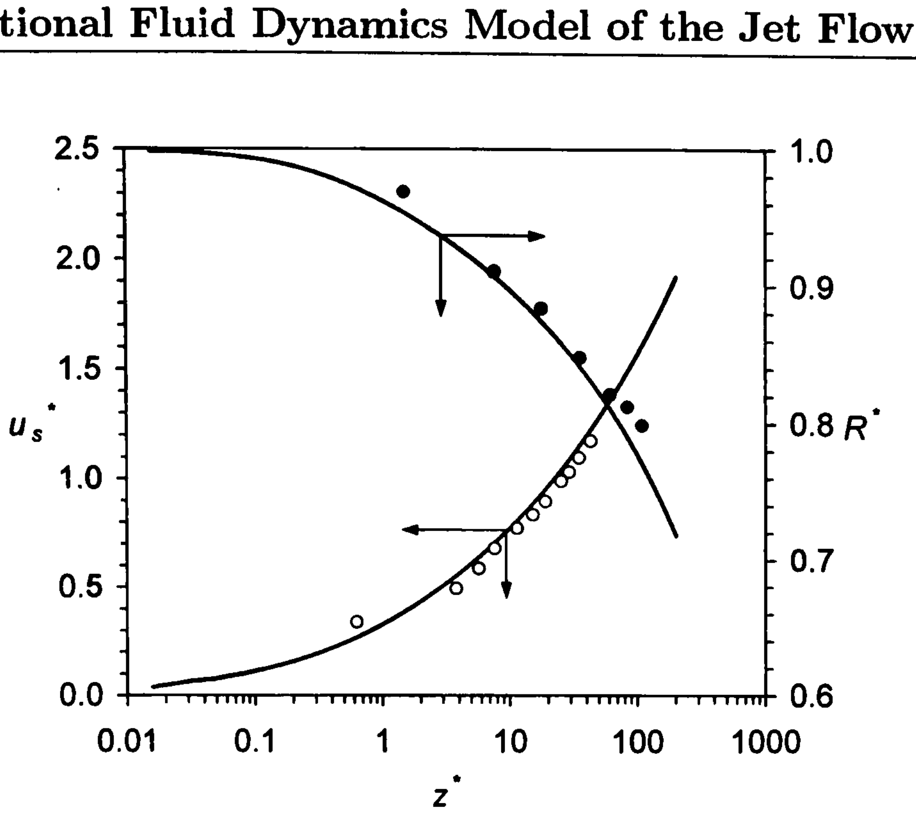

Figure 3.32: Axial surface velocity, $u_s^* = u_s/\bar{u}_0$, and free-surface position, $R^* = R/R_0$, in a vertical water jet as a function of the axial jet coordinate, $z^* = z/R_0$. Comparison of experimental data with CFD calculations. Re = 1950, $\mathrm{Ca}^{-1} = 58.9$, $(2\,\mathrm{Fr})^{-1} = 0.00507$, $\bar{u}_0 = 1.24$ m s^{-1}, $R_0 = 0.79$ mm.

and at Re = 1950 (Figure 3.33), which exhibit very good agreement with the CFD calculations. The good agreement between the experimentally obtained and computed velocity profiles at large distances from the nozzle at all four Reynolds numbers demonstrates further that the experimental set-up meets the requirement of providing axially symmetric jet flows very well.

In the case of the lowest Reynolds number, Re = 640, the jet appears to be fully relaxed at a downstream position of $z^* = 54.6$ ($z = 30$ mm), as demonstrated by curve c in Figure 3.25. At higher Reynolds number, the liquid must travel considerably longer distances to achieve full velocity profile relaxation. For example, at Re = 1550 and at a comparable distance of $z^* = 44.9$ ($z = 35$ mm), the velocity of the liquid in the surface of the jet is lower by about a factor 1.4 than the velocity in the centre of the jet (curve e in Figure 3.31). At this high Reynolds number, full relaxation is only achieved at downstream distances of $100 \times R_0$ and longer.

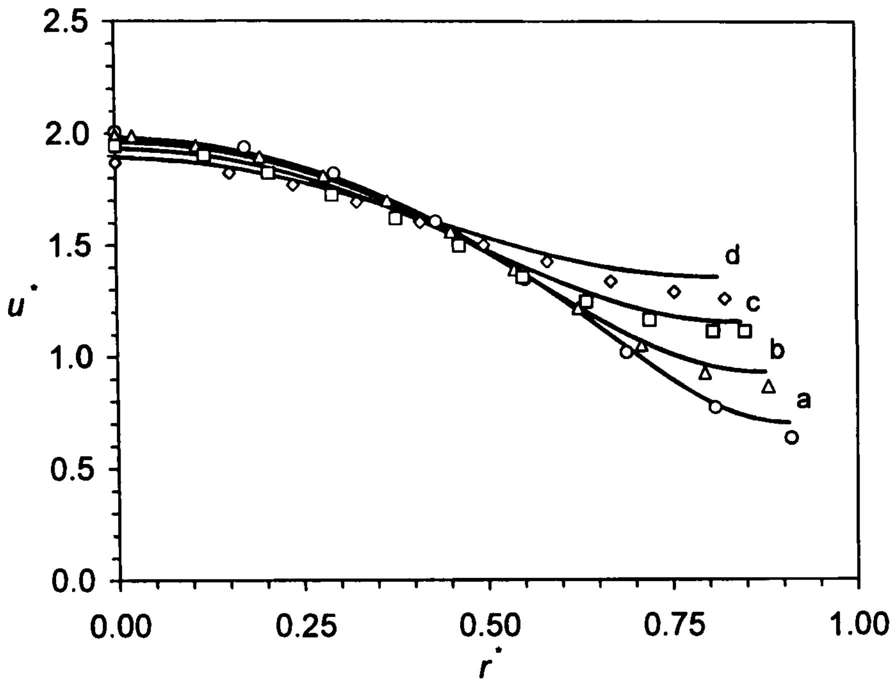

Figure 3.33: Axial velocity profiles, $u^*(r^*) = u(r)/\overline{u}_0$, in a vertical water jet at different downstream positions $z^* = z/R_0 = 7.6$ (a, circles), 17.7 (b, triangles), 35.4 (c, squares), and 60.8 (d, diamonds). Comparison of experimental data (symbols) with CFD calculations (solid lines). $\mathrm{Re} = 1950$, $\mathrm{Ca}^{-1} = 58.9$, $(2\,\mathrm{Fr})^{-1} = 0.00507$, $\overline{u}_0 = 1.24$ m s^{-1}, $R_0 = 0.79$ mm.

3.6.6 Effect of Wetting of the Nozzle Tip

In this section, we consider the effect of wetting of the nozzle tip on the hydrodynamics of the jet at the point of emergence from the nozzle. Clean stainless steel is hydrophilic and is therefore at least partially wetted by water (and also by surfactant solution). In order to reduce wetting of the nozzle tip to a minimum, we have tried coating the tip with gold and a monolayer of octadecanethiol to render it hydrophobic and non-wetting. While this treatment works for a time, the coatings are not robust—possibly due to the large shear forces acting at the nozzle exit. We have therefore to consider the likelihood that the flat end of the nozzle tip is wetted by liquid and that the point of detachment of the liquid from the nozzle is at y in Figure 7.3, and not at x.

The dimensionless flow geometry of the axi-symmetric jet in the presence of wetting at the nozzle tip is shown in the upper sketch in Figure 3.34. The lower sketch shows the mesh configuration, in which the number codes indicate the number of node intervals on the relevant edge and the grading along the the edge (see also Figure 3.3). The flat end has a length that corresponds to about

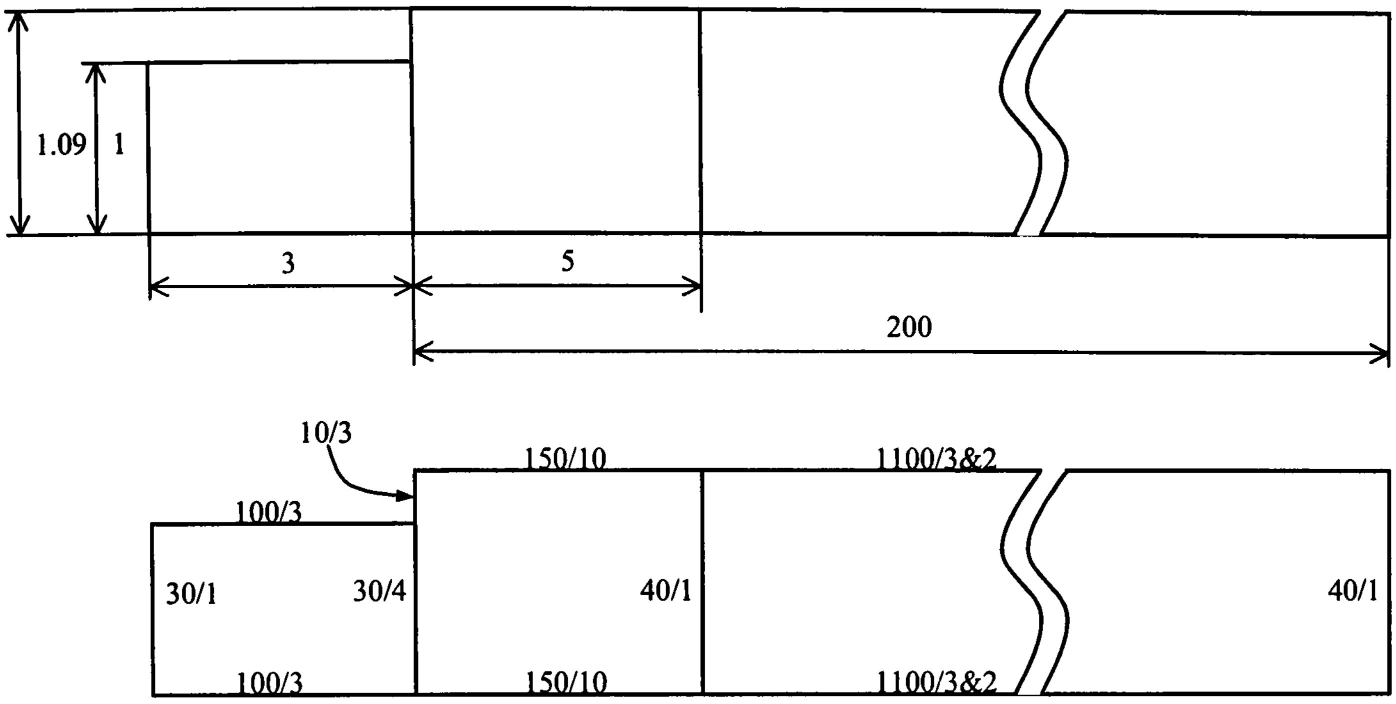

Figure 3.34: Flow geometry (upper drawing) and mesh configuration (lower drawing) of the axi-symmetric model of a pure liquid jet in the presence of wetting at the nozzle tip (not to scale).

9% of the nozzle radius and is assumed to be completely wetted by the liquid issuing from the nozzle. At the wetted nozzle tip we have a no-slip boundary condition, that is, $u^*, v^* = 0$. The surface node at $z^* = 0$ is fixed in space as before, and no contact angle is applied at that point. A section of the regular mesh around the nozzle exit, which corresponds to the flow geometry and mesh configuration displayed in Figure 3.34 is shown in Figure 3.35 (see Appendix B.2).

Figure 3.36 shows velocity vector plots that are the result of CFD calculations of water jets emerging from a nozzle in the presence of wetting. Case (a) in Figure 3.36 is computed for Re = 1950, and case (b) shows the velocity vectors at Re = 640. The flow is characterised in both cases by a circulating toroidal eddy at very low z^*, with negative surface velocities (upward flow) occurring. The axial position of the resulting stagnation line moves downstream with increasing Reynolds number; for Re = 640 (case (b) in Figure 3.36), the line is about 150 μm downstream of the nozzle tip, and for Re = 1950 (case (a) in Figure 3.36), the stagnation line is about 200 μm downstream of the nozzle tip. After this stagnation zone, the jet surface is accelerated rapidly, and the flow pattern is similar to that obtained in the case of no wetting at the nozzle tip.

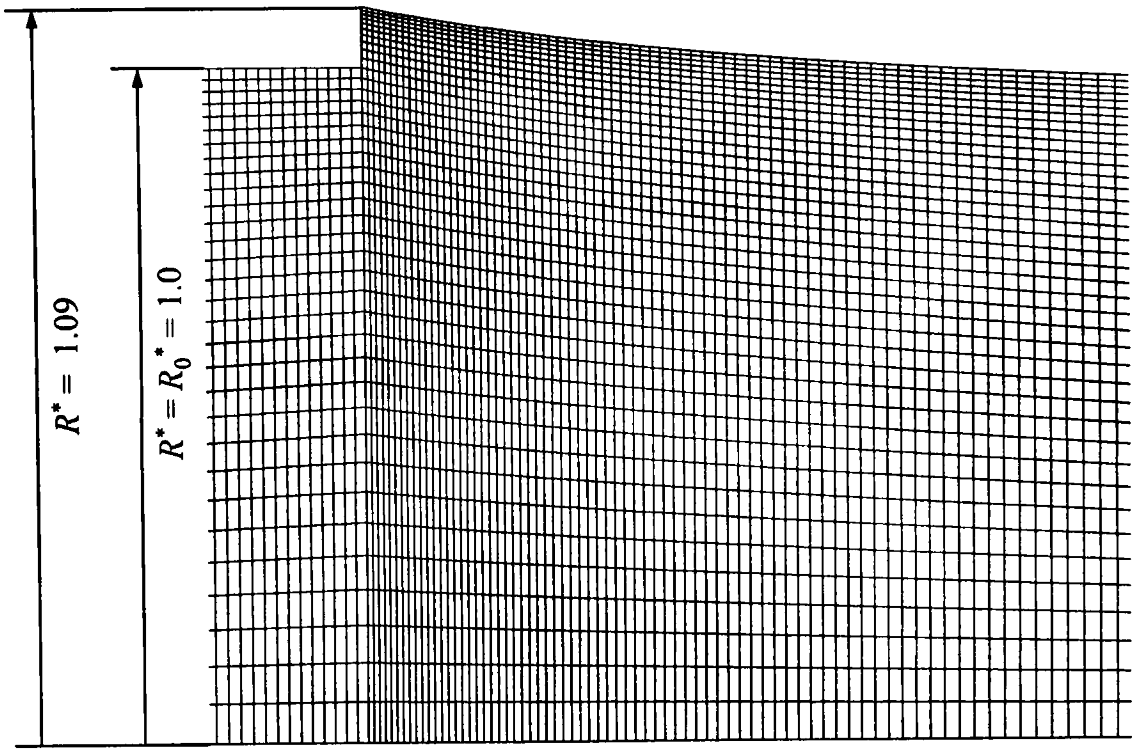

Figure 3.35: Regular mesh of the water jet in the nozzle exit region in the presence of wetting at the nozzle tip. The inner nozzle radius is $R_0 = 0.79$ mm, and the wetted (outer) nozzle radius is $R_0 + b = 0.86$ mm. The flow conditions are $\mathrm{Re} = 1550$, $\mathrm{Ca}^{-1} = 74.3$, and $(2\,\mathrm{Fr})^{-1} = 0.00807$.

In Figures 3.37 and 3.38, experimental velocity data of a vertical jet of water at $\mathrm{Re} = 1550$ are compared with a CFD calculation that accounts for a wetted nozzle tip in its flow geometry. The consideration of wetting phenomena at the nozzle tip leads to better agreement between the numerically and experimentally obtained values for the surface position (curve (b) for R^* and the closed circles in Figure 3.37). The agreement between the computed and measured surface velocities remains ambigious, and both numerical models (curves (a) and (b) for u_s^* in Figure 3.37) represent the experimental data equally well. Wetting of the nozzle tip has only a minor effect on the core velocities of the jet, as demonstrated in Figure 3.38. The effect is only visible in the layers adjacent to the surface and only at low values of z^*. At a downstream distance of $z^* = 25.3$, the effect of wetting of the nozzle tip has nearly vanished.

At the stagnation line, the strain rate is large but not infinite. This can be seen in Figure 3.37 from curve (b) for u_s^*, which has a lower slope at the point where $u_s^* = 0$ than curve (a) at $z^* = 0$. Wetting of the nozzle can therefore give rise to a situation where at low surfactant concentrations (and hence low mass transfer rates), the surface approximates to that of pure water at the stagnation

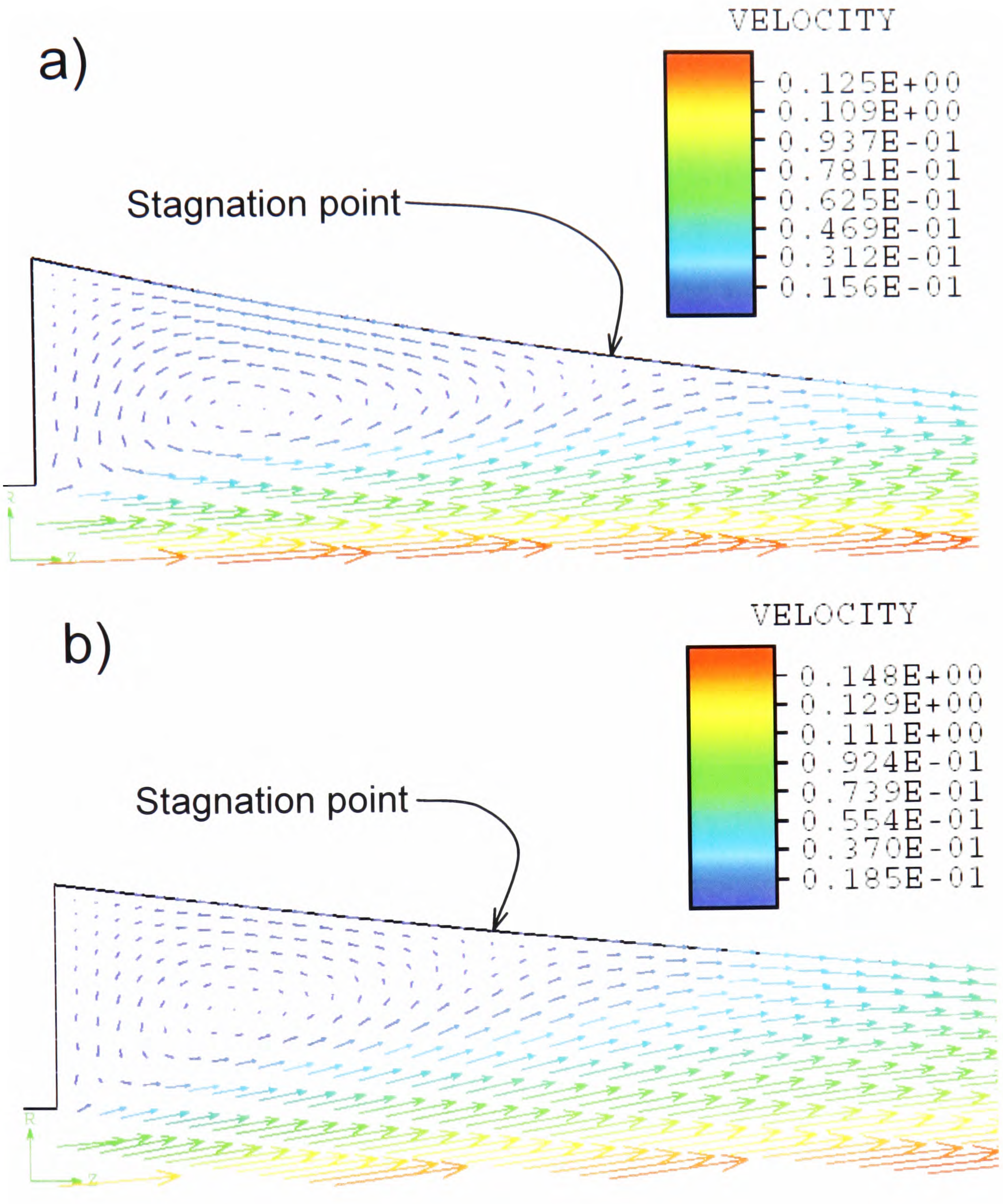

Figure 3.36: Velocity vector plots of the jet flow near the nozzle exit when wetting at the nozzle tip is considered in the CFD model at $\mathrm{Re} = 1950$, $\mathrm{Ca}^{-1} = 58.9$, and $(2\,\mathrm{Fr})^{-1} = 0.00507$ (a) and $\mathrm{Re} = 640$, $\mathrm{Ca}^{-1} = 125.1$, and $(2\,\mathrm{Fr})^{-1} = 0.0159$ (b).

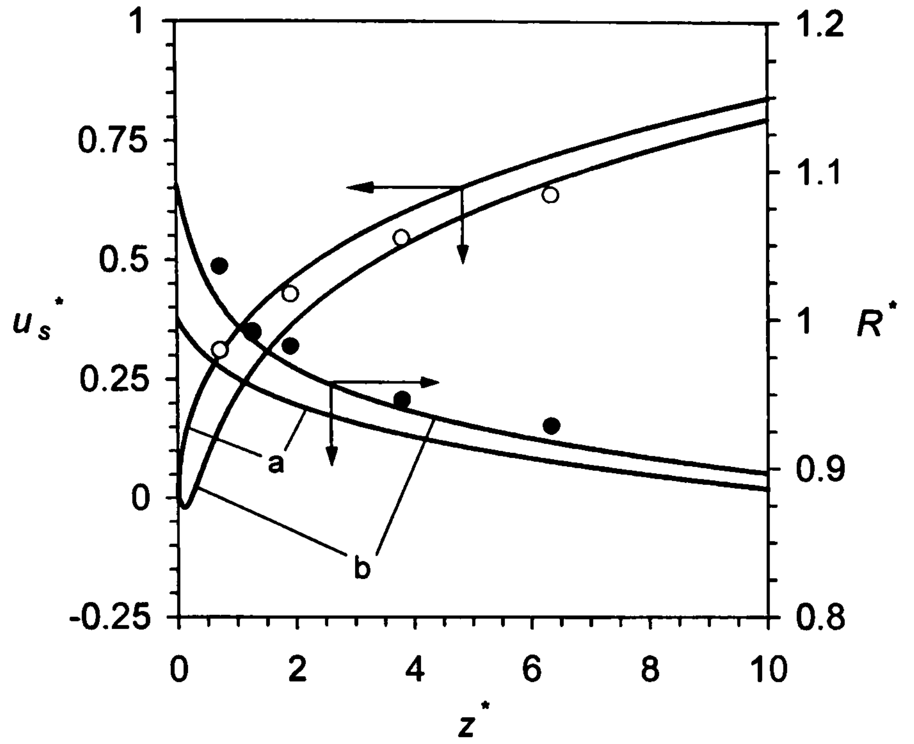

Figure 3.37: Surface velocity, $u_s^*(z^*)$, and free-surface position, $R^*(z^*)$, at $\mathrm{Re} = 1550$, $\mathrm{Ca}^{-1} = 74.3$, and $(2\,\mathrm{Fr})^{-1} = 0.00807$. Without wetting at the nozzle tip (a) and with wetting at the nozzle tip (b).

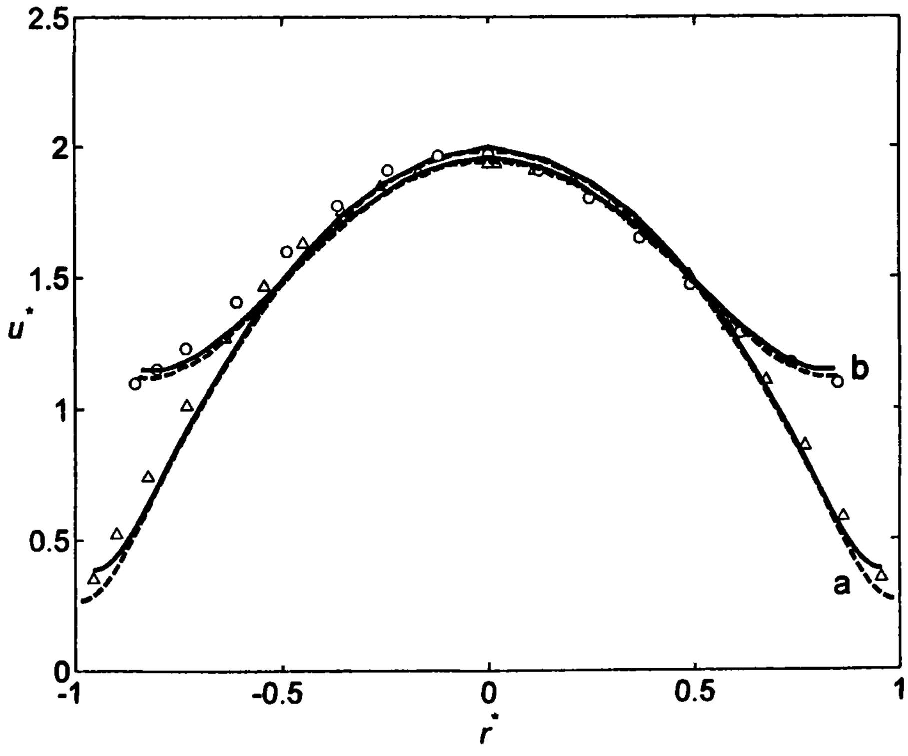

Figure 3.38: Velocity profiles, $u^*(r^*)$, at $z^* = 1.3$ (a, open triangles) and 25.3 (b, open circles) without wetting at the nozzle tip (solid lines) and with wetting at the nozzle tip (dashed lines) at $\mathrm{Re} = 1550$, $\mathrm{Ca}^{-1} = 74.3$, and $(2\,\mathrm{Fr})^{-1} = 0.00807$.

line, while at high concentrations mass transfer to the surface is faster and the surface concentration remains finite everywhere. In the current experimental apparatus, the stagnation line would lie too close to the nozzle to be detected readily.

Chapter 4

Surfactant Adsorption in the Jet: Theoretical Analysis

4.1 Boundary-Layer Development at the Nozzle Exit in the Presence of Surfactant

When a surfactant is present, its non-uniform surface concentration will give rise to a surface tension gradient—the Marangoni stress. The surface condition of the jet is no longer one of full slip, and the Marangoni stress gives rise to a velocity gradient in the layer adjacent to the surface, which is thus a region of reduced rather than zero vorticity (solid line in Figure 2.6). If this applied stress is τ_z at a distance z from the nozzle exit, then

$$\tau_z = -\mu \left(\frac{\partial u}{\partial y} \right)_{y=0}, \tag{4.1}$$

where for this approximate theory we have taken the coordinate y to be effectively perpendicular to the jet surface. If the velocity in the layer is again given by Equation (2.36), then a is the surface velocity, $u_s = u(y = 0, z)$, and b is $-\tau_z/\mu = (\partial u/\partial y)_{y=0}$. The velocity profile in the core of the jet flow is not changed and is given by Equation (2.35).

We set the condition that the velocity be continuous at the edge of the layer, so that $U(\delta) = u(\delta)$, which gives $\widehat{A}\delta + \widehat{B}\delta^2 = a + b\varepsilon$. Substituting for $\widehat{A}$, $\widehat{B}$, a, and b shows that the surface velocity is

$$u_s = 4\overline{u}_0 \left(\frac{\delta}{R_0} - \frac{\delta^2}{2R_0^2} \right) + \frac{\tau_z \varepsilon}{\mu}, \tag{4.2}$$

and since $\delta \ll R_0$,

$$u_s = \frac{4\overline{u}_0 \delta}{R_0} + \frac{\tau_z \varepsilon}{\mu}. \tag{4.3}$$

The thickness of the layer, ε, can be found by continuity. Applying Equation (2.39), we have $\widehat{A}\delta^2/2 + \widehat{B}\delta^3/3 = a\varepsilon + b\varepsilon^2/2$. Hence

$$\frac{2\overline{u}_0 R_0}{u_s}\left(\frac{\delta^2}{R_0^2} - \frac{\delta^3}{3R_0^3}\right) = \varepsilon\left(1 - \frac{\tau_z \varepsilon}{2\mu u_s}\right), \tag{4.4}$$

and since $\delta \ll R_0$,

$$u_s = \frac{2\overline{u}_0 \delta^2}{\varepsilon R_0} + \frac{\tau_z \varepsilon}{2\mu}. \tag{4.5}$$

Combining Equations (4.3) and (4.5), we find the relation between δ and ε,

$$\delta^2 - 2\delta\varepsilon - \frac{\tau_z}{4\mu\overline{u}_0/R_0}\varepsilon^2 = 0. \tag{4.6}$$

The negative solution of Equation (4.6) has no physical meaning, and the positive solution is

$$\delta = \left(1 + \sqrt{1 + \frac{\tau_z}{4\mu\overline{u}_0/R_0}}\right)\varepsilon = \alpha\varepsilon. \tag{4.7}$$

The surface-slip factor α is in the range $1 \leqslant \alpha \leqslant 2$, where the lower limit represents a no-slip condition at the jet surface, and the upper limit represents the stress-free surface analysed previously in Section 2.3. The term $4\mu\overline{u}_0/R_0$ is the shear stress at the nozzle wall, which results from the parabolic flow profile.

The rate of gain of momentum by fluid in the layer is equal to the force acting, which this time must include the surface tension. Again neglecting gravity, for unit width, and assuming the depth of the layer is small compared with the jet radius, the rate of momentum gain is

$$\rho \int_0^\delta U(y)\left\{u\left(\frac{\varepsilon y}{\delta} + \delta - \varepsilon\right) - U(y)\right\} dy = \mu\left(\frac{\partial U}{\partial y}\right)_{y=\delta} z + (\sigma_z - \sigma_0), \tag{4.8}$$

where σ_0 is the surface tension at the nozzle exit, and σ_z is the surface tension at the distance z. In this balance we have discounted the fact that the jet surface is not cylindrical, and therefore that the surface tensions do not quite act in the z-direction, and that the tension σ_z acts over a slightly smaller perimeter than σ_0 does. In the high Reynolds number limit, this simplification is made at little expense.

Again neglecting terms in δ^3 and higher powers of δ, we obtain $\widehat{A}a\delta^2/2 = \nu(\widehat{A} + 2\widehat{B}\delta)z + (\sigma_z - \sigma_0)/\rho$, so that

$$a = \frac{2\nu z}{\delta^2}\left(1 - \frac{\delta}{R_0}\right) + \frac{R_0 \Delta\sigma}{2\rho\bar{u}_0\delta^2}, \tag{4.9}$$

where $\Delta\sigma = \sigma_z - \sigma_0$ is the change in surface tension over the distance z. Since $\delta \ll R_0$, the surface velocity, $u_s = a$, is given by

$$u_s = \frac{2\nu z}{\delta^2} + \frac{R_0 \Delta\sigma}{2\rho\bar{u}_0\delta^2}. \tag{4.10}$$

We can use Equations (4.3) and (4.7) to eliminate δ from Equation (4.10) and find the surface velocity as

$$u_s = \left(\frac{32\bar{u}_0^2 \nu z}{R_0^2}\right)^{1/3} \left(1 + \frac{\Delta\sigma/z}{4\mu\bar{u}_0/R_0}\right)^{1/3} \left(1 + \frac{\tau_z/\alpha}{4\mu\bar{u}_0/R_0}\right)^{2/3}, \tag{4.11}$$

which can be rearranged to give

$$u_s = \left(\frac{32\bar{u}_0^2 \nu z}{R_0^2}\right)^{1/3} \left(1 + \frac{\Delta\sigma/z}{4\mu\bar{u}_0/R_0}\right)^{1/3} \left(1 + \frac{\tau_z}{4\mu\bar{u}_0/R_0}\right)^{1/3}. \tag{4.12}$$

Both the mean Marangoni stress $\Delta\sigma/z$ and the local value at z, $\tau_z = d\sigma/dz$, will in general be negative quantities, so that the result, as expected, is a reduction in the surface velocity from what it would be in the absence of the surfactant. Note that the maximum possible (negative) value of the Marangoni stress in the jet is $|d\sigma/dz| = 4\mu\bar{u}_0/R_0$, which is equal to the stress value inside the nozzle. We use this condition in the numerical computations to limit the Marangoni stress at $z = 0$.

The corresponding values of δ and ε are

$$\delta = \left(\frac{R_0 \nu z}{2\bar{u}_0}\right)^{1/3} \left(1 + \frac{\Delta\sigma/z}{4\mu\bar{u}_0/R_0}\right)^{1/3} \left(1 + \frac{\tau_z}{4\mu\bar{u}_0/R_0}\right)^{-1/6}, \tag{4.13}$$

and

$$\varepsilon = \frac{\delta}{\alpha}, \tag{4.14}$$

where the surface-slip factor α is defined in Equation (4.7). The relative narrowing of the jet due to acceleration of the surface layer is given by

$$\frac{R(z)}{R_0} = \frac{R_0 - (\delta - \varepsilon)}{R_0}, \tag{4.15}$$

or

$$\frac{R(z)}{R_0} = 1 - \frac{1}{\alpha}\left(\frac{\nu z}{2R_0^2 \bar{u}_0}\right)^{1/3}\left(1 + \frac{\Delta\sigma/z}{4\mu\bar{u}_0/R_0}\right)^{1/3}\left(1 + \frac{\tau_z}{4\mu\bar{u}_0/R_0}\right)^{1/3}. \qquad (4.16)$$

We can again derive dimensionless expressions, $u_s^* = u_s^*(z^*)$ and $R^* = R^*(z^*)$, for the surface velocity and the radius of the jet, respectively. Using our definitions for u_s^* and z^*, Equation (4.12) may be rewritten to give

$$u_s^* = \left(\frac{64z^*}{\mathrm{Re}}\right)^{1/3}\left(1 + \frac{(\sigma_z - \sigma_0)}{4z^*\mu\bar{u}_0}\right)^{1/3}\left(1 + \frac{\tau_z R_0}{4\mu\bar{u}_0}\right)^{1/3}. \qquad (4.17)$$

Defining

$$\mathrm{Ma} \equiv \left|\frac{1}{\mathrm{Ca}} - \frac{1}{\mathrm{Ca}_0}\right| = \frac{|\sigma_z - \sigma_0|}{\mu\bar{u}_0}, \qquad (4.18)$$

where Ma is the Marangoni number and Ca is the Capillary number, and introducing $\tau_z = d\sigma/dz$, we get

$$u_s^* = 4\left(\frac{z^*}{\mathrm{Re}}\right)^{1/3}\left(1 - \frac{\mathrm{Ma}}{4z^*}\right)^{1/3}\left(1 + \frac{1}{4}\frac{d}{dz^*}\left(\frac{1}{\mathrm{Ca}}\right)\right)^{1/3}. \qquad (4.19)$$

Correspondingly, the dimensionless radius of the jet is

$$R^* = 1 - \frac{1}{\alpha}\left(\frac{z^*}{\mathrm{Re}}\right)^{1/3}\left(1 - \frac{\mathrm{Ma}}{4z^*}\right)^{1/3}\left(1 + \frac{1}{4}\frac{d}{dz^*}\left(\frac{1}{\mathrm{Ca}}\right)\right)^{1/3}. \qquad (4.20)$$

In our expression for the surface velocity, Equation (4.19), we included terms for the Marangoni stress—the mean Marangoni stress Ma/z^* and the local value $d/dz^*(1/\mathrm{Ca})$. This stress cannot be determined from the dynamics of the jet, as it depends on the surface concentration, which in turn depends on the diffusion of surfactant to the surface. In order to solve the jet dynamics fully therefore, we must also solve the coupled mass-transfer problem.

4.2 Coupled Mass-Transfer Problem in the Absence of Micelles

Diffusion occurs when expansion of the surface, $du_s^*/dz^* = f'(z^*)$, reduces the sub-surface concentration of surfactant, $w_s = w(y^* = 0, z^*)$, below its equilibrium level. Note that in this section on modelling the mass transfer we take y^* to be measured from the surface of the jet. The sub-surface concentration is given as a mass fraction,

$$w_s = \frac{M}{\rho} c_s, \tag{4.21}$$

where M is the molecular weight of the surfactant species, ρ is the density of water, and c_s is the molar sub-surface concentration.

We note first that the thickness of the diffusion boundary layer will be small compared with the thickness of the hydrodynamic boundary layer, so that diffusion may be assumed to be taking place within a layer moving with the surface velocity, $u_s^* = f\left(z^*\right)$, throughout its depth. Within the diffusional boundary layer there is a velocity v^* perpendicular to the surface where by continuity (neglecting curvature and contraction of the jet)

$$\frac{\partial u_s^*}{\partial z^*} + \frac{\partial v^*}{\partial y^*} = 0 \Leftrightarrow -f'\left(z^*\right) = \frac{\partial v^*}{\partial y^*}. \tag{4.22}$$

This relationship shows that the velocity gradient within the diffusion boundary layer, $\partial v^* / \partial y^*$, is determined by the variation in surface velocity, $f'\left(z^*\right)$. We can integrate Equation (4.22) to find

$$v^* = -y^* f'(z^*), \tag{4.23}$$

since v^* is zero at the surface $(y^* = 0)$, and the streamwise velocity can be taken not to vary over the very thin boundary layer, at given z^*.

The convection-diffusion equation, in its dimensionless form, is

$$\frac{\partial^2 w}{\partial y^{*2}} + \frac{\mathrm{Re}}{2} \mathrm{Sc}\, y^* f'(z^*) \frac{\partial w}{\partial y^*} = \frac{\mathrm{Re}}{2} \mathrm{Sc}\, u_s^* \frac{\partial w}{\partial z^*}, \tag{4.24}$$

where axial diffusion has been neglected. This simplification is valid throughout the fluid, except very close to the point of detachment, where the surface concentration, and hence the sub-surface concentration, changes rapidly. In Equation (4.24), the Schmidt number, Sc, is defined as

$$\mathrm{Sc} \equiv \frac{\mu}{\rho D}, \tag{4.25}$$

where D is the coefficient of diffusivity of surfactant molecules in water. The right hand side of Equation (4.24) is zero at the nozzle exit, where the no-slip condition ensures that u_s^* is zero, and the requirement for a finite Marangoni stress (see Equation (4.37) in Section 4.2.2) ensures that $\partial w / \partial z^*$ remains finite.

The right hand side of Equation (4.24) may also be negligible further downstream where the gradient $\partial w/\partial z^*$ at the surface is low. We note further that the streamwise concentration gradient in the bulk liquid is always zero. In this simplified model, we therefore ignore the streamwise convective term (right hand side of Equation (4.24)) throughout the boundary layer.

The general solution of Equation (4.24) is given in Appendix A. The boundary conditions are that $w = w_s$ at $y^* = 0$, and $w \rightarrow w_b$ as $y^* \rightarrow \infty$, where w_b is the bulk concentration. With these boundary conditions we have

$$\frac{w - w_s}{w_b - w_s} = \operatorname{erf}\left\{\frac{y^*}{2}\sqrt{\mathrm{Re}\,\mathrm{Sc}\,f'(z^*)}\right\}, \qquad (4.26)$$

in which $f'(z^*) = du_s^*/dz^*$ is the rate of surface expansion.

The dimensionless diffusion mass flux to the surface, $q^*_{diff} = q_{diff}R_0(\rho D)^{-1}$, is given by

$$q^*_{diff} = \left(\frac{\partial w}{\partial y^*}\right)_{y^*=0} = (w_b - w_s(z^*))\sqrt{\frac{\mathrm{Re}\,\mathrm{Sc}}{\pi}\frac{du_s^*}{dz^*}}. \qquad (4.27)$$

Diffusion to the surface of the jet is balanced by convection in the surface, $q^*_{conv} = q_{conv}R_0(\rho D)^{-1}$. Neglecting the (small) change in perimeter of the jet, we obtain

$$q^*_{conv} = \frac{M\bar{u}_0\Gamma_{sat}}{\rho D}\left\{\frac{d}{dz^*}(u_s^*\Gamma^*) + \frac{2}{\mathrm{Re}\,\mathrm{Sc}_s}\frac{d^2\Gamma^*}{dz^{*2}}\right\}, \qquad (4.28)$$

where the term $2\,(\mathrm{Re}\,\mathrm{Sc}_s)^{-1}\,d^2\Gamma^*/dz^{*2}$ accounts for diffusion in the surface, which accompanies the convection $d/dz^*\,(u_s^*\Gamma^*)$. Sc_s is the Schmidt number in the surface, which contains the diffusivity of monomers in the surface, D_s.

If we assume that $D_s = D$, u_s^* is given by Equation (2.49), and Γ^* is given by Equation (4.31), we find that the surface diffusion contribution is negligibly small compared with the surface convection providing that $6\,\mathrm{Re}^{2/3}\,\mathrm{Sc}_s\,z^{*4/3} \gg 1$. Thus for $\mathrm{Re} \sim \mathcal{O}(10^3)$ and $\mathrm{Sc}_s \sim \mathcal{O}(10^3)$, we find that the surface diffusion contribution is negligible for $z^* > 10^{-4}$. However, if $z^* < 10^{-4}$, from Equation (4.40), we see that $d^2\Gamma^*/dz^{*2} = 0$. Therefore, we do not consider the surface diffusion contribution any further.

In Equation (4.28), $\Gamma^* = \Gamma/\Gamma_{sat}$ is the dimensionless surface concentration or surface coverage. We note that the saturation surface coverage, Γ_{sat}, is greater than the maximum surface coverage, which is reached at the critical micelle concentration and is about 80% of the saturation value for C_{16}TAB.

The set of equations which describes the coupled problem is too complex for analytical solution, and must be tackled using CFD methods. However it is useful to derive some approximate results, so as to understand the shape of the problem, and the features displayed by the computed solution. We tackle this by dividing the jet flow into two zones—the downstream jet flow and the flow of the jet near the nozzle, which we term the detachment region, the nozzle exit at $z^* = 0$ being the point of detachment.

4.2.1 Downstream Jet Flow

If the Marangoni stresses are small compared with the maximum value at the nozzle exit, then we can assume that the surface velocity has the surfactant-free value. This will be the case for dilute solutions, some way from the nozzle exit. In this case, the surface velocity, $u_s^* = u_s^*(z^*)$, is given by Equation (2.49). Substituting for the surface expansion, du_s^*/dz^*, in Equation (4.27), and assuming that the sub-surface concentration remains low compared to the concentration in the bulk, $w_b - w_s \approx w_b$, gives

$$q_{diff}^* = \left(\frac{\mathrm{Re}\,\mathrm{Sc}}{\pi}\right)^{1/2} \left(\frac{64}{27\,\mathrm{Re}}\right)^{1/6} w_b {z^*}^{-1/3}. \tag{4.29}$$

The surface concentration, $\Gamma^* = \Gamma^*(z^*)$, can be found by balancing convection and diffusion at the surface, Equations (4.28) and (4.29). We obtain

$$\left(\frac{\mathrm{Re}\,\mathrm{Sc}}{\pi}\right)^{1/2} \left(\frac{64}{27\,\mathrm{Re}}\right)^{1/6} w_b \int_0^{z^*} {z^*}^{-1/3} dz^* = \frac{M\bar{u}_0\Gamma_{sat}}{\rho D} \int_0^{z^*} d\left(u_s^*\Gamma^*\right), \tag{4.30}$$

and with Equation (2.49) for u_s^*, we find

$$\Gamma^* = 0.244\left(\frac{\rho D}{M\bar{u}_0\Gamma_{sat}}\right) \mathrm{Re}^{2/3}\,\mathrm{Sc}^{1/2}\, w_b {z^*}^{1/3} \tag{4.31}$$

when the Marangoni stress is small.

For low concentrations, the variation in surface tension, $d/dz^*(1/\mathrm{Ca})$, is obtained from Henry's law,

$$\frac{1}{\mathrm{Ca}} = \frac{1}{\mathrm{Ca}_w} - \frac{\widehat{N}\mathcal{R}T\Gamma_{sat}}{\mu\bar{u}_0}\Gamma^*, \tag{4.32}$$

to give

$$\frac{d}{dz^*}\left(\frac{1}{\mathrm{Ca}}\right) = -\frac{\widehat{N}\mathcal{R}T\Gamma_{sat}}{\mu\bar{u}_0}\frac{d\Gamma^*}{dz^*}, \tag{4.33}$$

and with $d\Gamma^*/dz^*$ from Equation (4.31),

$$\frac{d}{dz^*}\left(\frac{1}{\mathrm{Ca}}\right) = -\frac{\mathrm{E}}{12.28}\left(\frac{\rho D}{M\bar{u}_0\Gamma_{sat}}\right)\mathrm{Re}^{2/3}\,\mathrm{Sc}^{1/2}\,w_b {z^*}^{-2/3}, \tag{4.34}$$

where

$$\mathrm{E} \equiv \frac{\widehat{N}\mathcal{R}T\Gamma_{sat}}{\mu\bar{u}_0} \tag{4.35}$$

is the Elasticity number. It is a measure of the importance of the surface tension change caused by surfactant adsorption relative to the viscous force. In Equation (4.35), $\widehat{N}$ reflects the number of ions delivered to the surface by a molecule of surfactant ($\widehat{N} = 1$ for non-ionics, $\widehat{N} = 2$ for ionics with monovalent ions, etc.), $\mathcal{R}$ is the universal gas constant, and T is the temperature.

Both the surface concentration and the surface tension will vary approximately with the one-third power of distance from the nozzle, that is, $\Gamma^* \sim {z^*}^{1/3}$ and $\mathrm{Ca}^{-1} \sim {z^*}^{1/3}$, respectively. This implies that $d\Gamma^*/dz^*$ and $d/dz^*\,(1/\mathrm{Ca})$ scale as ${z^*}^{-2/3}$, so that $d\Gamma^*/dz^* \to \infty$ and $d/dz^*\,(1/\mathrm{Ca}) \to \infty$ as $z^* \to 0$. This contravenes our assumption that the Marangoni stress is small, so that the cube-root dependence of Equation (4.31) must break down as $z^* \to 0$.

The derivations made in this section apply to the region of the jet flow, where the Marangoni stress is small compared to the maximum shear stress at the nozzle exit. That is, outside the region of detachment (see Section 4.2.2), but still close enough to the nozzle exit for the assumptions of low concentration (Henry's law), and neglect of gravity and streamwise convection in the boundary layer to be valid.

4.2.2 Flow Near the Nozzle: The Detachment Region

It is important for the description of the flow further down the jet to know how the jet surface moves immediately after it detaches from the nozzle. In particular we wish to establish the conditions under which the acceleration of liquid at the point of detachment remains finite and what the surface concentration is near to the nozzle.

The surface concentration gradient at the point of detachment, $d\Gamma^*/dz^*$ at $z^* = 0$, must remain finite and sufficiently small that the maximum Marangoni stress, $4\mu\bar{u}_0/R_0$, consistent with a boundary-layer treatment of the hydrodynamics is not exceeded. Considering the fluxes from Equations (4.27) and

(4.28), we see that if they are to match each other we must have $(du_s^*/dz^*)^{1/2} \sim d(u_s^*\Gamma^*)/dz^*$. If we suppose that u_s^* varies as z^{*^n} $(n > 0)$ to leading order, then Γ^* must vary as $z^{*^{(1-n)/2}}$ as $z^* \longrightarrow 0$. Since Γ^* remains finite as $z^* \longrightarrow 0$, $n \leqslant 1$. However, near to the nozzle a value of n less than unity is precluded, as $d\Gamma^*/dz^*$ must remain finite as $z^* \longrightarrow 0$. Hence $n = 1$ and the leading order term in a Taylor expansion for Γ^* about $z^* = 0$ is a constant value $\Gamma_0^* = \Gamma_0/\Gamma_{sat}$. Near the nozzle, the surface velocity increases linearly with distance and the surface acceleration at $z^* = 0$ is finite.

From Equation (4.19), near the nozzle,

$$u_s^* = 4\left(\frac{z^*}{\mathrm{Re}}\right)^{1/3}\left(1 - \frac{\mathrm{Ma}}{4z^*}\right)^{1/3}\left(1 + \frac{1}{4}\frac{d}{dz^*}\left(\frac{1}{\mathrm{Ca}}\right)\right)^{1/3} \sim \kappa z^*, \tag{4.36}$$

where κ is a constant that is to be determined. It emerges from Equation (4.36) that as $z^* \longrightarrow 0$, where we have $-\mathrm{Ma}\,(4z^*)^{-1} = d/dz^*\,(4\,\mathrm{Ca})^{-1}$, if the surface acceleration is to remain finite, we must have

$$\left\{-\frac{\mathrm{Ma}}{z^*}\right\}_{z^*=0} = \left\{\frac{d}{dz^*}\left(\frac{1}{\mathrm{Ca}}\right)\right\}_{z^*=0} = \left\{\frac{d}{dz^*}\left(\frac{1}{\mathrm{Ca}}\right)\right\}_{\mathrm{max}} = -4. \tag{4.37}$$

The local Marangoni stress must have its maximum (negative) value at that point. We note that this result is independent of the concentration of surfactant.

We can integrate Equation (4.36) to obtain the dependence of the surface tension parameter, Ca^{-1}, on the axial distance, z^*, near the origin. We obtain

$$\frac{1}{\mathrm{Ca}} = \frac{1}{\mathrm{Ca}_0} - 4z^* + \frac{\kappa^{3/2}\sqrt{\mathrm{Re}}}{4}z^{*^2}, \tag{4.38}$$

which is valid as $z^* \longrightarrow 0$. From Equation (4.38) we obtain for the Marangoni stress in the detachment region,

$$\frac{d}{dz^*}\left(\frac{1}{\mathrm{Ca}}\right) = -4 + \frac{\kappa^{3/2}\sqrt{\mathrm{Re}}}{2}z^*. \tag{4.39}$$

We can now derive the expression for the dependence of the surface coverage, Γ^*, on z^* in the region of detachment using Henry's law, Equation (4.33), and Equation (4.39). We obtain through integration

$$\Gamma^* = \Gamma_0^* + \frac{4}{\mathrm{E}}z^* - \frac{\kappa^{3/2}\sqrt{\mathrm{Re}}}{4\mathrm{E}}z^{*^2}. \tag{4.40}$$

We have thus shown that there is a (short) detachment region in which the surface velocity increases linearly from zero at $z^* = 0$, and a region further from

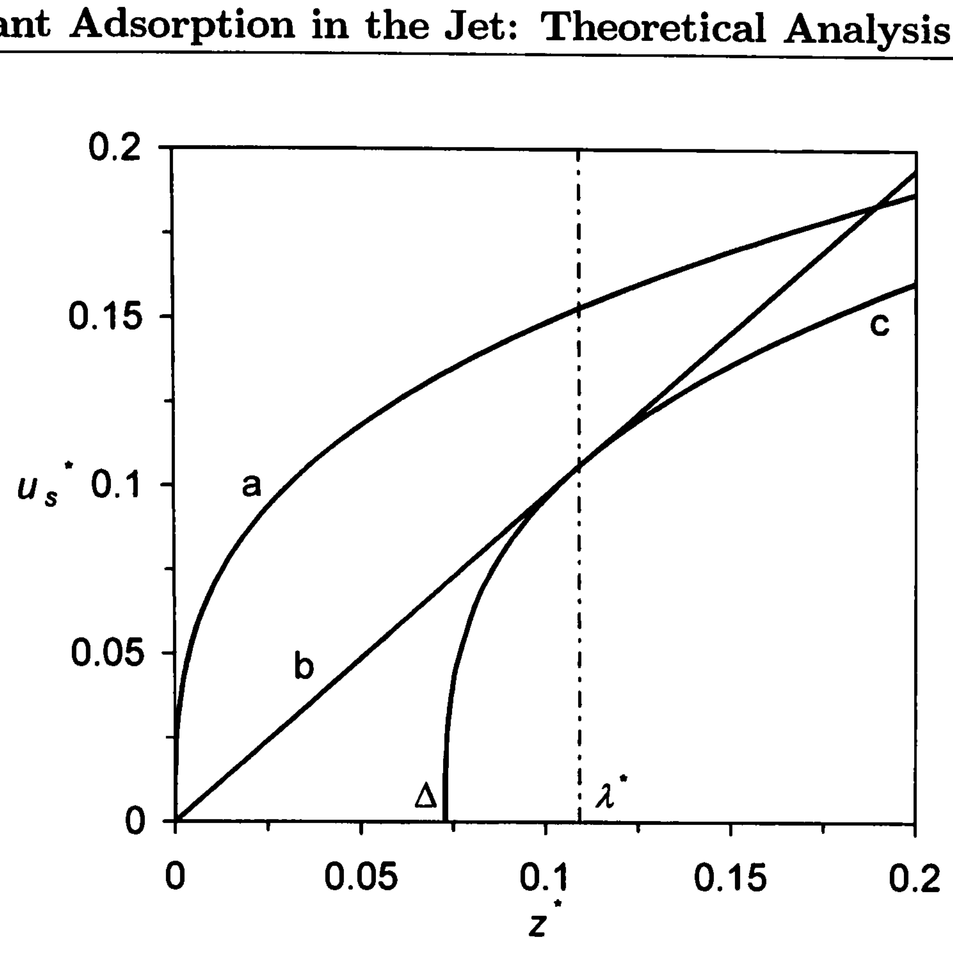

Figure 4.1: Definition of the length of the detachment region, λ^*, for Re = 1950 and $c_b = 0.9$ mol m^{-3} C_{16}TAB in water. Curve (a) is u_s^* of the surfactant-free jet, given by Equation (2.49). Curve (b) is u_s^* in the region of detachment, given by Equation (4.44). Curve (c) is u_s^* of the jet in the presence of surfactant outside the region of detachment, given by Equation (4.45).

the nozzle in which, according to Equation (2.49), the surface velocity varies with the cube root of the distance, as the Marangoni stress becomes negligible. We can estimate the length scale of the detachment region, $\lambda^* = \lambda/R_0$, which is defined as the length at which the detachment region solution and the far-field solution both exhibit the same surface velocity, u_s^*, and the same surface expansion, du_s^*/dz^*, in the following way (see Figure 4.1).

The upward Marangoni stress near the nozzle acts so as to reduce the surface velocity in the downstream region slightly. This velocity reduction may be considered equivalent to a slight displacement of the nozzle exit, say Δ, in a downward sense. Suppose that for large values of z^*, from Equation (2.49),

$$u_s^* = 4\left(\frac{z^* - \Delta}{\mathrm{Re}}\right)^{1/3}, \tag{4.41}$$

which is valid for $z^* \geqslant \Delta$ (curve (c) in Figure 4.1). In Equation (4.41), we can approximate $(z^* - \Delta)^{1/3} \approx {z^*}^{1/3} - (\Delta/3)\,{z^*}^{-2/3}$, so that for $z^* \to \infty$ we see that $(z^* - \Delta)^{1/3} \to {z^*}^{1/3}$. The Marangoni stress thus vanishes as the jet travels downstream and for $z^* \to \infty$, Equation (4.41) becomes Equation (2.49), which is given by curve (a) in Figure 4.1. For small z^*, we assume that u_s^* shows linear behaviour according to Equation (4.36), which is demonstrated by curve (b) in Figure 4.1. We match both u_s^* and du_s^*/dz^* at $z^* = \lambda^*$, from which we obtain

$$\Delta = \frac{2}{3}\lambda^*, \tag{4.42}$$

and

$$\kappa = \left(\frac{64}{3\,\mathrm{Re}}\right)^{1/3} {\lambda^*}^{-2/3}. \tag{4.43}$$

The velocity profiles are thus given by

$$u_s^* = \left(\frac{64}{3\,\mathrm{Re}}\right)^{1/3} {\lambda^*}^{-2/3} z^* \tag{4.44}$$

in the region of detachment, and

$$u_s^* = \left(\frac{64}{\mathrm{Re}}\right)^{1/3} \left(z^* - \frac{2}{3}\lambda^*\right)^{1/3} \tag{4.45}$$

in the downstream region.

The solutions for the surface concentration, Γ^*, in the downstream region and in the region of detachment, Equations (4.31) and (4.40), respectively, are matched using a similar procedure to that used for the matching of the surface velocity. As before, we introduce an off-set value into the downstream solution for Γ^*. This off-set value, say $\widetilde{\Delta}$, is different to Δ.

Equation (4.31) then becomes

$$\Gamma^* = \mathcal{A}\left(z^* - \widetilde{\Delta}\right)^{1/3}, \tag{4.46}$$

where

$$\mathcal{A} = 0.244\left(\frac{\rho D}{M\bar{u}_0\Gamma_{sat}}\right)\mathrm{Re}^{2/3}\,\mathrm{Sc}^{1/2}\,w_b. \tag{4.47}$$

We then match the values Γ^* and the slopes $d\Gamma^*/dz^*$ from Equations (4.46) and (4.40) at $z^* = \lambda^*$, which gives

$$\Gamma_0^* + \left(2 - \frac{1}{\sqrt{3}}\right)\frac{2\lambda^*}{\mathrm{E}} = \mathcal{A}\left(\lambda^* - \widetilde{\Delta}\right)^{1/3}, \tag{4.48}$$

and

$$\frac{\mathcal{A}}{3}\left(\lambda^* - \widetilde{\Delta}\right)^{-2/3} = \frac{4}{\mathrm{E}}\left(1 - \frac{1}{\sqrt{3}}\right), \tag{4.49}$$

respectively. From Equation (4.49), we find directly for the off-set value

$$\widetilde{\Delta} = \lambda^* - \left\{ \frac{12}{\mathrm{E}\mathcal{A}} \left(1 - \frac{1}{\sqrt{3}} \right) \right\}^{-3/2} . \tag{4.50}$$

The matching of the two solutions for Γ^* at $z^* = \lambda^*$ is shown graphically in Figure 4.2. The downstream solution for Γ^* without the off-set value $\widetilde{\Delta}$, Equation (4.31), is given by curve (a), and curve (b) represents the solution for Γ^* in the region of detachment, Equation (4.40). Curve (c) is the downstream solution for Γ^*, which is shifted in the axial direction by the off-set value $\widetilde{\Delta}$, Equation (4.46). We see from Figure 4.2 that the off-set value $\widetilde{\Delta}$ is a negative quantity. The reduced surface velocity decreases the convection in the surface. For the convective surface flux, $u_s^*\Gamma^*$, to balance diffusion of surfactant to the surface, requires that Γ^* increases. Thus it appears that the source of the jet has moved a distance $\widetilde{\Delta}$ upstream. The matched solution for Γ^* consists of curve (b) on the interval $0 \leqslant z^* \leqslant \lambda^*$, and curve (c) for $z^* \geqslant \lambda^*$.

Using Equation (4.50) to replace $\widetilde{\Delta}$ in Equation (4.48), we find a quadratic equation that contains λ^* and Γ_0^*, namely

$$\Gamma_0^{*2} + \left(2 - \frac{1}{\sqrt{3}} \right) \frac{4\lambda^*}{\mathrm{E}} \Gamma_0^* + \left\{ \left(2 - \frac{1}{\sqrt{3}} \right) \frac{2\lambda^*}{\mathrm{E}} \right\}^2 = \frac{\mathrm{E}\mathcal{A}^3}{12} \left(1 - \frac{1}{\sqrt{3}} \right)^{-1} , \tag{4.51}$$

which has the solution

$$\Gamma_0^* = -\frac{5.6906\lambda^*}{2\mathrm{E}} \pm \sqrt{\frac{\mathrm{E}\mathcal{A}^3}{5.0718}} . \tag{4.52}$$

Only the positive solution in Equation (4.52) has a physical meaning.

We have thus found a relation between the length of the detachment region, λ^*, and the surface concentration at the point of detachment, Γ_0^*. Both λ^* and Γ_0^* are still unknown, and a second relation is needed to determine them. Intuitively, it may seem that this second relation could be obtained from the matching of the solutions for the surface tension parameter, Ca^{-1}, which are given by Equations (4.32) and (4.31) in the downstream region, and by Equation (4.38) in the region of detachment, in a way that is analogous to the matching of the surface concentration, but that is in fact not the case. Indeed, if we carry out this matching procedure, we find that the downstream solution for Ca^{-1} is off set by a value that equals exactly $\widetilde{\Delta}$, and the relation that follows for λ^* and Γ_0^* is again Equation (4.52). It is, however, reassuring that the same results are found

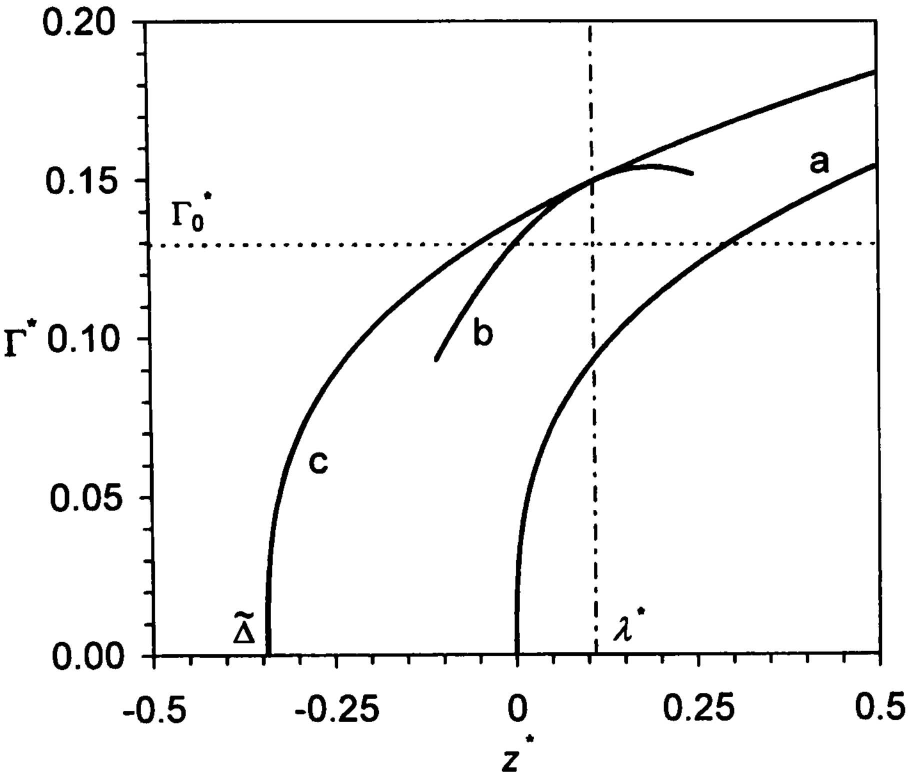

Figure 4.2: Matching of the solutions for Γ^* in the region of detachment (curve (b), Equation (4.40)) and in the downstream region, where curve (a), given by Equation (4.31), is the downstream solution for Γ^* if the surface velocity of the surfactant free jet is assumed, and curve (c), given by Equation (4.46), is the downstream solution for Γ^* with the reduced surface velocity of the jet in the presence of surfactant. The graphs are for Re = 1950 and $c_b = 0.9$ mol m^{-3} C_{16}TAB in water.

from the matching of Γ^* and Ca^{-1} since both are linked by the linear equation of state. One therefore defines the other and the two matching procedures are identical. Figure 4.3 shows the matching of the solutions for the surface tension parameter, Ca^{-1}, in the two flow regions graphically.

The second relation for λ^* and Γ_0^* is found from a mass balance around the surface at the point of detachment. Balancing diffusion and convection at $z^* = 0$, Equations (4.27) and (4.28), where we assume that $w_b \gg w_{s,0} = w_s\,(z^* = 0)$, and using the detachment region solution for u_s^*, Equation (4.44), gives

$$\Gamma_0^* = \mathcal{A}\frac{0.3388}{0.244}\lambda^{*1/3}. \tag{4.53}$$

Setting Equations (4.52) and (4.53) equal gives an equation for λ^*,

$$\mathcal{A}\frac{0.3388}{0.244}\lambda^{*1/3} + \frac{2.8453}{\mathrm{E}}\lambda^* = \frac{(\mathrm{E}\mathcal{A}^3)^{1/2}}{2.2521}. \tag{4.54}$$

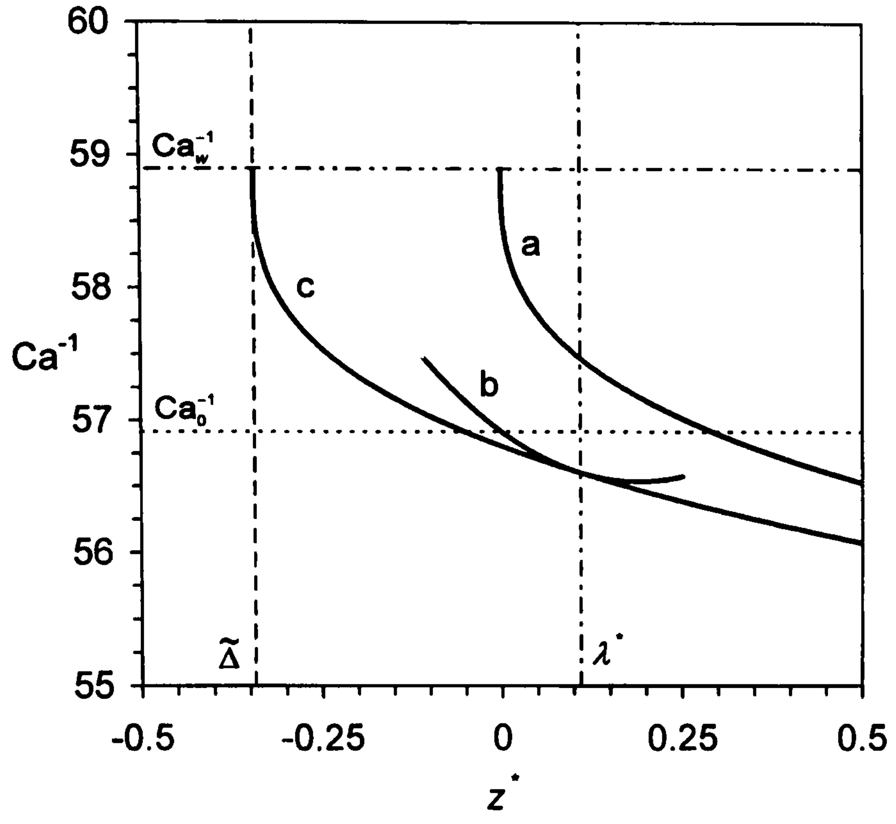

Figure 4.3: Matching of the solutions for Ca^{-1} in the region of detachment (curve (b), Equation (4.38)) and in the downstream region, where curve (a), given by Equations (4.32) and (4.31), is the downstream solution for Ca^{-1} if the surface velocity of the surfactant free jet is assumed, and curve (c), given by Equations (4.32) and (4.46), gives the downstream solution for Ca^{-1} with the reduced surface velocity of the jet in the presence of surfactant. The graphs are for $\mathrm{Re} = 1950$ and $c_b = 0.9$ mol m^{-3} $\mathrm{C_{16}TAB}$ in water.

Equation (4.54) is a reduced cubic equation, for which the solution can be found by standard procedures [209, p. 131], and is

$$\lambda^* = 0.0211\,(\mathrm{E}\mathcal{A})^{3/2}\,. \tag{4.55}$$

Resubstituting for $\mathcal{A}$ gives

$$\lambda^* = 2.543 \times 10^{-3}\left(\mathrm{E}\frac{\rho D}{M\bar{u}_0\Gamma_{sat}}\right)^{3/2} \mathrm{Re}\,\mathrm{Sc}^{3/4}\,w_b^{3/2}. \tag{4.56}$$

At first sight it may seem surprising that the surface acceleration at the point of detachment is fundamentally changed by the presence of surfactant, as this might suggest that the no-surfactant case is not obtained by reducing the surfactant concentration towards zero. In fact a steady reduction of surfactant concentration, w_b, reduces the length of the detachment region, λ^*, and increases the surface acceleration at the point of detachment. Putting the value of λ^* from Equation (4.56) into Equation (4.44) shows that $du_s^*/dz^* \sim {\lambda^*}^{-2/3} \sim w_b^{-1}$, which gives $du_s^*/dz^* \rightarrow \infty$ as $w_b \rightarrow 0$, so that the limiting (pure water) case emerges correctly. Another way of putting this argument is to let $\lambda^* \rightarrow 0$ in Equation (4.45), which gives the pure water expression for u_s^*.

Replacing λ^* in Equation (4.53) with Equation (4.56), and resubstituting for $\mathcal{A}$, we find

$$\Gamma_0^* = 0.0462 \left\{ \mathrm{E} \left(\frac{\rho D}{M \bar{u}_0 \Gamma_{sat}} \right)^3 \right\}^{1/2} \mathrm{Re}\, \mathrm{Sc}^{3/4}\, w_b^{3/2}. \tag{4.57}$$

The surface concentration at the point of detachment and the length of the detachment region thus show the same dependence on the bulk concentration.

The results for λ^* and Γ_0^*, Equations (4.56) and (4.57), respectively, are shown graphically in Figure 4.4 for the surfactant C_{16}TAB and a Reynolds number of Re = 1950. Figure 4.4 shows that the values for Γ_0^* are indeed very small, reaching a value of $\Gamma_0^* = 0.13$ at a relativly high bulk concentration of $c_b = 0.9$ mol m^{-3} ($w_b = 328.05 \times 10^{-6}$), which nearly equals the critical micelle concentration for C_{16}TAB ($c_{\mathrm{cmc}} = 0.92$ mol m^{-3}). This value for Γ_0^* is still well below the equilibrium value for this particular surfactant at this value for the bulk concentration ($\Gamma_{eq}^* \approx 0.8$). Using Langmuir's isotherm, Equation (4.85), we can calculate the corresponding value for the sub-surface concentration, $w_{s,0}$, at $c_b = 0.9$ mol m^{-3}, which is $w_{s,0} = 12.23 \times 10^{-6}$. Clearly, $w_{s,0} \ll w_b$.

The simplified theory shows that $(du_s^*/dz^*)_{z^*=0}$ is finite when surfactant is present. This is an important result, which may be contrasted with the no-surfactant case in which $(du_s^*/dz^*)_{z^*=0}$ is infinite. In a linked result, the simplified theory also shows that when surfactant is present, there is a finite amount, Γ_0^*, which is small, adsorbed at the surface of the jet at the point of detachment.

4.2.3 Region of Validity

The results for λ^* and Γ_0^* that were derived in the previous section, were obtained under the presumption that (i) the sub-surface concentration is much smaller than the bulk value, so that $w_b - w_s(z^*) \approx w_b$, and that ($ii$) Henry's law accurately describes the dependence of surface tension on the surface concentration. These assumptions must hold within the region of detachment.

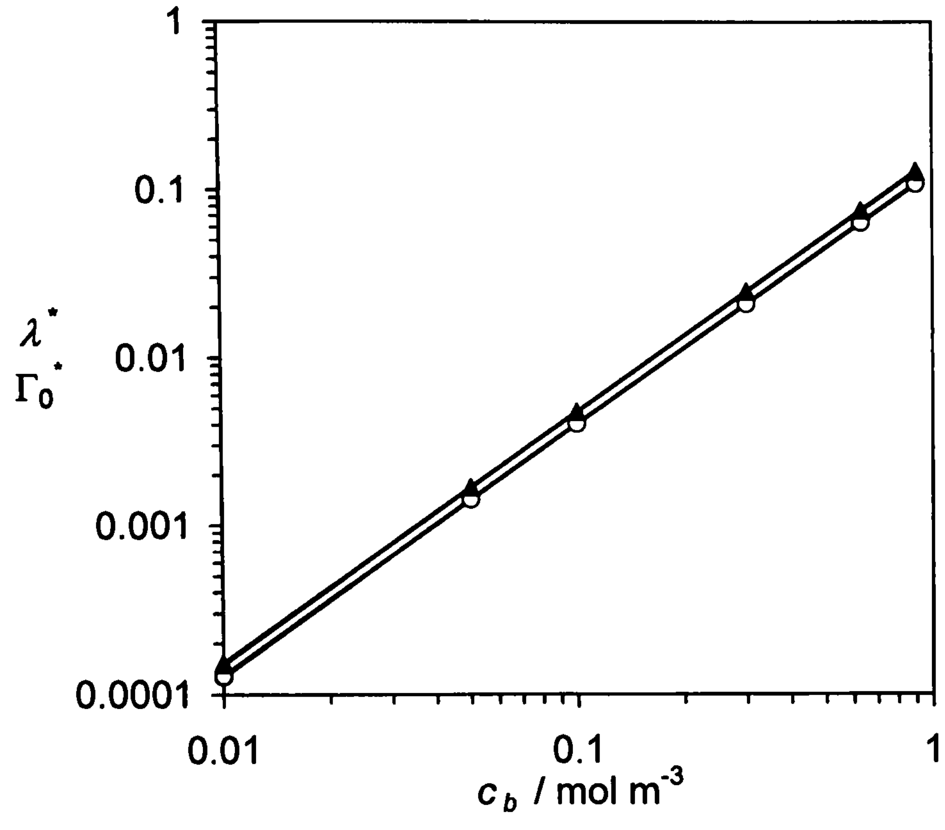

Figure 4.4: Length of the detachment region, λ^* (Equation (4.56), open circles), and surface concentration at the point of detachment, Γ_0^* (Equation (4.57), closed triangles), for varying bulk concentrations, c_b, of $C_{16}TAB$ at Re = 1950.

Sub-Surface Concentration

If the sub-surface concentration, $w_s(z^*)$, in the mass balance at the surface that gave Equation (4.31) had not been omitted, but assumed to be given by a power law of the form

$$w_s = Cz^{*^m}, \tag{4.58}$$

where $m > 0$, then the result for $\Gamma^*(z^*)$ would have been

$$\Gamma^* = 0.244\left(\frac{\rho D}{M\bar{u}_0\Gamma_{sat}}\right)\mathrm{Re}^{2/3}\,\mathrm{Sc}^{1/2}\,w_b\left\{1-\frac{2}{3w_b}\frac{Cz^{*^m}}{\left(m+\frac{2}{3}\right)}\right\}z^{*^{1/3}}. \tag{4.59}$$

Comparison of Equation (4.59) with Equation (4.31) shows that the consideration of $w_s(z^*)$ leads to lower values for Γ^*, which is due to the reduced driving concentration difference for the diffusive mass flux of surfactant between the bulk and the surface. Typical orders of magnitude of the parameters in the additional term in Equation (4.59) for the surfactant $C_{16}TAB$ at a high Reynolds number and a relatively high bulk concentration are

$$\begin{aligned} w_b &\sim \mathcal{O}(10^{-4}) \\ z^* &\sim \lambda^* \sim \mathcal{O}(10^{-1}) \\ C &\sim \mathcal{O}(10^{-5}) \\ m &\sim \mathcal{O}(10^{-1}) \end{aligned}$$

We can estimate the order of magnitude of the additional term in Equation (4.59) to give

$$\frac{2}{3w_b}\frac{C\lambda^{*m}}{\left(m+\frac{2}{3}\right)} \sim \mathcal{O}(10^{-2}) \ll 1 \tag{4.60}$$

within the region of detachment. The additional term is thus negligibly small, and we do not have to consider $w_s(z^*)$ to calculate λ^* and Γ_0^*.

Surface Equation of State

Henry's law, given by Equation (4.32), provides a linear relation between the surface tension parameter, Ca^{-1}, and the surface concentration, Γ^*. This linear relation only holds at low concentrations. As the concentration along the surface increases, with increasing distance from the nozzle, the relation between Ca^{-1} and Γ^* is more accurately represented by the non-linear Frumkin equation, given by

$$\frac{1}{\mathrm{Ca}} = \frac{1}{\mathrm{Ca}_w} + \mathrm{E}\ln\left(1-\Gamma^*\right), \tag{4.61}$$

from which we find for the Marangoni stress

$$\frac{d}{dz^*}\left(\frac{1}{\mathrm{Ca}}\right) = -\frac{\mathrm{E}}{\left(1-\Gamma^*\right)}\frac{d\Gamma^*}{dz^*}. \tag{4.62}$$

Comparison of Equation (4.62) and (4.33) shows that the local value of the Marangoni stress that arises from the Frumkin equation is larger by a factor $(1-\Gamma^*)^{-1} > 1$ than the local value obtained from Henry's law. The larger Marangoni stress results in lower surface velocities, u_s^*, which in turn diminishes the axial convection in the surface, given by the product of u_s^* and Γ^*. In order to balance the diffusion of surfactant to the surface, the surface concentration must thus increase.

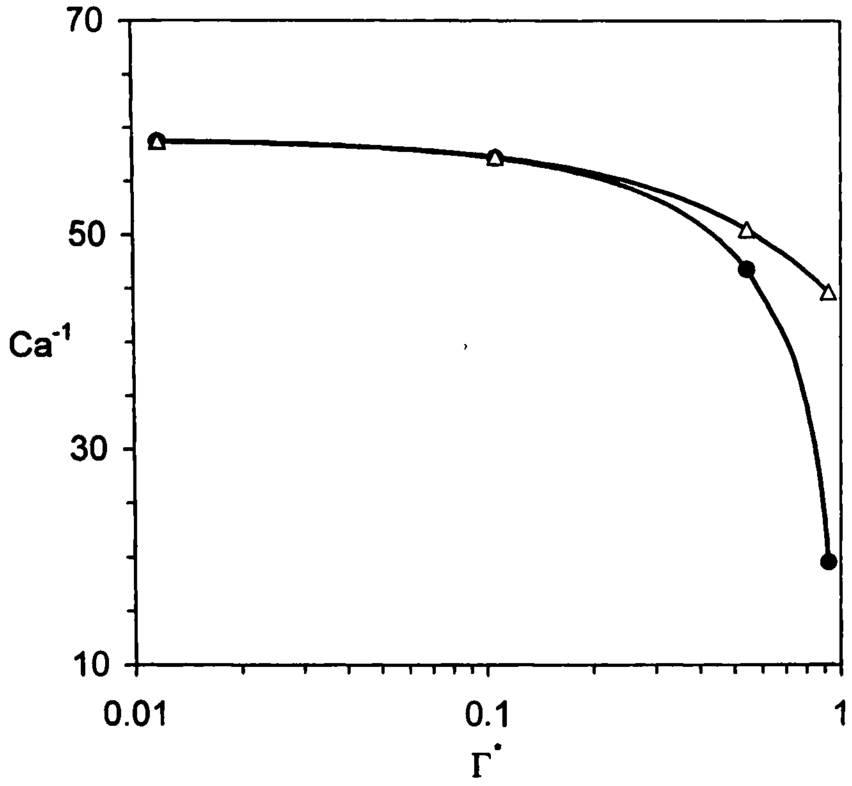

Figure 4.5: Surface tension parameter, Ca^{-1}, according to Henry's law (Equation (4.32), open triangles) and Frumkin equation (Equation (4.61), closed circles) as a function of the surface concentration, Γ^*. The graphs are for $\mathrm{Ca}_w^{-1} = 58.9$, $\mathrm{Re} = 1950$, and $\mathrm{E} = 15.35$.

Figure 4.5 shows a graphical comparison of Henry's law, Equation (4.32), and the Frumkin equation (4.61). We define a relative error according to

$$\epsilon = \left[\frac{\left(\mathrm{Ca}^{-1}\right)_{\mathrm{Henry}}}{\left(\mathrm{Ca}^{-1}\right)_{\mathrm{Frumkin}}} - 1\right] \times 100\%, \tag{4.63}$$

which exceeds a value of about 1% for $\Gamma^* > 0.25$. Within the region of detachment, from Figure 4.2, we find that at $c_b = 0.9$ mol m^{-3} $\mathrm{C_{16}TAB}$ and $\mathrm{Re} = 1950$, $\Gamma^* \leqslant 0.15$, which corresponds to a maximum error $\epsilon \approx 0.35\%$. Henry's law thus describes the dependence of the surface tension parameter, Ca^{-1}, on the surface concentration, Γ^*, with sufficient accuracy in the region of detachment and for some distance outside this region.

4.3 Coupled Mass-Transfer Problem in the Presence of Micelles

If we add surfactant to the solvent to give a concentration above some critical value, the excess can form a second dissolved species—micelles, which are aggregates containing many surfactant monomers. These aggregates can have a variety of shapes, including spheres and rods. The bulk concentration at which micelles are formed is the critical micellar concentration (cmc). Micelles formed in an aqueous solvent are composed of monomers oriented so that their hydrophobic parts are on the inside, with their hydrophilic groups on the outside and in contact with the water phase. Because the surface of the micelle is uniformly hydrophilic in character, micelles have no tendency to accumulate at the vapour/liquid interface. However, if the interface is swept by a fluid motion, which reduces the concentration of adsorbed monomer in the diffusion boundary layer adjacent to the surface, the equilibrium between monomer and micelle concentration is also disturbed. Both micelles and monomers will diffuse towards the surface, and the micelles will break down to supply monomer.

Above the cmc, we can therefore expect that the dynamic surface tension will depend on both the rate of diffusion of monomers and micelles to the surface, and the rate at which micelles break down, as well as on the rate of surface refreshment.

In what follows, we have adapted a theory of infinitely fast micellar breakdown that was originally developed to describe the adsorption of surfactant from micellar solutions in the centre of an overflowing cylinder [210].

4.3.1 Infinitely Fast Micellar Break-Down

We assume that all the surfactant present in excess of the cmc is in the form of micelles, and we further assume that only one micellar species is present that has the mean aggregation number N. The concentration of monomers in the bulk is taken to be that at the cmc. Additionally, we assume that the equilibrium between monomers and micelles is instantaneous, so that the monomer concentration can only fall below the value at the cmc when there are no micelles present. There is thus a layer, of dimensionless thickness $h^* = h/R_0$, in which monomers diffusing to the surface are found, but no micelles. The

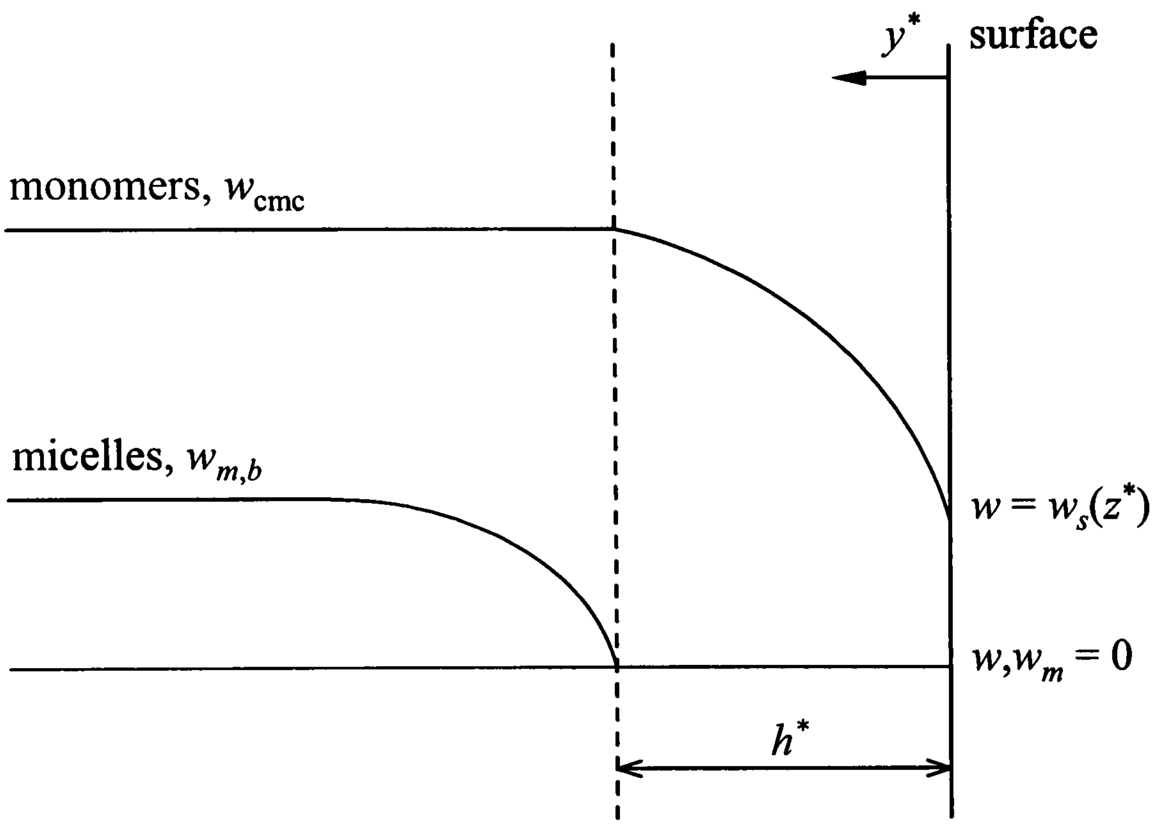

Figure 4.6: Concentration profiles of micelles and monomers adjacent to the surface for the case of infinitely fast micellar break down.

concentration profiles in the diffusion boundary layer adjacent to the surface are shown in Figure 4.6.

Both the monomer and micelle profiles have a finite slope at the edge of the monomer boundary layer, $y^* = h^*$, since at this plane, the micelles are converted into monomers. The dimensionless diffusion mass fluxes of monomers and micelles, q^*_{diff} and $q^*_{m,diff}$, respectively, at $y^* = h^*$, are related by

$$q^*_{m,diff}\Big|_{y^*=h^*} = \frac{D}{D_m}\, q^*_{diff}\Big|_{y^*=h^*}, \tag{4.64}$$

in which

$$q^*_{diff}\Big|_{y^*=h^*} = \left(\frac{\partial w}{\partial y^*}\right)_{y^*=h^*}, \tag{4.65}$$

and

$$q^*_{m,diff}\Big|_{y^*=h^*} = \left(\frac{\partial w_m}{\partial y^*}\right)_{y^*=h^*}. \tag{4.66}$$

Since $D/D_m > 1$, we have that $(\partial w_m/\partial y^*)_{y^*=h^*} > (\partial w/\partial y^*)_{y^*=h^*}$, which is indicated in Figure 4.6. Expressions for the concentration gradients $(\partial w/\partial y^*)_{y^*=h^*}$ and $(\partial w_m/\partial y^*)_{y^*=h^*}$ are obtained from the solution of the respective convection-diffusion equation.

The diffusion boundary layers are much thinner than the hydrodynamic boundary layer, so that we can assume that the velocity parallel to the surface is constant throughout the region in which micelle and monomer concentration are changing and is given by $y^* f'(z^*)$, where $f'(z^*) = du_s^*/dz^*$ is the rate of surface expansion. The convection-diffusion equation for the monomers, neglecting axial convection and diffusion, is given by

$$\frac{\partial^2 w}{\partial y^{*2}} + \frac{\mathrm{Re}}{2} \mathrm{Sc}\, y^* f'(z^*) \frac{\partial w}{\partial y^*} = 0 \tag{4.67}$$

and is identical with Equation (4.24). The general solution is derived in Appendix A. The boundary conditions in the presence of micelles are that $w = w_s(z^*)$ at $y^* = 0$, and $w = w_{\mathrm{cmc}}$ at $y^* = h^*$ (see Figure 4.6). With these boundary conditions, we obtain the solution

$$\frac{w - w_s(z^*)}{w_{\mathrm{cmc}} - w_s(z^*)} = \frac{\mathrm{erf}\left\{y^* \sqrt{\frac{\mathrm{Re}}{4} \mathrm{Sc}\, f'(z^*)}\right\}}{\mathrm{erf}\left\{h^* \sqrt{\frac{\mathrm{Re}}{4} \mathrm{Sc}\, f'(z^*)}\right\}}. \tag{4.68}$$

Using Equation (4.68), we can calculate the mass flux of monomers to the surface at $y^* = h^*$,

$$\begin{aligned} q^*_{\mathit{diff}}\Big|_{y^*=h^*} &= \left(\frac{\partial w}{\partial y^*}\right)_{y^*=h^*} \\ &= (w_{\mathrm{cmc}} - w_s) \sqrt{\frac{\mathrm{Re}}{\pi} \mathrm{Sc}\, f'(z^*)} \frac{\exp\left\{-h^{*2} \frac{\mathrm{Re}}{4} \mathrm{Sc}\, f'(z^*)\right\}}{\mathrm{erf}\left\{h^* \sqrt{\frac{\mathrm{Re}}{4} \mathrm{Sc}\, f'(z^*)}\right\}}. \end{aligned} \tag{4.69}$$

Similarly, we obtain for the mass flux of monomers at the surface ($y^* = 0$)

$$q^*_{\mathit{diff}}\Big|_{y^*=0} = \left(\frac{\partial w}{\partial y^*}\right)_{y^*=0} = (w_{\mathrm{cmc}} - w_s) \frac{\sqrt{\frac{\mathrm{Re}}{\pi} \mathrm{Sc}\, f'(z^*)}}{\mathrm{erf}\left\{h^* \sqrt{\frac{\mathrm{Re}}{4} \mathrm{Sc}\, f'(z^*)}\right\}}. \tag{4.70}$$

The error function in Equation (4.70) takes on values between 1 and 0, and a comparison of Equation (4.70) with Equation (4.27) shows that the presence of micelles enhances the flux of monomers to the surface.

The convection-diffusion equation for the micelles, again neglecting axial convection and diffusion, reads

$$\frac{\partial^2 w_m}{\partial y^{*2}} + \frac{\mathrm{Re}}{2} \mathrm{Sc}_m\, y^* f'(z^*) \frac{\partial w_m}{\partial y^*} = 0, \tag{4.71}$$

where the subscript m denotes the micellar species. The general solution of this equation is identical with that for the monomer equation and is given in Appendix A. Assuming infinitely fast micellar break-down, the boundary conditions are that $w_m = 0$ at $y^* = h^*$, and $w_m = w_{m,b}$ as $y^* \to \infty$ (see Figure 4.6), and we obtain the solution

$$\frac{w_m}{w_{m,b}} = 1 - \frac{\operatorname{erfc}\left\{y^* \sqrt{\frac{\mathrm{Re}}{4} \mathrm{Sc}_m f'(z^*)}\right\}}{\operatorname{erfc}\left\{h^* \sqrt{\frac{\mathrm{Re}}{4} \mathrm{Sc}_m f'(z^*)}\right\}}. \tag{4.72}$$

The mass flux of micelles to the surface at $y^* = h^*$ is given by

$$\begin{aligned} q^*_{m,diff}\Big|_{y^*=h^*} &= \left(\frac{\partial w_m}{\partial y^*}\right)_{y^*=h^*} \\ &= w_{m,b}\sqrt{\frac{\mathrm{Re}}{\pi}\mathrm{Sc}_m f'(z^*)}\frac{\exp\left\{-h^{*2}\frac{\mathrm{Re}}{4}\mathrm{Sc}_m f'(z^*)\right\}}{\operatorname{erfc}\left\{h^*\sqrt{\frac{\mathrm{Re}}{4}\mathrm{Sc}_m f'(z^*)}\right\}}. \end{aligned} \tag{4.73}$$

The concentration of micelles in the bulk, $w_{m,b}$, can be found from a mass balance of the whole surfactant inventory. In molar concentrations, we have

$$c_T = c_{\mathrm{cmc}} + N c_{m,b}, \tag{4.74}$$

where c_T is the total concentration of surfactant molecules, and N is the mean aggregation number of the micellar species. The molar concentration of micelles in the bulk, $c_{m,b}$, is given as

$$c_{m,b} = \frac{\rho}{NM} w_{m,b}. \tag{4.75}$$

Combining Equations (4.74) and (4.75) gives

$$w_{m,b} = \frac{M}{\rho}\left(c_T - c_{\mathrm{cmc}}\right) = w_T - w_{\mathrm{cmc}} \tag{4.76}$$

for the mass fraction of micelles in the bulk solution.

At the dividing plane $y^* = h^*$, the mass fluxes of monomers and micelles, q^*_{diff} and $q^*_{m,diff}$, are related by Equation (4.64). With Equations (4.69) and (4.73) for the mass fluxes of monomers and micelles, respectively, we obtain

$$W = \sqrt{\frac{\mathrm{Sc}_m}{\mathrm{Sc}}} \frac{\exp\left\{-\Psi^2\right\}}{\operatorname{erf}\left\{\Psi\right\}} \frac{\operatorname{erfc}\left\{\Psi\sqrt{\frac{\mathrm{Sc}_m}{\mathrm{Sc}}}\right\}}{\exp\left\{-\Psi^2\frac{\mathrm{Sc}_m}{\mathrm{Sc}}\right\}}, \tag{4.77}$$

where

$$W = \frac{w_T - w_{\mathrm{cmc}}}{w_{\mathrm{cmc}} - w_s(z^*)}, \tag{4.78}$$

and

$$\Psi = h^* \sqrt{\frac{\mathrm{Re}}{4} \mathrm{Sc}\, f'(z^*)}. \tag{4.79}$$

We have thus found a relationship that describes the dependence of the monomer concentration at the surface, in the form of a normalised concentration W, on the ratio of the diffusivities of micelles and monomers, $\mathrm{Sc}_m \,/\, \mathrm{Sc}$, and a parameter Ψ that contains the position of the dividing plane h^* and the surface expansion rate $f'(z^*)$. We use Equation (4.77) in Section 4.3.3 to find an estimate for Γ_0^* in the presence of micelles.

4.3.2 Effective Diffusivity and Pseudo-Diffusivity

The enhancing effect of the presence of micelles on the diffusion flux of monomers to the surface, as shown in Equation (4.70), can be regarded in one of two ways—through an effective diffusivity or through a pseudo-diffusivity.

Effective Diffusivity

If we assume that the driving force for the diffusion of monomers to the surface is $w_{\mathrm{cmc}} - w_s$, we can express the diffusion flux of monomers through a Schmidt number based on an effective diffusivity, $\mathrm{Sc}_{\mathit{eff}}$,

$$q^*_{\mathit{diff}}\Big|_{y^*=0} = (w_{\mathrm{cmc}} - w_s) \sqrt{\frac{\mathrm{Re}}{\pi} \mathrm{Sc}_{\mathit{eff}}\, f'(z^*)}. \tag{4.80}$$

Comparison of Equation (4.80) with (4.70) gives

$$\sqrt{\frac{\mathrm{Sc}}{\mathrm{Sc}_{\mathit{eff}}}} = \sqrt{\frac{D_{\mathit{eff}}}{D}} = \operatorname{erf}\{\Psi\}. \tag{4.81}$$

The error function dictates that $\mathrm{Sc} \,/\, \mathrm{Sc}_{\mathit{eff}} \leqslant 1$, so that the value of the effective diffusivity is greater than the value of the monomer diffusivity.

Pseudo-Diffusivity

We now compare the flux of monomers to the surface, Equation (4.70), with a pseudo-flux under the presumption that all surfactant were present as monomers.

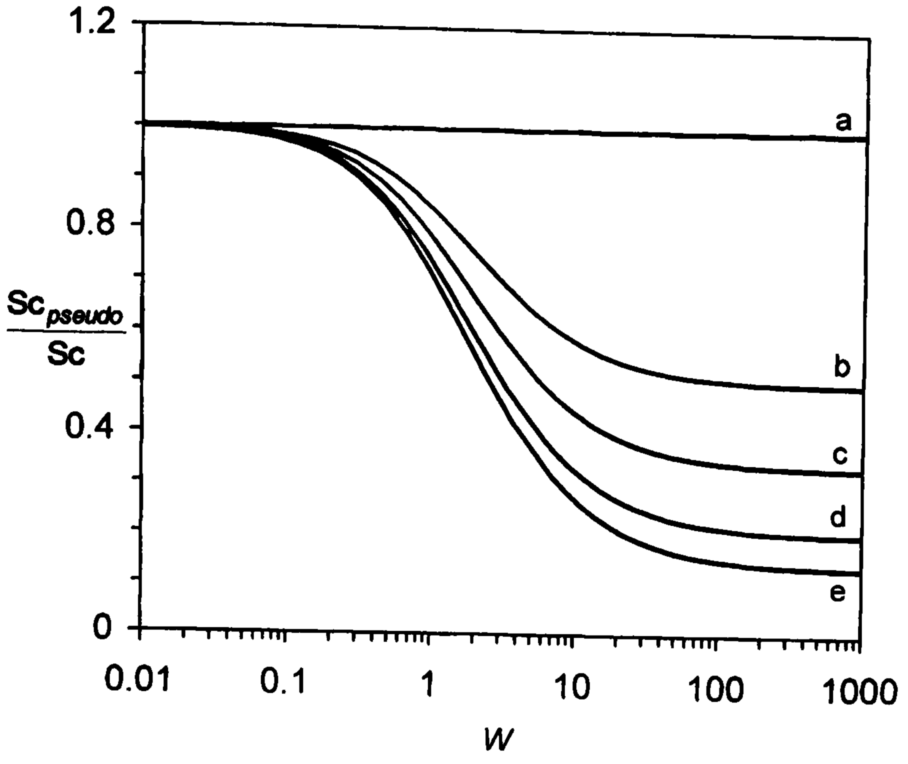

Figure 4.7: Schmidt number based on a pseudo-diffusivity, Sc_{pseudo}, as a function of the normalised concentration, W, according to Equation (4.83) for a total concentration of $c_T = 1.25$ mol m^{-3} $\mathrm{C_{16}TAB}$ and varying ratios of Sc_m / Sc = 1.0 (a), 2.0 (b), 3.0 (c), 5.0 (d), and 7.5 (e).

The monomers would then diffuse to the surface with a pseudo-diffusivity, defined by Sc_{pseudo}, and the concentration difference that drives the mass transfer would be $w_T - w_s$. We then have the flux

$$q^*_{diff}\Big|_{y^*=0} = (w_T - w_s)\sqrt{\frac{\mathrm{Re}}{\pi}\,\mathrm{Sc}_{pseudo}}\,f'(z^*). \tag{4.82}$$

We compare the flux given by Equation (4.82) with the flux given by Equation (4.70) and obtain

$$\sqrt{\frac{\mathrm{Sc}}{\mathrm{Sc}_{pseudo}}} = \sqrt{\frac{D_{pseudo}}{D}} = (1+W)\,\mathrm{erf}\,\{\Psi\}. \tag{4.83}$$

The ratio Sc_{pseudo} / Sc is plotted in Figure 4.7 for a total concentration of c_T = 1.25 mol m^{-3} ($w_T = 455.625 \times 10^{-6}$) $\mathrm{C_{16}TAB}$, which has a critical micellar concentration of $c_{\mathrm{cmc}} = 0.92$ mol m^{-3} ($w_{\mathrm{cmc}} = 335.34 \times 10^{-6}$), and varying diffusivity ratios Sc_m / Sc. We see from Figure 4.7 that Sc_{pseudo} / Sc $\leqslant 1$, so that the value of the pseudo-diffusivity is smaller than the monomer diffusivity.

4.3.3 Estimation of Γ_0^* in the Presence of Micelles

As before in the absence of micelles, we determine Γ_0^* from the matching of the solutions for Γ^* in the downstream region and in the region of detachment, and from a mass balance around the surface at the point of detachment. To a first approximation, we assume that Henry's law suffices to describe the link between surface tension and surface concentration, and we neglect the sub-surface concentration in the downstream solution for Γ^*. Although this assumption is likely to be invalid at a monomer bulk concentration that equals the cmc, it enables us to obtain an estimate for Γ_0^* in the presence of micelles. In the mass balance around the surface at the point of detachment, however, we account for the sub-surface concentration at that point, given as $w_{s,0}$. Furthermore, we assume that the surfactant in the bulk liquid consists entirely of surfactant monomers, and we thus balance the flux given by Equation (4.82). The result of this procedure is

$$\Gamma_0^* = 0.0462 \left\{ \mathrm{E} \left(\frac{\rho D}{M \bar{u}_0 \Gamma_{sat}} \right)^3 \right\}^{1/2} \mathrm{Re}\, \mathrm{Sc}_{pseudo}^{3/4} \left(w_T - w_{s,0} \right)^{3/2}, \tag{4.84}$$

where Sc_{pseudo} is defined in Equation (4.83), and $w_T - w_{s,0}$ is the driving concentration force of the diffusion of surfactant to the surface at $z^* = 0$, w_T being the total concentration, as defined in Equation (4.76).

Using Langmuir's equilibrium isotherm, we can replace $w_{s,0}$ with

$$w_{s,0} = \frac{k^* \Gamma_0^*}{(1 - \Gamma_0^*)}. \tag{4.85}$$

At the point of detachment, from Equation (4.83), Sc_{pseudo} is given as

$$\mathrm{Sc}_{pseudo} = \frac{\mathrm{Sc}}{\left[(1 + W_0) \operatorname{erf}\{\Psi_0\} \right]^2}, \tag{4.86}$$

where

$$W_0 = \frac{w_T - w_{\mathrm{cmc}}}{w_{\mathrm{cmc}} - w_{s,0}}, \tag{4.87}$$

and

$$\Psi_0 = h_0^* \sqrt{\frac{\mathrm{Re}}{4}\, \mathrm{Sc}\, f'(z^* = 0)}. \tag{4.88}$$

Equation (4.84) becomes implicit in Γ_0^* if we substitute for $w_{s,0}$, W_0, and Sc_{pseudo} and must be solved iteratively. It is plotted in Figure 4.8 for different total molar concentrations, c_T, of C_{16}TAB at a Reynolds number of $\mathrm{Re} = 1950$, given

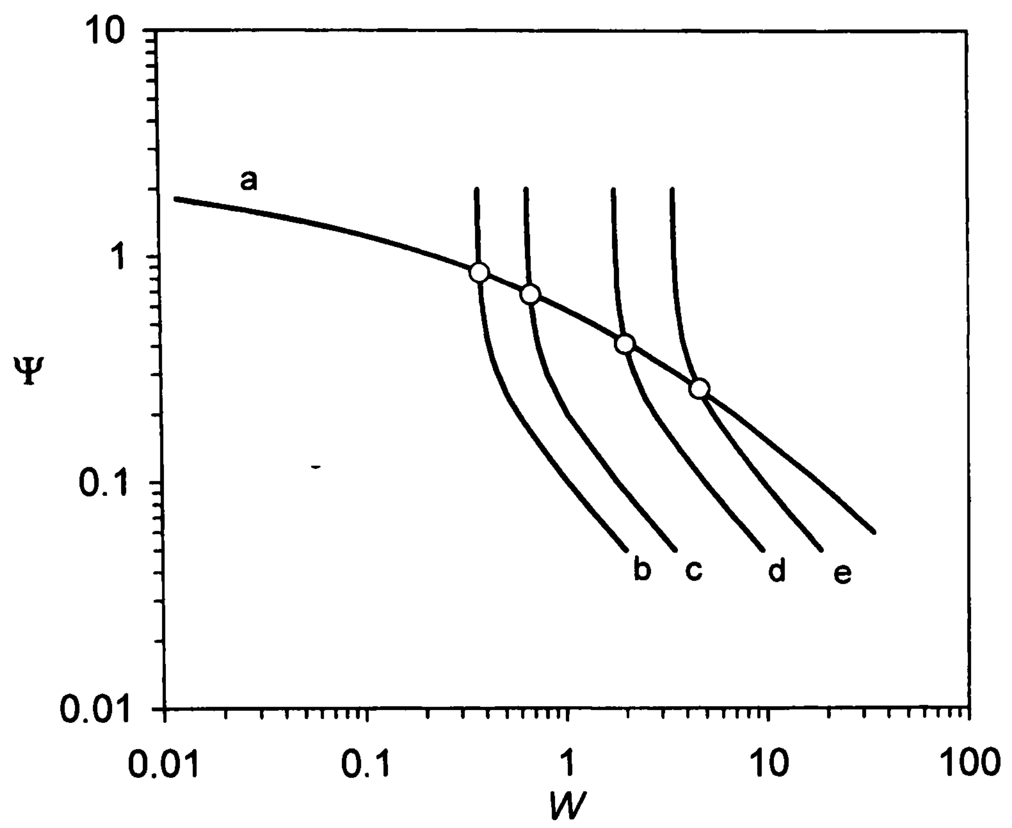

Figure 4.8: Dimensionless parameter Ψ_0 as a function of the normalised concentration W_0 at Re = 1950 according to Equation (4.84). The graphs are for $c_T = 1.25$ mol m^{-3} (b), 1.5 mol m^{-3} (c), 2.5 mol m^{-3} (d), and 4.0 mol m^{-3} (e) C_{16}TAB. Curve (a) is given by Equation (4.77) for $\mathrm{Sc}_m / \mathrm{Sc} = 7.5$.

by curves (b) to (e). Equation (4.77) is also plotted in Figure 4.8, given by curve (a). The intersection of the graphs from Equation (4.84) with the graph from Equation (4.77) provides us with the value pairs for Γ_0^* (through W_0) and Ψ_0 at the various total concentrations w_T. The values for Γ_0^* are used in the hybrid CFD model when micelles are present (see Section 6.3).

Chapter 5

Surfactant Adsorption in the Jet: CFD Model

5.1 General Outline of the Model

The governing field equations for the fluid mechanics (conservation of momentum and continuity) and the mass transfer (conservation of mass for each species) lie at the heart of the CFD model (see diagram in Figure 5.1). The fluid mechanics are computed as outlined in Chapter 3, with the exception that the tangential shear stress boundary condition on the surface will now become active due to variations in surface tension caused by the adsorption of surfactant. Up to two surfactant species (surface-active monomers and surface-inactive micelles) will be considered, each of which must be taken care of by separate conservation equations.

5.1.1 Monomer Branch

Surfactant monomers are transported to the surface of the jet through diffusion and convection from the bulk. In the liquid jet, diffusion is the main mechanism that is responsible for the delivery of surfactant molecules to the surface. This diffusive flux towards the jet surface is balanced by convection within the surface, which is determined by the rate of surface expansion. On the assumption of local equilibrium at the surface, the sub-surface concentration and surface concentration may be related by an appropriate adsorption isotherm. Surface concentration and surface tension are linked by a thermodynamical equilibrium

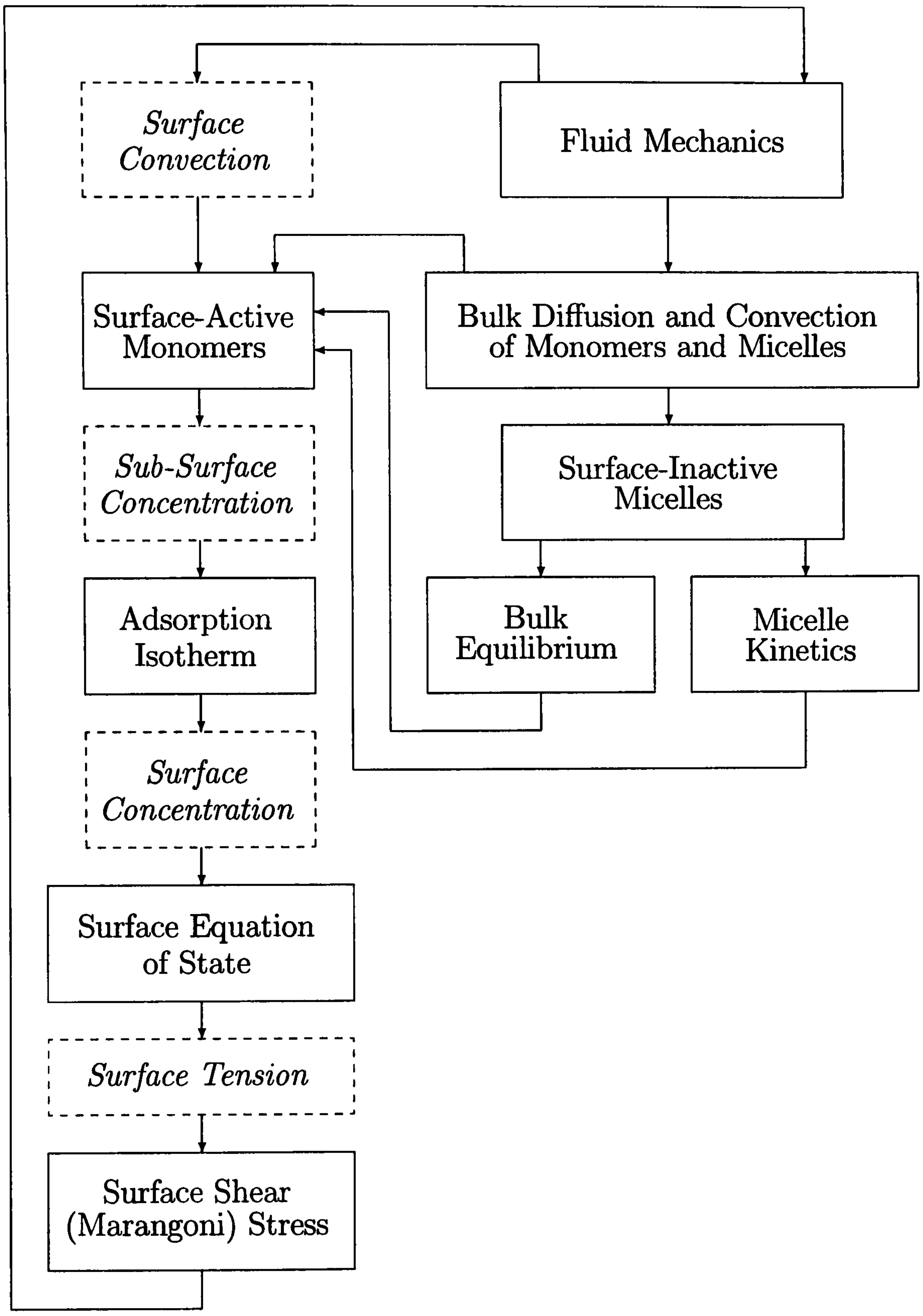

Figure 5.1: General outline of the CFD model of diffusion-controlled surfactant adsorption in the jet.

expression, where the small contribution of the diffusion layer to the dynamic surface tension has been neglected. Finally, the tangential surface shear stress (Marangoni stress), which results from local variations in surface tension, balances viscous traction underneath the surface, and couples mass transfer and fluid mechanics.

5.1.2 Micelle Branch

Micelles, which are considered surface-inactive, do not adsorb at the surface. In the bulk, micelles and monomers are in equilibrium. This equilibrium is disturbed near the surface, where monomers adsorb as a consequence of the surface expansion. Micelles then disintegrate to supply monomers. The process of micelle disintegration is described using kinetic relations.

5.2 Bulk Diffusion and Convection of Monomers and Micelles

The convection-diffusion equation describes the transport of surfactant species from the core of the jet towards the free surface. In cylindrical coordinates (r, z), this conservation equation for a surfactant species that is transported in the fluid under steady-state flow conditions is given in FIDAP as

$$\rho\left(v\frac{\partial w}{\partial r}+u\frac{\partial w}{\partial z}\right)=\rho D\left(\frac{1}{r}\frac{\partial}{\partial r}\left(r\frac{\partial w}{\partial r}\right)+\frac{\partial^2 w}{\partial z^2}\right)+s, \qquad (5.1)$$

where ρ is the density of the jet fluid, D is the coefficient of diffusivity of the surfactant species in water, and s is a general source/sink term, which has the units [kg/(m^3 s)]. The axial velocity component of the jet flow is denoted by u, and v represents the radial velocity component. We also note that the convection-diffusion equation in FIDAP is given in terms of the mass fraction of the surfactant species, w, which is defined as

$$w=\frac{M}{\rho}c, \qquad (5.2)$$

where c is the molar concentration and M is the molecular weight of the surfactant species.

Introducing the dimensionless variables defined in Equation (3.6) into Equation (5.1) results in

$$\frac{\rho\bar{u}_0}{R_0}\left(v^*\frac{\partial w}{\partial r^*}+u^*\frac{\partial w}{\partial z^*}\right)=\frac{\rho D}{R_0^2}\left(\frac{1}{r^*}\frac{\partial}{\partial r^*}\left(r^*\frac{\partial w}{\partial r^*}\right)+\frac{\partial^2 w}{\partial z^{*2}}\right)+s, \tag{5.3}$$

where $\bar{u}_0$ is the mean nozzle exit velocity, and R_0 is the nozzle radius as before.[21] We non-dimensionalise the source term using

$$s=\frac{\rho D}{R_0^2}s^*, \tag{5.4}$$

which leads to

$$\frac{\rho\bar{u}_0}{R_0}\left(v^*\frac{\partial w}{\partial r^*}+u^*\frac{\partial w}{\partial z^*}\right)=\frac{\rho D}{R_0^2}\left(\frac{1}{r^*}\frac{\partial}{\partial r^*}\left(r^*\frac{\partial w}{\partial r^*}\right)+\frac{\partial^2 w_i}{\partial z^{*2}}\right)+\frac{\rho D}{R_0^2}s^*. \tag{5.5}$$

Multiplication with $R_0^2/(\rho D)$ gives

$$\frac{R_0\bar{u}_0}{D}\left(v^*\frac{\partial w}{\partial r^*}+u^*\frac{\partial w}{\partial z^*}\right)=\left(\frac{1}{r^*}\frac{\partial}{\partial r^*}\left(r^*\frac{\partial w}{\partial r^*}\right)+\frac{\partial^2 w}{\partial z^{*2}}\right)+s^*, \tag{5.6}$$

where

$$\frac{R_0\bar{u}_0}{D}=\frac{R_0\bar{u}_0\rho}{\mu}\frac{\mu}{\rho D}=\frac{\mathrm{Re}}{2}\mathrm{Sc}. \tag{5.7}$$

The convection-diffusion equation for surfactant monomers may then be written in its final dimensionless form, namely

$$\frac{\mathrm{Re}}{2}\mathrm{Sc}\left(v^*\frac{\partial w}{\partial r^*}+u^*\frac{\partial w}{\partial z^*}\right)=\left(\frac{1}{r^*}\frac{\partial}{\partial r^*}\left(r^*\frac{\partial w}{\partial r^*}\right)+\frac{\partial^2 w}{\partial z^{*2}}\right)+s^*. \tag{5.8}$$

The corresponding governing field equation for the micelles, which are denoted by the subscript m, reads

$$\frac{\mathrm{Re}}{2}\mathrm{Sc}\left(v^*\frac{\partial w_m}{\partial r^*}+u^*\frac{\partial w_m}{\partial z^*}\right)=\frac{D_m}{D}\left(\frac{1}{r^*}\frac{\partial}{\partial r^*}\left(r^*\frac{\partial w_m}{\partial r^*}\right)+\frac{\partial^2 w_m}{\partial z^{*2}}\right)+s_m^*, \tag{5.9}$$

where

$$w_m=\frac{NM}{\rho}c_m, \tag{5.10}$$

in which N is the mean aggregation number of the micelles, and

$$s_m=\frac{\rho D}{R_0^2}s_m^*. \tag{5.11}$$

---

[21] Note that the mass fraction w is already dimensionless, and we thus do not need to apply scaling to it.

The dimensionless source term s_m^* is defined using the diffusivity of the surfactant monomers, which has been selected as the reference value. Both source terms, s^* and s_m^*, for which we derive expressions in Section 5.7, are zero if only surfactant monomers are present, at bulk concentrations below the critical micellar concentration (cmc). We then solely consider the convection-diffusion equation for the surfactant monomers.

We note here that the product of Reynolds number and Schmidt number is also known as the Péclet number, Pe, which is defined as

$$\mathrm{Pe} \equiv \frac{R_0 \overline{u}_0}{D} = \frac{\mathrm{Re}}{2}\mathrm{Sc} = \frac{\text{mass transfer by convection}}{\text{mass transfer by diffusion}}. \tag{5.12}$$

5.3 Computational Domain and Meshing

The added complexity that arises from the coupled mass transfer problem requires reconsideration of the meshing. The discretisation of the computational domain must allow for the accurate computation of both the velocity field and the concentration field. Their respective boundary layers determine the density of the mesh in the critical regions—underneath the surface in the radial direction, and at the nozzle exit in the axial direction.

In the radial direction, the hydrodynamic and diffusion boundary layers, ε and ε_c, start to grow at the point of detachment. The two boundary layers are related through

$$\frac{\varepsilon_c}{\varepsilon} \sim \sqrt{\frac{\rho D}{\mu}} = \frac{1}{\sqrt{\mathrm{Sc}}}. \tag{5.13}$$

For an aqueous surfactant solution of $\mathrm{C_{16}TAB}$, we find that $\varepsilon_c/\varepsilon \sim \mathcal{O}(10^{-2})$. The thickness of the diffusion boundary layer is given by

$$\varepsilon_c \sim \sqrt{\frac{D}{du_s/dz}}. \tag{5.14}$$

For $\mathrm{C_{16}TAB}$ we can estimate ε_c to be $\mathcal{O}(1\ \mu\mathrm{m})$. The density of the mesh underneath the free surface boundary must reflect the smallness of the diffusion boundary layer to accurately compute the concentration field. It is evident that the mesh used in the computation of the flow field (see Figures 3.3 and 3.4 in Section 3.3) is not able to meet this requirement. We must thus use a mesh with a much higher mesh density underneath the surface, which also requires

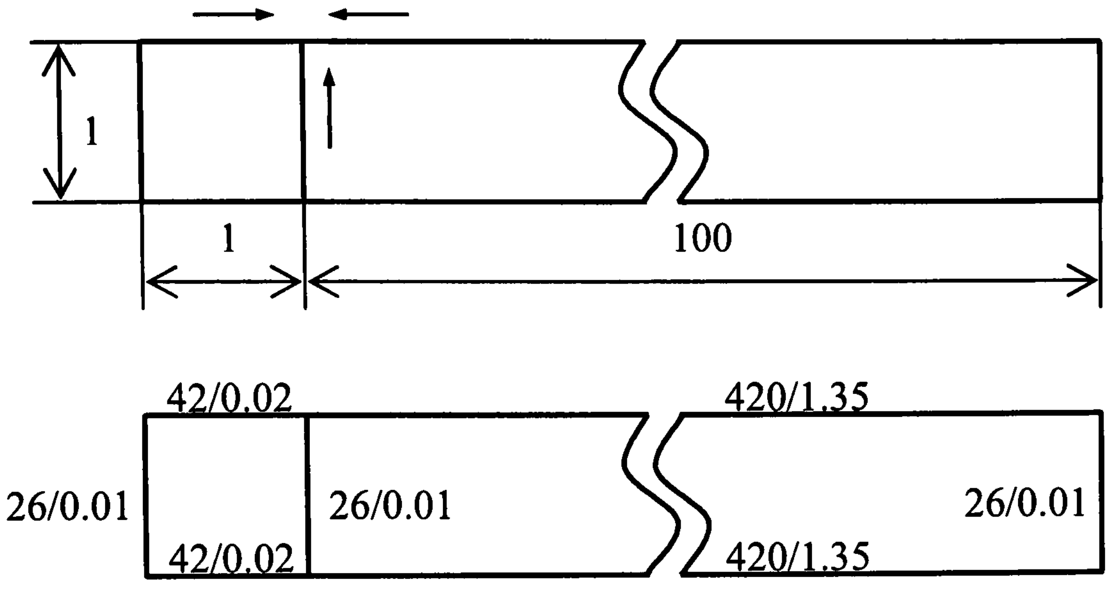

Figure 5.2: Dimensions of the computational jet flow domain (upper sketch) and grading of the mesh (lower sketch) in the presence of surfactant.

the mesh to be denser in the axial direction to give an element aspect ratio that ensures convergence of the numerical computation. As before, sufficient mesh density is particularly important in the region near the nozzle exit where the gradients of both the velocity field and the concentration field in the radial and axial direction are steepest.

In order to keep the size of the mesh (the number of elements within the computational domain) to a minimum, and hence the computation time and memory required to carry out the computation, the extension of the computational domain in the axial direction had to be reduced. We remember that the mesh configuration that was used in the computation of the flow field of the pure water jet has a length of 200 × R_0 for the free jet section, and a length of 3 × R_0 for the nozzle section. It was found possible to reduce the length of the free jet section to 100 × R_0 and the length of the nozzle section to one nozzle radius, without compromising the safe applicability of the boundary conditions at the inlet and the outlet of the computational domain (see upper sketch in Figure 5.2). This reduction in length greatly assisted in keeping the numerical size of the jet to a minimum.

To control the density of the mesh underneath the surface, the distance between the free-surface boundary and the first full row of mesh nodes was set to a value of 5×10^{-5} in the dimensionless coordinate system. A growth factor, which represents the ratio of the distance between the free-surface boundary and the first full row of nodes, and the distance between the second full row of nodes and the first full row of nodes, was set to a value of 1.4. Applying the growth factor to 7 full rows of mesh nodes resulted in a boundary-layer depth of about 1.2×10^{-3} in the dimensionless coordinate system. The GAMBIT journal file that creates this dense mesh is given in Appendix B.3.

In order to create a smooth transition in the mesh from the densely packed rows of nodes in the boundary layer to the much wider spacing of the rows of nodes in the bulk of the computational domain, we have used an exponential formula to determine the interval length ratios,

$$\mathcal{P} = \exp\left\{\frac{\mathcal{L}}{d}\left(x - \frac{1}{2}\right)\right\}, \tag{5.15}$$

which defines the grading of the mesh. In Equation (5.15), $\mathcal{P}$ is the interval length ratio, $\mathcal{L}$ is the length of the edge or boundary, d is the number of intervals, and x is the grading parameter. The lower sketch in Figure 5.2 shows the number of intervals along the edges and boundaries of the mesh. For example, the free-surface boundary, with a length of $\mathcal{L} = 100$, is divided into $d = 420$ intervals, the grading parameter being $x = 1.35$. In the radial direction, 26 intervals and a grading parameter of 0.01 were used. Note that the number of intervals in the radial direction is a total number, containing both the number of nodes in the bulk and in the boundary layer.

Figure 5.3 shows that the mesh immediately underneath the surface is indeed very dense. The distance from the row of surface nodes to the first row of nodes underneath the surface is only about 40 nm (for a nozzle radius of $R_0 = 0.79$ mm). The mesh consists of 12,012 elements in total, which resulted in average computation times of not more than 10 minutes for the water jet and not more than 30 minutes to 3 hours (depending on the convergence criterion set) if the hydrodynamics were solved along with the coupled mass transfer problem (no micelles present) on a Windows 2000 PC with 512 Mb RAM and a 1.0 GHz processor.

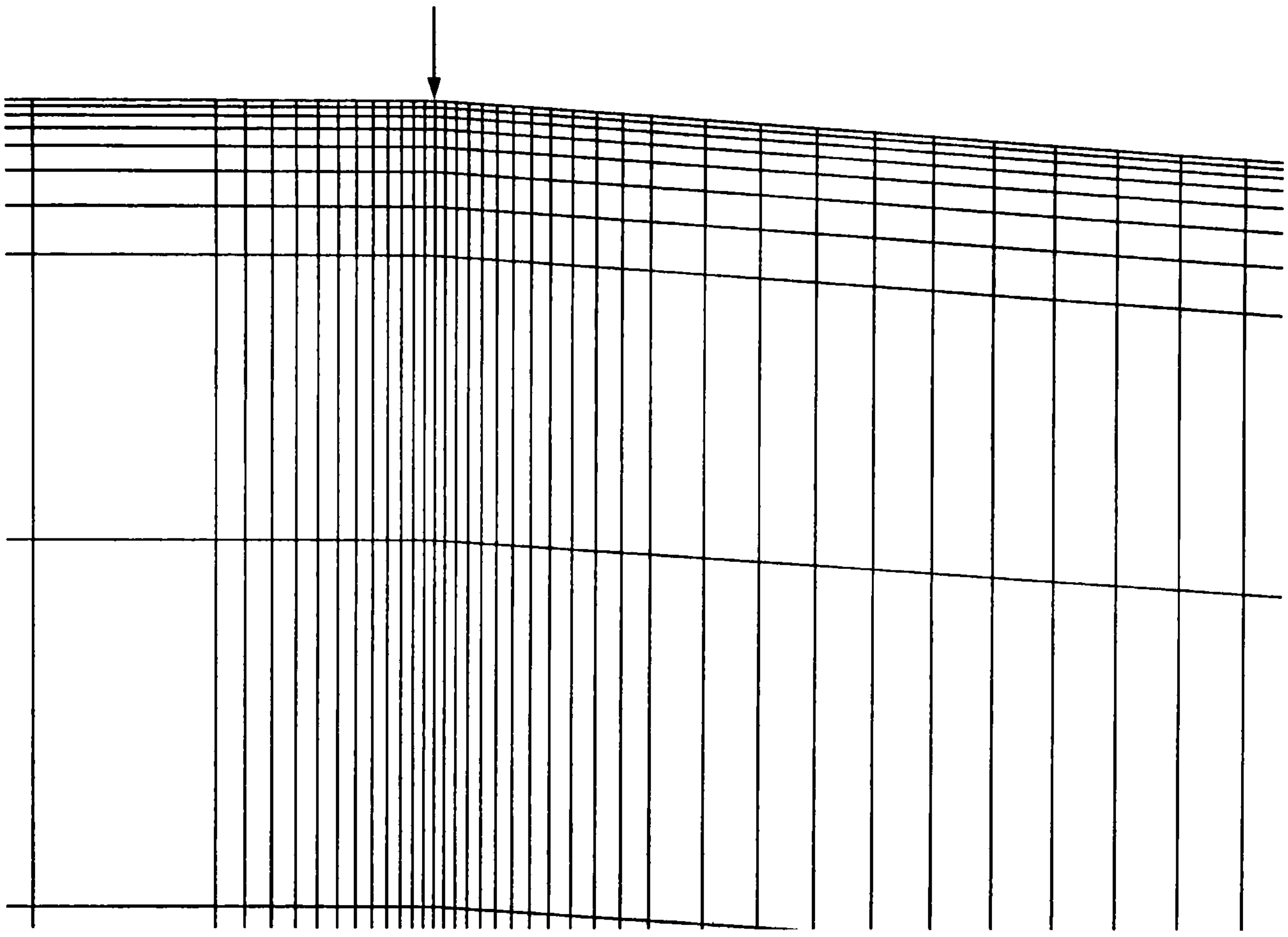

Figure 5.3: Regular mesh of the jet flow around the nozzle exit region after deformation. The section spans $\Delta z = 8.2$ μm in the axial direction and $\Delta r = 5.5$ μm in the radial direction around the nozzle exit at $r = R_0 = 0.79$ mm and $z = 0$ (marked by the arrow).

5.4 Boundary Conditions for the Monomers

5.4.1 Inlet of the Jet Flow Domain

At the inlet of the jet flow domain, sufficiently far upstream from the nozzle exit plane, bulk concentration, w_b, is assumed everywhere in the fluid, that is

$$w\left(r^*, z^* \ll 0\right) = w_b. \tag{5.16}$$

This boundary condition holds if no surfactant aggregates are present, which is only the case if the monomer bulk concentration is below the cmc. Above the cmc, w_b takes on the value at the cmc, w_{cmc}.

5.4.2 Nozzle Wall

The nozzle wall is made impenetrable for surfactant, and thus

$$\frac{1}{r^*}\frac{\partial}{\partial r^*}\left(r^* w\right)+\frac{\partial w}{\partial z^*}=0 \text{ at } r^*=1.0, z^*\leqslant 0. \tag{5.17}$$

5.4.3 Free Surface of the Jet

A flux boundary condition at the free surface of the jet allows the surface to take up surfactant from the bulk liquid. This flux boundary condition is

$$q^*_{diff}(r^*=R^*,z^*)=q^*_{conv}(r^*=R^*,z^*). \tag{5.18}$$

Hence, a diffusive mass flux that is directed along the outward unit normal of the free surface is prescribed on that boundary. This diffusive mass flux is given as

$$q^*_{diff}(r^*=R^*,z^*)=-\left(\frac{1}{r^*}\frac{\partial}{\partial r^*}\left(r^* w_s\right)+\frac{\partial w_s}{\partial z^*}\right), \tag{5.19}$$

where $w_s=w(r^*=R^*,z^*)$ is the sub-surface concentration. In Equation (5.19), the dimensionless diffusive mass flux is defined as $q^*_{diff}=\left(\rho D/R_0\right)^{-1} q_{diff}$. This diffusive mass flux, q^*_{diff}, of surfactant molecules is balanced by the rate of local redistribution by surface convection, $q^*_{conv}=\left(\rho D/R_0\right)^{-1} q_{conv}$, which can be written as

$$q^*_{conv}(r^*=R^*,z^*)\approx\frac{M\Gamma_{sat}\bar{u}_0}{\rho D}\frac{d}{dz^*}\left(\Gamma^* u^*_s\right). \tag{5.20}$$

In the high Reynolds number limit, the contraction of the jet is slight, which allowed us to simplify Equation (5.20). It is sufficient to consider the axial component of the tangential surface velocity, $u^*_t\approx u^*(r^*=R^*,z^*)=u^*_s(z^*)$, and we can then replace the surface gradient with the gradient in the axial direction, d/dz^*.

The surface coverage, Γ^*, in Equation (5.20) must be linked to the sub-surface concentration, w_s, to enable matching of diffusive and convective flux. Here, we assume diffusion-controlled surfactant adsorption, that is, each molecule that is being transported to the surface adsorbs immediately and diffusion is the rate-controlling transport step. Since we are neglecting electromigration, the location of the sub-surface layer is identical with the edge of the electrical double layer in the case of ionic surfactants. The double layer thickness is of the order of the Debye length, which is 10 nm for an ionic strength of 10^{-3}. Since the Debye length is less than the minimum mesh size, we assign the surface and sub-surface the same spatial location in the numerical simulations. Based on the assumption of local equilibrium everywhere along the jet surface, an equilibrium adsorption isotherm is used to link Γ^* and w_s. The simplest non-linear isotherm is the Langmuir isotherm [18], given as

$$\Gamma^* = \frac{\Gamma}{\Gamma_{sat}} = \frac{w_s}{(k^* + w_s)}, \tag{5.21}$$

where $k^* = Mk/\rho$ is the dimensionless Langmuir constant. Replacing Γ^* with Equation (5.21) in Equation (5.20) leads to the expression for the convective mass flux that is applied at the free surface of the jet. It reads

$$q^*_{conv}(r^* = R^*, z^*) = \frac{M\Gamma_{sat}\overline{u}_0}{D\rho\,(k^* + w_s)} \left[u^*_s \frac{dw_s}{dz^*} \left\{ \frac{k^*}{k^* + w_s} \right\} + w_s \frac{du^*_s}{dz^*} \right]. \tag{5.22}$$

Equation (5.22) provides the driving force for the transport of surfactant molecules (almost exclusively by diffusion) to the surface or, to be more precise, to the sub-surface. In our model, surface and sub-surface have been assigned the same spatial location, since the thickness of the sub-surface layer is only of molecular dimensions. Equation (5.22) is implemented into the CFD code FIDAP through a Fortran user-subroutine (see Appendix D.1). The derivatives, du^*_s/dz^* and dw_s/dz^*, within the user-subroutine are computed using fourth-order finite-difference approximations. Here, we have employed an algorithm published by Fornberg to compute the weights of the finite-difference approximations on arbitrarily spaced grids [211, 212]. This computing algorithm, which is built into the CFD code through a Fortran user-subroutine, is given in Appendix D.2.

In the CFD code FIDAP, by default, an applied flux that results in a net flow into the fluid would be specified as positive. When programming Equation (5.22) into the CFD code, we have therefore introduced a negative sign in the equation to account for the fact that the surfactant molecules diffuse towards the surface.

5.4.4 Downstream Position of the Jet Flow

In the absence of gravity, significantly far downstream from the nozzle exit plane, equilibrium conditions are reached at the surface, that is, $w_s\,(z^* \gg 0) \rightarrow w_b$. In the presence of gravity, however, the surface experiences constant expansion at the downstream position, and equilibrium conditions are never reached. Consequently, no constraints to the sub-surface concentration are applied at the outlet of the jet flow domain.

5.5 Equilibrium Thermodynamics

The surface tension, σ, is linked to the surface coverage, Γ, by means of the Frumkin equation,

$$\sigma - \sigma_w = \widehat{N}\mathcal{R}T\Gamma_{sat} \ln\left(1 - \frac{\Gamma}{\Gamma_{sat}}\right). \tag{5.23}$$

In Equation (5.23), σ_w is the surface tension of water, and $\widehat{N}$ accounts for possible ionic behaviour of surfactant molecules. Introducing Langmuir's adsorption isotherm, Equation (5.21), gives rise to the Szyszkowski equation,

$$\sigma - \sigma_w = \widehat{N}\mathcal{R}T\Gamma_{sat} \ln\left(1 - \frac{w_s}{k^* + w_s}\right). \tag{5.24}$$

The values for Γ_{sat} and k are determined by the surfactant system and can be found from a fit of Equation (5.24) to measured equilibrium surface tension data. The graphs in Figures 5.4 and 5.5 show such a fit for aqueous solutions of $C_{16}TAB$ and $C_{14}TAB$ ($\widehat{N} = 2$ and $T = 293$ K in both cases), respectively.[22] The values that were found for Γ_{sat} and k are displayed in Tables 6.2 and 6.7.

Multiplication of Equation (5.24) with $(\mu\overline{u}_0)^{-1}$ leads to

$$\frac{\sigma}{\mu\overline{u}_0} = \frac{\sigma_w}{\mu\overline{u}_0} + \frac{\widehat{N}\mathcal{R}T\Gamma_{sat}}{\mu\overline{u}_0} \ln\left(1 - \frac{w_s}{k^* + w_s}\right), \tag{5.25}$$

and the dimensionless relationship that links the surface tension parameter with the sub-surface concentration may be written as

$$\frac{1}{\mathrm{Ca}} = \frac{1}{\mathrm{Ca}_w} + \mathrm{E} \ln\left(1 - \frac{w_s}{k^* + w_s}\right). \tag{5.26}$$

The Marangoni number, Ma, appears in Equation (5.26) and is given as[23]

$$\mathrm{Ma} \equiv \frac{\sigma_w - \sigma}{\mu\overline{u}_0} = \left|\frac{1}{\mathrm{Ca}} - \frac{1}{\mathrm{Ca}_w}\right|. \tag{5.27}$$

The elasticity number, E, is defined in Equation (4.35).

The tangential stress boundary condition, Equation (3.44), becomes active when the surface tension parameter, $1/\mathrm{Ca}$, is not constant but varies along the

---

[22] The experimental data for both $C_{16}TAB$ and $C_{14}TAB$ were supplied by the research group of Dr. C.D. Bain of the Physical and Theoretical Chemistry Laboratory at Oxford University.

[23] Note that the Marangoni number given in Equation (5.27) is defined using the surface tension parameter of water, $1/\mathrm{Ca}_w$, which differs from the definition given in Equation (4.18), where the surface tension parameter at the point of detachment, $1/\mathrm{Ca}_0$, is used.

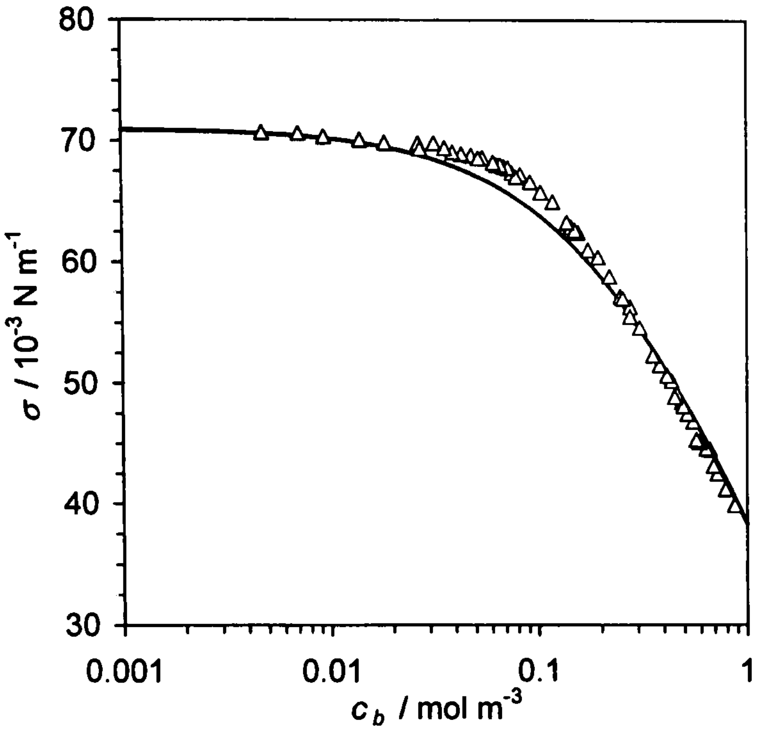

Figure 5.4: Measured equilibrium surface tension, σ, as a function of the bulk concentration, c_b, for aqueous $C_{16}TAB$ (c_{cmc} = 0.92 mol m^{-3}) at T = 293 K (open triangles). The solid line is a fit of the Szyszkowski equation to the experimental data.

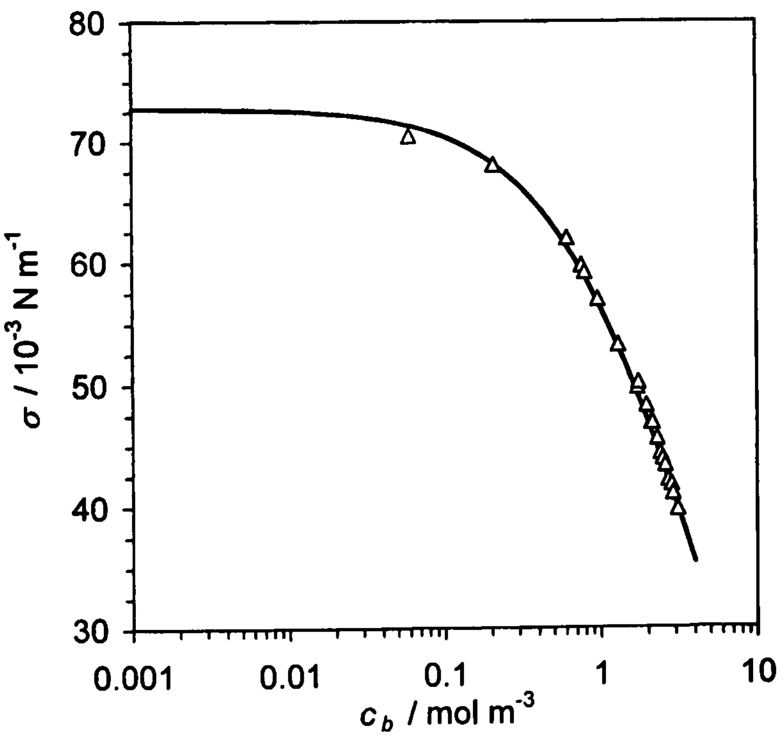

Figure 5.5: Measured equilibrium surface tension, σ, as a function of the bulk concentration, c_b, for aqueous $C_{14}TAB$ (c_{cmc} = 3.70 mol m^{-3}) at T = 293 K (open triangles). The solid line is a fit of the Szyszkowski equation to the experimental data.

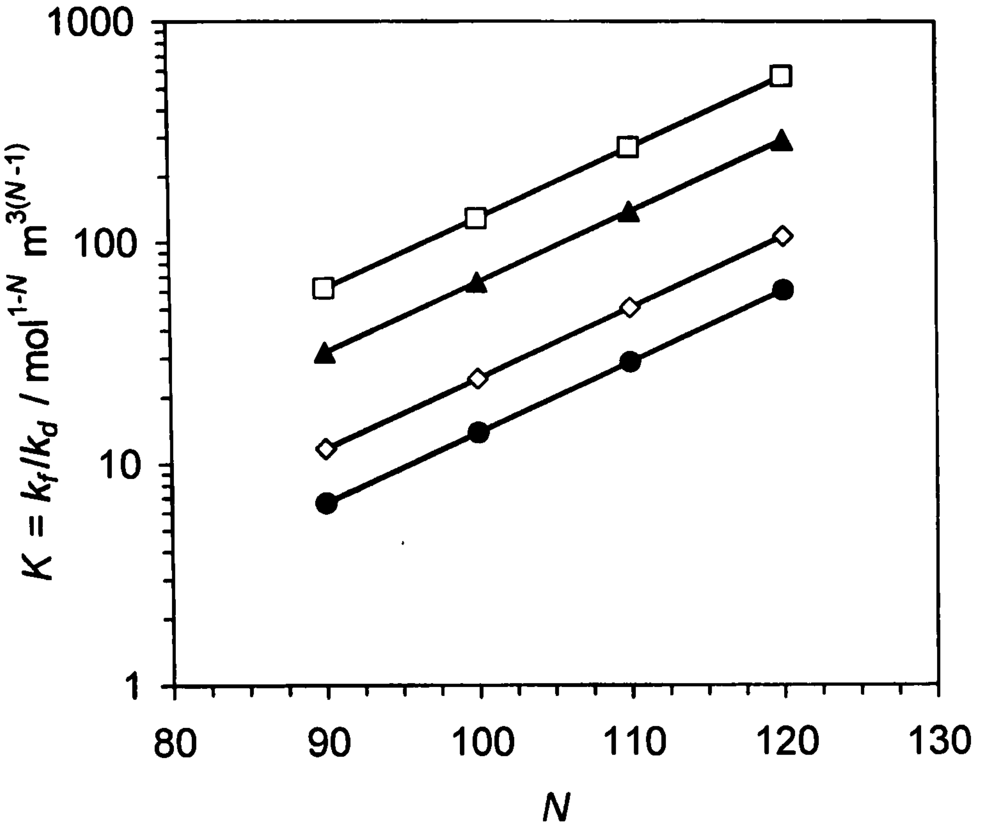

Figure 5.6: Equilibrium constant, K, according to Equation (5.30), as a function of the aggregation number, N, for varying total concentrations, c_T, of C_{16}TAB ($c_{\mathrm{cmc}} = 0.92$ mol m^{-3}). $c_T = 1.25$ mol m^{-3} (●), 1.5 mol m^{-3} (◇), 2.5 mol m^{-3} (▲), and 4.0 mol m^{-3} (□).

jet length z^*. Equation (5.26), which is built into the CFD code through a Fortran user-subroutine (see Appendix D.3), and the tangential stress boundary condition couple mass transfer and fluid mechanics in the jet.

5.6 Micelle-Monomer Equilibrium in the Bulk

The simplest model of aggregation assumes that N monomers, S, form one micelle, S_m, according to

$$N \cdot S \underset{k_d}{\overset{k_f}{\rightleftharpoons}} S_m, \tag{5.28}$$

where k_f and k_d are the rate constants of the formation and disintegration of the micelles, respectively.

The equilibrium between monomers and micelles in the bulk is described by the equilibrium constant, K. From (5.28), we obtain

$$K = \frac{k_f}{k_d} = \frac{c_{m,b}}{c_{\mathrm{cmc}}^N}, \tag{5.29}$$

where K has the units [mol^{1-N} m^{3N-3}]. As before, $c_{m,b}$ is the concentration of micelles in the bulk, given by Equation (4.74), and c_{cmc} is the concentration of monomers in the bulk at the cmc. Replacing $c_{m,b}$ in Equation (5.29) gives

$$K = \frac{k_f}{k_d} = \frac{c_T - c_{\mathrm{cmc}}}{N c_{\mathrm{cmc}}^N}. \tag{5.30}$$

Equation (5.30) is plotted for four different total concentrations of C_{16}TAB in Figure 5.6 as a fuction of the mean aggregation number, N, which assumes values of $90 \leqslant N \leqslant 120$. For example, at $c_T = 1.5$ mol m^{-3} and $N = 90$, we find a value of $K = 11.7026$ mol^{-89} m^{267} for the equilibrium constant. Choosing $k_d = 1.0$ s^{-1}, we thus have $k_f = 11.7026$ m^{267} s^{-1} mol^{-89}.

5.7 Micelle-Monomer Kinetics

From the principle of mass action to the reaction mechanism (5.28), we have

$$\frac{dc}{d\mathcal{T}} = N\left(k_d c_m - k_f c^N\right) \tag{5.31}$$

for the monomers, and

$$\frac{dc_m}{d\mathcal{T}} = k_f c^N - k_d c_m \tag{5.32}$$

for the micelles. We use Equations (5.31) and (5.32) to formulate the source terms in the convection-diffusion equations for the monomers and the micelles, Equations (5.8) and (5.9), respectively. The dimensionless mass source terms, s^* and s_m^*, then read

$$s^* = \frac{MR_0^2}{\rho D}\frac{dc}{d\mathcal{T}} = \frac{NMR_0^2}{\rho D}\left(k_d c_m - k_f c^N\right), \tag{5.33}$$

and

$$s_m^* = \frac{NMR_0^2}{\rho D}\frac{dc_m}{d\mathcal{T}} = \frac{NMR_0^2}{\rho D}\left(k_f c^N - k_d c_m\right). \tag{5.34}$$

The molar concentrations of monomers and micelles, c and c_m, are converted into the mass fractions w and w_m using Equations (5.2) and (5.10), respectively. Equations (5.33) and (5.34) are implemented into the CFD code through a Fortran user-subroutine, which is detailed in Appendix D.4.

5.8 Boundary Conditions for the Micelles

5.8.1 Inlet of the Flow Domain

At the inlet of the computational flow domain, sufficiently far upstream from the nozzle exit region, the equilibrium between surfactant monomers and micelles is undisturbed, and the concentration of micelles takes on the bulk value. We thus have

$$w_m(r^*, z^* \ll 0) = w_{m,b}, \tag{5.35}$$

which we calculate from the mass balance of the whole surfactant inventory, given by Equation (4.76). We note here that in the presence of micelles, the monomer bulk concentration, which represents the boundary condition for the monomers at the inlet of the flow domain, takes on the value at the cmc, as outlined before.

5.8.2 Nozzle Wall and Free Surface

As before in the case of surfactant monomers, the nozzle wall is made impenetrable for micelles also, that is,

$$\frac{1}{r^*}\frac{\partial}{\partial r^*}\left(r^* w_m\right) + \frac{\partial w_m}{\partial z^*} = 0 \text{ at } r^* = 1.0, z^* \leqslant 0. \tag{5.36}$$

Micelles are considered surface-inactive, which is expressed through a zero-flux condition that is directed along the outward unit normal of the surface,

$$\frac{1}{r^*}\frac{\partial}{\partial r^*}\left(r^* w_{m,s}\right) + \frac{\partial w_{m,s}}{\partial z^*} = 0 \text{ at } r^* = R^*, z^* > 0, \tag{5.37}$$

where $w_{m,s} = w_m(r^* = R^*, z^*)$ refers to the micellar sub-surface concentration.

5.8.3 Downstream Position

The micellar concentration at the outlet of the flow domain is not constrained, since it depends on the monomer concentration, which in turn does not reach its equilibrium value due to the action of gravity on the surface. Surfactant monomers continue to diffuse to the surface as a result of the surface expansion that is caused by gravity. A state of equilibrium between monomers and micelles at the outlet of the computational flow domain can therefore not be enforced.

5.9 Limiting Marangoni Stress at the Point of Detachment: Hybrid CFD Model

Converged numerical solutions of the model as outlined above are only achieved at very low values for the bulk concentration c_b of about 0.01 mol m^{-3} at our high Reynolds numbers. At higher bulk concentrations, direct coupling of surfactant adsorption and fluid mechanics—the link between the shear stress condition (3.44) and the equation of state (5.26)—led to failure of the Newton-Raphson iteration scheme. The Marangoni stress, $d/dz^*(1/\,\mathrm{Ca})$, very near to $z^* = 0$ was found to exceed the shear stress at the nozzle wall, as a consequence of which the surface velocity was not only reduced, but brought to rest and reversed. The result was the appearance of a closed vortex flow, much less in diameter than the nozzle radius, in the nozzle exit plane. With the occurrence of such a toroidal flow, convergence for the convection-diffusion equation could no longer be attained. Schunk reported a similar phenomenon in his numerical work on surfactant adsorption in an overflowing cylinder (OFC), where what he believed to be an oscillatory toroidal instability, which was caused by steep surface tension gradients, was observed near the centre of the OFC [15].

The failure of our numerical scheme results from its inability to handle the step change in sub-surface concentration that should occur at the point of detachment. In order to speed up convergence and to suppress the appearance of oscillations in the numerical solutions, we have introduced upwinding [213], a degree of numerical diffusion that does not affect the solution away from the nozzle. The CFD code FIDAP uses a streamline upwinding scheme that adds numerical diffusion only along the flow direction [214]. Axial diffusion and upwinding cause the step change in surface concentration to be smeared out over a few nodes, resulting in finite, but very large, concentration gradients immediately downstream of the point of detachment. When these concentration gradients are converted to surface tension gradients through the equation of state (5.26) and the tangential shear stress condition (3.44), large accelerations result. The whole calculation scheme then fails to converge.

We have tackled this problem by combining the theoretical solution at the nozzle exit, which we derived in Chapter 4, with the far-field solution that is obtained from the numerical computation. We apply a limiting Marangoni stress at the point of detachment. We also apply the finite surface concentration, Γ_0^*, at $z^* = 0$, which has been calculated from the theory. Stable solutions for the convection-diffusion equation are then obtained for a range of bulk concentrations at our high Reynolds numbers. The implementation in our numerical model is detailed in the following sections.

We note here that our boundary-layer theory, which we detailed in Chapter 4, is based on the supposition that reverse flow does not occur and consequently that the maximum Marangoni stress does not exceed the stress value at the nozzle wall. We have shown that this assumption can lead to a solution that does not show singular behaviour at the point of detachment. Our analysis, however, does not exclude the possibility that other families of solutions exist, such as the toroidal vortices observed in some of the numerical solutions.

5.9.1 Limitation Condition and Concentration Profile in the Region of Detachment

The condition that determines the Marangoni stress at the point of detachment is given by Equation (4.37). This limitation is implemented into the numerical computation through the sub-surface concentration profile, $w_s(z^*)$, at the point of detachment at $z^* = 0$.

The surface equation of state (5.26) determines the surface tension everywhere along the jet surface, including the point of detachment at $z^* = 0$. It must thus fulfil the limitation condition (4.37). Differentiating the Szyszkowski equation (5.26) with respect to z^*, and considering the limitation condition (4.37), gives

$$\frac{d}{dz^*}\left(\frac{1}{\mathrm{Ca}}\right) = -\frac{\mathrm{E}}{(k^* + w_s)}\frac{dw_s}{dz^*} = -4 \tag{5.38}$$

at $z^* = 0$. Integrating Equation (5.38) by separating the variables gives

$$\frac{k^* + w_s}{k^* + w_{s,0}} = \exp\left(\frac{4}{\mathrm{E}}z^*\right). \tag{5.39}$$

In Equation (5.39), $w_{s,0}$ is the sub-surface concentration at the nozzle exit ($z^* = 0$). For small values of z^*, Equation (5.39) can be linearised to give

$$\frac{k^* + w_s}{k^* + w_{s,0}} \approx 1 + \frac{4}{\mathrm{E}}z^*, \tag{5.40}$$

which we can rearrange to give the solution for w_s, which is valid as $z^* \to 0$, namely

$$w_s = w_{s,0} + \frac{4}{\mathrm{E}}\left(k^* + w_{s,0}\right) z^*. \tag{5.41}$$

5.9.2 Asymptotic Matching with the Numerical Downstream Solution

We match the linear solution for $w_s(z^*)$ at the point of detachment, Equation (5.41), with the numerical downstream solution for w_s that is computed by the CFD model. In order to carry out the matching, we approximate the numerical downstream solution with an analytical expression. Here, we distinguish two cases—the case of relatively low bulk concentrations which leads to a state of non-equilibrium at the sub-surface, so that $w_s\,(z^*) \ll w_b$ everywhere at the surface, and the case of relatively high bulk concentrations, which allows the sub-surface concentration to reach the bulk value with increasing axial distance from the nozzle, that is, $w_s\,(z^*) \sim w_b$ for large values of z^*, so that the state of equilibrium is approached at the sub-surface at the far downstream position.

State of Non-Equilibrium at the Sub-Surface

At sufficiently low bulk concentrations, the sub-surface concentration is far from reaching a state of equilibrium across the diffusion boundary layer, even at large distances from the nozzle exit. Under these circumstances, the numerical downstream solution was found to follow a power law equation of the form

$$w_s = C{z^*}^m, \tag{5.42}$$

with C and m being the parameters of a least-squares power-law fit.

Asymptotic matching of Equations (5.41) and (5.42) leads to a smooth solution for w_s that holds everywhere along the jet surface. We have used

$$w_s = \left\{ w_{s,0} + \frac{4}{\mathrm{E}}\left(k^* + w_{s,0}\right) z^* \right\} \left\{ \frac{{\ell^*}^2}{{\ell^*}^2 + {z^*}^2} \right\}^{\frac{1-m}{2}}, \tag{5.43}$$

with

$$\ell^* = \frac{\ell}{R_0} = \left\{ \frac{C}{\frac{4}{\mathrm{E}}\left(k^* + w_{s,0}\right)} \right\}^{\frac{1}{1-m}}. \tag{5.44}$$

The dimensionless length scale ℓ^* is related to the length of the detachment region, λ^*, which is defined in Equation (4.56), since it marks the point of transition from the (linear) upstream solution (5.41) to the downstream solution (5.42). The length scale ℓ^* is a function of the power-law parameters C and

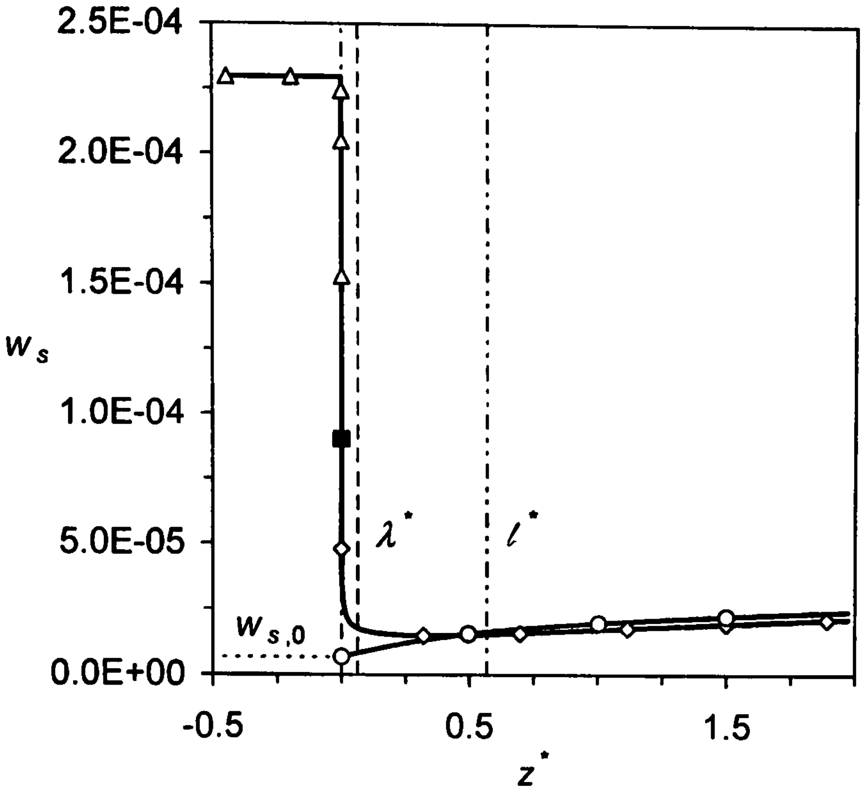

Figure 5.7: Hybrid solution for $w_s(z^*)$, Equations (5.43) and (5.44), used in the CFD calculations to limit the Marangoni stress at the point of detachment and to incorporate Γ_0^* (open circles). The CFD solution for $w_s(z^*)$ is given by the open triangles and diamonds along the nozzle wall and the free surface, respectively. The CFD solution for $w_s(z^* = 0)$ is given by the closed box. The data are for $c_b = 0.9$ mol m^{-3} C_{16}TAB and Re = 1950.

m, which in turn depend on the bulk concentration c_b, the Reynolds number and the physico-chemical properties of the surfactant.

Equation (5.43) provides us with a smooth fit through the downstream solution for w_s that is computed by the CFD model and gives the required maximum Marangoni stress at the point of detachment. This information is passed to the numerical computation through the equation of state (5.26), which is linked to Equation (5.43) instead of coupling it directly with the numerical solution for the sub-surface concentration. The programming is detailed in Appendix D.3. In this way, a smooth surface tension function, $\text{Ca}^{-1}(z^*)$, is obtained that accounts for the limiting Marangoni stress at the point of detachment. Note that "downstream" solution here refers to the region of the jet flow where $z^* \gg \ell^*$.

An estimate of the finite value of the surface concentration at the point of detachment, $\Gamma_0^* = \Gamma^*(z^* = 0)$, is provided by Equation (4.57). Using the Langmuir isotherm, Equation (5.21), we can calculate a value for the sub-surface concentration at that point, $w_{s,0} = w_s\left(z^* = 0\right)$, which is then used in Equations (5.43) and (5.44).

The hybrid solution for $w_s(z^*)$, Equation (5.43), is plotted in Figure 5.7 for $c_b = 0.9$ mol m^{-3} C$_{16}$TAB at Re = 1950 (open circles). This profile is used to calculate the surface tension profile, which is passed to the numerical computation. The result of this numerical computation is the sub-surface concentration profile that is given by the open triangles and diamonds in Figure 5.7, which represent the solutions along the nozzle wall and the surface, respectively. This iterative procedure was repeated until stable values for the parameters C and m were found. Typically 5 to 6 computations were necessary to attain stable solutions.

The hybrid CFD model is portrayed in Figure 5.8.

State of Equilibrium at the Sub-Surface

The simple power-law relation, Equation (5.42), ceases to accurately represent the numerical downstream sub-surface concentration profile at higher bulk concentrations, most noticeably above the critical micelle concentration. In this case, the sub-surface concentration approaches the bulk value at the downstream position, that is, $w_s \to w_b$ as z^* becomes large, and this behaviour must be accounted for.

We define a second length scale, L^*, which indicates the transition from the second to the third region of the downstream jet flow, in which $w_s \sim w_b$. This length scale is formally defined as

$$L^* = \frac{L}{R_0} = \left(\frac{w_b}{C}\right)^{\frac{1}{m}} . \tag{5.45}$$

The matched solution for $w_s\left(z^*\right)$, Equation (5.43), is then extended to include the second length scale,

$$w_s = \left\{ w_{s,0} + \frac{4}{\mathrm{E}} \left(k^* + w_{s,0}\right) z^* \right\} \left\{ \frac{\ell^{*2}}{\ell^{*2} + z^{*2}} \right\}^{\frac{1-m}{2}} \left\{ \frac{L^*}{L^* + z^*} \right\}^{m} , \tag{5.46}$$

which is used instead of Equation (5.43) to describe the sub-surface concentration profile. As before, the Szyszkowski equation (5.26) is linked to Equation (5.46), and in this way a smooth function Ca$^{-1}(z^*)$ is obtained for the surface tension profile that is used in the numerical computation. This case is not included

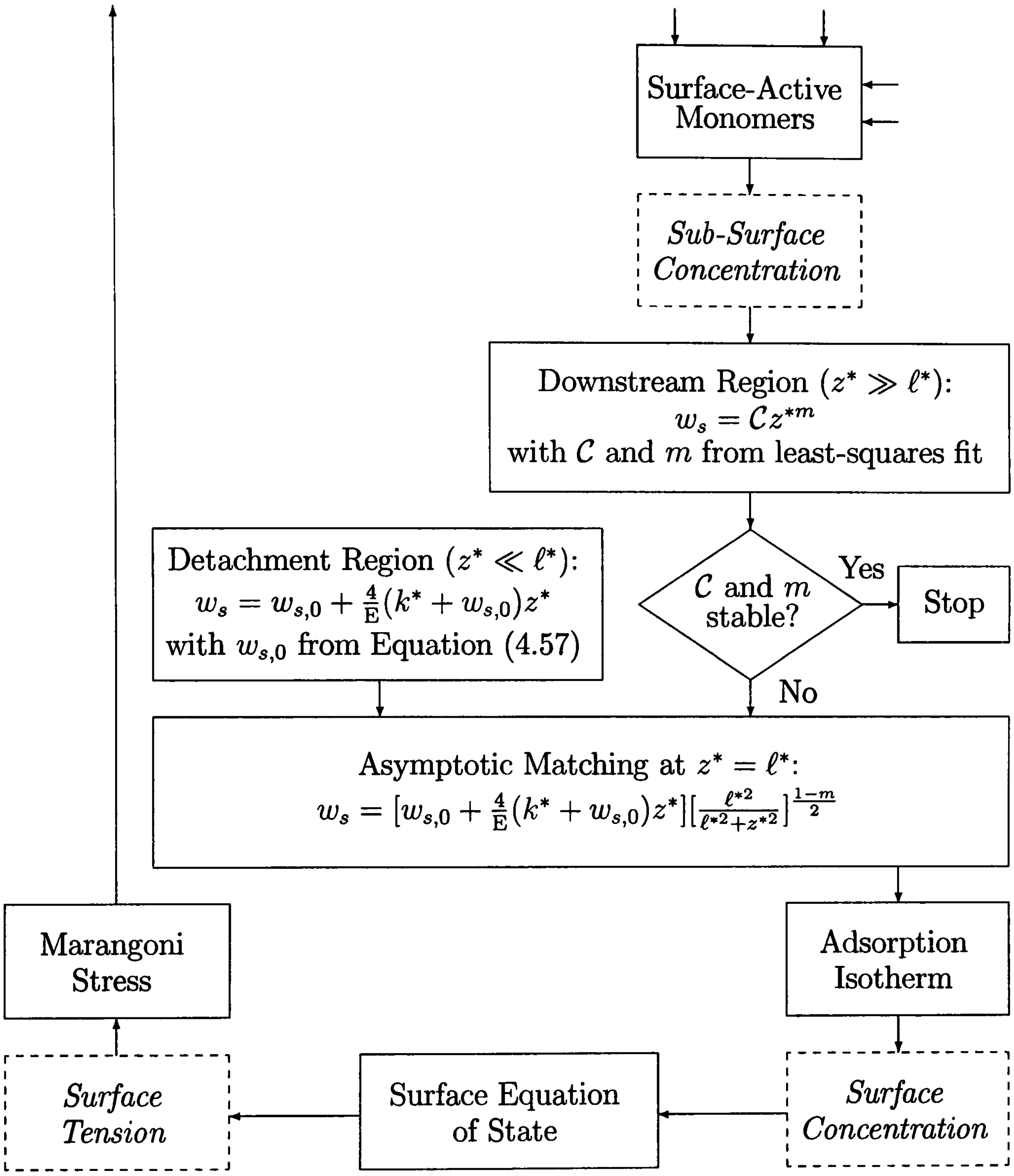

Figure 5.8: Outline of the hybrid CFD model of diffusion-controlled surfactant adsorption in the jet.

in the Fortran user-subroutine given in Appendix D.3. The programming is, however, straight forward. We note that the definition of ℓ^* has not changed.

For $z^* \ll L^*$, Equation (5.46) becomes Equation (5.43), and the solutions for w_s are given by Equations (5.41) and (5.42) in the region of detachment and in the downstream region, respectively. For $z^* \gg L^*$, which implies that $z^* \gg \ell^*$,

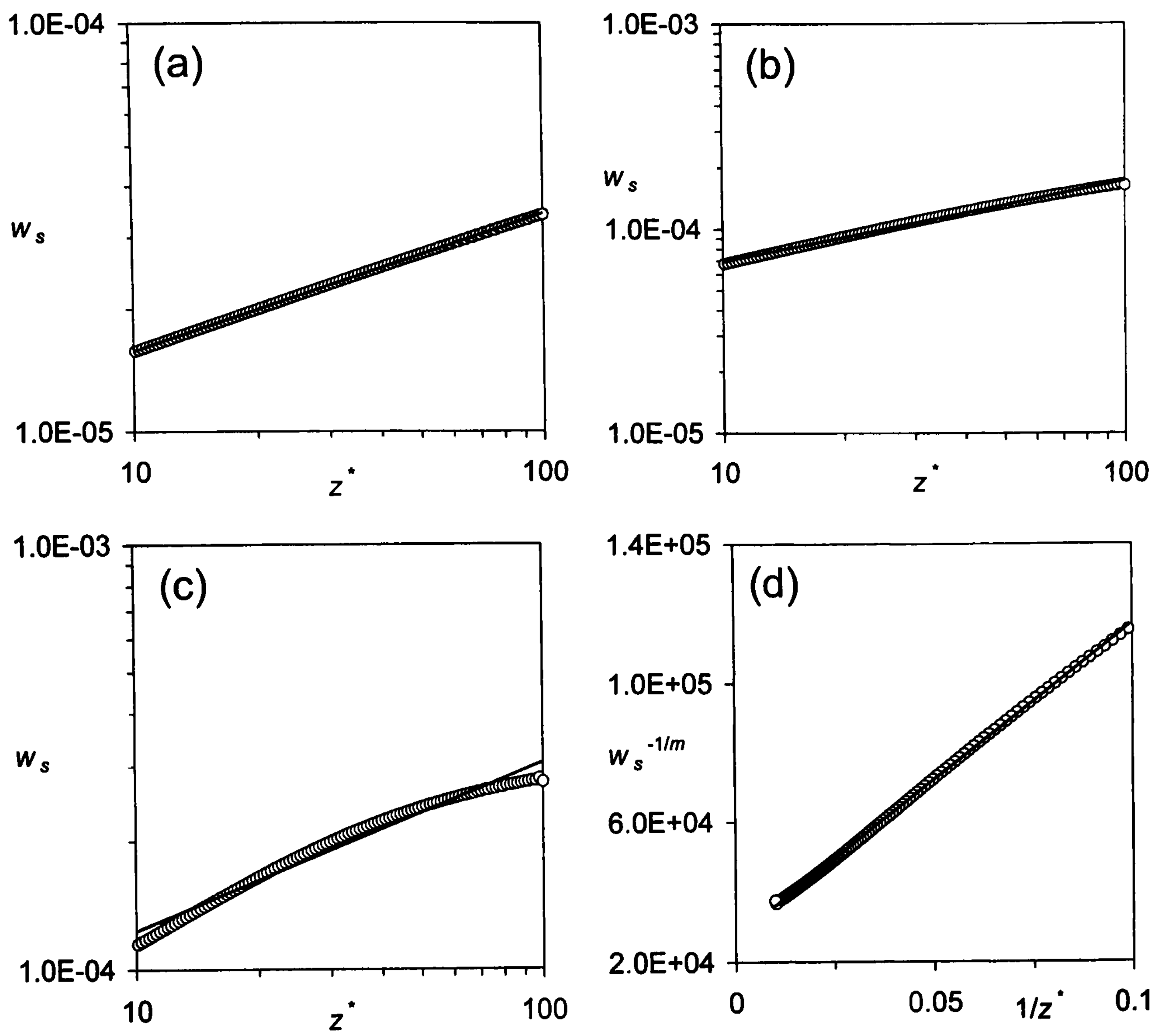

Figure 5.9: Approximation of the computed downstream solution $w_s(z^*)$. All data are for C_{16}TAB at Re = 1950; c_b = 0.3 mol m^{-3} (a), and 0.9 mol m^{-3} (b); c_T = 1.5 mol m^{-3} (c,d). Cases (a) to (c) show the least-squares fit of Equation (5.42); case (d) shows the least-squares fit of Equation (5.51).

we have that $w_s \to w_b$. If $z^* \sim L^*$, and large enough that $z^* \gg \ell^*$, we find that w_s is given by

$$w_s = w_b z^{*^m} \left\{ \left(\frac{w_b}{\mathcal{C}} \right)^{\frac{1}{m}} + z^* \right\}^{-m} \tag{5.47}$$

or

$$w_s^{-1/m} = \frac{\mathcal{C}^{-1/m}}{z^*} + w_b^{-1/m}. \tag{5.48}$$

Defining

$$\mathcal{X} = \mathcal{C}^{-1/m}, \tag{5.49}$$

and

$$\mathcal{Y} = w_b^{-1/m}, \tag{5.50}$$

results in

$$w_s^{-1/m} = \frac{\mathcal{X}}{z^*} + \mathcal{Y}, \tag{5.51}$$

where the dimensionless parameters $1/m$, $\mathcal{X}$, and $\mathcal{Y}$ are obtained from a least-squares fit of Equation (5.51) to the numerical downstream solution for $w_s(z^*)$ in the region where $z^* \gg \ell^*$.

The thermodynamical state of the jet surface, and its impact on the approximation of the computed downstream solution for the sub-surface concentration, $w_s(z^*)$, is illustrated by the four cases in Figure 5.9 for aqueous solutions of C_{16}TAB. At a moderate sub-micellar bulk concentration of $c_b = 0.3$ mol m^{-3}, case (a), the surface is far from reaching its state of equilibrium, even at long distances from the nozzle, and $w_s \ll w_b$ everywhere along the surface. In this case, the power-law approximation, Equation (5.42), gives an excellent fit to the values that were obtained from the CFD model. Although a state of equilibrium is not yet fully established at a higher bulk concentration, case (b), we see that the power-law fit of Equation (5.42) to the computed values is not as good as in case (a). Above the cmc, case (c) shows very clearly that at high total concentrations in the bulk, with the enhanced transport of surfactant monomers to the surface through the presence of micelles, the power-law fit of Equation (5.42) fails to approximate the computed values. At these high bulk concentrations, the surface approaches a state of equilibrium, $w_s \to w_b$ at large z^*, which cannot be neglected. A much improved approximation of the computed values is obtained if we account for the equilibration of the surface in our approximation, as demonstrated in case (d), where Equation (5.51) is used to give an approximation of the computed values for $w_s(z^*)$.

Surface concentration data, $\Gamma^*(z^*)$, which correspond to the sub-surface concentration profiles of cases (a) and (b) in Figure 5.9, are given in Section 6.1. For C_{16}TAB at high Reynolds numbers below the cmc, we have used Equation (5.42) to approximate the numerical downstream solution for $w_s(z^*)$ at all bulk concentrations. Using Equation (5.51) at the high values for c_b had only minor effects on the result for $\Gamma^*(z^*)$. This behaviour is reflected by the high values of L^*, which are well in excess of 100 ($L^* = \mathcal{X}/\mathcal{Y} = 422.7$ at $c_b = 0.9$ mol m^{-3} C_{16}TAB), thus lying outside the range of the computational domain.

Section 6.3 compares the surface concentration data that correspond to case (d) in Figure 5.9 with experimentally obtained values. In this case, for C_{16}TAB above the cmc, we have used Equation (5.51) to approximate the sub-surface concentration profile in our hybrid CFD model in all computations. Equation (5.51) was also used in the computation with C_{14}TAB at a bulk concentration of $c_b = 0.93$ mol m^{-3} (see Section 6.2).

Chapter 6

Comparison of CFD Model and Experiment

This chapter reports a comparison of results from the hybrid CFD model with experimental measurements of surface concentration and velocity. Most of the data in this chapter are for C_{16}TAB, below and above the critical micelle concentration. This particular surfactant has been the focus of most of the experimental and modelling work on the overflowing cylinder experiment (OFC) here at Oxford. The jet investigation benefitted from the wealth of data and insight that was gained from the OFC work. In addition, a comparison is also given for C_{14}TAB under sub-micellar conditions. Experimental data for other ionic and non-ionic surfactants may be found in Appendix E.

6.1 C_{16}TAB in the Absence of Micelles

In this section, CFD computations and experimental data for one type of surfactant (C_{16}TAB) at varying bulk concentrations and flow conditions (mean nozzle exit velocity $\overline{u}_0$ and nozzle radius R_0) are presented. The main parameter of variation is the bulk concentration, spanning widely from very dilute surfactant solutions (0.01 mol m^{-3}) to near the cmc (0.9 mol m^{-3}). The experimental jet apparatus does not allow for large variations in the flow parameters, which were thus kept at the same orders of magnitude, that is, $R_0 \sim \mathcal{O}(1 \text{ mm})$ and $\overline{u}_0 \sim \mathcal{O}(1 \text{ m s}^{-1})$ in all cases, and vary only slightly. In Appendix C.2, an example of a FIDAP journal file listing is given, which was used to obtain the computed data in the absence of micelles.

Table 6.1: Dimensionless simulation parameters used in the numerical computations with aqueous solutions of C_{16}TAB below the cmc.

c_b / mol m^{-3}	0.01 to 0.9	0.3 to 0.9	0.65
R_0 / mm	0.79	1.00	0.79
$\overline{u}_0$ / m s^{-1}	1.236	0.975	0.981
θ / °	89.99913	89.99888	89.99896
Re/2	975	975	775
Ca_w^{-1}	58.9	74.7	74.2
$(2\mathrm{Fr})^{-1}$	0.00507	0.01032	0.00805
Sc	1340.48	1340.48	1340.48
E	15.35	19.46	19.34
$\rho D \left(M\overline{u}_0\Gamma_{sat}\right)^{-1}$	0.4253	0.5392	0.5359
Figures	6.1 to 6.5 6.8 to 6.10 6.12 and 6.15	6.6 6.11 6.13	6.7 6.14

6.1.1 Parameters of the Hybrid CFD Model

Tables 6.1 and 6.2 summarise the dimensionless modelling parameters and the physico-chemical parameters of aqueous C_{16}TAB solution, respectively. For the viscosity and density of the surfactant solution, we assume the values of pure water since the solutions are very dilute, even at the higher bulk concentrations. The coefficient of diffusivity of the ionic surfactant C_{16}TAB in water, D, is an effective ionic diffusivity, which is calculated using

$$D = \frac{2D^+D^-}{D^+ + D^-}. \tag{6.1}$$

Equation (6.1) can be derived from the general formula given by Taylor and Krishna [215, Eq. (2.4.33), p. 45], and is also given in the work of Bird *et al.* [190, Eq. (18.L–1), p. 586].

We have used a value of $D^- = 20.8 \times 10^{-10}$ m^2 s^{-1} at $T = 298.15$ K for the diffusivity coefficient of the negatively charged bromide ions in water [216, Table 24.8, p. 1104]. Using the Wilke-Chang estimation method, the coefficient of diffusivity of the cations in water was found to be $D^+ = 4.50 \times 10^{-10}$ m^2 s^{-1} at $T = 298.15$ K [217, Eq. (11-9.1), p. 598]. The same values for D^- and D^+ were also used by Valkovska *et al.* to model the adsorption of ionic surfactants

Table 6.2: Physical model parameters of solutions of aqueous C_{16}TAB used in the numerical computations.

ρ	Density of water	10^3 kg m^{-3}
μ	Viscosity of water	10^{-3} kg m^{-1} s^{-1}
σ_w	Surface tension of water	72.8×10^{-3} N m^{-1}
M	Molecular weight of C_{16}TAB	364.5×10^{-3} kg mol^{-1}
k	Langmuir constant of C_{16}TAB	0.23 mol m^{-3}
Γ_{sat}	Saturation surface coverage of C_{16}TAB	3.9×10^{-6} mol m^{-2}
D	Diffusivity of C_{16}TAB in water	7.5×10^{-10} m^2 s^{-1}
$\widehat{N}$	Ionic number of C_{16}TAB	2
$\mathcal{R}$	Universal gas constant	8.314 J mol^{-1} K^{-1}
T	Temperature	293.15 K
g	Gravity	9.81 m s^{-2}

at the surface of an overflowing cylinder [52].

The values of the parameters that enter the hybrid CFD model (C, m, Γ_0^*, $w_{s,0}$, and ℓ^*) are displayed in Tables 6.3 to 6.5 for the bulk concentrations, nozzle radii and mean nozzle exit velocities under consideration.

In Figure 6.1, the first six value pairs $\lambda^*(c_b)$ and $\ell^*(c_b)$ of Table 6.5 are

Table 6.3: Parameters C and m of the power-law fit, Equation (5.42), as a function of the bulk concentration, c_b, of C_{16}TAB and for varying R_0 and $\overline{u}_0$.

No.	c_b / mol m^{-3}	w_b / $\times 10^{-6}$	R_0 / mm	Re	C	m
1	0.01	3.645	0.79	1950	2.28×10^{-7}	0.2960
2	0.05	18.225	0.79	1950	1.15×10^{-6}	0.3011
3	0.10	36.450	0.79	1950	2.33×10^{-6}	0.3075
4	0.30	109.350	0.79	1950	7.31×10^{-6}	0.3359
5	0.63	229.635	0.79	1950	1.66×10^{-5}	0.3872
6	0.90	328.050	0.79	1950	2.58×10^{-5}	0.4205
7	0.30	109.350	1.00	1950	8.89×10^{-6}	0.3309
8	0.65	236.925	1.00	1950	2.07×10^{-5}	0.4068
9	0.90	328.050	1.00	1950	3.06×10^{-5}	0.4688
10	0.65	236.925	0.79	1550	1.75×10^{-5}	0.4168

Table 6.4: Surface concentration at the point of detachment, Γ_0^*, calculated using Equation (4.57), and the corresponding values of the sub-surface concentration, $w_{s,0}$, calculated using Equation (5.21), for C_{16}TAB as a function of c_b and for varying R_0 and $\overline{u}_0$.

No.	c_b / mol m^{-3}	w_b / $\times 10^{-6}$	R_0 / mm	Re	Γ_0^*	$w_{s,0}$ / $\times 10^{-6}$
1	0.01	3.645	0.79	1950	0.00015	0.0125
2	0.05	18.225	0.79	1950	0.00169	0.1396
3	0.10	36.450	0.79	1950	0.00479	0.3962
4	0.30	109.350	0.79	1950	0.02488	2.1009
5	0.63	229.635	0.79	1950	0.07572	6.7451
6	0.90	328.050	0.79	1950	0.12928	12.2256
7	0.30	109.350	1.00	1950	0.03990	3.4219
8	0.65	236.925	1.00	1950	0.12740	12.0217
9	0.90	328.050	1.00	1950	0.20750	21.5591
10	0.65	236.925	0.79	1550	0.10000	9.1489

plotted ($R_0 = 0.79$ mm and $\overline{u}_0 = 1.236$ m s^{-1}). Both sets of values increase monotonically with increasing bulk concentration, and in the limit of $c_b \rightarrow 0$, correctly show $\lambda^*, \ell^* \rightarrow 0$. The λ^* values have a 3/2 power dependence on c_b (see Equation (4.56) and the closed circles in Figure 6.1), and the ℓ^* values (open

Table 6.5: Length of the region of detachment, λ^*, and the related value, ℓ^*, for C_{16}TAB as a function of c_b and for varying R_0 and $\overline{u}_0$.

No.	c_b / mol m^{-3}	w_b / $\times 10^{-6}$	R_0 / mm	Re	λ^*	ℓ^*
1	0.01	3.645	0.79	1950	0.000128	0.001572
2	0.05	18.225	0.79	1950	0.001426	0.015155
3	0.10	36.450	0.79	1950	0.004034	0.040238
4	0.30	109.350	0.79	1950	0.020963	0.190259
5	0.63	229.635	0.79	1950	0.063795	0.578526
6	0.90	328.050	0.79	1950	0.108928	1.082431
7	0.30	109.350	1.00	1950	0.042707	0.359465
8	0.65	236.925	1.00	1950	0.136203	1.115927
9	0.90	328.050	1.00	1950	0.221912	1.968054
10	0.65	236.925	0.79	1550	0.106287	0.874610

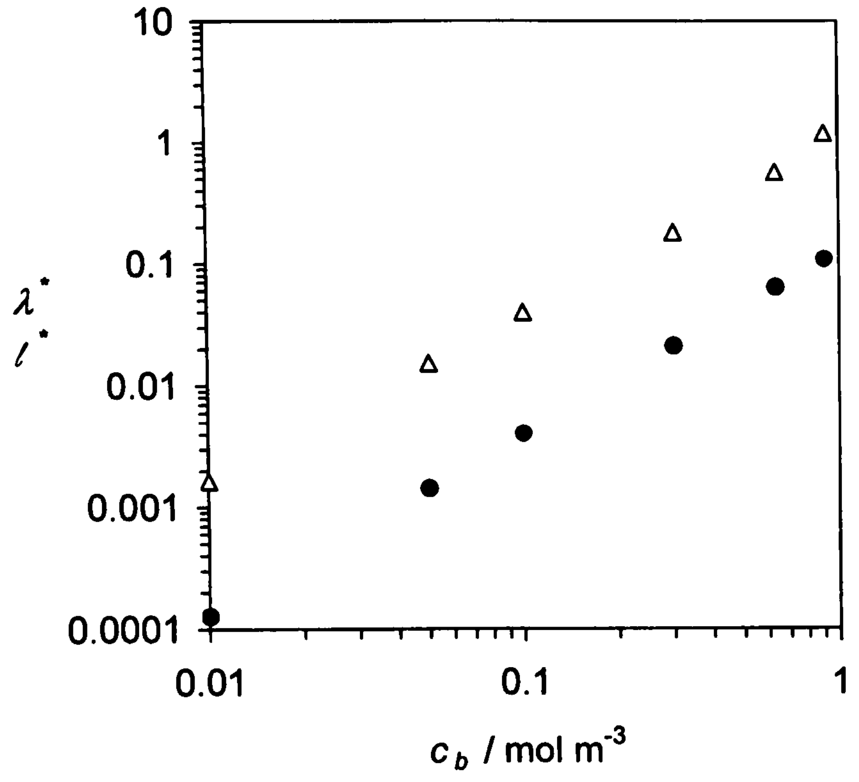

Figure 6.1: Length of the detachment region, $\lambda^* = \lambda/R_0$ (closed circles, Equation (4.56)), and the related parameter, $\ell^* = \ell/R_0$ (open triangles, Equation (5.44)), as a function of the bulk concentration, c_b, of C_{16}TAB at Re = 1950 and $(2\,\mathrm{Fr})^{-1} = 0.00507$.

triangles in Figure 6.1) show the same functional dependence on c_b.

Although the length scale ℓ^* is related to λ^*, which is expressed through the same functional dependence on c_b, the values for ℓ^* are about one order of magnitude larger than the values for λ^*. We can make out the same difference between λ^* and ℓ^* with a slightly larger nozzle radius (see Table 6.5, value pairs 7 to 9) and with a lower mean nozzle exit velocity (see Table 6.5, value pair no. 10). This difference in magnitude has its origin in the way both are defined. We remember that λ^* is defined as the point where the detachment region velocity solution is matched with a far-field solution that is extrapolated back to this point. In contrast, ℓ^* indicates the distance at which a linear dependence of the sub-surface concentration near to the nozzle makes a transition to the fitted power-law dependence of the computed solution for large z^*.

6.1.2 Surface Concentration

Figures 6.2 to 6.5 show computed surface concentration profiles, $\Gamma^* = \Gamma^*(z^*)$, for six different bulk concentrations of $C_{16}TAB$ ($c_{\mathrm{cmc}} = 0.92$ mol m^{-3}). The Reynolds number is high, at Re = 1950. In Figures 6.3 to 6.5, experimentally obtained surface concentration data for $c_b = 0.3$ mol m^{-3}, 0.63 mol m^{-3}, and 0.9 mol m^{-3} are compared with the computed values from the hybrid CFD model. The experimental surface concentration data were obtained from ellipticity measurements in the jet flow, details of which can be found in Chapter 7.

We can see very clearly that the jet surface is depleted of surfactant near the nozzle exit, due to the rapid surface expansion in this region of the jet. The surface concentration increases quite rapidly in the close vicinity of the nozzle exit. The increase of Γ^* with increasing z^* is less pronounced in the downstream region of the jet due to a decrease in surface expansion. At the low bulk concentrations (curves (a), (b), and (c) in Figure 6.2), the convective flux in the surface is too strong for the diffusion to 'fill' the surface with surfactant and Γ^* remains well below its equilibrium value, even at very long distances from the nozzle exit. At the higher bulk concentrations (Figures 6.3 to 6.5), significantly higher values for Γ^* are reached. Even here, the continuous surface expansion, caused by the presence of gravity, does not permit the establishment of equilibrium conditions at the jet surface.

At $c_b = 0.3$ mol m^{-3}, the predicted values and the measured data exhibit very good agreement, which suggests that at this bulk concentration, the adsorption of $C_{16}TAB$ at the jet surface is diffusion-controlled. Kochurova and Rusanov [152, 153], who inferred the adsorption behaviour of $C_{16}TAB$ in vertical jets from surface potential measurements, arrived at the same conclusion for a bulk concentration of 0.28 mol m^{-3} (see page 38). At $c_b = 0.63$ and 0.9 mol m^{-3}, the agreement is less good. At these higher concentrations, very near the cmc, the experimental data show that $\Gamma^*(z^*)$ increases less rapidly as the jet leaves the nozzle than the computed results suggest. Furthermore, at these high concentrations, the experimental data approach the state of equilibrium at the surface sooner than the computed values. Although the estimates for Γ_0^* that were used in the numerical computations agree reasonably well with the first experimental values for Γ^* at small z^* (see Table 6.4), the diffusion-controlled modelling approach with a Langmuir-type equilibrium adsorption isotherm of the CFD model seems to fail to correctly predict the adsorption behaviour of $C_{16}TAB$ in the jet at

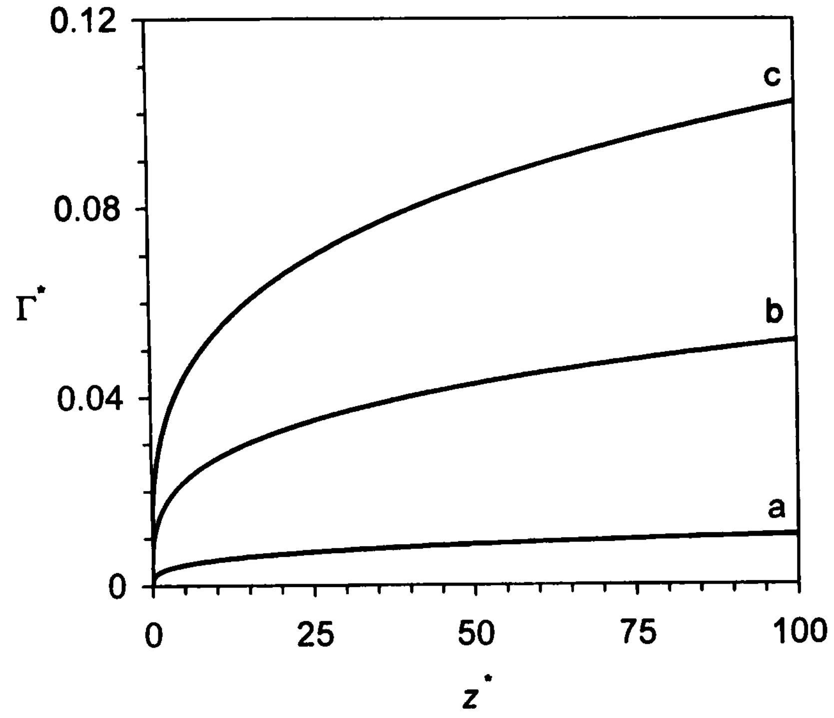

Figure 6.2: Surface concentration, $\Gamma^* = \Gamma/\Gamma_{sat}$, as a function of the axial jet coordinate, $z^* = z/R_0$, at Re = 1950 ($R_0 = 0.79$ mm) and $(2\,\mathrm{Fr})^{-1} = 0.00507$. Bulk concentrations of $c_b = 0.01$ mol m^{-3} (a), 0.05 mol m^{-3} (b), and 0.1 mol m^{-3} (c) C_{16}TAB in water are shown.

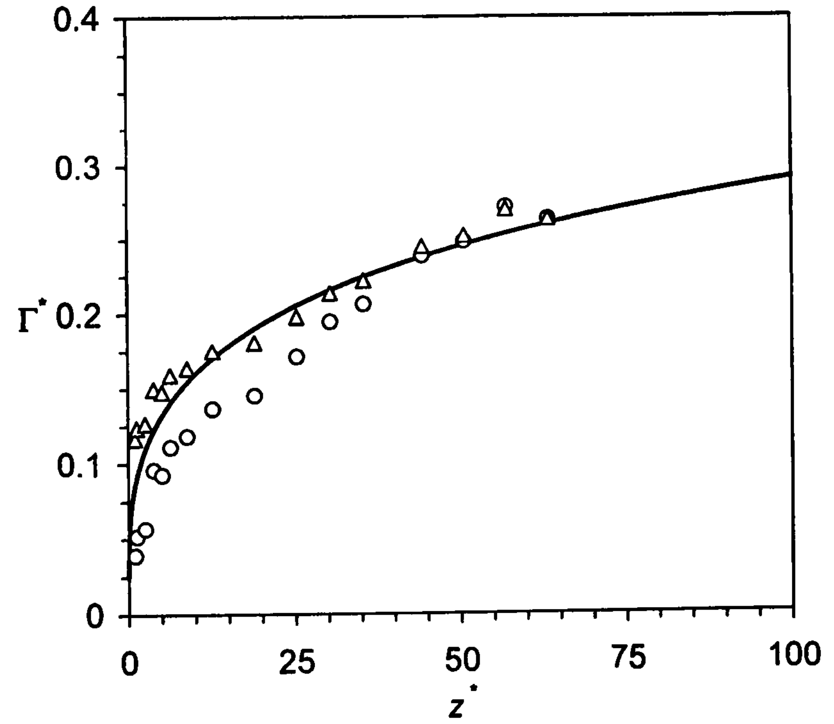

Figure 6.3: Surface concentration, $\Gamma^* = \Gamma/\Gamma_{sat}$, as a function of the axial jet coordinate, $z^* = z/R_0$, at Re = 1950 ($R_0 = 0.79$ mm), $(2\,\mathrm{Fr})^{-1} = 0.00507$, and $c_b = 0.3$ mol m^{-3} C_{16}TAB in water. Two sets of experimental data (△ and ○) are shown.

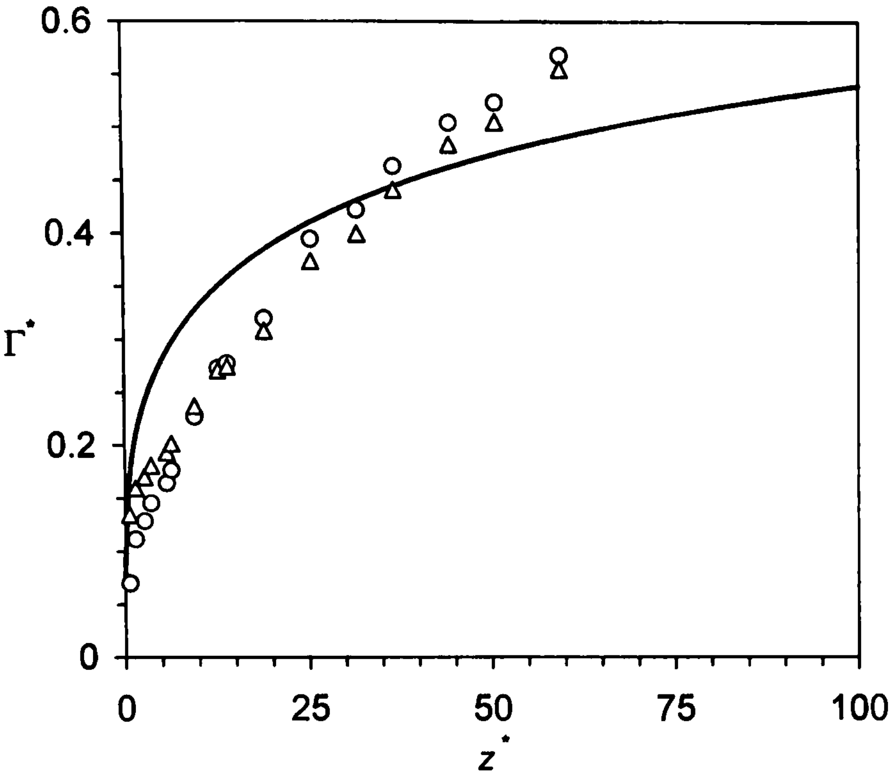

Figure 6.4: Surface concentration, $\Gamma^* = \Gamma/\Gamma_{sat}$, as a function of the axial jet coordinate, $z^* = z/R_0$, at Re = 1950 ($R_0 = 0.79$ mm), $(2\,\mathrm{Fr})^{-1} = 0.00507$, and $c_b = 0.63$ mol m^{-3} C_{16}TAB in water. Two sets of experimental data (△ and ○) are shown.

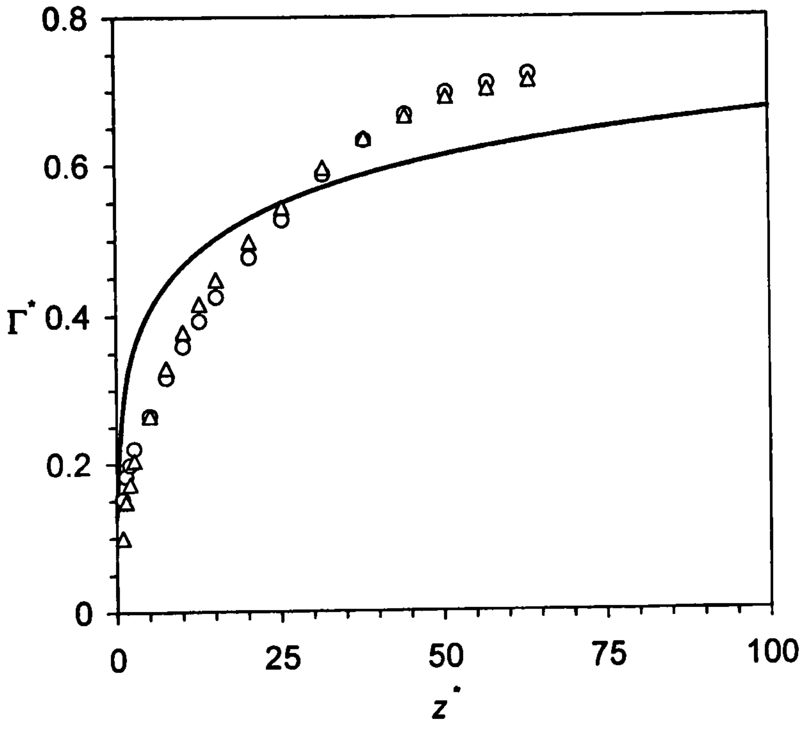

Figure 6.5: Surface concentration, $\Gamma^* = \Gamma/\Gamma_{sat}$, as a function of the axial jet coordinate, $z^* = z/R_0$, at Re = 1950 ($R_0 = 0.79$ mm), $(2\,\mathrm{Fr})^{-1} = 0.00507$, and $c_b = 0.9$ mol m^{-3} C_{16}TAB in water. Two sets of experimental data (△ and ○) are shown.

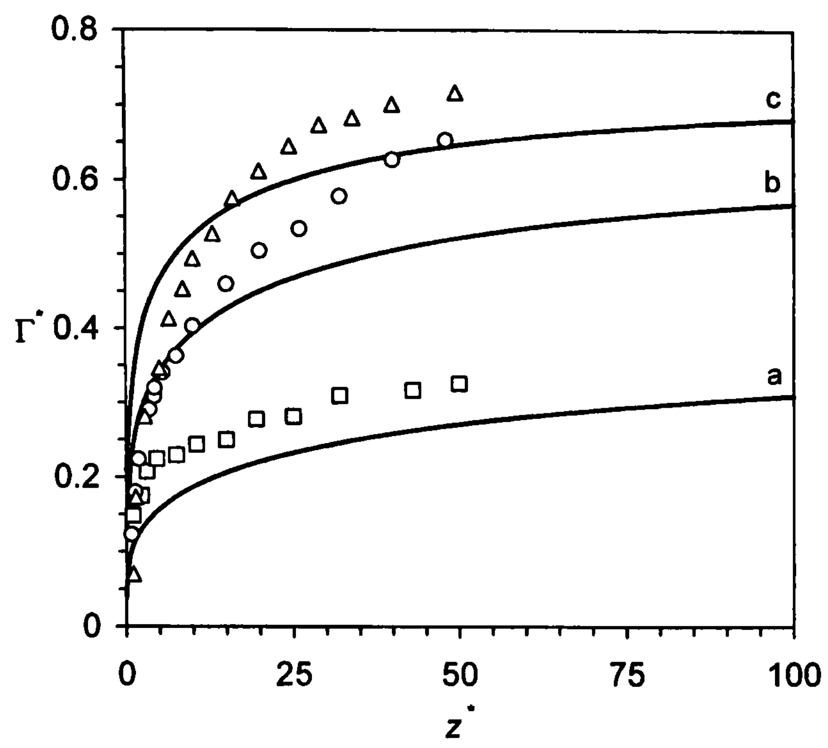

Figure 6.6: Surface concentration, $\Gamma^*(z^*)$, at Re = 1950 (R_0 = 1.0 mm), $(2\,\mathrm{Fr})^{-1} = 0.01032$, and $c_b = 0.3$ mol m^{-3} (a, squares), 0.65 mol m^{-3} (b, circles), and 0.9 mol m^{-3} (c, triangles) C_{16}TAB in water.

bulk concentrations around the cmc. In this context, our conclusion agrees with that of Kochurova and Rusanov [152,153], who observed deviation from diffusion-controlled adsorption of C_{16}TAB at a bulk concentration of 0.56 mol m^{-3} (see page 38). Our model neglects the presence of an electric double layer, which has the effect of reducing the rate of mass transfer to the surface, since adsorbing molecules must overcome the electrostatic resistance of the surface. This model deficiency might explain the deviation between the computation and the experimentally obtained values at higher bulk concentrations.

A behaviour very similar to that shown in Figures 6.3 to 6.5 is displayed in Figure 6.6. The nozzle radius is slightly increased to a value of R_0 = 1.0 mm. As before, at the higher bulk concentrations of 0.65 and 0.9 mol m^{-3}, the experimental values reach the downstream state of equilibrium much faster than the computed data, whereas in the upstream region, the predictions of the model suggest higher values than the measured data.

We note that at $c_b = 0.3$ mol m^{-3}, where the agreement between hybrid CFD model and experiment was found to be very good with the smaller nozzle (see Figure 6.3), we find that the experimental data and the computed values deviate by some constant factor.

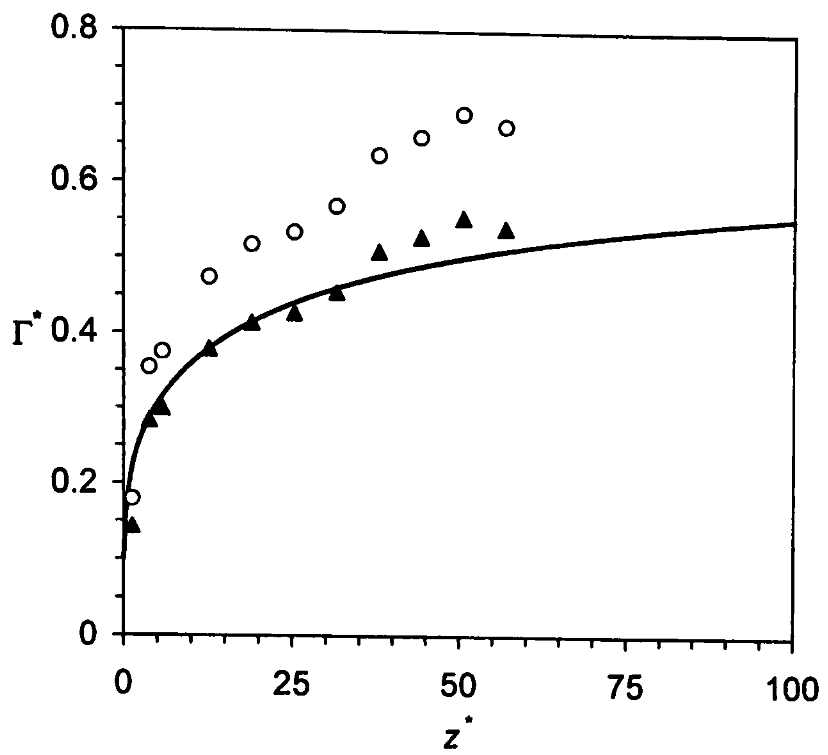

Figure 6.7: Surface concentration, $\Gamma^*(z^*)$, at Re = 1550 (R_0 = 0.79 mm), $(2\,\mathrm{Fr})^{-1} = 0.00805$, and $c_b = 0.65$ mol m^{-3} C_{16}TAB in water. The solid line is computed, and the open circles are the uncorrected experimental data. A correction factor of 0.8 was applied to the experimental data represented by the closed triangles.

As a final example of the adsorption behaviour of sub-micellar C_{16}TAB in the liquid jet, we compare the computed solution for $\Gamma^*(z^*)$ with experimets for a nozzle radius of $R_0 = 0.79$ mm and for Re = 1550 in Figure 6.7. The open circles in Figure 6.7 represent the uncorrected experimental data. The values given by the closed triangles were obtained by multiplying each experimental value with a correction factor of 0.8, which results in almost perfect agreement between computation and experiment. As explained in Section 7, there is uncertainty about the calibration of the ellipsometry data, which may perhaps explain a constant factor here, though this cannot be firmly established.

6.1.3 Radial Bulk Concentration Profiles

Figure 6.8 shows radial bulk concentration profiles, $w(r^*)$, at three different axial downstream positions, $10 \leqslant z^* \leqslant 50$, for a bulk concentration of $c_b = 0.9$ mol m^{-3} ($w_b = 328.05 \times 10^{-6}$) C_{16}TAB at Re = 1950. The radial gradients $\partial w/\partial r^*$ at the surface, which determine the diffusion of surfactant to the surface, become increasingly steep with shorter distances from the nozzle, emphasizing the need

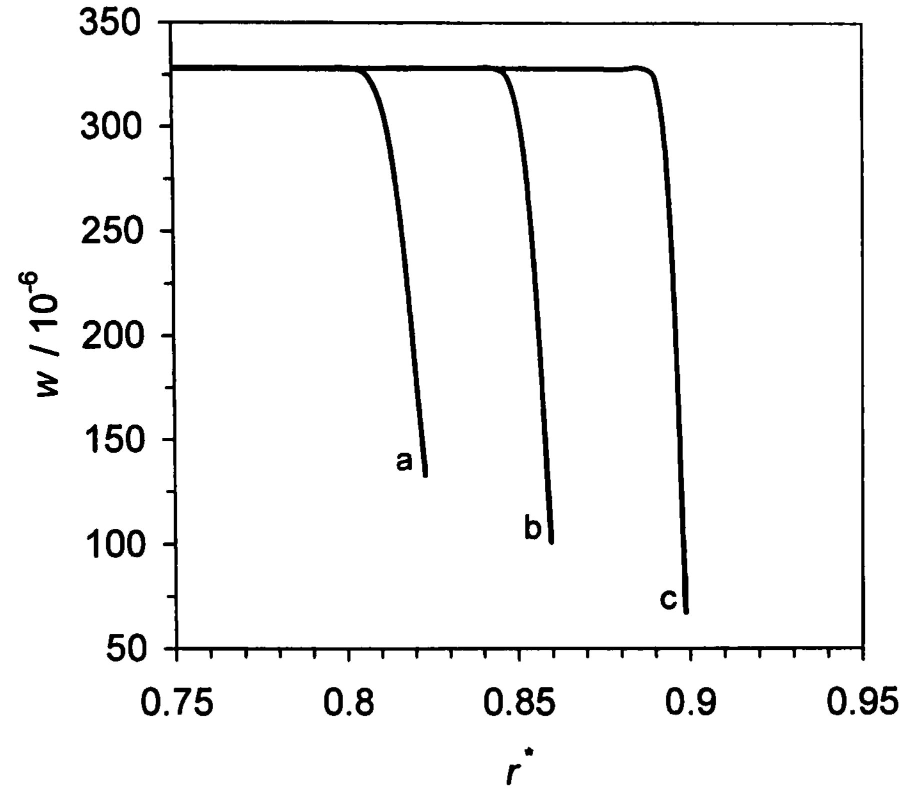

Figure 6.8: Bulk concentration profiles, $w = w(r^*)$, at $z^* = 50$ (a), 25 (b), and 10 (c) for Re = 1950 ($R_0 = 0.79$ mm), $(2\,\mathrm{Fr})^{-1} = 0.00507$, and $c_b = 0.9$ mol m^{-3} C_{16}TAB in water.

for a high mesh density underneath the surface. The concentration values at the surface are the sub-surface concentration values, $w(r^* = R^*, z^*) = w_s(z^*)$, which were converted to surface concentrations, $\Gamma^*(z^*)$, in the previous section by means of the Langmuir isotherm.

6.1.4 Dynamic Surface Tension

The dynamic surface tension calculations, $\mathrm{Ca}^{-1} = \mathrm{Ca}^{-1}(z^*)$, that correspond to the surface coverage data shown in Figures 6.2 to 6.5, for $R_0 = 0.79$ mm and Re = 1950, are shown in Figure 6.9. At the lowest concentration, $c_b = 0.01$ mol m^{-3}, the surface tension parameter remains nearly that of water and changes only very slightly over the length of the jet, which agrees with the low surface coverage values at this concentration (see Figure 6.2). We also note that only very small quantities of surfactant adsorb at the point of detachment at low bulk concentrations (curves (a) to (c) in Figure 6.2), and the surface tension parameter at that point is nearly that of pure water, that is, $\mathrm{Ca}^{-1}(z^* = 0) \approx \mathrm{Ca}_w^{-1} = 58.9$. At the point of detachment, from Equation (4.37), the local surface tension gradient is

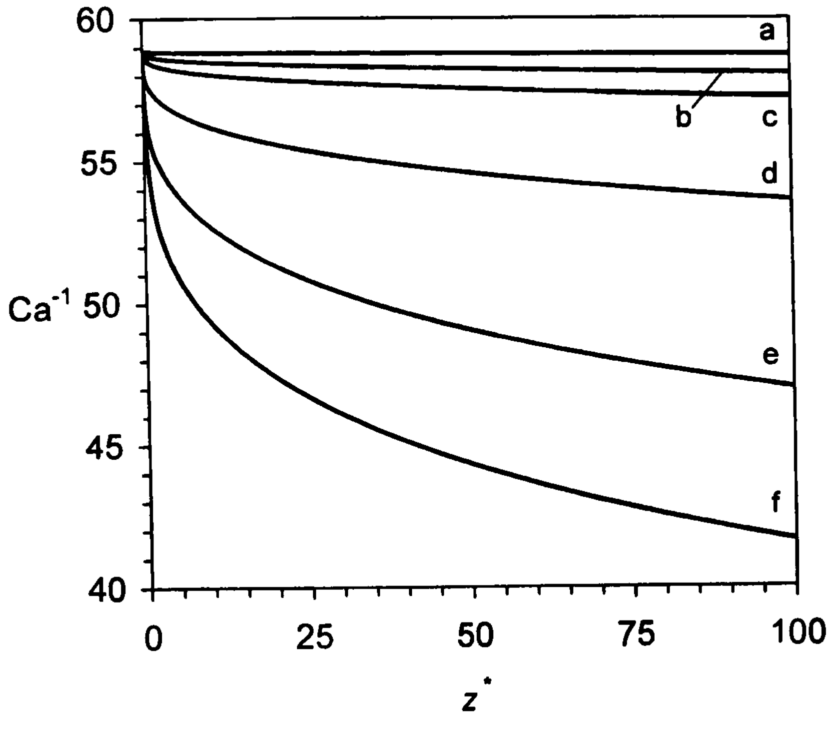

Figure 6.9: Surface tension parameter, $\mathrm{Ca}^{-1} = \sigma\left(\mu\bar{u}_0\right)^{-1}$, as a function of the axial jet coordinate, $z^* = z/R_0$, at Re = 1950 (R_0 = 0.79 mm) and $(2\,\mathrm{Fr})^{-1}$ = 0.00507. Bulk concentrations of c_b = 0.01 mol m^{-3} (a), 0.05 mol m^{-3} (b), 0.1 mol m^{-3} (c), 0.3 mol m^{-3} (d), 0.63 mol m^{-3} (e), and 0.9 mol m^{-3} (f) $\mathrm{C_{16}TAB}$ in water.

identical for all bulk concentrations, that is, $d/dz^*\left(\mathrm{Ca}^{-1}\right) = -4$ at $z^* = 0$ (see Figure 6.10). Within the region of detachment, the local Marangoni stress is linear, Equation (4.39). Outside the region of detachment, $z^* > \ell^*$, higher bulk concentrations lead to steeper surface tension gradients, which persist for significant jet lengths. At the highest concentration (0.9 mol m^{-3}), a relatively rapid decrease in surface tension is observed, which again is in accordance with the surface concentration data in Figure 6.5. In this case, the surface concentration at that point is $\Gamma_0^* = 0.13$ and thus $\mathrm{Ca}^{-1}(z^* = 0) = 56.9$.

The surface tension profiles that correspond to the surface concentration data shown in Figure 6.6 (R_0 = 1.0 mm and Re = 1950) are plotted in Figure 6.11. The curves in Figure 6.11 resemble the curves (d) to (f) in Figure 6.9.

6.1.5 Surface Velocity

The adsorption of surfactant at the expanding jet surface leads to a surface tension gradient, $d/dt^*(\mathrm{Ca}^{-1}) \approx d/dz^*(\mathrm{Ca}^{-1})$, that activates the tangential shear stress condition (3.44). The surface tension gradient acts in the upstream di-

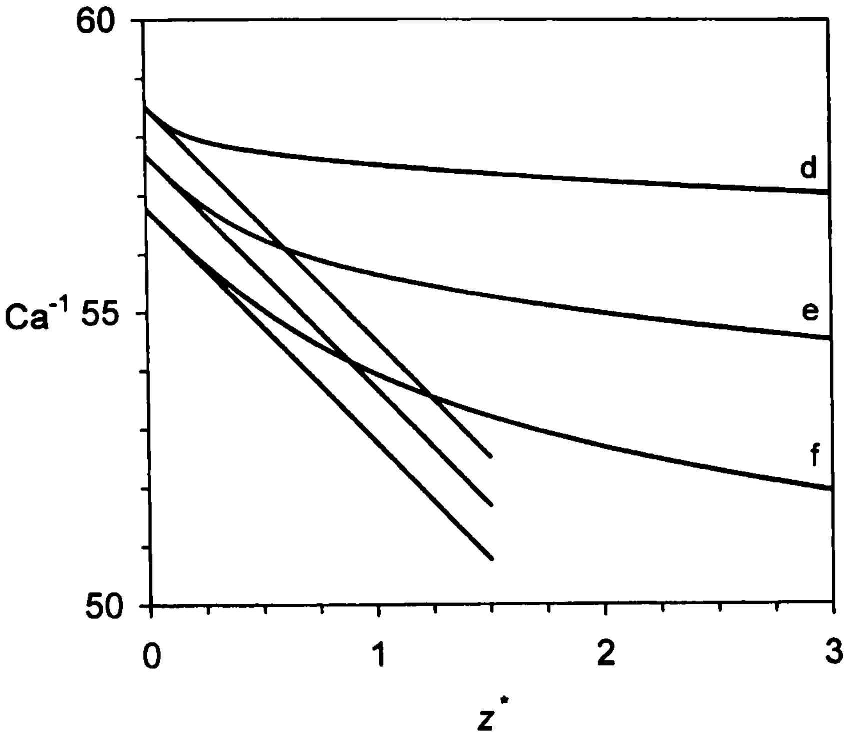

Figure 6.10: Surface tension parameter, $\mathrm{Ca}^{-1} = \mathrm{Ca}^{-1}(z^*)$, near the nozzle exit. All curves exhibit the constant slope of $d(\mathrm{Ca}^{-1})/dz^* = 4$ at $z^* = 0$. The data are for Re = 1950 (R_0 = 0.79 mm), $(2\,\mathrm{Fr})^{-1} = 0.00507$, and c_b = 0.3 mol m^{-3} (d), 0.63 mol m^{-3} (e), and 0.9 mol m^{-3} (f) $\mathrm{C_{16}TAB}$ in water.

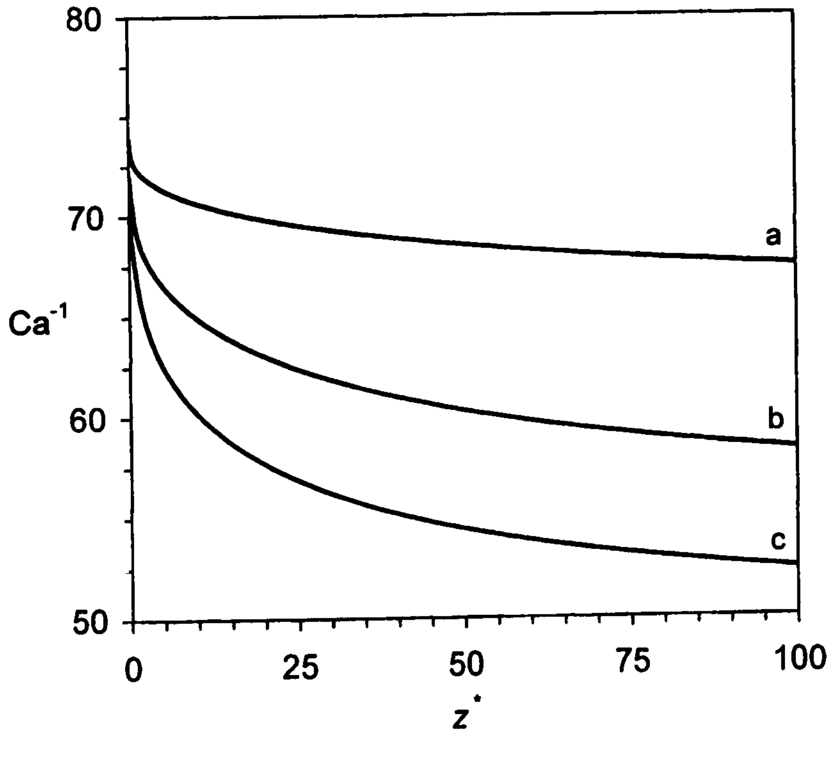

Figure 6.11: Surface tension parameter, $\mathrm{Ca}^{-1}(z^*)$, at Re = 1950 (R_0 = 1.0 mm), $(2\,\mathrm{Fr})^{-1} = 0.01032$, and c_b = 0.3 mol m^{-3} (a), 0.65 mol m^{-3} (b), and 0.9 mol m^{-3} (c) $\mathrm{C_{16}TAB}$ in water.

rection (see Figures 6.9 and 6.11) and retards the jet flow. The theory requires that in the presence of surfactant, the surface velocity at the point of detachment from the nozzle increases linearly with increasing distance from the nozzle, Equation (4.44). For $z^* \gg \ell^*$, the Marangoni effect vanishes and the surface velocity tends towards the pure water value. This behaviour is shown by the graphs in Figure 6.12, for $R_0 = 0.79$ mm and Re = 1950. The transition points of all curves compare well with the values for ℓ^* (see Figure 6.1).

In the experiments, a measurable reduction in surface velocity was only observed at bulk concentrations well above the cmc. As evident from Figure 6.12, the surface velocity retardation is rather low, and occurs very near the nozzle exit, even at bulk concentrations near the cmc. This position on the jet surface is not fully accessible for the lasers (see Chapter 7 for details).

The surface velocity profiles that are obtained with a slightly larger nozzle (R_0 = 1.0 mm) at Re = 1950 for bulk concentrations of c_b = 0.3, 0.65, and 0.9 mol m^{-3} are shown in Figure 6.13. The curves exhibit virtually the same behaviour as the curves (d) to (f) in the previous Figure 6.12, which is not surprising since the surface tension curves in both cases show nearly the same variation with axial distance z^*.

Figure 6.14 compares the surface velocity profile of the water jet with the surface velocity at a bulk concentration of c_b = 0.65 mol m^{-3}. The Reynolds number in this case is slightly lower than before, at Re = 1550.

6.1.6 Radial Bulk Velocity Profiles

The reduction in surface velocity has a significant effect on the velocity in the bulk liquid (see Figure 6.15). The shear stress that acts at the surface must be balanced by viscous traction within the boundary layer underneath the surface, thus altering the boundary layer development, as outlined before in our analytical treatment of the jet flow in the presence of surfactant (see Section 4.1). Very near the nozzle ($z^* = 0.1$), a relatively narrow layer of liquid ($0.05 \times R_0$) suffices to accomodate the reduction in surface velocity. The thickness of the layer grows to twice that value at a distance of one nozzle radius from the nozzle exit, and grows further as the jet travels downwards. At a relatively large axial distance of $10 \times R_0$ from the nozzle, the shear stress at the surface is reduced. Consequently, the viscous traction within the boundary layer is also reduced, and the velcocity gradient in the radial direction, $\partial u^*/\partial r^*$, becomes very small

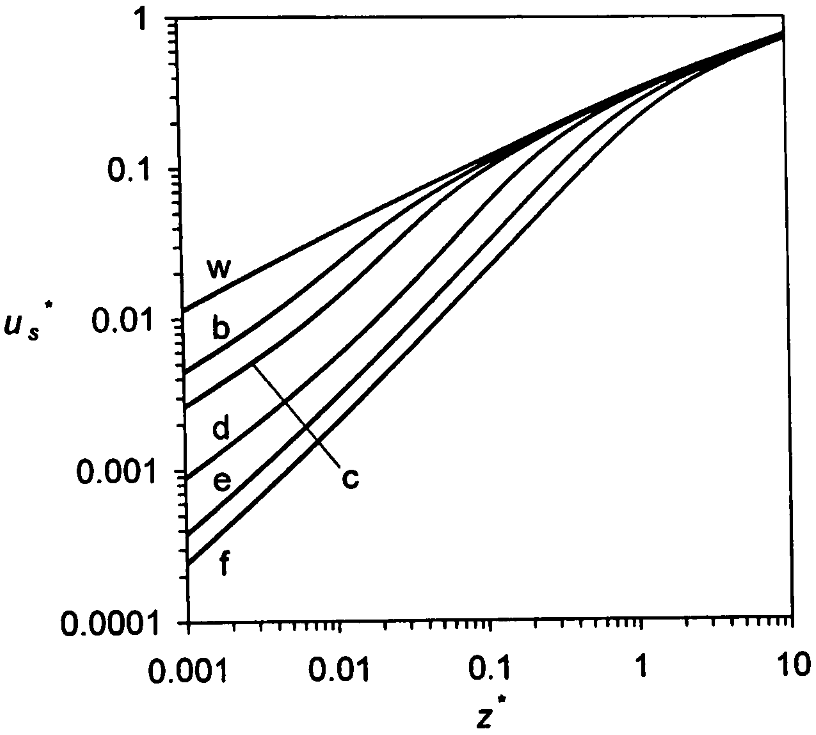

Figure 6.12: Surface velocity profiles, $u_s^* = u_s^*(z^*)$, for the bulk concentrations $c_b = 0.05$ mol m^{-3} (b), 0.1 mol m^{-3} (c), 0.3 mol m^{-3} (d), 0.63 mol m^{-3} (e), and 0.9 mol m^{-3} (f) C_{16}TAB in water at Re = 1950 (R_0 = 0.79 mm) and $(2\,\mathrm{Fr})^{-1} = 0.00507$ in comparison with the $u_s^*(z^*)$ profile of the water jet (w).

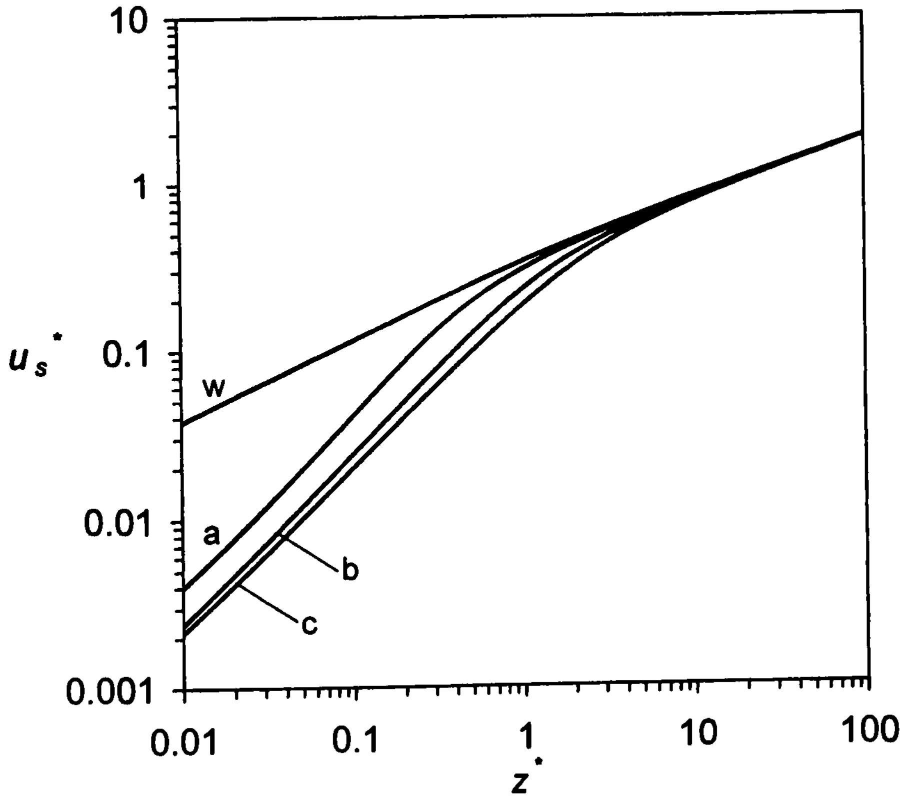

Figure 6.13: Surface velocity profiles, $u_s^*(z^*)$, at Re = 1950 (R_0 = 1.0 mm), $(2\,\mathrm{Fr})^{-1} = 0.01032$, and $c_b = 0.3$ mol m^{-3} (a), 0.65 mol m^{-3} (b), and 0.9 mol m^{-3} (c) C_{16}TAB in comparison with the water jet (w).

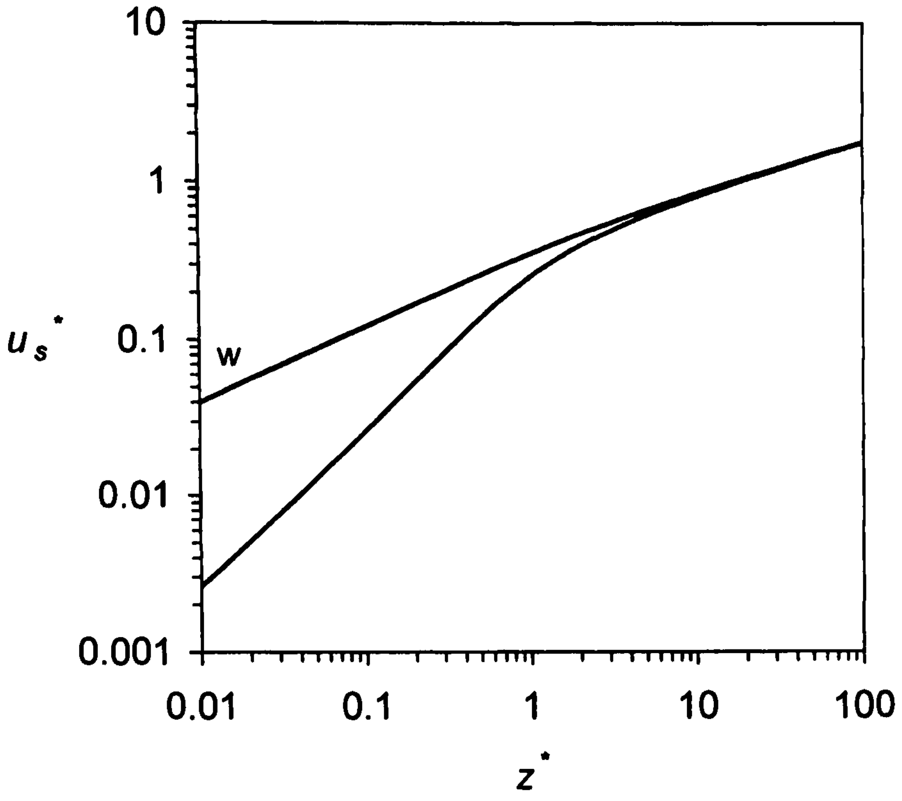

Figure 6.14: Surface velocity profile, $u_s^*(z^*)$, at Re = 1550 (R_0 = 0.79 mm), $(2\,\mathrm{Fr})^{-1}$ = 0.00805, and c_b = 0.65 mol m^{-3} C_{16}TAB in comparison with the water jet (w).

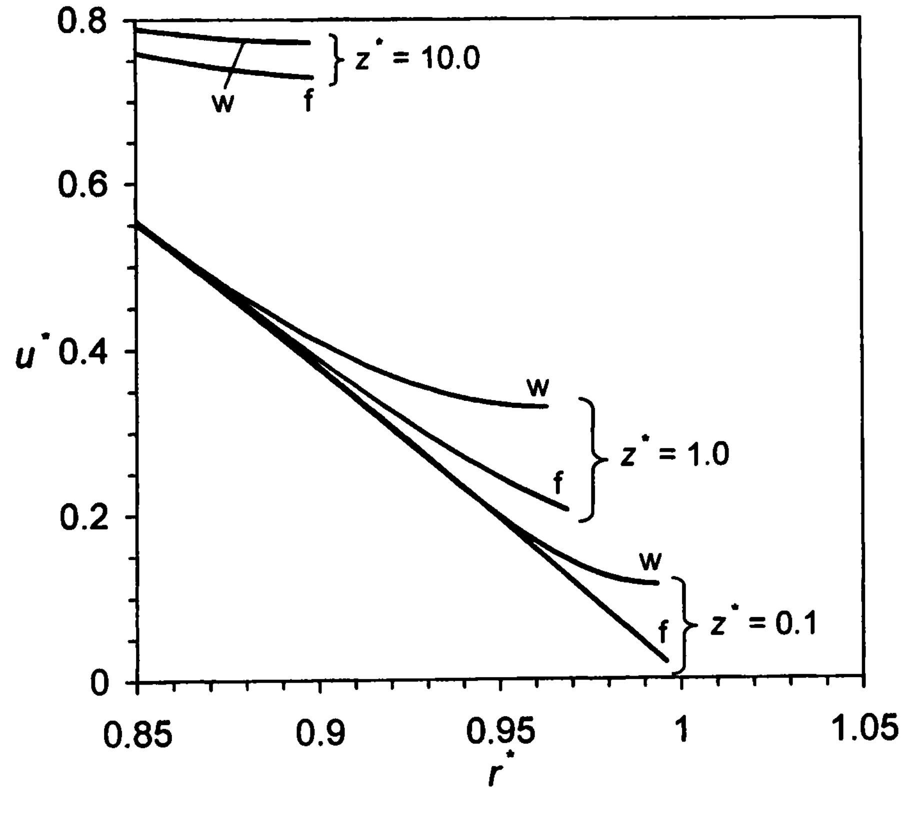

Figure 6.15: Radial velocity profiles, $u^* = u^*(r^*)$, for the water jet (w) and a bulk concentration of c_b = 0.9 mol m^{-3} (f) C_{16}TAB in water at Re = 1950 (R_0 = 0.79 mm) and $(2\,\mathrm{Fr})^{-1}$ = 0.00507.

at the surface. However, a velocity deficit still exists between curve (w) and (f), which is a consequence of the alteration of the boundary layer development at shorter jet lengths.

6.2 C_{14}TAB in the Absence of Micelles

6.2.1 Parameters of the Hybrid CFD Model

Tables 6.6 and 6.7 summarise the dimensionless modelling parameters and the physico-chemical parameters of aqueous C_{14}TAB solution, respectively. As before in the case of aqueous sub-micellar C_{16}TAB, we assume that the density and viscosity of the dilute surfactant solution is accurately described by the pure water values. The coefficient of diffusivity was obtained in a way completely analogous to the procedure used before with C_{16}TAB in Section 6.1. Thus, we use $D^- = 20.8 \times 10^{-10}$ m^2 s^{-1}for the counter-ions, and $D^+ = 4.31 \times 10^{-10}$ m^2 s^{-1} for the cations, which are both given for $T = 298.15$ K. These values were also used by Valkovska *et al.* to model the adsorption of C_{14}TAB at the surface of an overflowing cylinder [52]. We find the value for the effective ionic diffusivity of C_{14}TAB in water, which is given in Table 6.7, from Equation (6.1).

Table 6.6: Dimensionless simulation parameters used in the numerical computations with aqueous solutions of C_{14}TAB below the cmc.

c_b / mol m^{-3}	0.93
w_b / $\times 10^{-6}$	316.665
R_0 / mm	0.79
$\overline{u}_0$ / m s^{-1}	0.81
θ / °	89.99885
Re/2	640
Ca_w^{-1}	89.86
$(2\mathrm{Fr})^{-1}$	0.01181
Sc	1390.82
E	26.94
$\rho D \left(M\overline{u}_0\Gamma_{sat}\right)^{-1}$	0.5821
Figures	6.16 and 6.17

Table 6.7: Values of physical and flow parameters used in the numerical computation with C_{14}TAB below the cmc.

ρ	Density of water	10^3 kg m^{-3}
μ	Viscosity of water	10^{-3} kg m^{-1} s^{-1}
σ_w	Surface tension of water	72.8×10^{-3} N m^{-1}
M	Molecular weight of C_{14}TAB	340.5×10^{-3} kg mol^{-1}
k	Langmuir constant of C_{14}TAB	0.88 mol m^{-3}
Γ_{sat}	Saturation surface coverage of C_{14}TAB	4.48×10^{-6} mol m^{-2}
D	Diffusivity of C_{14}TAB	7.2×10^{-10} m^2 s^{-1}
$\widehat{N}$	Ionic number of C_{14}TAB	2
$\mathcal{R}$	Universal gas constant	8.314 J mol^{-1} K^{-1}
T	Temperature	293.15 K
g	Gravity	9.81 m s^{-2}

The hybrid CFD model requires a value for the sub-surface concentration at the point of detachment, $w_{s,0}$, which we obtain from Equation (4.57) and the Langmuir isotherm, Equation (4.85). For a bulk concentration of c_b = 0.93 mol m^{-3}, a nozzle radius of $R_0 = 0.79$ mm, and a mean nozzle exit velocity of $\overline{u}_0 = 0.81$ m s^{-1}, we find $\Gamma_0^* = 0.1753$, and hence $w_{s,0} = 63.6369 \times 10^{-6}$. From Equation (4.56), we find $\lambda^* = 0.2594$ for the length of the region of detachment.

The computed solution for the downstream sub-surface concentration profile, $w_s(z^*)$, was approximated using the three-parameter fit, Equation (5.51), with $1/m = 3.614$, $\mathcal{X} = 7.1915 \times 10^{14}$, and $\mathcal{Y} = 1.1833 \times 10^{13}$. The values for the two length scales are $\ell^* = 1.6515$ and $L^* = 60.7750$.

6.2.2 Surface Concentration

Figure 6.16 shows measured surface concentration profiles, $\Gamma^*(z^*)$, for three bulk concentrations. For c_b = 0.93 mol m^{-3}, the result of the hybrid CFD model, given by the solid line, is also plotted in Figure 6.16.

A large discrepancy exists between our estimate of Γ_0^* and the value of the first experimental point. In the case of C_{16}TAB, the estimates for Γ_0^* agreed well with the values of the experimental data near the nozzle exit. For C_{14}TAB, the theory seems to largely over-predict this value. This over-prediction becomes more obvious at higher bulk concentrations. For c_b = 1.85 mol m^{-3}, we calculate Γ_0^* =

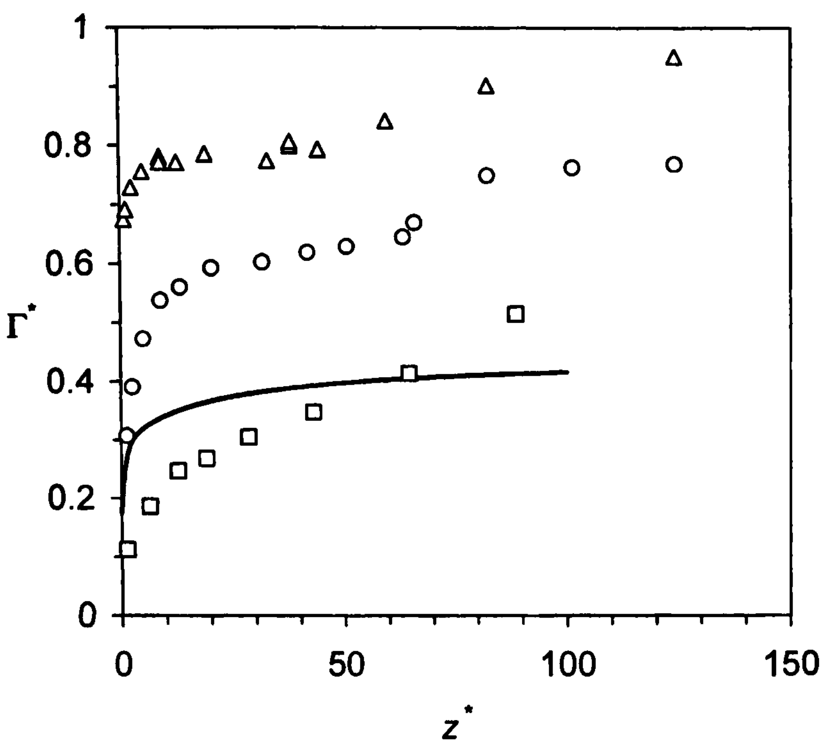

Figure 6.16: Surface concentration, $\Gamma^*(z^*)$, at Re = 1280 (R_0 = 0.79 mm), $(2\,\mathrm{Fr})^{-1} = 0.01181$, and c_b = 0.93 mol m^{-3} (solid line, squares), 1.85 mol m^{-3} (circles), and 3.70 mol m^{-3} (triangles) C_{14}TAB in water.

0.4919, and for $c_b = 3.70$ mol m^{-3}, which equals the critical micelle concentration, we find that the estimate for Γ_0^* is larger than unity, which is not possible. It thus appears that in the case of C_{14}TAB, at least for high bulk concentrations, the relation $\Gamma_0^* \sim w_b^{3/2}$ does not hold. As a consequence of the high value for Γ_0^*, the hybrid CFD model computes a much higher surface coverage in the upstream region of the jet flow than measured in the experiment.

At a bulk concentration of $c_b = 0.93$ mol m^{-3}, from the Langmuir isotherm, the equilibrium surface concentration value is about half the saturation value, that is, $\Gamma_{eq}^* \approx 0.5$. The computed surface concentration values remain below this equilibrium value, at $\Gamma^* \approx 0.4$ for large z^*. In contrast, the measured data not only reach the equilibrium value, but suggest that surfactant continues to adsorb at greater jet lengths, which is not possible. At the cmc, the equilibrium value is about 80% of the saturation value, and we see that the measured data exceed this value as well.

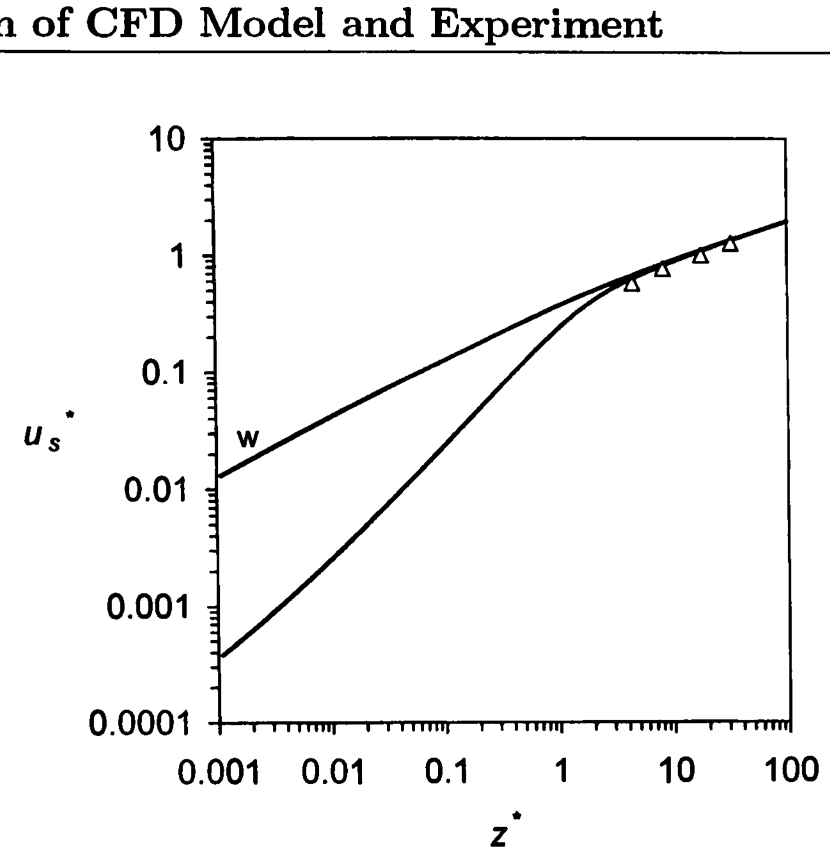

Figure 6.17: Surface velocity, $u_s^*(z^*)$, at Re = 1280 (R_0 = 0.79 mm), $(2\,\mathrm{Fr})^{-1}$ = 0.01181, and c_b = 0.93 mol m^{-3} C_{14}TAB in comparison with the water jet (w). The symbols are measured data.

6.2.3 Surface Velocity

The surface velocity profile that corresponds to the computed surface concentration profile in Figure 6.16 is plotted in Figure 6.17, along with measured data at 0.93 mol m^{-3} and in comparison with the water jet. Pure water values are reached at a downstream distance of about two nozzle radii.

6.3 C_{16}TAB in the Presence of Micelles

This section presents the computed results that were obtained from the hybrid CFD model for bulk concentrations above the cmc. The numerical data are compared with experimental data for both the surface concentration and the surface velocity. The hydrodynamic flow parameters, $\bar{u}_0$ and R_0, are kept constant, as well as the total concentration of surfactant in the bulk, c_T. We use the hybrid CFD model to investigate the effects of variations in the dissociation rate constant and mean aggregation number of the micelle species, k_d and N, respectively, on the adsorption behaviour of C_{16}TAB in the jet.

The motivation of this parameter study is to gain understanding of the effect of micellar break-down kinetics on the adsorption of surfactant. We note that values for the parameters of the micelle kinetic relations, in particular for the dissociation constant, k_d, are rare, and we seek to establish the order of magnitude of this parameter. Furthermore, our model assumes that only one micelle species is present that has a mean aggregation number N. It is desireable to study the sensitivity of the model to variations in N.

The FIDAP journal file that is given in Appendix C.3 computes the coupled mass transfer problem in the presence of micelles.

6.3.1 Parameters of the Hybrid CFD Model

The physical and flow parameters that were employed in the computations are given in Table 6.8. Bain *et al.*, using the Stokes-Einstein relation,

$$D_m = \frac{\mathcal{R}T}{6\pi\mu_w r_m}, \tag{6.2}$$

calculated the coefficient of diffusivity of the micelle species to give $D_m = 1.0 \times 10^{-10}$ m^2 s^{-1} at $T = 298.15$ K [32]. Their calculation assumed micelles of spherical shape, with a radius of $r_m = 25$ Å. We use this value for D_m in our hybrid CFD model.

Lianos and Zana measured values ranging from 88 to 92 for the mean aggregation number of the micelle species [218]. In this work, we assume a value of $N = 90$, which represents the lower limit for the mean aggregation number, the upper limit being $N = 120$. The resulting values for the equilibrium constant, K, at the given total bulk concentration of $c_T = 1.5$ mol m^{-3} C_{16}TAB are summarised in Table 6.9, together with the values for the dissociation and formation rate constants of the micelle species, k_d and k_f, respectively. K was calculated using Equation (5.30) and is also plotted in Figure 5.6. We have chosen a value for k_d, which, through the given values for K and N, determines the value for k_f. In this way, parameter studies for k_d and N could be carried out.

An estimate for the surface concentration at the point of detachment, Γ_0^*, must be forwarded to the hybrid CFD model. This estimate is provided by Equation (4.84). Several values for Γ_0^* at different total bulk concentrations for C_{16}TAB at Re = 1950 ($R_0 = 0.79$ mm) are plotted in Figure 6.18. These values are shown together with the estimates for Γ_0^* at sub-micellar bulk concentrations. We had previously shown that the presence of micelles enhances the mass transfer

Table 6.8: Values of physical and flow parameters used in the numerical computations with $C_{16}TAB$ above the cmc.

R_0	Nozzle radius	0.79×10^{-3} m
$\bar{u}_0$	Mean nozzle exit velocity	1.236 m s^{-1}
c_T	Total molar concentration of $C_{16}TAB$	1.5 mol m^{-3}
c_{cmc}	Critical micelle concentration of $C_{16}TAB$	0.92 mol m^{-3}
θ	Downstream contact angle	89.97 °
ρ	Density of water	10^3 kg m^{-3}
μ	Viscosity of water	10^{-3} kg m^{-1} s^{-1}
σ_w	Surface tension of water	72.8×10^{-3} N m^{-1}
M	Molecular weight of $C_{16}TAB$	364.5×10^{-3} kg mol^{-1}
k	Langmuir constant of $C_{16}TAB$	0.23 mol m^{-3}
Γ_{sat}	Saturation surface coverage of $C_{16}TAB$	3.9×10^{-6} mol m^{-2}
D	Diffusivity of $C_{16}TAB$ (monomers)	7.5×10^{-10} m^2 s^{-1}
D_m	Diffusivity of $C_{16}TAB$ (micelles)	1.0×10^{-10} m^2 s^{-1}
$\hat{N}$	Ionic number of $C_{16}TAB$	2
$\mathcal{R}$	Universal gas constant	8.314 J mol^{-1} K^{-1}
T	Temperature	293.15 K
g	Gravitational acceleration	9.81 m s^{-2}

of surfactant monomers to the surface (see Equation (4.70) in Section 4.3.1), which means that all estimates for Γ_0^* above the cmc must be higher in their

Table 6.9: Values of the mean aggregation numbers, N, the equilibrium constants, K, and the dissociation and formation rate constants, k_d and k_f, respectively (see also Figure 5.6). The total bulk concentration is c_T = 1.5 mol m^{-3} $C_{16}TAB$ (c_{cmc} = 0.92 mol m^{-3}).

$\Gamma^*(z^*)$ Figures (curve)	N	$K \Big/ \frac{\mathrm{mol}^{1-N}}{\mathrm{m}^{3-3N}}$	$k_d \Big/ \frac{1}{\mathrm{s}}$	$k_f \Big/ \frac{\mathrm{mol}^{1-N}}{\mathrm{m}^{3-3N}\,\mathrm{s}}$
6.21 (a)	90	11.7026	1.0	11.7026
6.21 (b)	90	11.7026	10.0	117.026
6.21 (c) and 6.22 (a)	90	11.7026	100.0	1170.26
6.21 (d)	90	11.7026	1000.0	11702.6
6.22 (b)	120	107.0798	100.0	10707.98

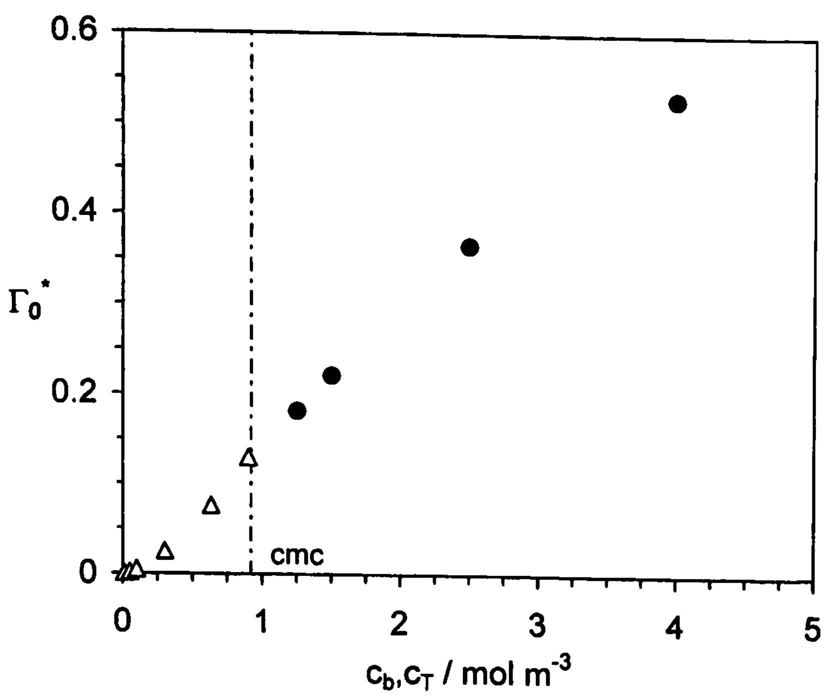

Figure 6.18: Surface concentration at the point of detachment, Γ_0^*, for $C_{16}TAB$ at Re = 1950 (R_0 = 0.79 mm) as a function of the bulk concentration, c_b, in the region below the cmc (Equation (4.57), open triangles), and as a function of the total concentration, c_T, in the region above the cmc (Equation (4.84), closed circles).

values than the value for Γ_0^* at the cmc. This behaviour is shown by the data in Figure 6.18.

The value for Γ_0^* that corresponds to $c_T = 1.5$ mol m^{-3} $C_{16}TAB$ at Re = 1950, from Figure 6.18, is $\Gamma_0^* = 0.2212$. This value is transformed to the corresponding sub-surface concentration value, $w_{s,0}$, by means of the Langmuir isotherm. We find the value $w_{s,0} = 23.8128 \times 10^{-6}$, which is used in the hybrid CFD model.

We have outlined in Section 5.9.2 that at high concentrations in the bulk, the surface approaches a state of equilibrium at the downstream position. The simple power-law relation, Equation (5.42), which approximated the numerical downstream solution $w_s(z^*)$ well if only small to moderate amounts of surfactant were dissolved, does not yield a satisfactory representation of the computed downstream data for $w_s(z^*)$ at high bulk concentrations.

A second length scale, L^*, which is defined in Equation (5.45), was introduced to take the equilibration of the surface into account, when $w_s \rightarrow w_b$ as z^* becomes large. Equation (5.51), which contains three fitting parameters $\mathcal{X}$, $\mathcal{Y}$, and $1/m$, gave the approximation of the numerical downstream data for $w_s(z^*)$. With the values for the three fitting parameters known, the matched solution for $w_s(z^*)$

that spans the entire length of the sub-surface is given by Equation (5.46). The surface equation of state was linked to Equation (5.46), and the computation was carried out.

An iterative procedure was applied, during which several computations, usually fewer than ten, were necessary to attain stable values for the three fitting parameters (see Figure 6.19). In contrast to the computations without micelles, the numerics required significantly more computational time (up to 10 hours on a Windows 2000 PC with 512 Mb RAM and a 1.0 GHz processor) and memory, when the concentration field of the micelles in the jet was computed along with the distribution of monomers in the jet.

Figure 6.20 shows the dependence of the downstream fitting parameters on the micelle dissociation rate constant for a fixed mean aggregation number (see also Table 6.10, which includes values for $\mathcal{X}$, $\mathcal{Y}$, and $1/m$ for a different mean aggregation number). The values for the two length scales ℓ^* and L^*, which were computed using the values for $\mathcal{X}$, $\mathcal{Y}$, and $1/m$, are also displayed in Table 6.10.

6.3.2 Surface Concentration

Effect of the Dissociation Rate Constant

At a constant mean aggregation number of $N = 90$, we have varied the value of the dissociation rate constant, k_d, to investigate its effect on the adsorption behaviour in the jet. The result of this parameter study is shown in Figure 6.21, where four $\Gamma^*(z^*)$ curves are shown in comparison with one set of experimental

Table 6.10: Values of the parameters of the least-squares fit to the numerical downstream solution $w_s(z^*)$, Equation (5.51), and the resulting values for the length scales ℓ^* and L^*. The total bulk concentration is $c_T = 1.5$ mol m^{-3} $C_{16}TAB$ ($c_{cmc} = 0.92$ mol m^{-3}).

k_d / s^{-1}	N	$\mathcal{X}$	$\mathcal{Y}$	$1/m$	ℓ^*	L^*
1.0	90	3.4516×10^9	2.0488×10^7	2.066	0.7498	168.4693
10.0	90	6.7004×10^8	1.9998×10^6	1.906	0.6835	335.0535
100.0	90	9.0086×10^5	2.7207×10^4	1.285	0.4276	33.1113
100.0	120	9.0096×10^5	2.7098×10^4	1.285	0.4548	33.2482
1000.0	90	3.0616×10^7	7.8812×10^5	1.700	2.3741	38.8469

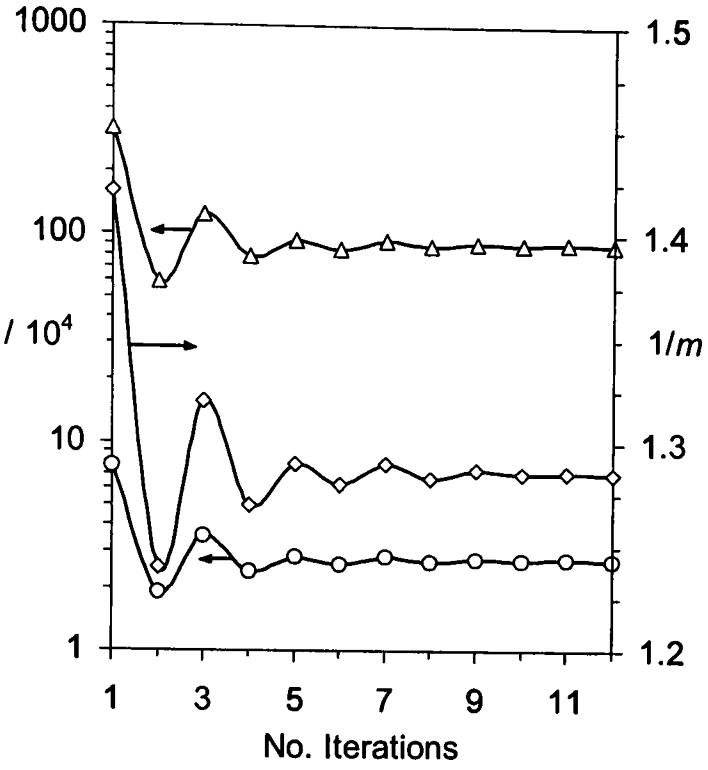

Figure 6.19: Dynamic behaviour of the parameters $\mathcal{X}$ ($\triangle$), $\mathcal{Y}$ ($\circ$), and $1/m$ ($\Diamond$) of the least-squares fit of Equation (5.51) to the downstream solution $w_s(z^*)$. The data are for $c_T = 1.5$ mol m^{-3} C$_{16}$TAB, Re = 1950 ($R_0 = 0.79$ mm), $N = 90$, $k_d = 100$ s^{-1}, and $K = 11.7026$ mol^{-89} m^{267}.

data. For $k_d < 100$ s^{-1}, curves (a) and (b), variations in k_d affect the solution for $\Gamma^*(z^*)$ in both the downstream and the upstream region of the jet. For $k_d = 100$ s^{-1}, curve (c), the numerical data at the downstream position ($z^* > 50$) seem to plateau at a surface concentration value of $\Gamma^* \approx 0.75$. A further increase of the value of k_d to 1000 s^{-1} affects the solution only in the upstream region, curve (d). The computed results seem to suggest that for $k_d > 1000$ s^{-1}, the solution for $\Gamma^*(z^*)$ becomes rather insensitive to variations in k_d.

The expanding jet surface causes monomers to diffuse to the surface. This diffusion process in turn disturbs the equilibrium between the monomers and the micelles. As a consequence of this disruption, micelles release monomers in an attempt to re-establish equilibrium between monomers and micelles. The whole process is thus governed by two time scales—the time scale of surface expansion, given by the reciprocal of the surface expansion rate, $(du_s/dz)^{-1}$, and the time scale over which micelles disintegrate, given by the reciprocal of the dissociation rate constant, $1/k_d$.

The graphs in Figure 6.21 were computed for dissociation rate constants of

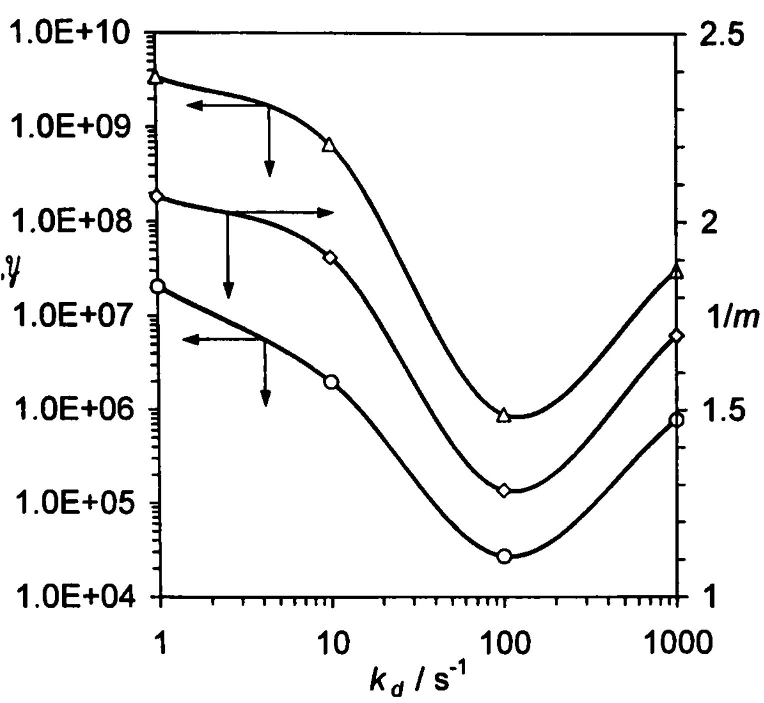

Figure 6.20: Parameters $\mathcal{X}$ (△), $\mathcal{Y}$ (○), and $1/m$ (◇) of the least-squares fit of Equation (5.51) to the downstream solution $w_s(z^*)$ as a function of the dissociation rate constant, k_d, at c_T = 1.5 mol m^{-3} C_{16}TAB and Re = 1950 (R_0 = 0.79 mm). The mean aggregation number is N = 90, and the equilibrium constant is K = 11.7026 mol^{-89} m^{267}.

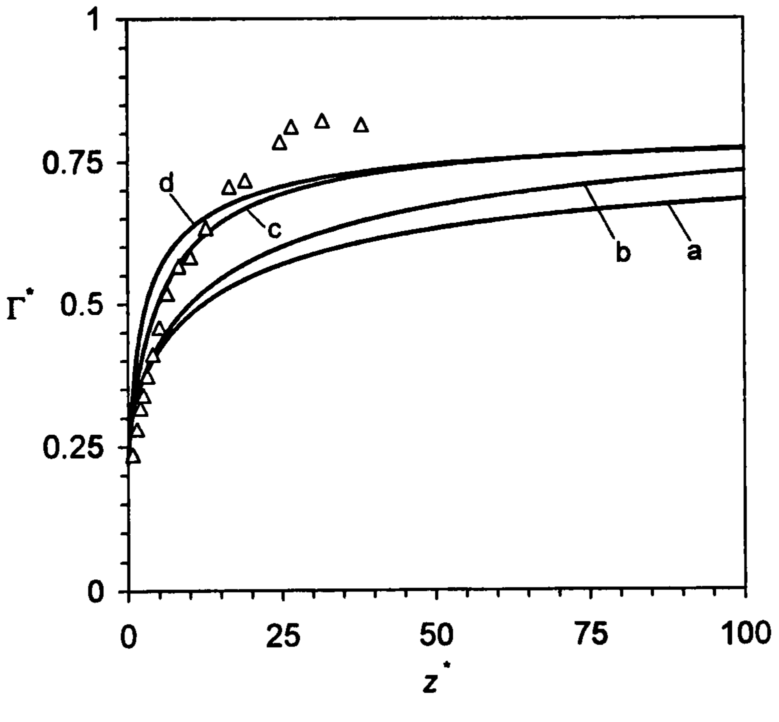

Figure 6.21: Surface concentration curves, $\Gamma^*(z^*)$, for varying dissociation rate constants, k_d, in comparison with experimental data (symbols). The total concentration is c_T = 1.5 mol m^{-3} C_{16}TAB at Re = 1950 (R_0 = 0.79 mm). The data are for N = 90 and k_d = 1.0 s^{-1} (a), 10.0 s^{-1} (b), 100.0 s^{-1} (c), and 1000.0 s^{-1} (d).

$1 \leqslant k_d \leqslant 1000\ \mathrm{s}^{-1}$, that is, $1 \geqslant 1/k_d \geqslant 10^{-3}$ s. The surface expansion rate varies along the jet surface and has its maximum value within the region of detachment. Using our theory, Equation (4.44), we can estimate this maximum value to give $du_s/dz \sim 10^3\ \mathrm{s}^{-1}$, from which follows that $(du_s/dz)^{-1} \sim 10^{-3}$ s. With increasing distance from the nozzle exit, the surface expansion rate decreases rapidly, and the time scale of surface expansion becomes larger. Thus for small values of k_d, the transport of monomers to the surface is determined by the surface expansion rate in the region near the nozzle exit, and the break-down of micelles enhances the transport of monomers to the surface only in the region further away from the nozzle exit. On the other hand, for large values of k_d, the disintegration of micelles enhances the transport of monomers to the surface near the nozzle as well. The graphs in Figure 6.21 reflect this behaviour.

We note here that in our analytical treatment of monomer adsorption in the presence of micelles, Section 4.3.1, we assumed the case of infinitely fast micellar break-down kinetics, that is, $k_d \to \infty$ and $1/k_d \to 0$.

In the upstream region of the jet, good agreement between computation and experiment is obtained with a value for k_d that is of the order 100 s^{-1}. Using the stopped-flow method and conductometric registration, Czerniawski [219] measured the rate of micellisation of C_{16}TAB in water and gave a value of $k_d = 47.6\ \mathrm{s}^{-1}$ at a temperature of 25°C and for total concentrations of 1 to 10 mol m^{-3}. This value agrees reasonably well with the value found from our CFD computation. Chan *et al.* [220], on the other hand, obtained a value of $k_d = 0.4\ \mathrm{s}^{-1}$ at 30°C and for a total concentration of 1.5 mol m^{-3} C_{16}TAB in water.

The asymptotic values for the surface concentration in the experiment and in the computation at large z^* disagree. Above the cmc and in the case of C_{16}TAB, we would expect an equilibrium value of $\Gamma^*_{eq} \approx 0.8$ at larger distances from the nozzle. This value seems to have been observed in the experiments, but the computations exhibit a lower value, presumably because the distance of $z^* = 100$ (the length of the computational domain) is not sufficient for equilibrium at the surface to be reached.

Effect of the Mean Aggregation Number

The effect of the mean aggregation number on the adsorption of C_{16}TAB in the jet was investigated at a fixed micelle dissociation rate constant of $k_d = 100\ \mathrm{s}^{-1}$.

The computations were carried out with two different mean aggregation numbers of $N = 90$ and 120 (see Table 6.9 for the values of the equilibrium constants, and Table 6.10 for the values of the downstream solution fitting parameters and length scales). The results of this parameter study for $\Gamma^*(z^*)$ are shown in Figure 6.22, curves (a) and (b), where curve (a) is identical with curve (c) in Figure 6.21.

It is evident from the graphs in Figure 6.22 that the effect of the mean aggregation number on the adsorption behaviour is small, as both curves (a) and (b) virtually cover each other up. Also plotted in Figure 6.22 is a relative deviation factor $\mathcal{F}(z^*)$, curve (c), given by

$$\mathcal{F} = \frac{|\Gamma^*(N=120) - \Gamma^*(N=90)|}{\Gamma^*(N=90)} \times 100\%, \tag{6.3}$$

which is a measure of the relative deviation of the two solutions along the jet surface. In Equation (6.3), Γ^* $(N = 90)$ is given by curve (a), and Γ^* $(N = 120)$ is given by curve (b). Although the relative deviation increases with increasing jet length, it is very small, reaching a value of only little more than 0.05% at the outlet of the computational domain. The effect of the mean aggregation number N on the adsorption behaviour in the jet is thus negligibly small.

6.3.3 Radial Bulk Concentration Profiles

Radial monomer and micelle bulk concentration profiles, $w(r^*)$ and $w_m(r^*)$, are shown in Figures 6.23 and 6.24, respectively, for three different axial downstream positions. The profiles of the monomer concentrations very nearly resemble those shown in Figure 6.8, which were obtained under sub-micellar conditions. However, due to the presence of micelles, which enhances the transport of surfactant monomers to the surface, the profiles in Figure 6.23 show higher values for the sub-surface concentrations, $w_s(z^*)$, at the different axial positions.

The profiles of the micelle concentration in the bulk liquid in Figure 6.24 show that the boundary layer for this species—the distance from the surface to the point at which the bulk value, $w_{m,b}$, is reached—has about the same thickness as that of the surfactant monomers in Figure 6.23. The data shown in Figures 6.25 and 6.26, where the bulk concentration profiles $w(r^*)$ and $w_m(r^*)$ within the boundary layer at $z^* = 10$ and 50 are displayed, show clearly that the concentrations reach their respective bulk value at about the same distance

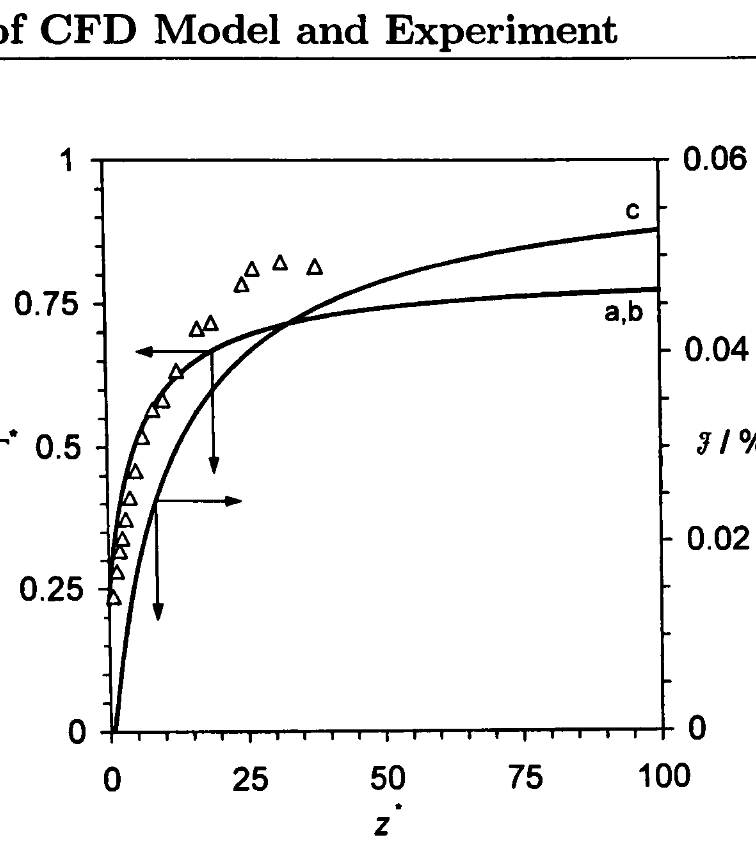

Figure 6.22: Surface concentration curves, $\Gamma^*(z^*)$, for $N = 90$ (a) and 120 (b), in comparison with experimental data (symbols). The total concentration is $c_T = 1.5$ mol m^{-3} C_{16}TAB at Re = 1950 ($R_0 = 0.79$ mm). The dissociation rate constant is $k_d = 100.0$ s^{-1} in both cases. Curve (c) is the relative deviation, $\mathcal{F}$, according to Equation (6.3).

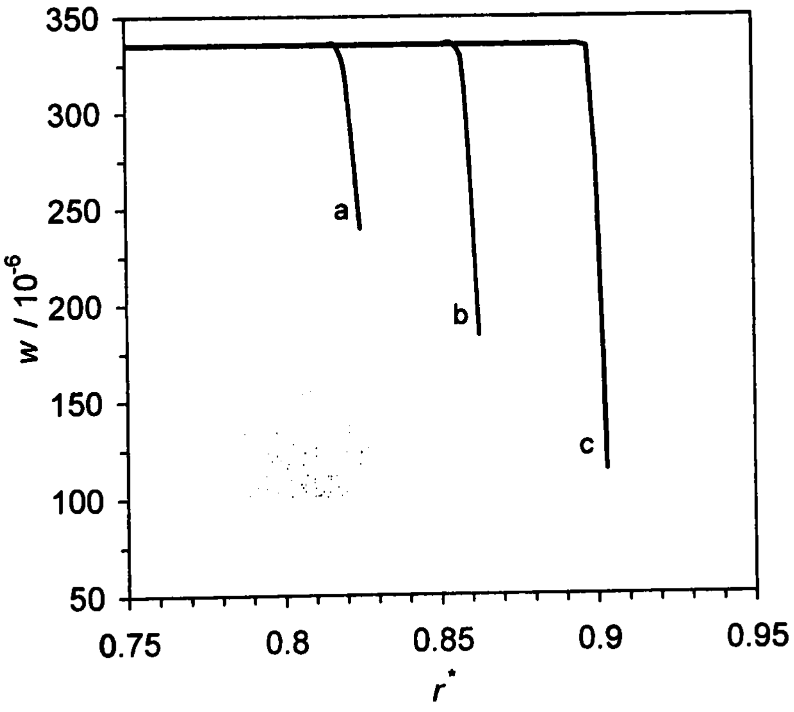

Figure 6.23: Monomer bulk concentration profiles, $w(r^*)$, at three different axial downstream positions, $z^* = 50$ (a), 25 (b), and 10 (c), for $c_T = 1.5$ mol m^{-3} C_{16}TAB and Re = 1950 ($R_0 = 0.79$ mm). The mean aggregation number is $N = 90$ and the dissociation rate constant is $k_d = 100.0$ s^{-1}.

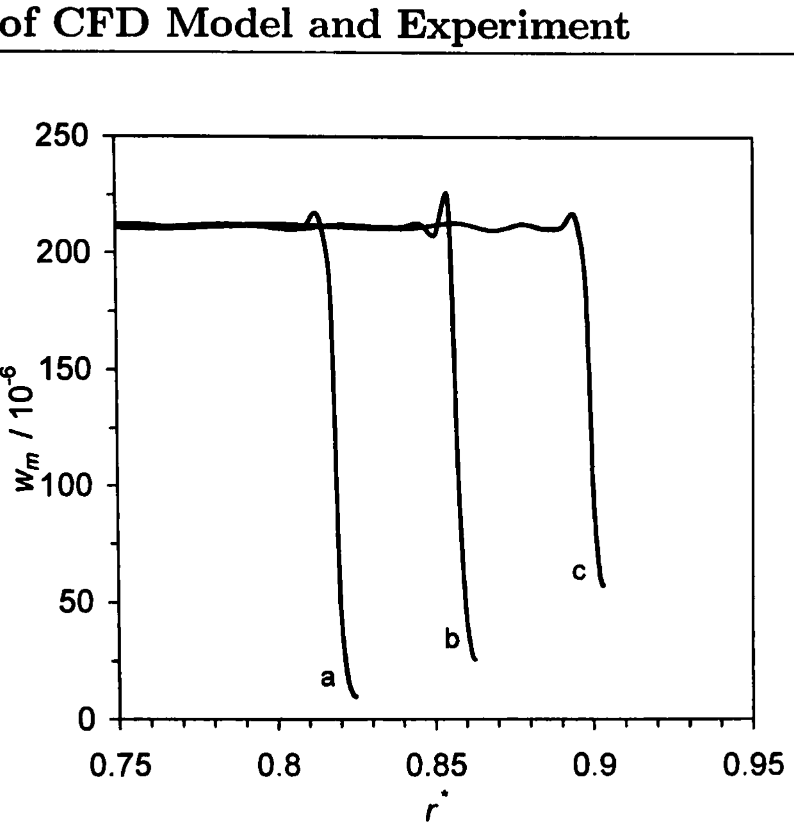

Figure 6.24: Micelle bulk concentration profiles, $w_m(r^*)$, at three different axial downstream positions, $z^* = 50$ (a), 25 (b), and 10 (c), for $c_T = 1.5$ mol m^{-3} $C_{16}TAB$ and Re = 1950 ($R_0 = 0.79$ mm). The mean aggregation number is $N = 90$ and the dissociation rate constant is $k_d = 100.0$ s^{-1}.

from the surface. The numerical solutions found by Breward and Howell exhibit the same behaviour [64]. The data shown in Figures 6.25 and 6.26 correspond to curves (a) and (c) in Figures 6.23 and 6.24.

Within our model, the micelle species is treated as surface-inactive through the zero-flux boundary condition at the surface, Equation (5.37). The micelle concentration profiles in Figures 6.25 and 6.26 reflect this boundary condition at the surface, where the gradients $\partial w_m / \partial r^*$ exhibit a slope of zero.

At small z^*, where the surface expands rapidly, the transport of monomers to the surface is dominated by the rate of surface expansion. At large z^*, the time scale of micelle disintegration is significant compared to the time scale of surface expansion. In this region, the contribution of the disintegration of micelles to the transport of monomers to the surface is larger, and hence the lower values for $w_{m,s}$ for large z^*.

Thus, if the micelles disintegrate at a finite rate k_d, then a region exists over which both micelles and monomers are present together, as the monomer concentration falls below the cmc. This case may be contrasted with the assumption of infinitely fast micelle break down ($k_d \rightarrow \infty$), which we assumed in

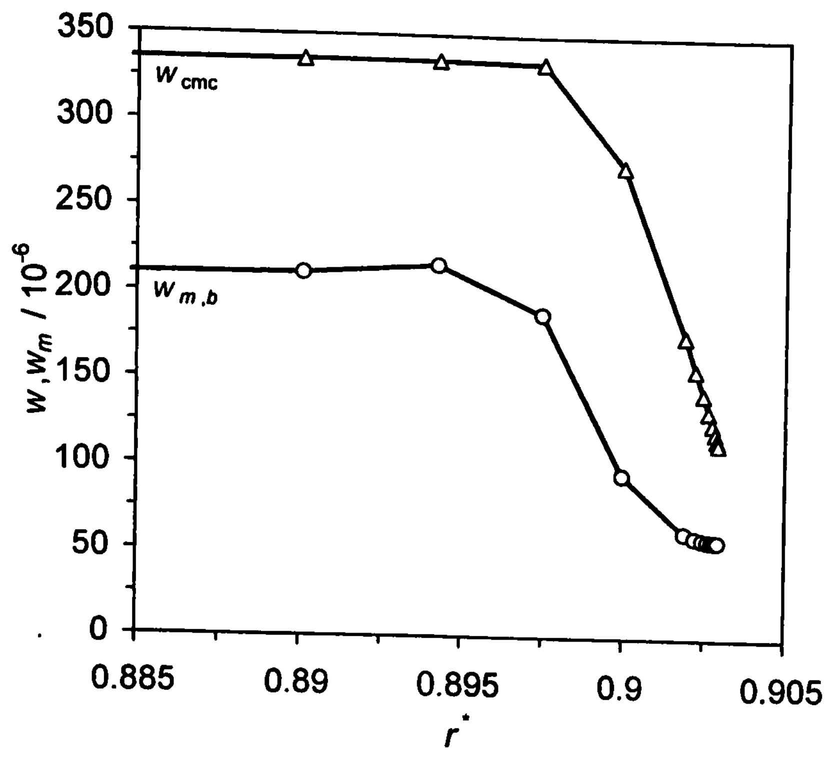

Figure 6.25: Bulk concentration profiles, $w(r^*)$ and $w_m(r^*)$, of monomers ($\triangle$) and micelles ($\circ$) in the boundary layer at $z^* = 10$. The data are for c_T = 1.5 mol m^{-3} $C_{16}TAB$ and Re = 1950 (R_0 = 0.79 mm). The mean aggregation number is $N = 90$ and the dissociation rate constant is $k_d = 100.0$ s^{-1}.

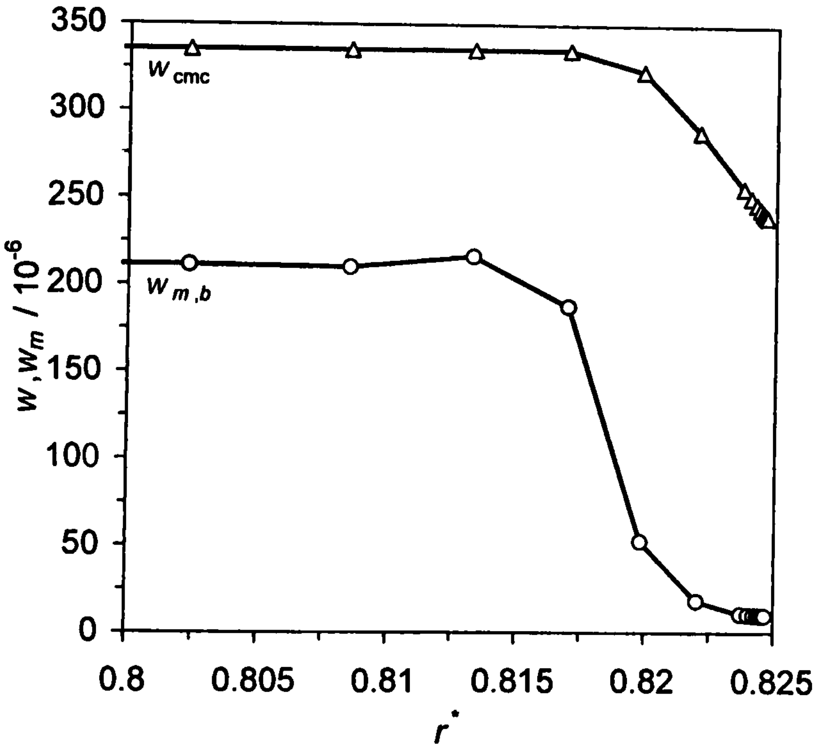

Figure 6.26: Bulk concentration profiles, $w(r^*)$ and $w_m(r^*)$, of monomers ($\triangle$) and micelles ($\circ$) in the boundary layer at $z^* = 50$. The data are for c_T = 1.5 mol m^{-3} $C_{16}TAB$ and Re = 1950 (R_0 = 0.79 mm). The mean aggregation number is $N = 90$ and the dissociation rate constant is $k_d = 100.0$ s^{-1}.

our theoretical treatment in Section 4.3.1 (see Figure 4.6). As the rate of disintegration decreases, the concentration of micelles within the diffusion boundary layer increases. As a consequence of this increase in the micelle concentration at low k_d, the monomer concentration decreases, since less monomers are supplied from the disintegrating micelles. Curves (a) and (b) in Figure 6.21 show this situation at low k_d. When the rate of disintegration is very low, so that $k_d \rightarrow 0$, the bulk concentration of micelles exists up to the surface.

As before in the sub-micellar model, the surfactant monomer profiles are smooth and well-behaved, and do not show any oscillations in the solution. The profiles of the micelle species on the other hand exhibit some oscillatory behaviour, which is particularly pronounced at the edge of the boundary layer within the bulk liquid. This behaviour may be related to the discretisation of the computational flow domain. Although the mesh allows for sufficient accuracy when solving the monomer mass transfer, this may not be the case for solving the micelle mass transfer. Computations on a mesh that has a greater density towards the edge of the boundary layer would be necessary to establish the impact of the discretisation of the flow domain on the solution for $w_m(r^*, z^*)$. The data displayed in Figures 6.25 and 6.26 show that as the boundary layer grows, with increasing distance from the nozzle exit, less nodes underneath the surface are necessary to accurately compute the gradients at the surface. Redistributing the nodes within the boundary layer would allow for greater density at the inner edge of the boundary layer without increasing the total number of elements within the computational flow domain, which ensures that the computational efforts remain the same. Also, the upwinding scheme employed to suppress the occurrence of such oscillations, which adds a small amount of artificial diffusion in the streamwise direction only, may not sufficiently work for the micelle species transport problem.

6.3.4 Surface Tension

The curves of the computed surface tension parameter, $\mathrm{Ca}^{-1}(z^*)$, which are plotted in Figure 6.27, correspond to the surface concentration curves in Figure 6.21. We see that for larger values of k_d, the surface tension curves reach a plateau at long axial distances from the nozzle. This plateau defines the state of equilibrium at the surface for this particular surfactant.

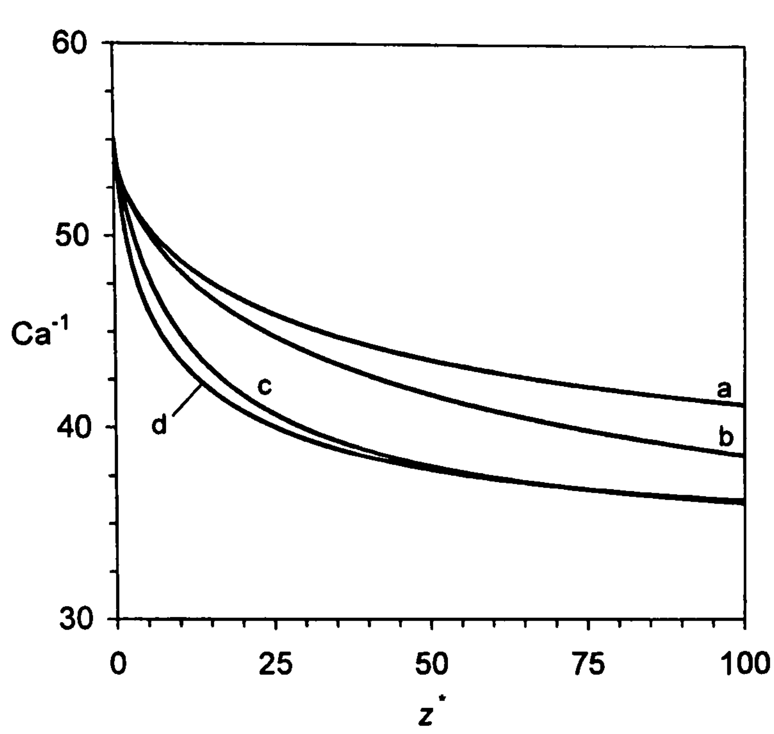

Figure 6.27: Surface tension parameter, $\mathrm{Ca}^{-1}(z^*)$, for varying dissociation rate constants, k_d. The total concentration is $c_T = 1.5$ mol m^{-3} $\mathrm{C_{16}TAB}$ at Re = 1950 ($R_0 = 0.79$ mm). The data are for $N = 90$ and $k_d = 1$ s^{-1} (a), 10 s^{-1} (b), 100 s^{-1} (c), and 1000 s^{-1} (d).

6.3.5 Surface Velocity

The computed surface velocity curves, $u_s^*(z^*)$, that correspond to the computed surface concentration data in Figure 6.21 are plotted in Figure 6.28, curves (a) to (d), along with one set of experimentally obtained surface velocity data. The four curves show the effect of the micelle dissociation rate constant, k_d, on the velocity retardation at the surface.

In general, we can say that the point of transition from the linear to the far-field region of the jet moves towards larger values with an increase in k_d. In the cases of curves (a) and (b), where $k_d = 1$ s^{-1} and 10 s^{-1}, respectively, this point of transition lies at about $z^* = 1$. At the highest value for k_d, curve (d), this point has moved downstream, to about $z^* = 5$. Curve (c) shows an intermediate behaviour.

Experimental velocity data are available to within a distance of about one nozzle radius from the nozzle exit. At this downstream distance, the velocity reduction as a consequence of the surface shear has largely subsided, and the surface velocity is approaching the behaviour of the water jet. We were thus not able to generate experimental data that show the reduction in surface velocity

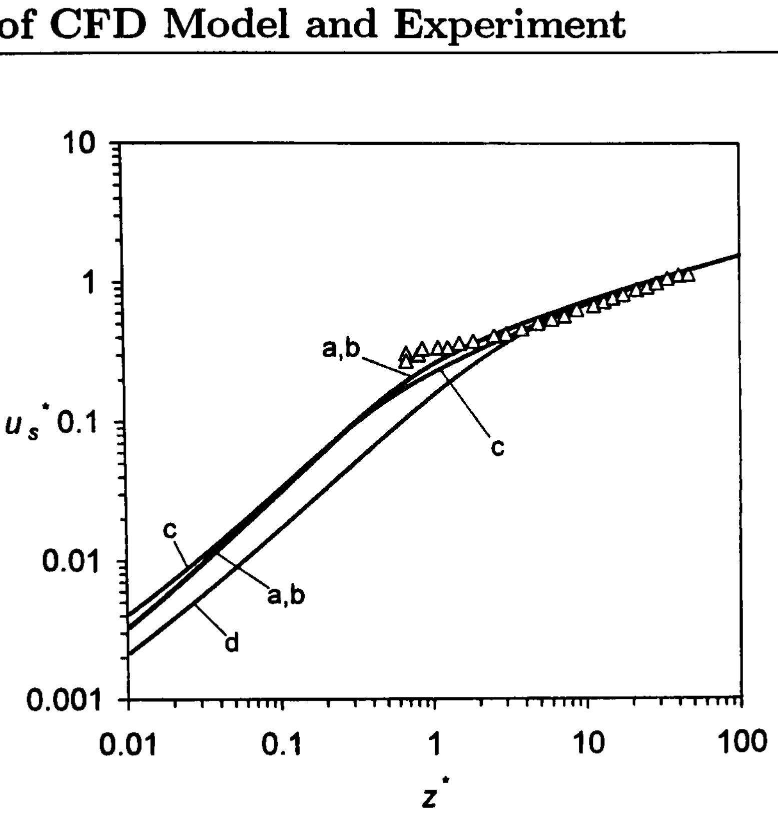

Figure 6.28: Surface velocity curves, $u_s^*(z^*)$, for varying dissociation rate constants, k_d, in comparison with experimental data (symbols). The data are for c_T = 1.5 mol m^{-3} C_{16}TAB at Re = 1950 (R_0 = 0.79 mm), N = 90, and k_d = 1 s^{-1} (a), 10 s^{-1} (b), 100 s^{-1} (c), and 1000 s^{-1} (d).

at a total bulk concentration of 1.5 mol m^{-3} C_{16}TAB. Larger quantities of surfactant had to be dissolved in order to identify the Marangoni flow in the jet experimentally. Appendix E shows surface velocity measurements that were carried out at total bulk concentrations of c_T = 2.5 mol m^{-3} (Re = 1550) and c_T = 4.0 mol m^{-3} (Re = 1950) C_{16}TAB, which clearly indicate the reduction in surface velocity.

Chapter 7

Experimental Investigation

The liquid jet was designed to generate a stable expanding surface under steady-state conditions. Specific requirements in the design were (*i*) an axisymmetric fully developed laminar flow profile, (*ii*) the minimisation of wetting at the nozzle tip, (*iii*) isolation from sources of vibration to retard jet break-up and to avoid interference with the optical systems, (*iv*) a minimum total volume, (*v*) accurate thermostatting, and (*vi*) the control of foaming [208].

7.1 Nozzle Design

It may be shown that the pressure drop, Δp, in a vertical capillary pipe of length l is given by [221]

$$\frac{\Delta p}{l} = \frac{8\mu\overline{u}_0}{R_0^2} - \rho g. \tag{7.1}$$

The derivation of Equation (7.1) assumes fully developed laminar flow in the pipe (see Figure 7.1). In a gravity-driven flow, the pressure drop is determined by the pressure head in the reservoir, that is,

$$\Delta p = \rho g H, \tag{7.2}$$

where H is liquid height in the reservoir. Substituting Δp in Equation (7.1) with Equation (7.2) gives

$$\frac{H}{l} = \frac{8\mu\overline{u}_0}{\rho g R_0^2} - 1. \tag{7.3}$$

Using Torricelli's theorem, we can express the mean nozzle exit velocity as a function of H and l,

$$\overline{u}_0 = \sqrt{2g\,(H+l)}. \tag{7.4}$$

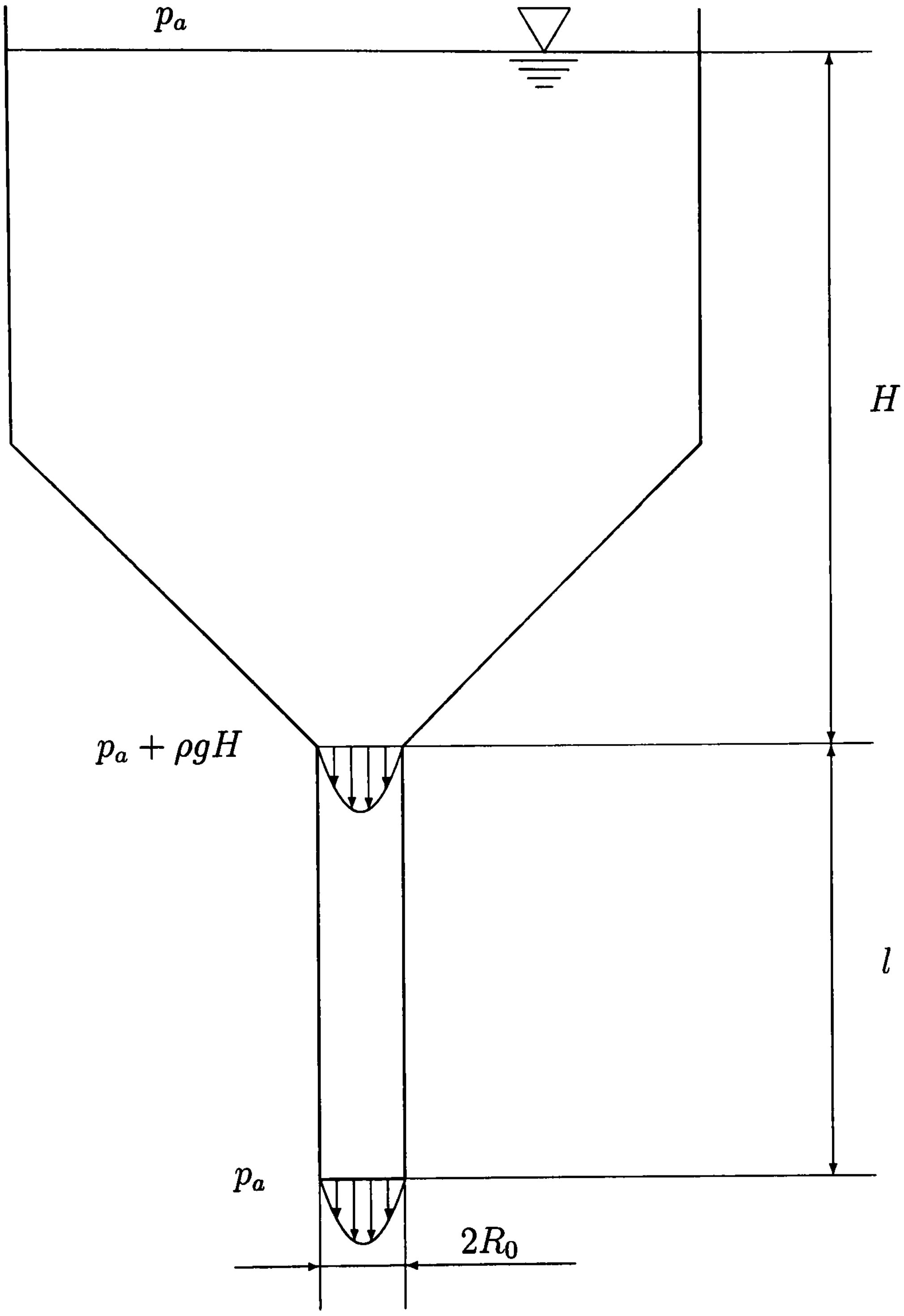

Figure 7.1: Reservoir liquid height, H, and nozzle length, l (not to scale).

We then find a relation for the pressure head in the reservoir as a function of the nozzle radius and the nozzle length,

$$H = l\left\{\frac{128\mu^2 l}{\rho^2 g R_0^4} - 1\right\}. \tag{7.5}$$

In Equation (7.5), we have discounted the entry length of the flow that is necessary to achieve Poiseuille flow. This entry length, l_e, can be obtained from the empirical formula

$$\frac{l_e}{2R_0} \approx 0.056\,\mathrm{Re}. \tag{7.6}$$

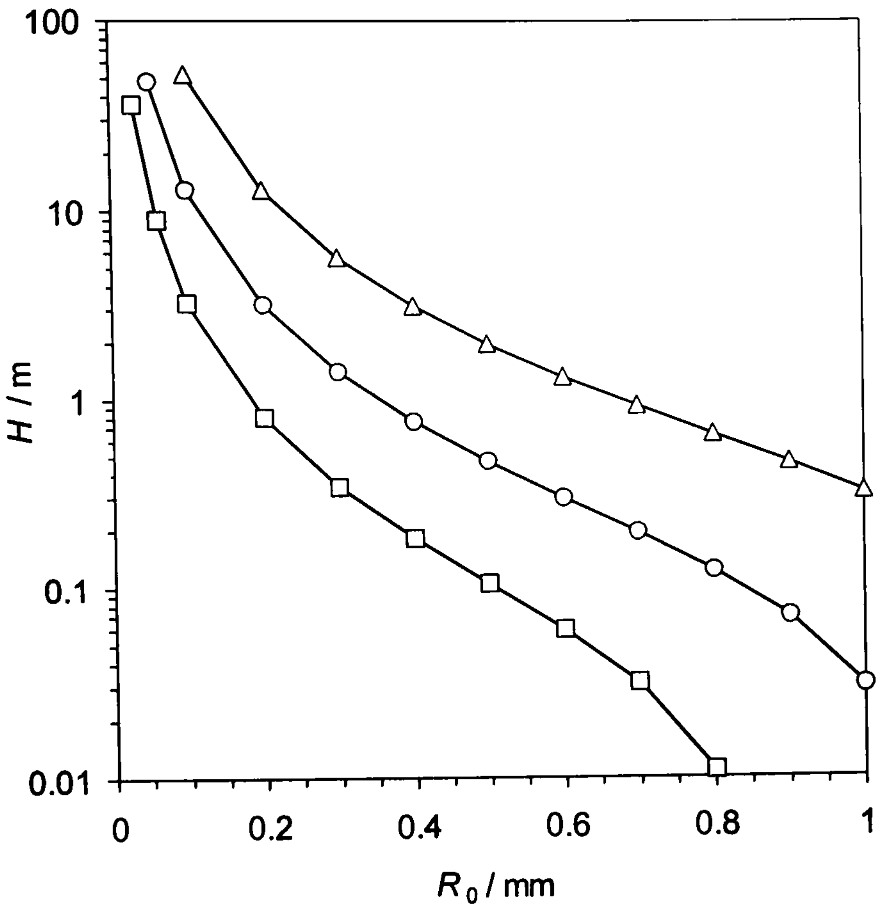

Figure 7.2: Liquid height in the reservoir, H, as a function of the nozzle length, l, and the nozzle radius, R_0, according to Equation (7.5). The graphs are computed for the properties of water at 20°C and varying nozzle lengths l = 200 × R_0 (△), 100 × R_0 (○), and 50 × R_0 (□).

At the length l_e, the velocity on the symmetry line has reached 99% of the value of the Poiseuille velocity (twice the mean velocity) [222,223]. In order to operate with fully developed laminar flow at a Reynolds number of up to Re $\sim$ 2000, the nozzles have to be 100 times the internal nozzle diameter in length.

For a given nozzle length and nozzle radius, Equation (7.5) gives an estimate of the height of liquid in the reservoir that is necessary to overcome the pressure drop in the capillary pipe. Equation (7.5) is plotted in Figure 7.2 for three different nozzle lengths. With a nozzle length of 200 × R_0, in a purely gravity-driven jet flow, it is not feasible to operate the apparatus with nozzle radii of much less than 0.8 mm due to the large liquid heights at Re $\sim$ 2000.

Shorter capillary nozzles would allow for smaller nozzle diameters, but at the expense of operating with lower Reynolds numbers. Alternatively, pressurising the reservoir would provide additional driving force for the flow, allowing for the

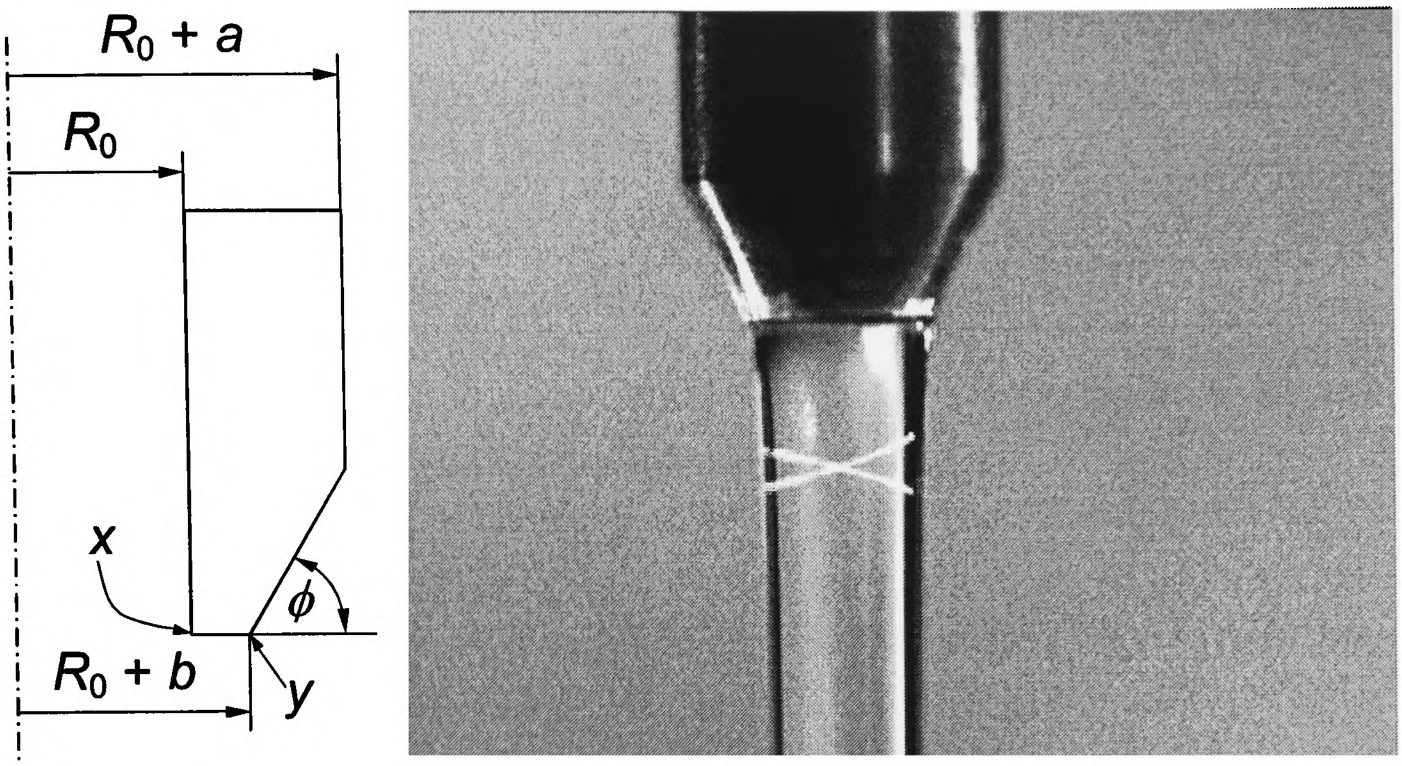

(a) (b)

Figure 7.3: (a) Schematic drawing (not to scale) of the axi–symmetric tip of the nozzle. $2R_0 = 1.58$ mm, $a = 0.665$ mm, $b = 0.07$ mm, $\phi = 65°$. x and y represent the inner and outer edges of the tip of the nozzle, respectively. (b) Photograph of the nozzle and the liquid jet used in the experimental investigation. The crossing of two laser beams inside the jet is shown.

use of very small nozzles (~ 0.1 mm) at Re ~ 2000.

We used high precision stainless-steel tube nozzles (Coopers Needle Works) with internal diameters of $2R_0 = 1.10$, 1.58, and 2.0 mm. In all three cases, the nozzle length was chosen to be $200 \times R_0$. Clean stainless steel is hydrophilic so the tip of the nozzle is wetted by surfactant solution unless it is treated chemically to create a hydrophobic surface. This wetting effect can be important as reported by Lienhard [193]. In his experiments jet contraction was affected by wetting phenomena at the tip of the nozzle, so that it influenced the contact angle of the jet on leaving the nozzle. We have demonstrated the effect of wetting of the nozzle tip on the hydrodynamics of the jet numerically in Section 3.6.6. To minimise the area of wetting, either a conically shaped nozzle end or a thin capillary wall is therefore be the preferred choice. The nozzle wall is required to have a certain thickness to enable machining of it, which made a conically shaped nozzle end the preferred option. The conical shape of the nozzle tip had the added advantage of giving the flow region very near the nozzle exit better accessibility for the laser beams. The dimensions of the tip of the $2R_0 = 1.58$ mm nozzle used in this experimental investigation and a photograph of the nozzle and the liquid jet are given in Figure 7.3.

7.2 Experimental Jet Apparatus

Figure 7.4 shows the basic design of our jet apparatus. The fluid was pumped continuously around the system in the direction indicated by the arrows. A magnetic drive pump (CP Instruments, model AC-2CP-MD) with shaft seals was used to reduce contamination of the surfactant solution and to facilitate cleaning (P). These pumps produce low levels of vibration and have a steady, continuous action. In order to maintain a constant temperature to within ± 0.5°C, the solution was passed through a glass coil immersed in a thermostatted water bath (Grant LVF6) (WB). The experiments were performed at 20°C.

To prevent vibrations from the pump coupling into the nozzle of the jet, a direct pipework connection between the pump and the nozzle was avoided. The fluid from the pump was allowed to flow over the outside of an inverted funnel (F) and then to fall freely onto the internal walls of a cylindrical reservoir (R). The inverted funnel serves to minimise air entrainment and hence suppresses foaming, as well as providing a smooth flow of liquid into the reservoir. A Teflon resistance plate (RP) with a thickness of 5 mm and an array of holes of 2 to 3 mm diameter was fitted near the bottom of the reservoir to prevent any flow instabilities reaching the nozzle. The reservoir was mounted on a coarse vertical z-translation stage with a range of 400 mm and a resolution of 0.1 mm, and a fine horizontal x-y-translation stage equipped with differential micrometers with a sensitivity of 0.1 μm (TS). This combination of stages allows precision mapping of the flow profile across the jet (y-direction) and measurements over the whole length of the jet before break-up.

A nozzle (N) was attached to the lower end of the reservoir by means of a 1/8 inch BSP coupling so that they were interchangeable. The flow rate through the nozzle is dependent on the hydrodynamic pressure difference across the nozzle (H), which was controlled with an adjustable air-trap valve (AV) that fixes the height of the fluid in the reservoir. Fluid emerging from the nozzle (J) and fluid overflowing from the reservoir through the air-trap valve fell freely into a sump (C) and was then fed back to the inlet of the pump (P).

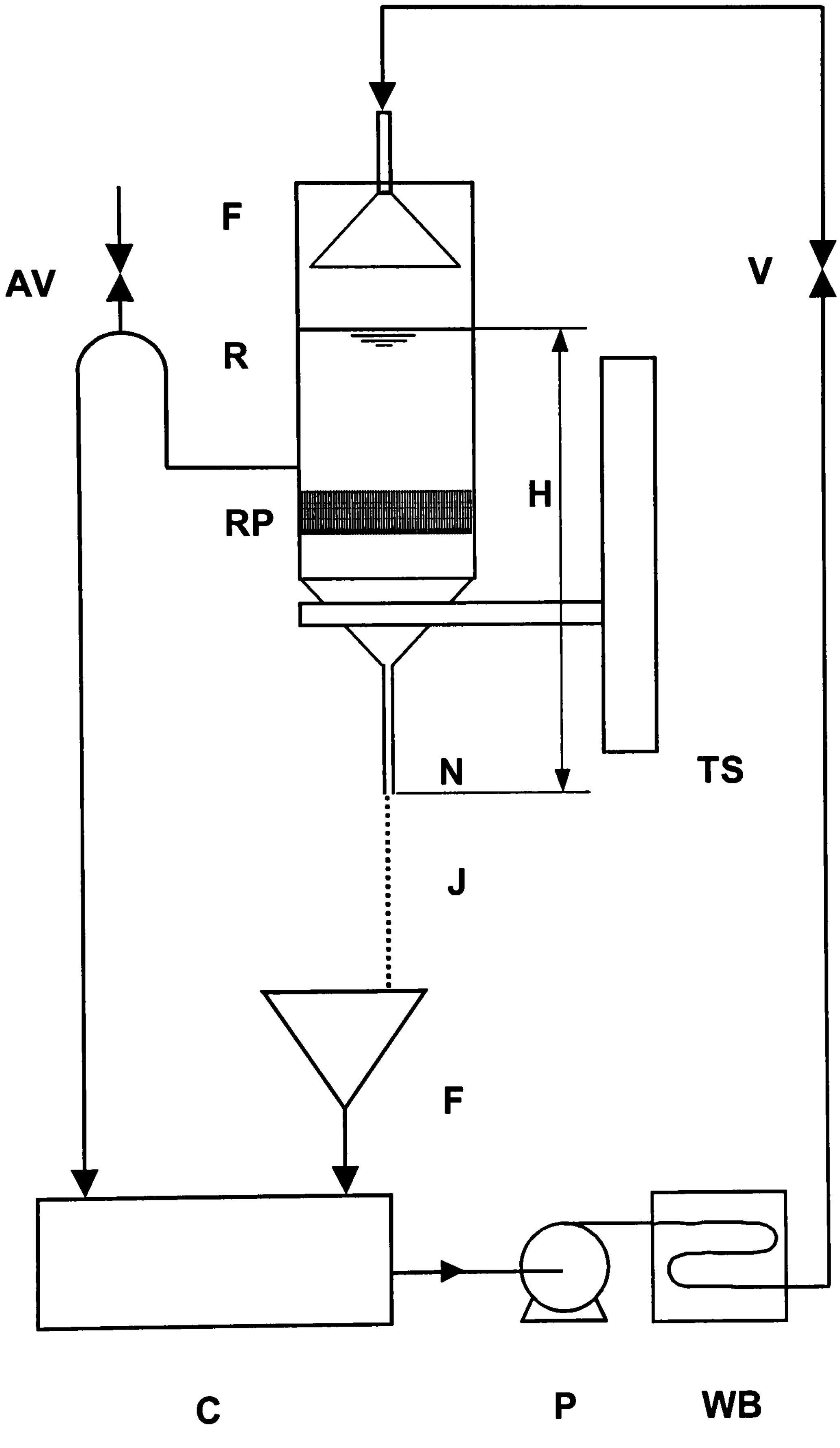

Figure 7.4: Schematic diagram of the liquid jet pumping system. P – magnetic drive pump, WB – water bath, V – valve, TS – *xyz* translation stage, R – stainless steel reservoir, RP – resistance plate, AV – air vent, J – jet, N – nozzle, F – funnel, C – container (sump), H – head.

To minimise vibrations from the surrounding environment the entire experiment was set up on a 12 inch thick optical table (Melles Griot) and enclosed with heavy curtains to exclude air draughts. A description of the optical bench may be found elsewhere [208].

7.3 Measurement of the Velocity Field

A laser Doppler velocimeter has been constructed to measure the jet velocity. This technique was applied very successfully in the overflowing cylinder experiment (see Section 1.7.1). In laser Doppler velocimetry (LDV), a laser beam is split into two equal parts, which are then refocused within the jet (shown in Figure 7.3). The angle of intersection of the two laser beams was 50° in air. This angle is reduced to 37° inside the fluid as a result of refraction of the beams at the air-water interface. In the intersection of the two beams, a standing wave pattern of interference fringes is set up. TiO_2 particles with a mean diameter of 2 μm pass through the focal volume and scatter laser light. The scattered light signal is then detected, filtered, digitised, and Fourier-transformed to yield the frequency, which depends on the velocity component of the particle perpendicular to the fringes. In the jet, this is the axial velocity component, u.

The angles of incidence of the laser beams limit full sections of the jet to axial distances, z, greater than 1 mm. Measurements of the jet surface velocity alone can be made to within 300 μm of the nozzle tip. The probed volume has a width of 10 μm in the axial direction, and 30 μm in the radial direction. For measurements of the surface velocity, in which the focus is placed at the surface, the average depth from which the signal arises is 9 μm. The error introduced by the finite sampling depth of the LDV experiment can be estimated from

$$\frac{d\sigma}{dz} = \mu \frac{du}{dr}, \tag{7.7}$$

where the contraction of the jet has been neglected. For a typical surface tension gradient of 3×10^{-2} N m^{-1} over a distance of 2×10^{-2} m, the velocity gradient $du/dr = 1.5 \times 10^3$ s^{-1}. Thus, for the viscosity of water, the velocity u at a distance 9 μm beneath the surface would be 1.4 cm s^{-1} higher than the surface velocity, $u_s = u(z, r = R)$. This error is small compared with a typical surface velocity, except very near the nozzle.

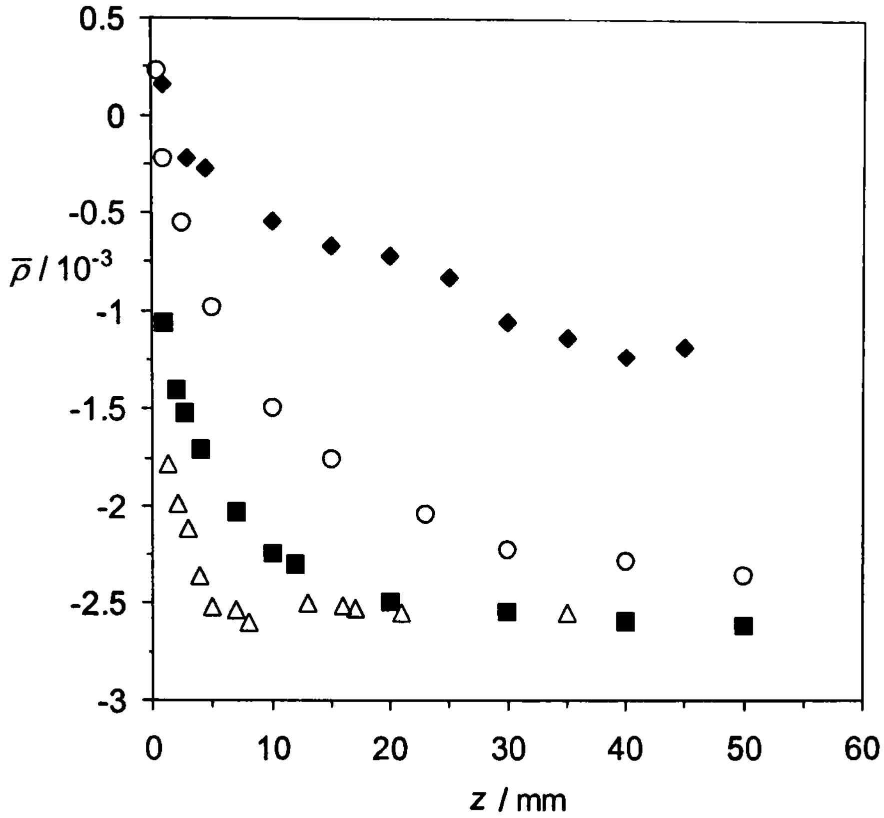

Figure 7.5: Coefficient of ellipticity, $\bar{p}(z)$, for C_{16}TAB at Re = 1950 (R_0 = 0.79 mm). The data are for c_b = 0.63 mol m^{-3} (◆), 1.25 mol m^{-3} (○), 2.5 mol m^{-3} (■), and 4.0 mol m^{-3} (△).

7.4 Measurement of the Surface Concentration

In ellipsometry, the change in polarisation of light upon reflection is measured, which is determined by the optical properties of the sample. Ellipsometry allows us to map the amount of surfactant adsorbed at the jet surface and has been applied before in the overflowing cylinder experiment (see Section 1.7.1). Although the coefficient of ellipticity, $\bar{p}$, is determined directly by the adsorbed surfactant monolayer, it is not an absolute measure of surface concentration. Therefore, it is necessary to calibrate ellipsometric data against another direct measurement of surface excess. A calibration curve, $\bar{p} = \bar{p}(\Gamma)$, has been determined by neutron reflection and ellipsometry on an overflowing cylinder [224].

Figure 7.5 shows typical $\bar{p}(z)$ measurements for C_{16}TAB below and above the cmc. A value of $\bar{p} \approx -2.5 \times 10^{-3}$ corresponds to a monolayer, and a value of $\bar{p} \approx 0.4 \times 10^{-3}$ represents pure water. The variation in $\bar{p}$, from repeated measurements at identical concentrations of C_{16}TAB and jet speed, was about 1×10^{-4}, which represents less than 5% of a monolayer of C_{16}TAB. Very close to the nozzle, however, contraction of the jet deflects the laser beam in the vertical plane and defocuses the reflected beam. These effects of curvature, together with the finite diameter of the laser beam, limited ellipsometric measurements in practice to axial distances z from the nozzle tip greater than 1 mm.

7.5 Experimental Data

Experimental data were collected by our co-workers in the Physical and Theoretical Chemistry Laboratory at Oxford University for a variety of ionic and non-ionic surfactant systems. These data sets are summarised in Appendix E.

Chapter 8

Conclusions

Using a simplified boundary-layer treatment, we have demonstrated that near the nozzle exit, the axial surface velocity of the water jet shows a cube-root dependence on the axial distance, $u_s \sim z^{1/3}$. From this result follows that the rate of surface expansion, du_s/dz scales as $z^{-2/3}$, thus for $z \to 0$ leading to $du_s/dz \to \infty$. The jet shows singular behaviour at the point of emergence of liquid from the nozzle (the detachment point).

In the presence of surfactant, the boundary-layer treatment was extended to account for the variation in surface tension at the surface of the jet. From this extension, we found that, to leading order, the surface velocity depends linearly on the axial distance, $u_s \sim z$, within a short distance from the nozzle (the region of detachment), which means that the rate of surface expansion is finite and constant within this region. The adsorption of surfactant thus eliminates the singularity at the point of detachment.

Downstream of the detachment region the Marangoni stress decreases rapidly, and the surface velocity tends to vary with $z^{1/3}$, as in the case of the pure water jet. We have described how downstream surface velocity and surface concentration profiles can be modelled approximately, making use of "off-set" distances. These off-set distances, and the length of the detachment region, are found to scale with $w_b^{3/2}$, where w_b is the bulk concentration of surfactant.

We have also shown that there is a finite concentration of adsorbed surfactant at the point of detachment, Γ_0, which also scales with $w_b^{3/2}$.

In a linked result, we found that the surface shear stress at the point of detachment is equal to the wall stress inside the nozzle that arises from the parabolic flow profile. This limitation on the surface shear stress, however, is based on the physically intuitive supposition that the jet emerges from the nozzle with parabolic flow. We are currently lacking proof of this assumption, both experimentally and theoretically. Removing this constraint would inevitably lead to a different family of solutions. In fact, CFD computations, in which the surface shear stress at the point of detachment exceeded the stress value inside the nozzle, resulted in the appearance of a vortex flow, much less in diameter than the nozzle, in the nozzle exit plane. As a consequence of this reversal of surface flow, the velocity profile of the emerging jet was altered, ensuring continuity of stress at the point of detachment.

With the occurrence of the toroidal vortices in the numerical computations, convergence for the convection-diffusion equation could no longer be attained. The failure of the numerical scheme was caused by its inability to handle the step change in sub-surface concentration that should occur at the point of detachment. We have therefore used two results of our theory—the maximum Marangoni stress and the finite surface concentration at the point of detachment—with the CFD model, which gave our hybrid CFD model. In this way, we were able to obtain converged solutions over a range of bulk concentrations.

Most of the computations presented in this thesis were carried out for the properties of aqueous solutions of the cationic surfactant C_{16}TAB. At low to moderate bulk concentrations of C_{16}TAB, the predictions of our diffusion-controlled adsorption model for the surface concentration agreed very well with experimental data, suggesting that the effect of the electric double layer on the rate of the mass transfer to the surface is negligible and that an adsorption barrier is absent. At bulk concentrations near the critical micelle concentration, however, the hybrid CFD model over-predicted the surface concentration in the upstream region of the jet. This over-prediction may indicate that the effect of the electric double layer, which reduces the rate of mass transfer to the surface due to the electrostatic repulsion of the charged surface, is important at higher bulk concentrations.

For sub-micellar C_{14}TAB, a shorter homologue of C_{16}TAB which has a much higher critical micelle concentration, our simplified theory strongly over-predicted the value for the surface concentration at the point of detachment, Γ_0. There was thus no agreement between the predictions of the hybrid CFD model and the experimental data for this surfactant. This strong over-prediction may again indicate that electrostatic repulsion effects of the surface are important, and perhaps more important than in the case of $C_{16}TAB$.

In all computations with the hybrid CFD model, as expected, the surface velocity increased linearly with distance within the region of detachment and exhibited water-like behaviour outside this region. The smallness of the detachment region, usually not more than one nozzle diameter in length, made the detection of this behaviour in the experiments impossible. Experimental evidence of the Marangoni stress was only obtained at high bulk concentrations, about 2.5 times higher than the critical micelle concentration of $C_{16}TAB$.

The conservation equation of a second species, micelles, was solved alongside that of the monomers above the critical micelle concentration for one concentration of $C_{16}TAB$. It was found that considering one micelle species suffices to study the effects of micelle break-down kinetics on the adsorption at the jet surface. Good agreement between computed and measured surface concentration data was found with a micelle disintegration rate constant that is of order 100 s^{-1} at an aggregation number of 90. These values are consistent with literature values, though the literature on micelle break-down kinetics is sparse. The computed results were found to be insensitive to variations in the aggregation number.

Chapter 9

Future Work

We have successfully developed a (hybrid) CFD model that is capable of predicting surfactant adsorption and Marangoni flow in liquid jets. However, the CFD model has a number of shortcomings. Based on the modelling work that has been presented in this thesis, we suggest

(*i*) to determine theoretically whether other families of solutions for the jet flow at the point of detachment in the presence of surfactant exist,

(*ii*) to extend the hybrid CFD model to incorporate electric double layer effects,

(*iii*) to use more sophisticated isotherms, such as the Frumkin or van der Waals isotherm,

(*iv*) to develop a CFD model that is capable of predicting mixed diffusion-kinetic adsorption,

(*v*) to design an experimental apparatus that allows for measurements within the region of detachment,

(*vi*) to account for the curvature of the surface in the flux boundary condition, given by Equation (5.22), and to apply the CFD model to other free-surface flow configurations.

Under (*i*), we address the chief assumption of our boundary-layer treatment in Section 4.1—fully developed laminar flow of the liquid jet on emergence from the nozzle. The Assumption of parabolic flow enabled us to carry out the boundary layer analysis with comparatively simple mathematical means. However, performing the analysis without any constraints on the surface shear stress at the point of detachment would provide valuable inside, which we are unlikely to obtain from the experiment.

Recommendation (*ii*) arises from the over-prediction of the surface concentration by the hybrid CFD model at bulk concentrations of C_{16}TAB close to the critical micelle concentration. This over-prediction was even more pronounced in the C_{14}TAB results. Electrostatic repulsion of the surface, which increases with increasing bulk concentration, may hinder the mass transfer to the surface and may provide an explanation for the discrepancy between model prediction and experimental data. The assumption of local equilibrium between sub-surface and surface would still hold, and the diffusion-controlled character of the adsorption model would remain. If we could include these effects correctly, the jet would become a more precise instrument for investigating them.

The use of more sophisticated isotherms may improve the agreement between computation and experiment in the downstream flow region, where the equilibrium values for the surface concentration in the experiments often seem to be somewhat higher than the computed values. The Frumkin isotherm, for example, takes molecule interactions into account, which the Langmuir isotherm neglects. These interaction effects become important at higher concentrations.

Under (*iv*), we put forward the use of adsorption kinetics instead of an equilibrium isotherm, such as the Langmuir-Hinshelwood relation in Equation (1.10). The implementation of a kinetic relation is particularly desirable with respect to the generality of the model, as these kinetic relations reduce to the respective equilibrium isotherm for fast adsorption at the surface.

The lack of experimental data very near the nozzle exit has been a major drawback in the validation of the modelling results in that region of the jet. The implementation of suggestion (*v*) will certainly require a major re-design of the apparatus, in particular of the optical system.

Finally, in order to apply the CFD model to other types of free-surface flows, the flux boundary condition (5.22), which is central to the model, must be generalised. In a high-speed laminar liquid jet, the curvature is only slight and may be neglected. But in general, this boundary condition must be formulated in terms of a local tangential-normal coordinate system. Such a generalisation requires the implementation of a coordinate transformation.

Bibliography

[1] Karsa, D.R., "*Innovative Approaches to Surfactant Development*", in "*Industrial Applications of Surfactants II*", Karsa, D.R. (Ed.), Special Publication No. 77, Royal Society of Chemistry, Cambridge, 1990.

[2] Patel, M., "*Closing Carbon Cycles - Carbon Use for Materials in the Context of Resource Efficiency and Climate Change*", PhD Thesis, University of Utrecht, The Netherlands, 1999.

[3] Fainerman, V.B., Möbius, D., Miller, R., "*Surfactants: Chemistry, Interfacial Properties, Applications*", Vol. 13 in "*Studies in Interface Science*", Möbius, D. and Miller, R. (Eds.), Elsevier, Amsterdam, 2001.

[4] Shchukin, E.D., Pertsov, A.V., Amelnia, E.A., Zelenev, A.S., "*Colloid and Surface Chemistry*", Vol. 12 in "*Studies in Interface Science*", Möbius, D. and Miller, R. (Eds.), Elsevier, Amsterdam, 2001.

[5] Karsa, D.R., "*Industrial Applications of Surfactants – An Overview*", in "*Industrial Applications of Surfactants*", Karsa, D.R. (Ed.), Special Publication No. 59, Royal Society of Chemistry, London, 1987.

[6] Joos, P., "*Dynamic Surface Phenomena*", VSP, Zeist, The Netherlands, 1999.

[7] Hansen, R.S., "*The Calculation of Surface Age in Vibrating Jet Measurements*", Journal of Physical Chemistry, **68**, 7, 2012–2014, July 1964.

[8] Miller, R., Joos, P., Fainerman, V.B., "*Dynamic Surface and Interfacial Tensions of Surfactant and Polymer Solutions*", Advances in Colloid and Interface Science, **49**, 249–302, 1994.

[9] Noskov, B.A., "*Fast Adsorption at the Liquid-Gas Interface*", Advances in Colloid and Interface Science, **69**, 63–129, 1996.

[10] Harper, J.F., "*Surface Ages in Vibrating-Jet Experiments*", Chemical Engineering Science, **28**, 323–325, 1973

[11] Davies, J.T., Makepeace, R.W., "*Measurement of the Surface Ages of Water Jets*", AIChE Journal, **24**, *3*, 524–530, May 1978.

[12] Everett, D.H., "*Basic Principles of Colloid Science*", Royal Society of Chemistry, London, 1988.

[13] Myers, D., "*Surfactant Science and Technology*", 2nd Edition, VCH Publishers, New York, 1992.

[14] Porter, M.R., "*Handbook of Surfactants*", 2nd Edition, Blackie Academics & Professional, London, 1994.

[15] Schunk, P.R., "*Surfactant and Polymer Additives in Coating and Related Flows*", University of Minnesota, Ph.D. Thesis, 1989.

[16] Ward, A.F.H., Tordai, L., "*Time-Dependence of Boundary Tensions of Solutions. I. The Role of Diffusion in Time-Effects*", The Journal of Chemical Physics, **14**, *7*, 453–461, July 1946.

[17] Eastoe, J., Dalton, J.S., "*Dynamic Surface Tension and Adsorption Mechanisms of Surfactants at the Air-Water Interface*", Advances in Colloid and Interface Science, **85**, 103–144, 2000.

[18] Langmuir, I., "*The Adsorption of Gases on Plane Surfaces of Glass, Mica and Platinum.*", Journal of the American Chemical Society, **40**, 1361–1403, 1918.

[19] Miller, R., "*On the Solution of Diffusion Controlled Adsorption Kinetics for Any Adsorption Isotherms*", Colloid & Polymer Science, **259**, 375–381, 1981.

[20] McCoy, B.J., "*Analytical Solutions for Diffusion-Controlled Adsorption Kinetics with Non-Linear Adsorption Isotherms*", Colloid & Polymer Science, **261**, 535–539, 1983.

[21] Ferri, J.K., Stebe, K.J., "*Which Surfactants Reduce Surface Tension Faster? A Scaling Argument for Diffusion-Controlled Adsorption*", Advances in Colloid and Interface Science, **85**, 61–97, 2000.

[22] Chang, C.-H., Franses, E.I., "*Adsorption Dynamics of Surfactants at the Air/Water Interface: A Critical Review of Mathematical Models, Data, and Mechanisms*", Colloids and Surfaces A: Physicochemical and Engineering Aspects, **100**, 1–45, 1995.

[23] Danov, K.D., Kralchevsky, P.A., Ivanov, I.B., "*Equilibrium and Dynamics of Surfactant Adsorption Monolayers and Thin Films*", Chapter 9 in

"*Handbook of Detergents. Part A: Properties*", Broze, G. (Ed.), Marcel Dekker Inc., 1999.

[24] Miller, R., Kretzschmar, G., "*Adsorption Kinetics of Surfactants at Fluid Interfaces*", Advances in Colloid and Interface Science, **37**, 97–121, 1991.

[25] Ziller, M., Miller, R., "*On the Solution of Diffusion Controlled Adsorption Kinetics by Means of Orthogonal Collocation*", Colloid & Polymer Science, **264**, 611–615, 1986.

[26] Miller, R., Ziller, M., "*On the Application of Quantitative Models of Diffusion-Controlled Adsorption Kinetics at Fluid Interfaces*", Colloid & Polymer Science, **266**, 532–538, 1988.

[27] Hansen, R.S., "*The Theory of Diffusion Controlled Adsorption Kinetics with Accompanying Evaporation*", Journal of Physical Chemistry, **64**, 637–641, May 1960.

[28] Rampazzo, L., "*Diffusion to a Plane with Adsorption According to Frumkin's Isotherm*", Electrochimica Acta, **14**, 733–739, 1969.

[29] Levich, V.G., "*Physicochemical Hydrodynamics*", Prentice-Hall, Englewood Cliffs, New Jersey, 1962.

[30] Krotov, V.V., Rusanov, A.I., "*Physicochemical Hydrodynamics of Capillary Systems*", Imperial College Press, London, 1999.

[31] Van Voorst Vader, F., Erkens, T.F., van den Tempel, M., "*Measurement of Dilatational Surface Properties*", Transactions of the Faraday Society, **60**, 1170–1177, 1964.

[32] Bain, C.D., Manning-Benson, S., Darton, R.C., "*Rates of Mass Transfer and Adsorption of CTAB at an Expanding Air-Water Interface*", Journal of Colloid and Interface Science, **229**, *1*, 247–256, 2000.

[33] Breward, C.J.W., Darton, R.C., Howell, P.D., Ockendon, J.R., "*The Effect of Surfactants on Expanding Free Surfaces*", Chemical Engineering Science, **56**, *8*, 2867–2878, 2001.

[34] Schunk, P.R., Scriven, L.E., "*Surfactant Effects in Coating Processes*", Chapter 11d in "*Liquid Film Coating*", Kistler, S.F. and Schweizer, P.M. (Eds.), 495–536, London, Chapman & Hall, 1997.

[35] Ghadiali, S.N., Halpern, D., Gaver III., D.P., "*A Dual-Reciprocity Boundary Element Method for Evaluating Bulk Convective Transport of Surfactant in Free-Surface Flows*", Journal of Computational Physics, **171**, 534-559, 2001.

[36] Cerro, R.L., Whitaker, S., "*The Effect of Surfactants on the Hydrodynamic Development of Thin Liquid Films*", Journal of Colloid and Interface Science, **37**, 33–51, 1971.

[37] Hansen, R.S., "*Diffusion and the Kinetics of Adsorption of Aliphatic Acids and Alcohols at the Water-Air Interface*", Journal of Colloid Science, **16**, 549–560, 1961.

[38] Tsonopoulos, C., Newman, J., Prausnitz, J.M., "*Rapid Aging and Dynamic Surface Tension of Dilute Aqueous Solutions*", Chemical Engineering Science, **26**, 817–827, 1971.

[39] Eastoe, J., Rankin, A., Wat, R., Bain, C.D., "*Surfactant Adsorption Dynamics*", International Reviews in Physical Chemistry, **20**, *3*, 357–386, 2001.

[40] Borwankar, R.P., Wasan, D.T., "*The Kinetics of Adsorption of Surface Active Agents at Gas-Liquid Surfaces*", Chemical Engineering Science, **38**, *10*, 1637–1649, 1983.

[41] Ravera, F., Liggieri, L., Steinchen, A., "*Sorption Kinetics Considered as a Renormalized Diffusion Process*", Journal of Colloid and Interface Science, **156**, 109–116, 1993.

[42] Liggieri, L., Ravera, F., Passerone, A., "*A Diffusion-Based Approach to Mixed Adsorption Kinetics*", Colloids and Surfaces A: Physicochemical and Engineering Aspects, **114**, 351–359, 1996.

[43] Ravera, F., Liggieri, L., Miller, R., "*Molecular Orientation as a Controlling Process in Adsorption Dynamics*", Colloids and Surfaces A: Physicochemical and Engineering Aspects, **175**, 51–60, 2000.

[44] Diamant, H., Andelman, D., "*Kinetics of Surfactant Adsorption at Fluid-Fluid Interfaces*", Journal of Physical Chemistry, **100**, *32*, 13732–13742, 1996.

[45] Diamant, H., Andelman, D., "*Kinetics of Surfactant Adsorption at Fluid/Fluid Interfaces: Non-Ionic Surfactants*", Europhysics Letters, **34**, *8*, 575–580, 1996.

[46] Ariel, G., Diamant, H., Andelman, D., "*Kinetics of Surfactant Adsorption at Fluid-Fluid Interfaces: Surfactant Mixtures*", Langmuir, **15**, 3574–3581, 1999.

[47] Andelman, D., Diamant, H., Ariel, G., "*Dynamic Surface Tension and Kinetics of Surfactant Adsorption at Fluid Interfaces*", International Journal of Engineering Science, **38**, 995, 2000.

[48] Manning-Benson, S., "*The Dynamics of Surfactant Adsorption*", D.Phil Thesis, University of Oxford, 1998.

[49] MacLeod, C.A., Radke, C.J., "*Charge Effects in the Transient Adsorption of ionic Surfactants at Fluid Interfaces*", Langmuir, **10**, 3555–3566, 1994.

[50] Vlahovska, P.M., Danov, K.D., Mehreteab, A., Broze, G., "*Adsorption Kinetics of Ionic Surfactants with Detailed Account for the Electrostatic Interactions. I. No Added Electrolyte*", Journal of Colloid and Interface Science, **192**, 194–206, 1997.

[51] Filippov, L.K., "*On the Theory of Dynamic Surface Tension of Ionic Surfactant Solutions. I. Diffusion-Convective Adsorption*", Journal of Colloid and Interface Science, **182**, 330–347, 1996.

[52] Valkovska, D.S., Shearman, G.C., Bain, C.D., Darton, R.C., Eastoe, J., "*Adsorption of Ionic Surfactants at an Expanding Air-Water Interface*", Langmuir, **20**, 4436–4445, 2004.

[53] Danov, K.D., Vlahovska, P.M., Kralchevsky, P.A., Broze, G., Mehreteab, A., "*Adsorption Kinetics of Ionic Surfactants with Detailed Account for the Electrostatic Interactions: Effect of the Added Electrolyte*", Colloids and Surfaces A: Physicochemical and Engineering Aspects, **156**, 389–411, 1999.

[54] Aniansson, E.A.G., Wall, S.N., Almgren, M., Hoffmann, H., Kielmann, I., Ulbricht, W., Zana, R., Lang, J., Tondre, C., "*Theory of the Kinetics of Micellar Equilibria and Quantitative Interpretation of Chemical Relaxation Studies of Micellar Solutions of Ionic Surfactants*", Journal of Physical Chemistry, **80**, *9*, 905–922, 1976.

[55] Kahlweit, M., Teubner, M., "*On the Kinetics of Micellization in Aqueous Solutions*", Advances in Colloid and Interface Science, **13**, 1–64, 1980.

[56] Patist, A., Oh, S.G., Leung, R., Shah, D.O., "*Kinetics of Micellization: Its Significance to Technological Processes*", Colloids and Surfaces A: Physicochemical and Engineering Aspects, **176**, 3–16, 2000.

[57] Patist, A., Kanicky, J.R., Shukla, P.K., Shah, D.O., "*Importance of Micellar Kinetics in Relation to Technological Processes*", Journal of Colloid and Interface Science, **245**, 1–15, 2002.

[58] Noskov, B.A., "*Kinetics of Adsorption from Micellar Solutions*", Advances in Colloid and Interface Science, **95**, 237–293, 2002.

[59] Hoffmann, H., Nagel, R., Platz, G., Ulbricht, W., "*Zur Kinetik der Mizellbildung von Alkylpyridiniumhalogeniden*", Colloid & Polymer Science, **254**, 812–834, 1976.

[60] Bidner, M.S., Larson, R.G., Scriven, L.E., "*On the Theory of Micellization with Reference to Petroleum Recovery*", Latin American Journal of Chemical Engineering and Applied Chemistry, **6**, 1–32, 1976.

[61] Muller, N., "*Kinetics of Micellization*", in "*Solution Chemistry of Surfactants*", Vol. 1, Mittal, K.L. (Ed.), Plenum Press, New York and London, 1979.

[62] Miller, R., "*Adsorption Kinetics of Surfactants from Micellar Solutions*", Colloid and Polymer Science, **259**, 1124–1128, 1981.

[63] Danov, K.D., Vlahovska, P.M., Horozov, T., Dushkin, C.D., Kralchevsky, P.A., Mehreteab, A., Broze, G., "*Adsorption from Micellar Surfactant Solutions: Nonlinear Theory and Experiment*", Journal of Colloid and Interface Science, **183**, 223–235, 1996.

[64] Breward, C.J.W., Howell, P.D., "*Straining Flow of a Micellar Surfactant Solution*", accepted for publication in European Journal of Applied Mathematics, 2004.

[65] Frumkin, A., "*Die Kapillarkurve der höheren Fettsäuren und die Zustandsgleichung der Oberflächenschicht.*", Zeitschrift für Physikalische Chemie, **116**, 466–484, 1925.

[66] von Szyszkowski, B., "*Experimentelle Studien über kapillare Eigenschaften der wässerigen Lösungen von Fettsäuren.*", Zeitschrift für Physikalische Chemie, **64**, 385–414, 1908.

[67] Scriven, L.E., Sternling, C.V., "*The Marangoni Effects*", Nature, **187**, 186–188, 1960.

[68] Levich, V.G., Krylov, V.S., "*Surface-Tension-Driven Phenomena*", Annual Review of Fluid Mechanics, **1**, 293–316, 1969.

[69] Grotberg, J.B., Gaver III., D.P., "*A Synopsis of Surfactant Spreading Research*", Journal of Colloid and Interface Science, **178**, 377–378, 1996.

[70] Marangoni, C., "*Ueber die Ausbreitung der Tropfen einer Flüssigkeit auf der Oberfläche einer anderen*", Poggendorff's Annalen der Physik und Chemie, **143**, 337–354, 1871.

[71] Brochard, F., "*Motions of Droplets on Solid Surfaces Induced by Chemical or Thermal Gradients*", Langmuir, **5**, 432–438, 1989.

[72] Brzoska, J.B., Brochard-Wyart, F., Rondelez, F., "*Motions of Droplets on Hydrophobic Model Surfaces Induced by Thermal Gradients*", Langmuir, **9**, 2220–2224, 1993.

[73] Bénard, H., "*Les Tourbillons Cellulaires Dans une Nappe Liquid. Première Partie: Description Générale des Phénomènes*", Revue Générale des Sciences Pures et Appliquées, **11**, 1261–1271, 15 January – 30 December, 1900.

[74] Bénard, H., "*Les Tourbillons Cellulaires Dans une Nappe Liquid. Deuxième Partie: Procédés Mécaniques et Optiques d'Examen. Lois Numériques des Phénomènes*", Revue Générale des Sciences Pures et Appliquées, **11**, 1309–1328, 15 January – 30 December, 1900.

[75] Lord Rayleigh, "*On Convection Currents in a Horizontal Layer of Fluid, when the Higher Temperature is on the Under Side*", The London, Edinburgh, and Dublin Philosophical Magazine and Journal of Science, 6th Series, **32**, 529–546, December 1916.

[76] `http://www-math.mit.edu/~bush/tears.html` (18 March 2004)

[77] Bain, C.D., Burnett-Hall, G.D., Montgomerie, R.R., "*Rapid Motion of Liquid Drops*", Nature, **372**, 414–415, 1994.

[78] Stebe, K.J., Maldarelli, C., "*Remobilizing Surfactant Retarded Fluid Particle Interfaces. II. Controlling the Surface Mobility at Interfaces of Solutions Containing Surface Active Compounds*", Journal of Colloid and Interface Science, **163**, 177–189, 1994.

[79] Chen, J., Stebe, K.J., "*Marangoni Retardation of the Terminal Velocity of a Settling Droplet: The Role of Surfactant Physico-Chemistry*", Journal of Colloid and Interface Science, **178**, 144–155, 1996.

[80] Stebe, K.J., Lin, S.-Y., Maldarelli, C., "*Remobilizing Surfactant Retarded Fluid Particle Interfaces. I. Stress-Free Conditions at the Interfaces of Micellar Solutions of Surfactants with Fast Sorption Kinetics*", Physics of Fluids A, **3**, *1*, 3–20, 1991.

[81] Stebe, K.J., Barthès-Biesel, D., "*Marangoni Effects of Adsorption-Desorption Controlled Surfactants on the Leading End of an Infinitely Long Bubble in a Capillary*", Journal of Fluid Mechanics, **286**, 25–48, 1995.

[82] Liger-Belair, G., Marchal, R., Robillard, B., Dambrouck, T., Maujean, A., Vignes-Adler, M., Jeandet, P., "*On the Velocity of Expanding Spherical Gas Bubbles Rising in Line in Supersaturated Hydroalcoholic Solutions: Application to Bubble Trains in Carbonated Beverages*", Langmuir, **16**, 1889–1895, 2000.

[83] Kataoka, D.E., Troian, S.M., "*Patterning Liquid Flow on the Microscopic Scale*", Nature, **402**, 794–797, 1999.

[84] Bain, C.D., "*Motion of Liquids on Surfaces*", ChemPhysChem, **2**, 580–582, 2001.

[85] Jobert, P.P., Leblond, J., "*Effects of Surface-Active Materials on the Hydrodynamic Development in a Liquid Jet*", Journal of Colloid and Interface Science, **68**, *3*, 478–485, 1979.

[86] Sato, Y., Yamamoto, K., Mizushina, T., "*Fluid Velocity Measurement by a Laser Doppler Technique on a Practical Measuring Instrument*", International Chemical Engineer, **18**, *1*, 26–32, 1978.

[87] Gonzáles-Mendizabal, D., Olivera-Fuentes, C., Guzmán, J.M., "*Hydrodynamics of Laminar Liquid Jets. Experimental Study and Comparison with Two Models*", Chemical Engineering Communications, **56**, 117–137, 1987.

[88] Dukhin, S.S., Kretzschmar, G., Miller, R., "*Dynamics of Adsorption at Liquid Interfaces*", Vol. 1 in "*Studies in Interface Science*", Möbius, D. and Miller, R. (Eds.), Elsevier, Amsterdam, 1995.

[89] Weaire, D., Hutzler, S., "*The Physics of Foams*", Clarendon Press, Oxford, 1999.

[90] Lockett, M.J., "*Distillation Tray Fundamentals*", Cambridge University Press, Cambridge, 1986.

[91] Kister, H.Z., "*Distillation Operation*", McGraw-Hill, New York, 1990.

[92] Kister, H.Z., "*Distillation Design*", McGraw-Hill, New York, 1992.

[93] Darton, R.C., Supino, S., Sweeting, K.J., "*Development of a Multistaged Foam Fractionation Column*", Chemical Engineering and Processing, **43**, *3*, 477–482, 2004.

[94] Thomas, P.D., Darton, R.C., Whalley, P.B., "*Liquid Foam Structure Analysis by Visible Light Tomography*", The Chemical Engineering Journal, **56**, 187–192, 1995.

[95] Darton, R.C., Sun, K.-H., "*The Effects of Surfactants on Foam and Froth Properties*", Transactions of the IChemE, **77**, Part A, 535–542, 1999.

[96] Tuinier, R., Bisperink, C.G.J., van den Berg, C., Prins, A., "*Transient Foaming Behavior of Aqueous Alcohol Solutions as Related to Their Dilatational Surface Properties*", Journal of Colloid and Interface Science, **179**, 327–334, 1996.

[97] Breward, C.J.W., Darton, R.C., Howell, P.D., Ockendon, J.R., "*Modelling Foam Drainage*", IChemE Symposium Series, **142**, 1009–1019, 1997.

[98] Howell, P.D., "*The Draining of a Two-Dimensional Bubble*", Journal of Engineering Mathematics, **35**, 251-272, 1999.

[99] Breward, C.J.W., "*The Mathematics of Foam*", D.Phil Thesis, University of Oxford, 1999.

[100] Breward, C.J.W., Howell, P.D., "*The Drainage of a Foam Lamella*", Journal of Fluid Mechanics, **458**, 379–406, 2002.

[101] Koehler, S.A., Stone, H.A., Brenner, M.P., Eggers, J., "*Dynamics of Foam Drainage*", Physical Review E, **58**, *2*, 2097–2106, 1998.

[102] Koehler, S.A., Hilgenfeldt, S., Stone, H.A., "*Liquid Flow Through Aqueous Foams: The Node-Dominated Foam Drainage Equation*", Physical Review Letters, **82**, *21*, 4232–4235, 1999.

[103] Koehler, S.A., Hilgenfeldt, S., Stone, H.A., "*A Generalized View of Foam Drainage: Experiment and Theory*", Langmuir, **16**, 6327–6341, 2000.

[104] Hilgenfeldt, S., Kraynik, A.M., Koehler, S.A., Stone, H.A., "*An Accurate von Neumann's Law for Three-Dimensional Foams*", Physical Review Letters, **86**, *12*, 2685–2688, 2001.

[105] Koehler, S.A., Hilgenfeldt, S., Stone, H.A., "*Flow Along Two Dimensions of Liquid Pulses in Foams: Experiment and Theory*", Europhysics Letters, **54**, *3*, 335–341, 2001.

[106] Hilgenfeldt, S., Koehler, S.A., Stone, H.A., "*Dynamics of Coarsening Foams: Accelerated and Self-Limited Drainage*", Physical Review Letters, **86**, *20*, 4704–4707, 2001.

[107] Aubert, J.H., Kraynik, A.M., Rand, P.B., "*Aqueous Foams*", Scientific American, **254**, *5*, 58–66, 1986.

[108] Kraynik, A.M., "*Foam Flows*", Annual Review of Fluid Mechanics, **20**, 325–357, 1988.

[109] Leike, A., "*Demonstration of the Exponential Decay Law Using Beer Froth*", European Journal of Physics, **23**, 21–26, 2002.

[110] Ruschak, K.J., "*Coating Flows*", Annual Review of Fluid Mechanics, **17**, 65–89, 1985.

[111] Scriven, L.E., Suszynski, W.J., "*Take a Closer Look at Coating Problems*", Chemical Engineering Progress, **86**, *9*, 24–29, September 1990.

[112] Miyamoto, K., Katagiri, Y., "*Curtain Coating*", Chapter 11c in "*Liquid Film Coating*", Kister, P.M. and Schweizer, P.M. (Eds.), Chapman & Hall, London, 1997.

[113] Blake, T.D., Ruschak, K.J., "*Wetting: Static and Dynamic Contact Lines*", Chapter 3 in "*Liquid Film Coating*", Kister, P.M. and Schweizer, P.M. (Eds.), Chapman & Hall, London, 1997.

[114] Clarke, A., "*The Application of Particle Tracking Velocimetry and Flow Visualisation to Curtain Coating*", Chemical Engineering Science, **50**, *15*, 2397–2407, 1995.

[115] Blake, T.D., Clarke, A., Ruschak, K.J., "*Hydrodynamic Assist of Dynamic Wetting*", AIChE Journal, **40**, *2*, 229–242, 1994.

[116] Blake, T.D., Bracke, M., Shikhmurzaev, Y.D., "*Experimental Evidence of Nonlocal Hydrodynamic Influence on the Dynamic Contact Angle*", Physics of Fluids, **11**, *8*, 1995–2007, 1999.

[117] Clarke, A., Blake, T.D., Ruschak, K.J., "*Method for Curtain Coating at High Speed*", United States Patent No. 6,099,913, 2000.

[118] Schwartz, L.W., "*On the Asymptotic Analysis of Surface-Stress-Driven Thin-Layer Flow*", Journal of Engineering Mathematics, **39**, 171–188, 2001.

[119] Röntgen, W.C., "*Verfahren zur Herstellung reiner Wasser- und Quecksilberoberflächen*", Wiedemann's Annalen der Physik und Chemie, **46**, 152–157, 1892.

[120] Grunnet-Jepsen, H., "*A Fundamental Study of Foaming in Chemical Processes*", D.Phil Thesis, University of Oxford, 1997.

[121] Manning-Benson, S., Bain, C.D., Darton, R.C., Sharpe, D., Eastoe, J., Reynolds, P., "*Invasive and Noninvasive Measurements of Dynamic Surface Tensions*", Langmuir, **13**, 5808–5810, 1997.

[122] Manning-Benson, S., Bain, C.D., Darton, R.C., "*Measurement of Dynamic Interfacial Properties in an Overflowing Cylinder by Ellipsometry*", Journal of Colloid and Interface Science, **189**, 109–116, 1997.

[123] Manning-Benson, S., Parker, S.R.W., Bain, C.D., "*Measurement of the Dynamic Surface Excess in an Overflowing Cylinder by Neutron Reflection*", Langmuir, **14**, 990–996, 1998.

[124] Howell, P.D., Breward, C.J.W., "*Mathematical Modelling of the Overflowing Cylinder Experiment*", Journal of Fluid Mechanics, **474**, 275–298, 2003.

[125] Sir Isaac Newton, "*The Principia – Mathematical Principles of Natural Philosophy*", A new translation by I.B. Cohen and A. Whitman, University of California Press, Berkeley, 1999.

[126] Savart, F., "*Ueber die Beschaffenheit der durch kreisrunde Oeffnungen aus dünner Wand strömenden Flüssigkeitsstrahlen*", Poggendorff's Annalen der Physik und Chemie, **33**, 451–477, 1834.

[127] Plateau, J., "*Experimentelle und theoretische Untersuchungen über die Gleichgewichtsfiguren einer flüssigen Masse ohne Schwere*", Poggendorff's Annalen der Physik und Chemie, **82**, 387–406, 1851.

[128] Hagen, G., "*Ueber die Auflösung flüssiger Cylinder in Tropfen*", Poggendorff's Annalen der Physik und Chemie, **80**, 559–566, 1850.

[129] Plateau, J., "*Ueber die Gränze der Stabilität eines flüssigen Cylinders*", Poggendorff's Annalen der Physik und Chemie, **80**, 566–569, 1850.

[130] Magnus, G., "*Hydraulische Untersuchungen*", Poggendorff's Annalen der Physik und Chemie, **95**, 1–59, 1855.

[131] Magnus, G., "*Hydraulische Untersuchungen, Zweiter Theil. Ueber die Bäuche der Strahlen aus kreisförmigen Oeffnungen*", Poggendorff's Annalen der Physik und Chemie, **106**, 1–32, 1859.

[132] Lord Rayleigh, "*On the Capillary Phenomena of Jets*", Proceedings of the Royal Society, London, **29**, 71–97, 1879.

[133] Buff, H., "*Schreiben an Hrn. Prof. G. Magnus vom Prof. Buff*", Poggendorff's Annalen der Physik und Chemie, **100**, 168–171, 1857.

[134] Lord Rayleigh, "*On the Tension of Recently Formed Liquid Surfaces*", Proceedings of the Royal Society, London, **47**, 281–287, 1890.

[135] Pedersen, P.O., "*On the Surface-Tension of Liquids Investigated by the Method of Jet Vibration*", Philosophical Transactions of the Royal Society, London, Series A, **207**, 341–399, 1907.

[136] Meyer, G., "*Die Oberflächenspannung von Quecksilber gegen Gase*", Wiedemann's Annalen der Physik und Chemie, **66**, 523–529, 1898.

[137] Bohr, N., "*Determination of the Surface Tension of Water by the Method of Jet Vibration*", Philosophical Transactions of the Royal Society, London, Seris A, **209**, 281–317, 1909.

[138] Bohr, N., "*On the Determination of the Tension of a Recently Formed Water-Surface*", Proceedings of the Royal Society, London, Series A, **84**, 395–403, 1911.

[139] Addison, C.C., "*The Properties of Freshly Formed Surfaces. Part I. The Application of the Vibrating Jet Technique to Surface-Tension Measurements on Mobile Liquids.*", Journal of the Chemical Society, Part II., 535–541, 1943.

[140] Addison, C.C., "*The Properties of Freshly Formed Surfaces. Part II. The Rate of Adsorption of* iso*Amyl Alcohol at the Air-Water Surface.*", Journal of the Chemical Society, Part I., 252–256, 1944.

[141] Addison, C.C., "*The Properties of Freshly Formed Surfaces. Part III. The Mechanism of Adsorption, with Particular Reference to the* sec.-*Octyl Alcohol-Water System.*", Journal of the Chemical Society, Part II., 477–480, 1944.

[142] Addison, C.C., "*The Measurement of Surface and Interfacial Tensions at Fresh Surfaces by the Vibrating Jet Method*", The London, Edinburgh, and Dublin Philosophical Magazine and Journal of Science, 7th Series, **36**, *253*, 73–100, 1945.

[143] Hansen, R.S., Purchase, M.E., Wallace, T.C., Woody, R.W., "*Extension of the Vibrating Jet Method for Surface Tension Measurement to Jets of Non-Uniform Velocity Profiles*", Journal of Physical Chemistry, **62**, 210–214, February 1958.

[144] Defay, R., Pétré, G., "*Correcting Surface Tension Data Obtained by the Oscillating Jet Method*", Journal of Colloid Science, **17**, 565–569, 1962.

[145] Rideal, E.K., Sutherland, K.L., "*The Variation of the Surface Tension of Solutions with Time*", Transactions of the Faraday Society, **48**, 1109–1123, 1952.

[146] Quinn, G.P., Saville, D.A., "*The Effects of Surface-Active Materials on the Oscillations of a Liquid Jet*", Chemical Engineering Science, **29**, 247–253, 1974.

[147] Thomas, W.D.E., Potter, L., "*Solution/Air Interfaces: I. An Oscillating Jet Relative Method for Determining Dynamic Surface Tensions*", Journal of Colloid and Interface Science, **50**, *3*, 397–412, March 1975.

[148] Defay, R., Hommelen, J.R., "*I. Measurement of Dynamic Surface Tensions of Aqueous Solutions by the Oscillating Jet Method*", Journal of Colloid Science, **13**, 553–564, 1958.

[149] Kochurova, N.N., Rusanov, A.I., "*Dynamic Surface Properties of Water: Surface Tension and Surface Potential*", Journal of Colloid and Interface Science, **81**, 297–303, 1981.

[150] Caskey, J.A., Barlage, W.B., "*An Improved Experimental Technique for Determining Dynamic Surface Tension of Water and Surfactant Solutions*", Journal of Colloid and Interface Science, **35**, *1*, 46–52, January 1971.

[151] Castro, A., Ong, S., Eisenthal, K.B., "*Studies of Molecular Properties at the Surface of a Liquid Jet by Second Harmonic Generation*", Chemical Physics Letters, **163**, 412–416, 1989.

[152] Kochurova, N.N., Rusanov, A.I., "*Surface Potential and Kinetics of Surfactant Adsorption*", Colloids and Surfaces A: Physicochemical and Engineering Aspects, **76**, 1–5, 1993.

[153] Kochurova, N.N., Rusanov, A.I., "*Special Properties of Freshly Formed Surfaces of Water and Aqueous Solutions*", Colloid Journal, **57**, *4*, 571–573, 1995.

[154] Posner, A.M., Alexander, A.E., "*A New Technique for the Determination of Dynamic Surface Tensions*", Transactions of the Faraday Society, **45**, 651–661, 1949.

[155] Posner, A.M., Alexander, A.E., "*The Kinetics of Adsorption from Solution to the Air/Water Interface. Part I. Normal Aliphatic Alcohols*", Journal of Colloid Science, **8**, 575–584, 1953.

[156] Posner, A.M., Alexander, A.E., "*The Kinetics of Adsorption from Solution to the Air/Water Interface. Part II. Anionic and Cationic Soaps*", Journal of Colloid Science, **8**, 585–592, 1953.

[157] Hutchinson, J., Klenerman, D., Manning-Benson, S., Bain, C., "*Measurements of the Adsorption Kinetics of a Cationic Surfactant in a Liquid Jet by Ellipsometry*", Langmuir, **15**, 7530–7533, 1999.

[158] Marmottant, P., Villermaux, E., Clanet, C., "*Transient Surface Tension of an Expanding Liquid Sheet*", Journal of Colloid and Interface Science, **230**, 29–40, 2000.

[159] Cullen, E.J., Davidson, J.F., "*Absorption in Gases in Liquid Jets*", Transactions of the Faraday Society, **15**, 743–750, 1957.

[160] Scriven, L.E., Pigford, R.L., "*On Phase Equilibrium at the Gas-Liquid Interface During Absorption*", AIChE Journal, **4**, *4*, 439–444, 1958.

[161] Scriven, L.E., Pigford, R.L., "*Fluid Dynamics and Diffusion Calculations for Laminar Liquid Jets*", AIChE Journal, **5**, *3*, 397–402, 1959.

[162] Thomas, W.J., "*Absorption in Laminar Jets*", Journal of Applied Chemistry, **17**, 350–355, 1967.

[163] Duda, A., Vrentas, J.S., "*Laminar Liquid Jet Diffusion Studies*", AIChE Journal, **14**, *2*, 286–294, 1968.

[164] Brignole, E.A., Echarte, R., "*Mass Transfer in Laminar Liquid Jets – Measurement of Diffusion Coefficients*", Chemical Engineering Science, **36**, 695–703, 1981.

[165] Addison, C.C., Elliott, T.A., "*The Properties of Freshly Formed Surfaces. Part X. A New Contracting Liquid-Jet Technique for the Study of Soluble Films at Small Surface Ages*", Journal of the Chemical Society, Part IV., 2789–2805, 1949.

[166] Awati, K.M., Howes, T., "*Surfactant Induced Stationary Modes on a Cylindrical Fluid Jet*", Journal of Colloid and Interface Science, **181**, 344–346, 1996.

[167] Joshi, J.B., Ranade, V.V., "*Computational Fluid Dynamics for Designing Process Equipment: Expectations, Current Status, and Path Forward*", Industrial & Engineering Chemistry Research, **42**, 1115–1128, 2003.

[168] Harmon, D.B., "*Drop Sizes from Low Speed Jets*", Journal of the Franklin Institute, **259**, 519–522, 1955.

[169] Goren, S.L., Wronski, S., "*The Shape of Low-Speed Capillary Jets of Newtonian Liquids*", Journal of Fluid Mechanics, **25**, 185–198, 1966.

[170] Middleman, S., Gavis, J., "*Expansion and Contraction of Capillary Jets of Newtonian Liquids*", The Physics of Fluids, **4**, *3*, 355–359, March 1961.

[171] Middleman, S., Gavis, J., "*Erratum: I. Expansion and Contraction of Capillary Jets of Newtonian Liquids; II. Expansion and Contraction of Capillary Jets of Viscoelastic Liquids*", The Physics of Fluids, **4**, 1450, 1961.

[172] Oliver, D.R., "*The Expansion/Contraction Behavior of Laminar Liquid Jets*", Canadian Journal of Chemical Engineering, 100–107, April 1966.

[173] Gavis, J., Modan, M., "*Expansion and Contraction of Jets of Newtonian Liquid in Air: Effect of Tube Length*", The Physics of Fluids, **10**, *3*, 487–497, March 1967.

[174] Gear, R.L., Keentok, M., Milthorpe, J.F., Tanner, R.I., "*The Shape of Low Reynolds Number Jets*", Physics of Fluids, **26**, *1*, 7–9, January 1983.

[175] Gavis, J., "*Contribution of Surface Tension to Expansion and Contraction of Capillary Jets*", The Physics of Fluids, **7**, 1097–1098, 1964.

[176] Middleman, S., "*Profile Relaxation in Newtonian Jets*", Industrial and Engineering Chemistry Fundamentals, **3**, *2*, 118–122, May 1964.

[177] Joseph, D.D., "*Slow Motion and Viscometric Motion; Stability and Bifurcation of the Rest State of a Simple Fluid. Part III. Die Swell—The Final Diameter of a Capillary Jet*", Archive for Rational Mechanics and Analysis, **56**, 99–157, 1974.

[178] Brun, R.F., Lienhard, J.H., "*Behavior of Free Laminar Jets Leaving Poiseuille Tubes*", ASME Paper No. 68-FE-44, 1–8, 1968.

[179] Scheuermann, R., "*Über die Gestalt und die Auflösung des fallenden Flüssigkeitsstrahles*", Annalen der Physik, **60**, *3*, 233–259, 1919.

[180] Anno, J.N., "*The Mechanics of Liquid Jets*", 47–55, Lexington Books, 1977.

[181] Adachi, K., Tagashira, K., Banba, Y., Tatsumi, H., Machida, H., Yoshioka, N., "*Steady Laminar Round Jets of a Viscous Liquid Falling Vertically in the Atmosphere*", AIChE Journal, **36**, *5*, 738–744, May 1990.

[182] Adachi, K., "*Laminar Jets of a Plane Liquid Sheet Falling Vertically in the Atmosphere*", Journal of Non-Newtonian Fluid Mechanics, **24**, 11–30, 1987.

[183] von Lang, V., "*Experimente über die Reibung zwischen Wasser und Luft*", Wiedemann's Annalen der Physik und Chemie, **3**, 219–236, 1878.

[184] Trouton, F.T., "*On the Coefficient of Viscous Traction and its Relation to that of Viscosity*", Proceedings of the Royal Society, London, **A 77**, 426–440, 1906.

[185] Goren, S.L., "*Development of the Boundary Layer at a Free Surface from a Uniform Shear Flow*", Journal of Fluid Mechanics, **25**, 87–95, 1966.

[186] Tillett, J.P.K., "*On the Laminar Flow in a Free Jet of Liquid at High Reynolds Numbers*", Journal of Fluid Mechanics, **32**, 273–292, 1968.

[187] Middleman, S., "*Modeling Axisymmetric Flows-Dynamics of Films, Jets, and Drops*", Academic Press, San Diego, 1995.

[188] Fisher, R.J., Denn, M.M., Tanner, R.I., "*Initial Profile Development in Melt Spinning*", Industrial and Engineering Chemistry Fundamentals, **19**, 195–197, 1980.

[189] Dutta, A., Ryan, M.E., "*Dynamics of a Creeping Newtonian Jet with Gravity and Surface Tension: A Finite Difference Technique for Solving Steady Free-Surface Flows Using Orthogonal Curvilinear Coordinates*", AIChE Journal, **28**, *2*, 220–232, 1982.

[190] Bird, R.B., Stewart, W.E., Lightfoot, E.N., "*Transport Phenomena*", John Wiley & Sons, New York, 1960.

[191] Vrentas, J.S., Vrentas, C.M., Shirazi, A.F., "*Downstream Boundary Conditions for Vertical Jets*", AIChE Journal, **31**, *6*, 1044–1046, June 1985.

[192] Scriven, L.E., "*Dynamics of a Fluid Interface – Equation of Motion for Newtonian Surface Fluids*", Chemical Engineering Science, **12**, 98–108, 1960.

[193] Lienhard, J.H., "*Effects of Gravity and Surface Tension Upon Liquid Jets Leaving Poiseuille Tubes*", Transactions of the ASME, Journal of Basic Engineering, 262–268, June 1968.

[194] Schlichting, H., "*Boundary-Layer Theory*", p. 115, 7th Edition, McGraw-Hill, New York, 1979.

[195] Duda, J.L., Vrentas, J.S., "*Fluid Mechanics of Laminar Liquid Jets*", Chemical Engineering Science, **22**, 855–869, 1967.

[196] Jones, C.W., Watson, E.J., "*Laminar Boundary Layers*", Rosenhead, L. (Ed.), p. 200, Oxford University Press, 1963.

[197] Horsfall, F., "*A Theoretical Treatment of Die Swell in a Newtonian Liquid*", Polymer, **14**, 262–266, June 1973.

[198] Nickell, R.E., Tanner, R.I., Caswell, B., "*The Solution of Viscous Incompressible Jet and Free-Surface Flows Using Finite Element Methods*", Journal of Fluid Mechanics, **65**, 189–206, 1974.

[199] Trang, C.T., Yeow, Y.L., "*Extrudate Swell of Newtonian and Non-Newtonian Fluids—The Effect of Gravitational Body Force*", Journal of Non-Newtonian Fluid Mechanics, **20**, 103–116, 1986.

[200] Omodei, B.J., "*Computer Solutions of a Plane Newtonian Jet with Surface Tension*", Computers and Fluids, **7**, 79–96, 1979.

[201] Omodei, B.J., "*On the Die-Swell of an Axisymmetric Newtonian Jet*", Computers and Fluids, **8**, 275–289, 1980.

[202] Georgiou, G.C., Papanastasiou, T.C., Wilkes, J.O., "*Laminar Newtonian Jets at High Reynolds Number and High Surface Tension*", AIChE Journal, **34**, *9*, 1559–1562, 1988.

[203] Chacha, M., Occelli, R., Tadrist, L., "*Heat Transfer in High-Temperature Liquid Jets*", International Journal of Heat and Mass Transfer, **37**, *18*, 2871–2883, 1994.

[204] Mitrovic, J., Ricoeur, A., "*Fluid Dynamics and Condensation-Heating of Capillary Jets*", International Journal of Heat and Mass Transfer, **38**, *8*, 1483–1494, 1995.

[205] Mitrovic, J., "*Kontur kapillarer Flüssigkeitsstrahlen*", Brennstoff-Wärme-Kraft, **47**, *10*, 421–425, Oktober 1995.

[206] Tsai, C.-C., Liu, T.-J., "*Numerical Simulation of an Optical Fiber-Forming Process*", Chemical Engineering Science, **52**, *2*, 221–235, 1997.

[207] Chauhan, A., Maldarelli, C., Rumschitzki, D.S., Papageorgiou, D.T., "*An Experimental Investigation of the Convective Instability of a Jet*", Chemical Engineering Science, **58**, 2421–2432, 2003.

[208] Battal, T., Bain, C.D., Weiß, M., Darton, R.C., "*Surfactant Adsorption and Marangoni Flow in Liquid Jets: I. Experiments*", Journal of Colloid and Interface Science, **263**, 250–260, 2003.

[209] Bronstein, I.N., Semendjajew, K.A., "*Taschenbuch der Mathematik*", 25th Edition, B.G. Teubner Verlagsgesellschaft, Leipzig, 1991.

[210] Darton, R.C., "*Dynamic Surfactant Adsorption at Gas/Liquid Interfaces in the Presence of Micelles*", in preparation.

[211] Fornberg, B., "*Generation of Finite Difference Formulas on Arbitrarily Spaced Grids*", Mathematics of Computation, **51**, *184*, 699–706, October 1988.

[212] Fornberg, B., "*Calculation of Weights in Finite Difference Formulas*", SIAM Review, **40**, 685–691, 1998.

[213] Anderson Jr., J.D., "*Computational Fluid Dynamics – The Basics with Applications*", New York, McGraw-Hill, 1995.

[214] Hughes, T.J.R., Brooks, A.N., "*A Multidimensional Upwind Scheme with No Cross-Wind Diffusion*", in "*Finite Element Methods for Advection-Dominated Flows*", Hughes, T.J.R. (Ed.), ASME Publication ASME-AMD, *34*, 1979.

[215] Taylor, R., Krishna, R., "*Multicomponent Mass Transfer*", John Wiley & Sons, Inc., New York, 1993.

[216] Atkins, P., De Paula, J., "*Atkins' Physical Chemistry*", 7th Edition, Oxford University Press, 2002.

[217] Reid, R.C., Prausnitz, J.M., Poling, B.E., "*The Properties of Liquids and Gases*", 4th Edition, McGraw-Hill, 1987.

[218] Lianos, P., Zana, R., "*Fluorescence Probe Studies of the Effect of Concentration on the State of Aggregation of Surfactants in Aqueous Solutions*", Journal of Colloid and Interface Science, **84**, *1*, 100–107, 1981.

[219] Czerniawski, M., "*The Double Layer Structure of Colloidal Electrolytes. VI. Rate of Micellization Process of Colloidal Electrolytes in Aqueous Solutions*", Chemical Abstracts, **64**, 13430–13431, 1966.

[220] Chan, S.-K., Herrmann, U., Ostner, W., Kahlweit, M., "*On the Kinetics of the Formation of Micelles in Aqueous Solutions III*", Berichte der Bunsengesellschaft für Physikalische Chemie, **82**, 380–384, 1978.

[221] Becker, E., "*Technische Strömungslehre*", B.G. Teubner, Stuttgart, Germany, 1986.

[222] Langhaar, H.L., "*Steady Flow in the Transition Length of a Straight Tube*", Transactions of the ASME, A-55–A-58, June 1942.

[223] Baehr, H.D., Stephan, K. "*Wärme- und Stoffübertragung*", Springer-Verlag, Berlin, 1994.

[224] Battal, T., Shearman, G.C., Valkovska, D., Bain, C.D., Darton, R.C., Eastoe, J., "*Determination of the Dynamic Surface Excess of a Homologous Series of Cationic Surfactants by Ellipsometry*", Langmuir, **19**, 1244–1248, 2003.

Appendix A

Solving the Convection-Diffusion Equation

We derive the general solution of the convection-diffusion equation,

$$\frac{\partial^2 w}{\partial y^{*2}} + \frac{\mathrm{Re}}{2} Scy^* f'(z^*) \frac{\partial w}{\partial y^*} = 0. \tag{A.1}$$

Introducing the substitution

$$\psi = \frac{\partial w}{\partial y^*} \Rightarrow \frac{\partial \psi}{\partial y^*} = \frac{\partial^2 w}{\partial y^{*2}}, \tag{A.2}$$

we obtain

$$\frac{\partial \psi}{\partial y^*} + \frac{\mathrm{Re}}{2} \mathrm{Sc}\, y^* f'(z) \psi = 0. \tag{A.3}$$

Integrating the factor $(\mathrm{Re}/2)\,\mathrm{Sc}\, y^* f'(z)$ according to

$$\exp\left\{\frac{\mathrm{Re}}{2} \mathrm{Sc}\, f'(z) \int y^* dy^*\right\} = \exp\left\{\frac{\mathrm{Re}}{2} \mathrm{Sc}\, f'(z) \frac{y^{*2}}{2}\right\}, \tag{A.4}$$

and multiplying Equation (A.3) with it, leads to

$$\frac{\partial \psi}{\partial y^*} \exp\left\{\frac{\mathrm{Re}}{2} \mathrm{Sc}\, f'(z) \frac{y^{*2}}{2}\right\} + \frac{\mathrm{Re}}{2} \mathrm{Sc}\, y^* f'(z) \psi \exp\left\{\frac{\mathrm{Re}}{2} \mathrm{Sc}\, f'(z) \frac{y^{*2}}{2}\right\} = 0. \tag{A.5}$$

Applying the chain rule to Equation (A.5) results in

$$\frac{\partial}{\partial y^*}\left[\psi \exp\left\{\frac{\mathrm{Re}}{2} \mathrm{Sc}\, f'(z) \frac{y^{*2}}{2}\right\}\right] = 0. \tag{A.6}$$

Integrating once gives

$$\psi = \frac{\partial w}{\partial y^*} = \xi_1 \exp\left\{-\frac{\mathrm{Re}}{2} \mathrm{Sc}\, f'(z) \frac{y^{*2}}{2}\right\}, \tag{A.7}$$

where ξ_1 is an integration constant. Integrating again gives

$$w = \xi_1 \int_0^{y^*} \exp\left\{-\frac{\mathrm{Re}}{2}\,\mathrm{Sc}\,f'(z)\frac{y^{*2}}{2}\right\} dy^* + \xi_2, \tag{A.8}$$

where ξ_2 is the second constant of integration. In order to solve the integral in Equation (A.8), we perform a second substitution,

$$\zeta = y^*\sqrt{\frac{\mathrm{Re}}{4}\,\mathrm{Sc}\,f'(z)}, \tag{A.9}$$

and we can then re-write Equation (A.8) to give

$$w = \xi_1 \int_0^{\zeta} \exp\left\{-\zeta^2\right\} \frac{d\zeta}{\sqrt{\frac{\mathrm{Re}}{4}\,\mathrm{Sc}\,f'(z)}} + \xi_2. \tag{A.10}$$

Replacing the integral in Equation (A.10) with an error function gives the general solution for $w(y^*)$, namely

$$w = \xi_1 \frac{\sqrt{\pi}}{2} \frac{\operatorname{erf}\left\{y^*\sqrt{\frac{\mathrm{Re}}{4}\,\mathrm{Sc}\,f'(z)}\right\}}{\sqrt{\frac{\mathrm{Re}}{4}\,\mathrm{Sc}\,f'(z)}} + \xi_2. \tag{A.11}$$

Appendix B

GAMBIT Geometry and Mesh Journal Files

B.1 Water Jet

```
/
/ SOLVER SELECTION
/
solver select "FIDAP"
/
/ FLOW GEOMETRY
/
vertex create coordinates 0 0 0
vertex create coordinates -3 0 0
vertex create coordinates -3 1 0
vertex create coordinates 0 1 0
vertex create coordinates 10 1 0
vertex create coordinates 200 1 0
vertex create coordinates 200 0 0
vertex create coordinates 10 0 0
edge create straight "vertex.2" "vertex.3"
edge create straight "vertex.1" "vertex.4"
edge create straight "vertex.8" "vertex.5"
edge create straight "vertex.2" "vertex.1"
edge create straight "vertex.3" "vertex.4"
edge create straight "vertex.1" "vertex.8"
edge create straight "vertex.4" "vertex.5"
edge create straight "vertex.8" "vertex.7"
edge create straight "vertex.7" "vertex.6"
edge create straight "vertex.5" "vertex.6"
```

```
face create wireframe "edge.4" "edge.1" "edge.5" "edge.2" real
face create wireframe "edge.6" "edge.2" "edge.7" "edge.3" real
face create wireframe "edge.8" "edge.3" "edge.10" "edge.9" real
/
/ MESH EDGES
/
edge picklink "edge.1"
edge mesh "edge.1" firstlast ratio1 3 intervals 20
edge picklink "edge.2"
edge mesh "edge.2" firstlast ratio1 18 intervals 20
edge picklink "edge.5"
edge mesh "edge.5" firstlast ratio1 12 intervals 50
edge picklink "edge.4"
edge mesh "edge.4" firstlast ratio1 12 intervals 50
edge picklink "edge.7"
edge mesh "edge.7" lastfirst ratio1 20 intervals 100
edge picklink "edge.6"
edge mesh "edge.6" lastfirst ratio1 20 intervals 100
edge picklink "edge.3"
edge mesh "edge.3" firstlast ratio1 3 intervals 20
edge picklink "edge.9"
edge mesh "edge.9" firstlast ratio1 3 intervals 20
edge picklink "edge.10"
edge mesh "edge.10" lastfirst ratio1 3 intervals 300
edge picklink "edge.8"
edge mesh "edge.8" lastfirst ratio1 3 intervals 300
/
/ MESH FACES
/
face mesh "face.1" map size 1
face mesh "face.2" map size 1
face mesh "face.3" map size 1
/
/ CREATE ENTITIES
/
physics create "inflow" btype "PLOT" edge "edge.1"
physics create "symmetry" btype "PLOT" edge "edge.4" "edge.6" "edge.8"
physics create "wall" btype "PLOT" edge "edge.5"
physics create "freesurface" btype "SURFACE" edge "edge.7" "edge.10"
physics create "outflow" btype "OUTFLOW" edge "edge.9"
/
/ EXPORT MESH
```

```
/
export fidap "waterjet.FDNEUT"
```

B.2 Water Jet with Wetted Nozzle Tip

```
/
/ SOLVER SELECTION
/
solver select "FIDAP"
/
/ FLOW GEOMETRY
/
vertex create coordinates 0 0 0
vertex create coordinates -3 0 0
vertex create coordinates -3 1 0
vertex create coordinates 0 1 0
vertex create coordinates 0 1.09 0
vertex create coordinates 5 1.09 0
vertex create coordinates 200 1.09 0
vertex create coordinates 200 0 0
vertex create coordinates 5 0 0
edge create straight "vertex.1" "vertex.2" "vertex.3" "vertex.4"
edge create straight "vertex.1" "vertex.4"
edge create straight "vertex.4" "vertex.5"
edge create straight "vertex.5" "vertex.6" "vertex.9" "vertex.1"
edge create straight "vertex.9" "vertex.6" "vertex.7" "vertex.8"
edge create straight "vertex.9" "vertex.8"
face create wireframe "edge.1" "edge.2" "edge.3" "edge.4" real
face create wireframe "edge.4" "edge.5" "edge.6" "edge.7" "edge.8" real
face create wireframe "edge.12" "edge.7" "edge.10" "edge.11" real
/
/ MESH EDGES
/
edge picklink "edge.4"
edge mesh "edge.4" firstlast ratio1 4 intervals 30
edge picklink "edge.5"
edge mesh "edge.5" firstlast ratio1 3 intervals 10
edge picklink "edge.3"
edge mesh "edge.3" firstlast ratio1 3 intervals 100
edge picklink "edge.1"
edge mesh "edge.1" lastfirst ratio1 3 intervals 100
edge picklink "edge.2"
```

```
edge mesh "edge.2" successive ratio1 1 intervals 30
edge picklink "edge.7"
edge mesh "edge.7" successive ratio1 1 intervals 40
edge picklink "edge.11"
edge mesh "edge.11" successive ratio1 1 intervals 40
edge picklink "edge.10"
edge mesh "edge.10" lastfirst ratio1 3 ratio2 2 intervals 1100
edge picklink "edge.12"
edge mesh "edge.12" lastfirst ratio1 3 ratio2 2 intervals 1100
edge picklink "edge.6"
edge mesh "edge.6" lastfirst ratio1 10 intervals 150
edge picklink "edge.8"
edge mesh "edge.8" firstlast ratio1 4 ratio2 1 intervals 150
edge picklink "edge.12"
edge mesh "edge.12" lastfirst ratio1 3 ratio2 2 intervals 1100
edge delete "edge.6" keepsettings onlymesh
edge mesh "edge.6" lastfirst ratio1 10 intervals 150
edge delete "edge.8" keepsettings onlymesh
edge mesh "edge.8" firstlast ratio1 10 intervals 150
/
/ MESH FACES
/
face mesh "face.1" map size 1
face mesh "face.2" map size 1
face mesh "face.3" map size 1
/
/ CREATE ENTITIES
/
physics create "inflow" btype "PLOT" edge "edge.2"
physics create "wall" btype "PLOT" edge "edge.3" "edge.5"
physics create "freesurface" btype "SURFACE" edge "edge.6" "edge.10"
physics create "outflow" btype "OUTFLOW" edge "edge.11"
physics create "symmetry" btype "PLOT" edge "edge.12" "edge.8" "edge.1"
/
/ EXPORT MESH
/
export fidap "waterjet2.FDNEUT"
```

B.3 Surfactant Solution Jet

```
/
/ SOLVER SELECTION
```

```
/
solver select "FIDAP"
/
/ FLOW GEOMETRY
/
vertex create coordinates 0 0 0
vertex create coordinates -1 0 0
vertex create coordinates -1 1 0
vertex create coordinates 0 1 0
vertex create coordinates 100 1 0
vertex create coordinates 100 0 0
edge create straight "vertex.2" "vertex.3"
edge create straight "vertex.3" "vertex.4"
edge create straight "vertex.2" "vertex.1"
edge create straight "vertex.1" "vertex.4"
edge create straight "vertex.4" "vertex.5"
edge create straight "vertex.6" "vertex.5"
edge create straight "vertex.1" "vertex.6"
face create wireframe "edge.3" "edge.1" "edge.2" "edge.4" real
face create wireframe "edge.7" "edge.4" "edge.5" "edge.6" real
/
/ BOUNDARY LAYER CREATION
/
blayer create first 5e-05 growth 1.4 total 0.00119267 rows 7 transition 1
\ trows 0
blayer attach "b_layer.1" face "face.1" "face.2" edge "edge.2" "edge.5"
blayer create first 8e-05 growth 1.1 total 0.00171074 rows 12 transition 1
\ trows 0
blayer attach "b_layer.2" face "face.1" "face.2" edge "edge.4" "edge.4"
/
/ MESH EDGES
/
edge picklink "edge.5"
edge mesh "edge.5" exponent ratio1 1.35 intervals 420
edge picklink "edge.7"
edge mesh "edge.7" exponent ratio1 1.35 intervals 420
edge picklink "edge.4"
edge mesh "edge.4" exponent ratio1 0.01 intervals 26
edge picklink "edge.2"
edge mesh "edge.2" exponent ratio1 0.02 intervals 42
edge picklink "edge.3"
edge mesh "edge.3" exponent ratio1 0.02 intervals 42
```

```
edge picklink "edge.1"
edge mesh "edge.1" exponent ratio1 0.01 intervals 26
edge picklink "edge.6"
edge mesh "edge.6" exponent ratio1 0.01 intervals 26
/
/ MESH FACES
/
face mesh "face.1" map size 1
face mesh "face.2" map size 1
/
/ CREATE ENTITIES
/
physics create "freesurface" btype "SURFACE" edge "edge.5"
physics create "wall" btype "PLOT" edge "edge.2"
physics create "inflow" btype "PLOT" edge "edge.1"
physics create "symmetry" btype "PLOT" edge "edge.3" "edge.7"
physics create "outflow" btype "OUTFLOW" edge "edge.6"
/
/ EXPORT MESH
/
export fidap "surfactantjet.FDNEUT"
```

Appendix C

FIDAP Model Journal Files

C.1 Water Jet

```
/
/ FICONV
/
FICONV( NEUTRAL )
INPUT( FILE="waterjet.FDNEUT" )
OUTPUT( DELETE )
END
/
TITLE( )
wa1550
/
/ FIPREP
/
FIPREP( )
PROBLEM( STEA, NONL, AXI-, FREE )
PRESSURE( MIXE=1.E-10, DISC )
EXECUTION( NEWJ )
SOLUTION( N.R. = 200, VELC = 1E-5, RESC = 1E-3, SCHANGE=0 )
RELAXATION
0.3 0.3 0 0.8 0 0.85
OPTIONS( STRE )
POSTPROCESS( )
DATAPRINT( NORM )
PRINTOUT( NONE )
RENUMBER( PROF )
/
DENSITY( CONS = 774.2 )
```

```
VISCOSITY( CONS = 1.0 )
SURFACETENSION( CONS = 74.3, PRES = 0 )
/
ENTITY( FLUI, NAME = "fluid" )
ENTITY( SURF, NAME = "freesurface", DEPT = 20, ANG1 = -0.035 )
ENTITY( PLOT, NAME = "inflow" )
ENTITY( OUTFLOW, NAME = "outflow" )
ENTITY( PLOT, NAME = "wall" )
ENTITY( PLOT, NAME = "symmetry" )
/
BCNODE( UX, POLY = 1, ENTI = "inflow" )
2.0, -2.0, 0, 2, 0
BCNODE( UY, ZERO, ENTI = "inflow" )
BCNODE( VELO, ZERO, ENTI = "wall" )
BCNODE( UY, ZERO, ENTI = "symmetry" )
BCNODE( COOR, NODE = 6323 )
BCNODE( COOR, NODE = 22 )
BCNODE( SURF, NODE = 6323, CONS = 0 )
/
BODYFORCE( CONSTANT, FZC = 0.00807 )
/
FILES( RENA, FROM = "old.FDPOST", TO = "wa1550.FDREST" )
FILES( RENA, FROM = "old.FDSTAT", TO = "wa1550.s.FDSTAT" )
/
ICNODE( VELO, READ )
ICNODE( SURF, READ )
/
END( )
/
/ FISOLV
/
CREATE( FISO )
RUN( FISOLV )
```

C.2 Surfactant Jet in the Absence of Micelles

```
/
/ CONVERSION OF NEUTRAL FILE TO FIDAP DATABASE
/
FICONV( NEUTRAL )
INPUT( FILE="surfactantjet.FDNEUT" )
OUTPUT( DELETE )
```

```
END
/
TITLE( )
new07 Re = 1950 0.3 mM C16TAB
/
/ FIPREP
/
FIPREP( )
PROBLEM( STEA, NONL, AXI-, FREE, SPECIES=1 )
PRESSURE( MIXE = 1.E-10, DISC )
EXECUTION( NEWJ )
SOLUTION( N.R. = 1000, VELC = 1E-12, RESC = 1E-3, SCHANGE = 0 )
RELAXATION
0.8 0.85 0 0.7 0 0.85 0 0 0.9985
OPTIONS( UPWINDING )
POSTPROCESS( )
DATAPRINT( NORM )
PRINTOUT( NONE )
RENUMBER( PROF )
/
DENSITY( CONS = 974.5 )
VISCOSITY( CONS = 1.0 )
SURFACETENSION( SUBROUTINE = 6, PRESSURE = 0.0 )
/  C        m      w_s0    1/Ca_0  E       k*
7.245e-6 0.3383 2.1009e-6 58.9 15.35 82.34e-6
DIFFUSIVITY( CONS = 0.00103 )
CAPACITY( CONS = 1340.5 )
/
ENTITY( FLUI, NAME = "fluid" )
ENTITY( SURF, NAME = "freesurface", DEPT = 26, ANG1 = -0.0546 )
ENTITY( PLOT, NAME = "inflow" )
ENTITY( OUTFLOW, NAME = "outflow" )
ENTITY( PLOT, NAME = "wall" )
ENTITY( PLOT, NAME = "symmetry" )
/
BCNODE( UX, POLY = 1, ENTI = "inflow" )
 2.0, -2.0, 0, 2, 0
BCNODE( UY, ZERO, ENTI = "inflow" )
BCNODE( VELO, ZERO, ENTI = "wall" )
BCNODE( UY, ZERO, ENTI = "symmetry" )
BCNODE( COOR, NODE = 1 )
BCNODE( COOR, NODE = 2 )
```

```
BCNODE( SURF, NODE = 1, CONS = 0 )
BCSYSTEM ( SET=1, CORNER )
BCNODE( SPECIES=1, CONS = 109.35e-6, ENTI = "inflow" )
BCFLUX( SPECIES=1, ENTI = "wall", CONS = 0.0 )
BCFLUX( SPECIES=1, ENTI = "freesurface", FSUB )
/
BODYFORCE( CONSTANT, FZC = 0.00507 )
/
FILES( RENA, FROM = "new06.FDPOST", TO = "new07.FDREST" )
FILES( RENA, FROM = "new06.FDSTAT", TO = "new07.s.FDSTAT" )
/
ICNODE( VELO, READ )
ICNODE( SURF, READ )
ICNODE( SPECIES=1, READ )
/
END( )
CREATE( FISO )
RUN( FISOLV, IDEN = "new07", FORE, FISOLVEX = "myflux9.exe", COMP )
```

C.3 Surfactant Jet in the Presence of Micelles

```
/
/ CONVERSION OF NEUTRAL FILE TO FIDAP DATABASE
/
FICONV( NEUTRAL )
INPUT( FILE="surfactantjet.FDNEUT" )
OUTPUT( DELETE )
END
/
TITLE( )
m69new Re=1950 c_T=1.5 mM C16TAB N=90 k_d=100 1/s
/
/ FIPREP
/
FIPREP( )
PROBLEM( STEA, NONL, AXI-, FREE, SPECIES=1, SPECIES=2 )
PRESSURE( MIXE = 1.E-10, DISC )
EXECUTION( NEWJ )
SOLUTION( N.R. = 1000, VELC = 1E-12, RESC = 1E-3, SCHANGE = 0 )
RELAXATION
0.8 0.85 0 0.7 0 0.85 0 0 0.9985 0.95
OPTIONS( UPWINDING )
```

```
POSTPROCESS( )
DATAPRINT( NORM )
PRINTOUT( NONE )
RENUMBER( PROF )
/
DENSITY( CONS = 974.5 )
VISCOSITY( CONS = 1.0 )
SURFACETENSION( SUBROUTINE = 7, PRESSURE = 0.0 )
/   X         Y        w_s0   1/Ca_w  E      k*     1/m
9.0929e+5 2.7417e+4 23.8128e-6 58.9 15.35 82.34e-6 1.286
DIFFUSIVITY( SET="monomers", CONS = 0.00103 )
DIFFUSIVITY( SET="micelles", CONS = 0.00014 )
CAPACITY( CONS = 1340.5 )
/
ENTITY( FLUI, NAME = "fluid", SPECIES=1, MDIFF="monomers", SPECIES=2,
\ MDIFF="micelles" )
ENTITY( SURF, NAME = "freesurface", DEPT = 26, ANG1 = -0.0546 )
ENTITY( PLOT, NAME = "inflow" )
ENTITY( OUTFLOW, NAME = "outflow" )
ENTITY( PLOT, NAME = "wall" )
ENTITY( PLOT, NAME = "symmetry" )
/
BCNODE( UX, POLY = 1, ENTI = "inflow" )
2.0, -2.0, 0, 2, 0
BCNODE( UY, ZERO, ENTI = "inflow" )
BCNODE( VELO, ZERO, ENTI = "wall" )
BCNODE( UY, ZERO, ENTI = "symmetry" )
BCNODE( COOR, NODE = 1 )
BCNODE( COOR, NODE = 2 )
BCNODE( SURF, NODE = 1, CONS = 0 )
BCSYSTEM ( SET=1, CORNER )
BCNODE( SPECIES=1, CONS = 335.34e-6, ENTI = "inflow" )
BCNODE( SPECIES=2, CONS = 211.41e-6, ENTI = "inflow" )
BCFLUX( SPECIES=1, ENTI = "wall", CONS = 0.0 )
BCFLUX( SPECIES=1, ENTI = "freesurface", FSUB )
BCFLUX( SPECIES=2, ENTI = "wall", CONS = 0.0 )
BCFLUX( SPECIES=2, ENTI = "freesurface", CONS = 0.0 )
/
/ Source terms
/
SOURCE( SPECIES=1, ENTITY="fluid", SUBROUTINE=7 )
1000 364.5e-3 90 1170.26 100.0 0.79e-3 7.46e-10
```

```
SOURCE( SPECIES=2, ENTITY="fluid", SUBROUTINE=7 )
1000 364.5e-3 90 1170.26 100.0 0.79e-3 7.46e-10
/
BODYFORCE( CONSTANT, FZC = 0.00507 )
/
FILES( RENA, FROM = "m68new.FDPOST", TO = "m69new.FDREST" )
FILES( RENA, FROM = "m68new.FDSTAT", TO = "m69new.s.FDSTAT" )
/
ICNODE( VELO, READ )
ICNODE( SURF, READ )
ICNODE( SPECIES=1, READ )
ICNODE( SPECIES=2, READ )
/
END( )
CREATE( FISO )
RUN( FISOLV, IDEN = "m69new", FORE, FISOLVEX = "mymicelle_flux.exe", COMP )
```

Appendix D

Fortran User Sub-Routines

D.1 Convective Flux Boundary Condition

```
SUBROUTINE USRBCF (VAL,NODE,IDF,TIME,SOL,NUMEQA,NDOF,NUMNP,LDOFU,
     1             CONSTR,nodepr,xyz,iflag)
C
C     USER DEFINED FLUX COEFFICIENTS FOR APPLIED FLUX BOUNDARY
C     CONDITIONS
C
C     VAL = COMPUTED (SPECIFIED) FLUX COEFFICIENT
C     SOL = GLOBAL SOLUTION VECTOR
C     NUMEQA = GLOBAL EQUATION NUMBER ARRAY
C     NDOF = ACTIVE NUMBER OF DEGREES OF FREEDOM
C     NUMNP = NUMBER OF NODAL POINTS
C     NODE = NODE NUMBER OF B.C.
C     IDF = DEGREE OF FREEDOM FOR NODE
C     TIME = TIME
C     LDOFU = ACTIVE DEGREE OF FREEDOM ARRAY
C     CONSTR = ARRAY OF SPECIFIED NONZERO BOUNDARY CONDITIONS
C     XYZ = nodal coordinates
C     iflag = flag for user to set (not equal to 0) if coordinates
C             are updated
C     NODEPR = reverse permutation array
C     node(external) = NODEPR(NODE) where NODE = internal node no.
C
#include "IMPLCT.COM"
#include "PARUSR.COM"
      DIMENSION SOL(*),NUMEQA(NUMNP,NDOF),CONSTR(*),LDOFU(*)
      DIMENSION NODEPR(*),XYZ(NUMNP,*)
      DIMENSION grid(0:4)         !Corresponds to x in subroutine
```

```
      DIMENSION wghts(0:4,0:1)    !Corresponds to c in subroutine
      F_DOUBLEPRECISION GETSOL
      F_DOUBLEPRECISION GETSOLP
      ZRO = 0.D0
      total = 4            !Corresponds to n in subroutine
      max_size = 4         !Corresponds to nd in subroutine
      order = 1            !Corresponds to m in subroutine
C     First the core of the nodes.
      IF ((NODE .LE. 11287) .AND. (NODE .GE. 55)) THEN
C     Number of element intervals in the radial direction.
      int = 27
C     Get velocities.
      vel0 = GETSOL(NODE+2*int,KDU)
      vel1 = GETSOL(NODE+int,KDU)
      vel2 = GETSOL(NODE,KDU)
      vel3 = GETSOL(NODE-int,KDU)
      vel4 = GETSOL(NODE-2*int,KDU)
C     Get concentrations.
      conc0 = GETSOL(NODE+2*int,KDS+1)
      conc1 = GETSOL(NODE+int,KDS+1)
      conc2 = GETSOL(NODE,KDS+1)
      conc3 = GETSOL(NODE-int,KDS+1)
      conc4 = GETSOL(NODE-2*int,KDS+1)
C     Get axial grid point locations.
      grid(0) = XYZ(NODE+2*int,1)
      grid(1) = XYZ(NODE+int,1)
      grid(2) = XYZ(NODE,1)
      grid(3) = XYZ(NODE-int,1)
      grid(4) = XYZ(NODE-2*int,1)
C     Location of node NODE.
      axpos = XYZ(NODE,1)    !Corresponds to z in subroutine
C     Pass information to subroutine fornberg.
      CALL fornberg (axpos,grid,total,max_size,order,wghts)
C     Finite-difference weights.
      f0 = wghts(0,1)
      f1 = wghts(1,1)
      f2 = wghts(2,1)
      f3 = wghts(3,1)
      f4 = wghts(4,1)
C     Computation of derivatives at node NODE.
      dvel = f0*vel0 + f1*vel1 + f2*vel2 + f3*vel3 + f4*vel4
      dconc = f0*conc0 + f1*conc1 + f2*conc2 + f3*conc3 + f4*conc4
```

```
C     Velocity and concentration at node NODE.
      unode = vel2
      cnode = conc2
C     Now the first node (at z = 0).
      ELSEIF (NODE .EQ. 11341) THEN
C     Number of element intervals in the radial direction.
      int = 27
C     Get velocities.
      vel0 = GETSOL(NODE,KDU)
      vel1 = GETSOL(NODE-int,KDU)
      vel2 = GETSOL(NODE-2*int,KDU)
      vel3 = GETSOL(NODE-3*int,KDU)
      vel4 = GETSOL(NODE-4*int,KDU)
C     Get concentrations.
      conc0 = GETSOL(NODE,KDS+1)
      conc1 = GETSOL(NODE-int,KDS+1)
      conc2 = GETSOL(NODE-2*int,KDS+1)
      conc3 = GETSOL(NODE-3*int,KDS+1)
      conc4 = GETSOL(NODE-4*int,KDS+1)
C     Get axial grid point locations.
      grid(0) = XYZ(NODE,1)
      grid(1) = XYZ(NODE-int,1)
      grid(2) = XYZ(NODE-2*int,1)
      grid(3) = XYZ(NODE-3*int,1)
      grid(4) = XYZ(NODE-4*int,1)
C     Location of node NODE.
      axpos = XYZ(NODE,1)
C     Pass information to subroutine fornberg.
      CALL fornberg (axpos,grid,total,max_size,order,wghts)
C     Finite-difference weights.
      f0 = wghts(0,1)
      f1 = wghts(1,1)
      f2 = wghts(2,1)
      f3 = wghts(3,1)
      f4 = wghts(4,1)
C     Computation of derivatives at node NODE.
      dvel = f0*vel0 + f1*vel1 + f2*vel2 + f3*vel3 + f4*vel4
      dconc = f0*conc0 + f1*conc1 + f2*conc2 + f3*conc3 + f4*conc4
C     Velocity and concentration at node NODE.
      unode = vel0
      cnode = conc0
C     Now the second node.
```

```
      ELSEIF (NODE .EQ. 11314) THEN
C     Number of element intervals in the radial direction.
      int = 27
C     Get velocities.
      vel0 = GETSOL(NODE+int,KDU)
      vel1 = GETSOL(NODE,KDU)
      vel2 = GETSOL(NODE-int,KDU)
      vel3 = GETSOL(NODE-2*int,KDU)
      vel4 = GETSOL(NODE-3*int,KDU)
C     Get concentrations.
      conc0 = GETSOL(NODE+int,KDS+1)
      conc1 = GETSOL(NODE,KDS+1)
      conc2 = GETSOL(NODE-int,KDS+1)
      conc3 = GETSOL(NODE-2*int,KDS+1)
      conc4 = GETSOL(NODE-3*int,KDS+1)
C     Get axial grid point locations.
      grid(0) = XYZ(NODE+int,1)
      grid(1) = XYZ(NODE,1)
      grid(2) = XYZ(NODE-int,1)
      grid(3) = XYZ(NODE-2*int,1)
      grid(4) = XYZ(NODE-3*int,1)
C     Location of node NODE.
      axpos = XYZ(NODE,1)
C     Pass information to subroutine fornberg.
      CALL fornberg (axpos,grid,total,max_size,order,wghts)
C     Finite-difference weights.
      f0 = wghts(0,1)
      f1 = wghts(1,1)
      f2 = wghts(2,1)
      f3 = wghts(3,1)
      f4 = wghts(4,1)
C     Computation of derivatives at node NODE.
      dvel = f0*vel0 + f1*vel1 + f2*vel2 + f3*vel3 + f4*vel4
      dconc = f0*conc0 + f1*conc1 + f2*conc2 + f3*conc3 + f4*conc4
C     Velocity and concentration at node NODE.
      unode = vel1
      cnode = conc1
C     Now the node before the last node.
      ELSEIF (NODE .EQ. 28) THE
C     Number of element intervals in the radial direction.
      int = 27
C     Get velocities.
```

```
      vel4 = GETSOL(NODE-int,KDU)
      vel3 = GETSOL(NODE,KDU)
      vel2 = GETSOL(NODE+int,KDU)
      vel1 = GETSOL(NODE+2*int,KDU)
      vel0 = GETSOL(NODE+3*int,KDU)
C     Get concentrations.
      conc4 = GETSOL(NODE-int,KDS+1)
      conc3 = GETSOL(NODE,KDS+1)
      conc2 = GETSOL(NODE+int,KDS+1)
      conc1 = GETSOL(NODE+2*int,KDS+1)
      conc0 = GETSOL(NODE+3*int,KDS+1)
C     Get axial grid point locations.
      grid(4) = XYZ(NODE-int,1)
      grid(3) = XYZ(NODE,1)
      grid(2) = XYZ(NODE+int,1)
      grid(1) = XYZ(NODE+2*int,1)
      grid(0) = XYZ(NODE+3*int,1)
C     Location of node NODE.
      axpos = XYZ(NODE,1)
C     Pass information to subroutine fornberg.
      CALL fornberg (axpos,grid,total,max_size,order,wghts)
C     Finite-difference weights.
      f0 = wghts(0,1)
      f1 = wghts(1,1)
      f2 = wghts(2,1)
      f3 = wghts(3,1)
      f4 = wghts(4,1)
C     Computation of derivatives at node NODE.
      dvel = f0*vel0 + f1*vel1 + f2*vel2 + f3*vel3 + f4*vel4
      dconc = f0*conc0 + f1*conc1 + f2*conc2 + f3*conc3 + f4*conc4
C     Velocity and concentration at node NODE.
      unode = vel3
      cnode = conc3
C     Finally the last node.
      ELSEIF (NODE .EQ. 1) THEN
C     Number of element intervals in the radial direction.
      int = 27
C     Get velocities.
      vel4 = GETSOL(NODE,KDU)
      vel3 = GETSOL(NODE+int,KDU)
      vel2 = GETSOL(NODE+2*int,KDU)
      vel1 = GETSOL(NODE+3*int,KDU)
```

```
      vel0 = GETSOL(NODE+4*int,KDU)
C     Get concentrations.
      conc4 = GETSOL(NODE,KDS+1)
      conc3 = GETSOL(NODE+int,KDS+1)
      conc2 = GETSOL(NODE+2*int,KDS+1)
      conc1 = GETSOL(NODE+3*int,KDS+1)
      conc0 = GETSOL(NODE+4*int,KDS+1)
C     Get axial grid point locations.
      grid(4) = XYZ(NODE,1)
      grid(3) = XYZ(NODE+int,1)
      grid(2) = XYZ(NODE+2*int,1)
      grid(1) = XYZ(NODE+3*int,1)
      grid(0) = XYZ(NODE+4*int,1)
C     Location of node NODE.
      axpos = XYZ(NODE,1)
C     Pass information to subroutine fornberg.
      CALL fornberg (axpos,grid,total,max_size,order,wghts)
C     Finite-difference weights.
      f0 = wghts(0,1)
      f1 = wghts(1,1)
      f2 = wghts(2,1)
      f3 = wghts(3,1)
      f4 = wghts(4,1)
C     Computation of derivatives at node NODE.
      dvel = f0*vel0 + f1*vel1 + f2*vel2 + f3*vel3 + f4*vel4
      dconc = f0*conc0 + f1*conc1 + f2*conc2 + f3*conc3 + f4*conc4
C     Velocity and concentration at node NODE.
      unode = vel4
      cnode = conc4
      ENDIF
C     Computation of the flux value at node NODE.
      const = 82.34D-6 + cnode
      flux = -1.855D0/const*(unode*dconc*(82.34D-6/const)+cnode*dvel)
      VAL = flux
      RETURN
      END
```

D.2 Fornberg Algorithm

```
      SUBROUTINE fornberg (z,x,n,nd,m,c)
C
C     Input Parameters
```

```
C     z                  location where approximations are to be accurate
C                        (may but need not be a grid point)
C     x(0:nd)            grid point locations, found in x(0:nd)
C     n                  one less than total number of grid points;
C                        must not exceed the parameter nd below
C     nd                 dimension of x- and c-arrays in calling program;
C                        x(0:nd) and c(0:nd,0:m), respectively
C     m                  highest derivative for which wheights are sought
C
C     Output Parameter
C     c(0:nd,0:m)        weights at grid locations x(0:n) for derivatives
C                        of order 0:m, found in c(0:n,0:m)
C
      IMPLICIT REAL*8 (a-h,o-z)
      DIMENSION x(0:nd),c(0:nd,0:m)
      n = 4          !  n and m were not passed to the subroutine
      m = 1          !  for some reason.
      c1 = 1.0D0
      c4 = x(0) - z
      DO 10 k = 0,m
         DO 10 j = 0,n
 10         c(j,k) = 0.0D0
      c(0,0) = 1.0D0
      DO 50 i = 1,n
         mn = MIN(i,m)
         c2 = 1.0D0
         c5 = c4
         c4 = x(i) - z
            DO 40 j = 0,i-1
               c3 = x(i) - x(j)
               c2 = c2 * c3
               IF (j .EQ. i-1) THEN
                  DO 20 k = mn,1,-1
 20                  c(i,k) = c1*(k*c(i-1,k-1)-c5*c(i-1,k))/c2
                  c(i,0) = -c1*c5*c(i-1,0)/c2
               ENDIF
               DO 30 k = mn,1,-1
 30               c(j,k) = (c4*c(j,k)-k*c(j,k-1))/c3
 40            c(j,0) = c4*c(j,0)/c3
 50      c1 = c2
      RETURN
      END SUBROUTINE fornberg
```

D.3 Surface Tension

```
      SUBROUTINE USRSRF (NELT,NE,NG,COEF,VARI,NDFCD,LDOFU,SHP,XYZL,
     1                   PROP,TIME,NPTS,ndp,MNDP,IERR)
C
C     USER DEFINED SURFACE TENSION
C
C     NELT = GLOBAL ELEMENT NUMBER
C     NE = LOCAL ELEMENT NUMBER
C     NG = GROUP NUMBER
C     COEF = SURFACE TENSION
C     VARI = SOLUTION VARIABLE ARRAY AT THE INTEGRATION POINTS
C     LDOFU = pointer array for accessing vari and dvari information
C     XYZL = X,Y,Z COORDINATES
C     PROP = USER DEFINED PARAMETERS
C     MNDP = FIRST DIMENSION OF SHAPE FUNCTION MATRICES
C     TIME = TIME
C     NPTS = NUMBER OF POINTS
C
#include "IMPLCT.COM"
#include "PARUSR.COM"
      DIMENSION COEF(NPTS),SHP(NPTS,MNDP),XYZL(NPTS,NDFCD)
      DIMENSION PROP(*),VARI(NPTS,*),LDOFU(*)
      ZRO = 0.D0
      DO 121 N = 1,NPTS
         axpos = XYZL(N,1)
         B = (4.D0/PROP(5))*(PROP(6)+PROP(3))
         quotient = ((PROP(1)/B)**(2.D0/(1.D0-PROP(2)))+
     1                         axpos**(2.D0))**((1.D0-PROP(2))/2.D0)
         spec = (PROP(1)/B)*(PROP(3)+B*axpos)/quotient
         COEF(N) = PROP(4)+PROP(5)*LOG(1.D0-spec/(PROP(6)+spec))
  121 CONTINUE
      RETURN
      END
```

D.4 Micelle Source Terms

```
      SUBROUTINE USRSRC (NELT,NE,NG,SORCE,VARI,DVARI,NDFCD,LDOFU,SHP,
     1                   DSDX,XYZL,deter,PROP,TIME,NPTS,ndp,MNDP,IERR,
     2                   IOPT)
C
C     USER DEFINED SOURCE FOR ENERGY OR SPECIES EQUATIONS
```

```
C
C     NELT = GLOBAL ELEMENT NUMBER
C     NE = LOCAL ELEMENT NUMBER
C     NG = GROUP NUMBER
C     SORCE = HEAT OR SPECIES SOURCE (RETURNED VALUES)
C     VARI = ARRAY OF SOLUTION VARIBLES AT INTEGRATION POINTS
C     DVARI = GRADIENTS OF SOLUTION VARIABLES AT INTEGRATION POINTS
C     LDOFU = pointer array for accessing vari and dvari information
C     XYZL = X,Y,Z COORDINATES
C     DETER = the value of the transformation determinant at
C             each of the npts points.  For axi-symmetric problem it is
C             R*determinant
C     SHP = ELEMENT SHAPE FUNCTIONS
C     DSDX = SHAPE FUNCTION DERIVATIVES IN THE X,Y,Z DIRECTION
C     PROP = USER DEFINED PARAMETERS
C     MNDP = FIRST DIMENSION OF SHAPE FUNCTION MATRICES
C     TIME = TIME
C     NPTS = NUMBER OF POINTS
C     IOPT = 0 ENERGY EQUATION
C     IOPT = N TRANSPORT EQUATION FOR SPECIES N (0<N<16)
C
#include "IMPLCT.COM"
#include "PARUSR.COM"
      DIMENSION SORCE(NPTS)
      DIMENSION SHP(NPTS,MNDP),DSDX(NPTS,NDFCD,MNDP),XYZL(NPTS,NDFCD)
      DIMENSION PROP(*),VARI(NPTS,*),DVARI(NPTS,NDFCD,*),LDOFU(*)
      DIMENSION DETER(NPTS)
C
C     Declaration of additional arrays
C
      DIMENSION w1(NPTS)
      DIMENSION w2(NPTS)
      DIMENSION c1(NPTS)
      DIMENSION c2(NPTS)
      DIMENSION dc1dt(NPTS)
      DIMENSION dc2dt(NPTS)
      DIMENSION dw1dt(NPTS)
      DIMENSION dw2dt(NPTS)
C
      ZRO = 0.D0
C
C     Monomers, i = 1
```

```
C
      IF (IOPT .EQ. 1) THEN
          IERR = 0
          DO 100 j = 1,NPTS
             w1(j)=VARI(j,LDOFU(KDS+1))
             w2(j)=VARI(j,LDOFU(KDS+2))
C     Conversion of mass fraction to molar concentration
             c1(j)=prop(1)/prop(2)*w1(j)
             c2(j)=prop(1)/(prop(3)*prop(2))*w2(j)
C     Computation of source term dc1dt in [mol/m^3 s]
             dc1dt(j)=prop(3)*(prop(5)*c2(j)-prop(4)*((c1(j))**prop(3)))
C     Conversion of molar source to mass source in [kg/m^3 s]
             dw1dt(j)=prop(2)*dc1dt(j)
C     Non-dimensionalisation of mass source and return of value
             SORCE(j)=(prop(6)**2)/(prop(1)*prop(7))*dw1dt(j)
  100     CONTINUE
C
C     Micelles, i = 2
C
      ELSEIF (IOPT .EQ. 2) THEN
          IERR = 0
          DO 200 j = 1,NPTS
             w1(j)=VARI(j,LDOFU(KDS+1))
             w2(j)=VARI(j,LDOFU(KDS+2))
C     Conversion of mass fraction to molar concentration
             c1(j)=prop(1)/prop(2)*w1(j)
             c2(j)=prop(1)/(prop(3)*prop(2))*w2(j)
C     Computation of source term dc2dt in [mol/m^3 s]
             dc2dt(j)=prop(4)*((c1(j))**prop(3))-prop(5)*c2(j)
C     Conversion of molar source to mass source in [kg/m^3 s]
             dw2dt(j)=prop(3)*prop(2)*dc2dt(j)
C     Non-dimensionalisation of mass source and return of value
             SORCE(j)=(prop(6)**2)/(prop(1)*prop(7))*dw2dt(j)
  200     CONTINUE
      ENDIF
      RETURN
      END
```

Appendix E

Experimental Data

Table E.1: Collection of experimental data.

Surfactant	c_{cmc}/mM	Re	R_0/mm	c_b/mM	Figures
C_{12}TAB + NaBr	2.4	1280	0.79	0.26 to 5.0	E.1 and E.2
C_{14}TAB	3.7	1280	0.79	0.93 to 3.7	E.3 and E.4
C_{16}TAB	0.92	1280	0.79	0.24 to 5.0	E.5 and E.6
C_{16}TAB	0.92	1550	0.79	2.5	E.7 to E.9
C_{16}TAB	0.92	1950	0.79	0.3 to 6.17	E.10 to E.12
C_{16}TAB	0.92	1950	1.0	0.9 to 3.0	E.13 and E.14
C_{18}TAB	0.31	1280	0.79	0.31 to 18.0	E.15 and E.16
$C_{10}E_8$	1.0	1280	0.79	0.5 to 4.0	E.17 and E.18
$C_{12}E_8$	0.1	1280	0.79	0.5 to 4.0	E.19 and E.20

E.1 C_{12}TAB

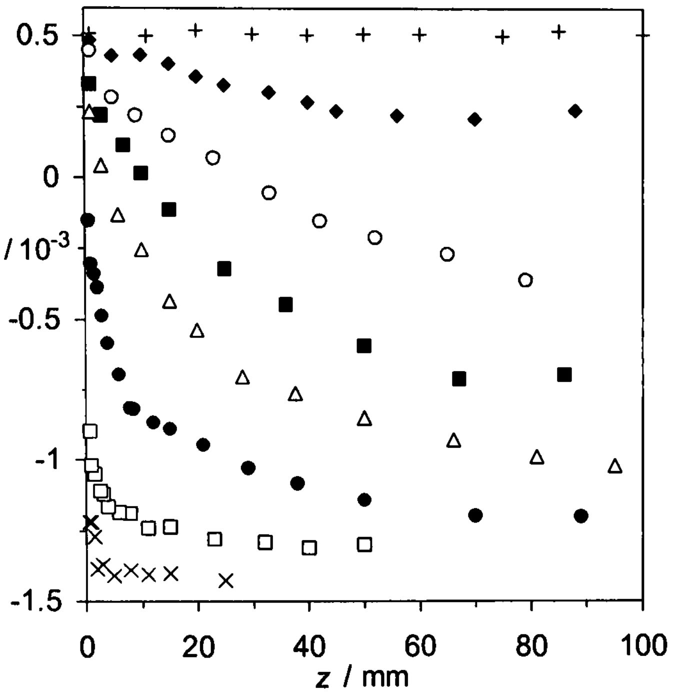

Figure E.1: Coefficient of ellipticity, $\bar{p}(z)$, for varying bulk concentrations, c_b, of C_{12}TAB in the presence of $c_{\mathrm{NaBr}} = 0.2$ M NaBr at Re = 1280 ($R_0 = 0.79$ mm). The data are for $c_b = 0.26$ mM (♦), 0.52 mM (○), 0.78 mM (■), 1.04 mM (△), 1.3 mM (●), 2.6 mM (□), 5.0 mM (×), and water (+).

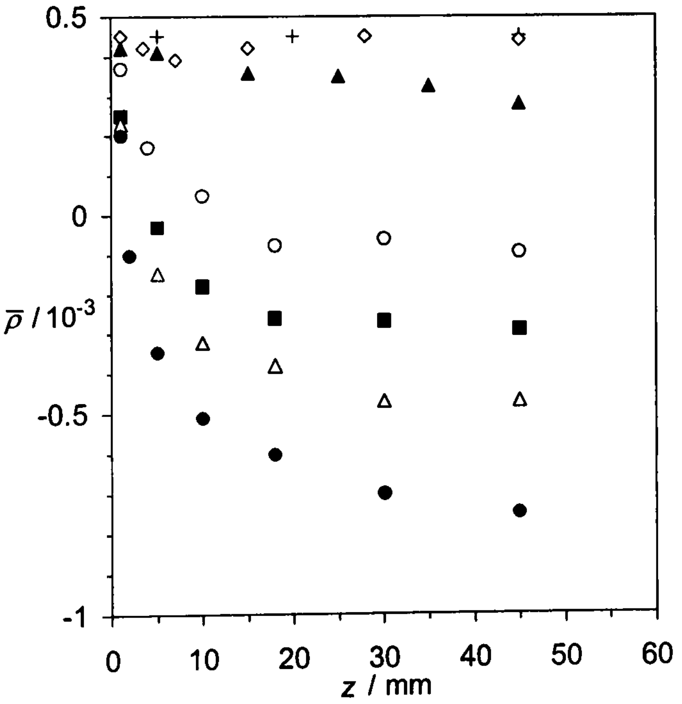

Figure E.2: Coefficient of ellipticity, $\bar{p}(z)$, for $c_b = 1.0$ mM C_{12}TAB in the presence of varying amounts of NaBr, c_{NaBr}, at Re = 1280 ($R_0 = 0.79$ mm). The data are for $c_{\mathrm{NaBr}} = 0$ (◇), 1 mM (▲), 5 mM (○), 10 mM (■), 20 mM (△), 100 mM (●), and water (+).

E.2 C_{14}TAB

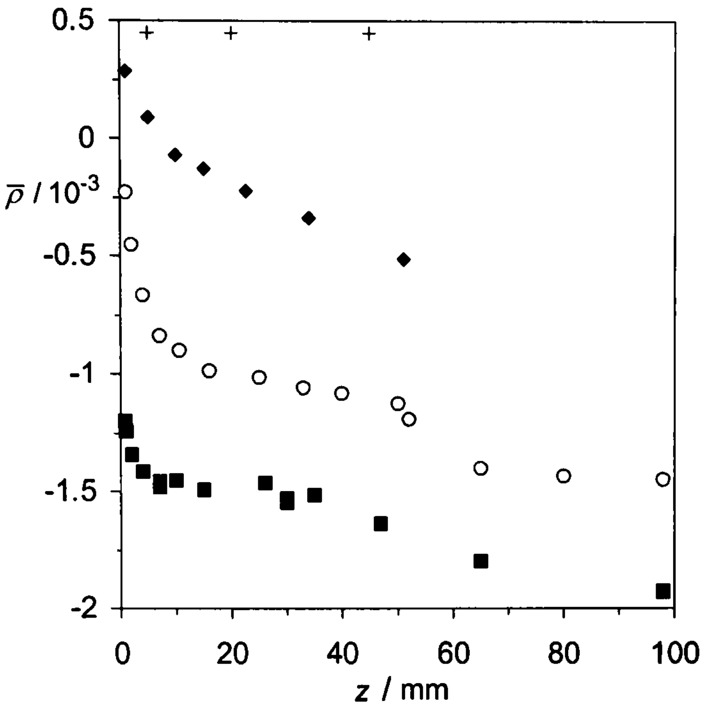

Figure E.3: Coefficient of ellipticity, $\bar{p}(z)$, for varying bulk concentrations, c_b, of C_{14}TAB at Re = 1280 ($R_0 = 0.79$ mm). The data are for $c_b = 0.93$ mM (♦), 1.85 mM (○), 3.7 mM (■), and water (+).

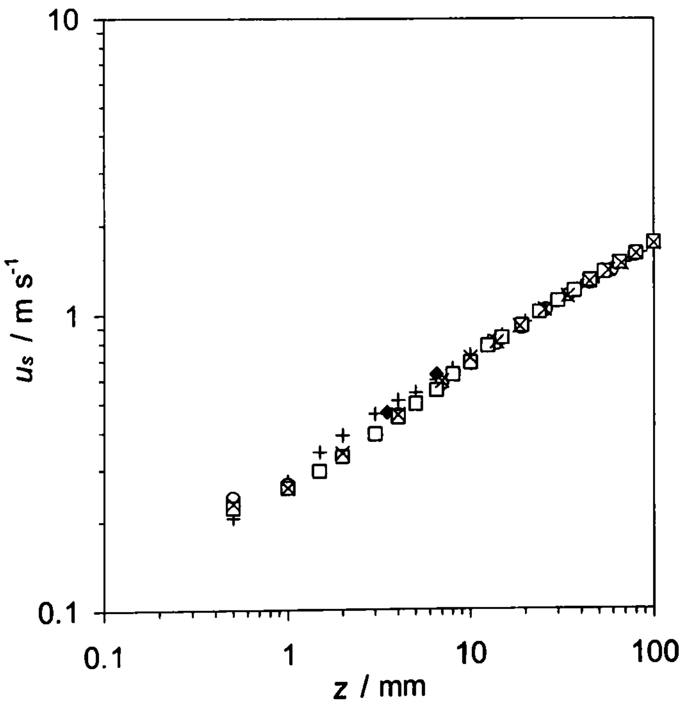

Figure E.4: Axial surface velocity, $u_s(z)$, for varying bulk concentrations, c_b, of C_{14}TAB at Re = 1280 ($R_0 = 0.79$ mm). The data are for $c_b = 0.93$ mM (♦), 1.85 mM (○), 3.7 mM (□ and ×), and water (+).

E.3 C_{16}TAB

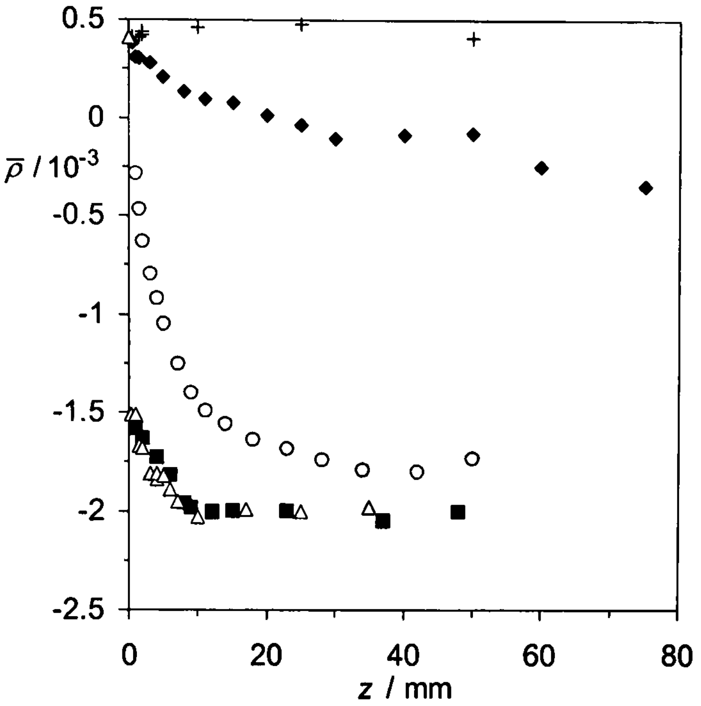

Figure E.5: Coefficient of ellipticity, $\bar{p}(z)$, for varying bulk concentrations, c_b, of C_{16}TAB at Re = 1280 (R_0 = 0.79 mm). The data are for c_b = 0.24 mM (◆), 1.25 mM (○), 3.0 mM (■), 5.0 mM (△), and water (+).

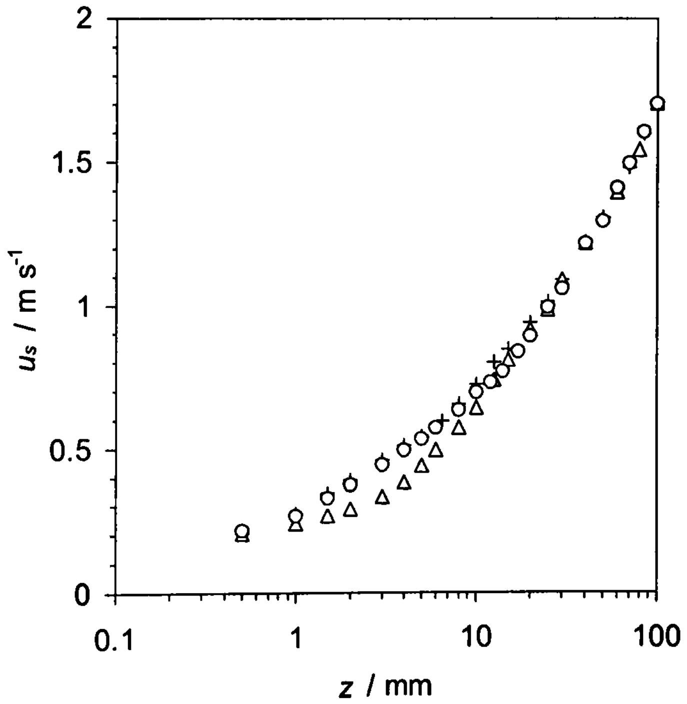

Figure E.6: Axial surface velocity, $u_s(z)$, for varying bulk concentrations, c_b, of C_{16}TAB at Re = 1280 (R_0 = 0.79 mm). The data are for c_b = 1.25 mM (○), 5.0 mM (△), and water (+).

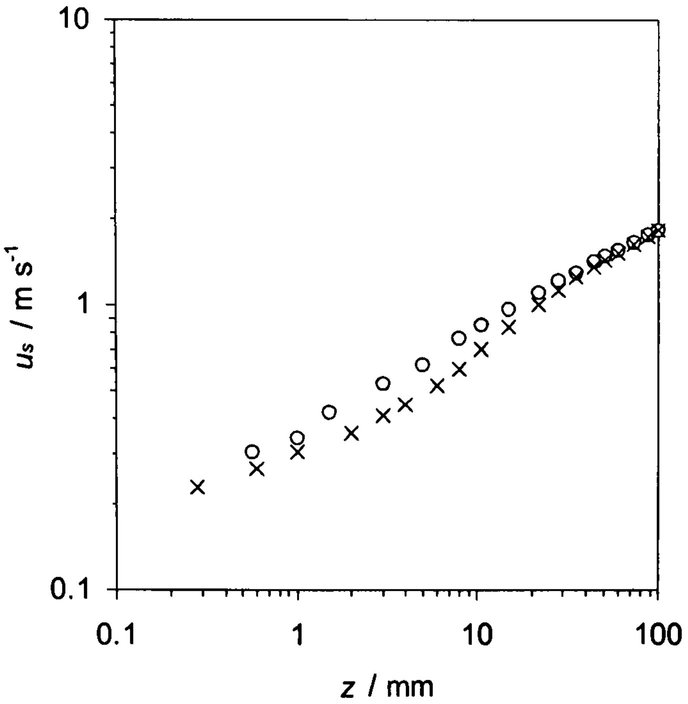

Figure E.7: Axial surface velocity, $u_s(z)$, for c_b = 2.5 mM of C_{16}TAB (×) and water (o) at Re = 1550 (R_0 = 0.79 mm).

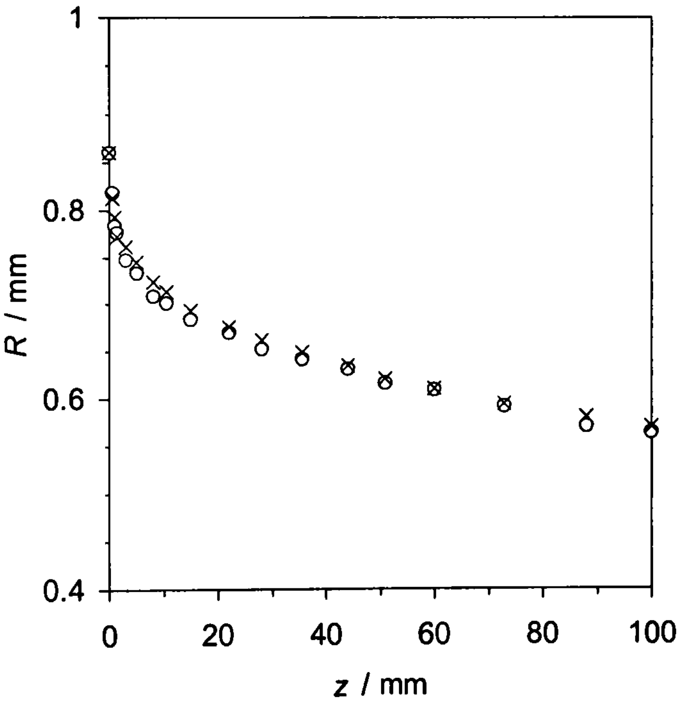

Figure E.8: Surface position, $R(z)$, for c_b = 2.5 mM of C_{16}TAB (×) and water (o) at Re = 1550 (R_0 = 0.79 mm).

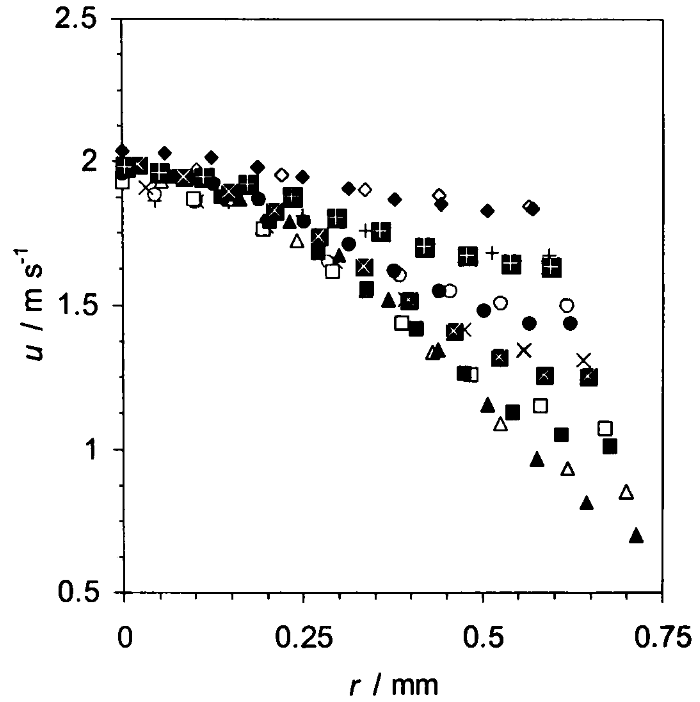

Figure E.9: Radial velocity profiles, $u(r)$, at varying axial positions, z, for c_b = 2.5 mM of C_{16}TAB (closed symbols) and water (open symbols) at Re = 1550 (R_0 = 0.79 mm). The data are for z = 10.5 mm (△), 20 mm (□), 35.5 mm (×), 51 mm (○), 73 mm (+), and 100 mm (◇).

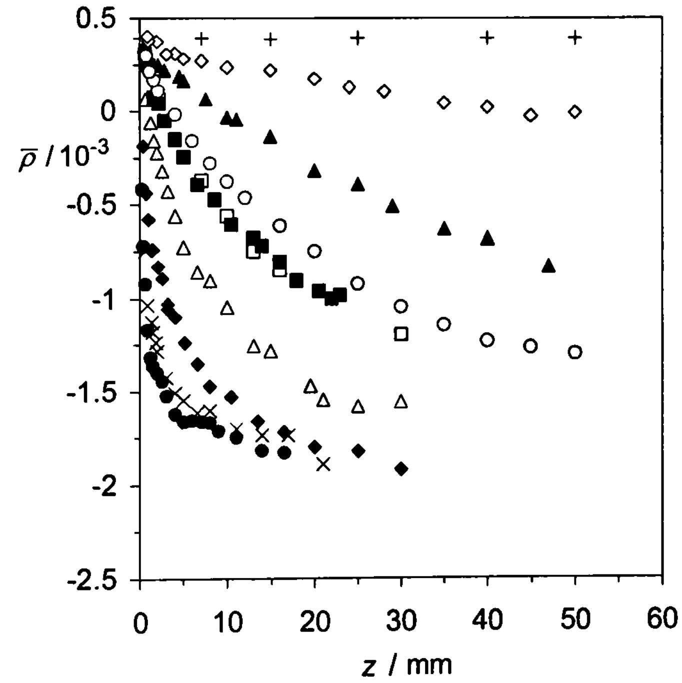

Figure E.10: Coefficient of ellipticity, $\bar{p}(z)$, for varying bulk concentrations, c_b, of C_{16}TAB at Re = 1950 (R_0 = 0.79 mm). The data are for c_b = 0.3 mM (◇), 0.65 mM (▲), 0.9 mM (○), 1.1 mM (■ and □), 1.5 mM (△), 2.48 mM (♦), 3.08 mM (×), 4.88 mM (•), and water (+).

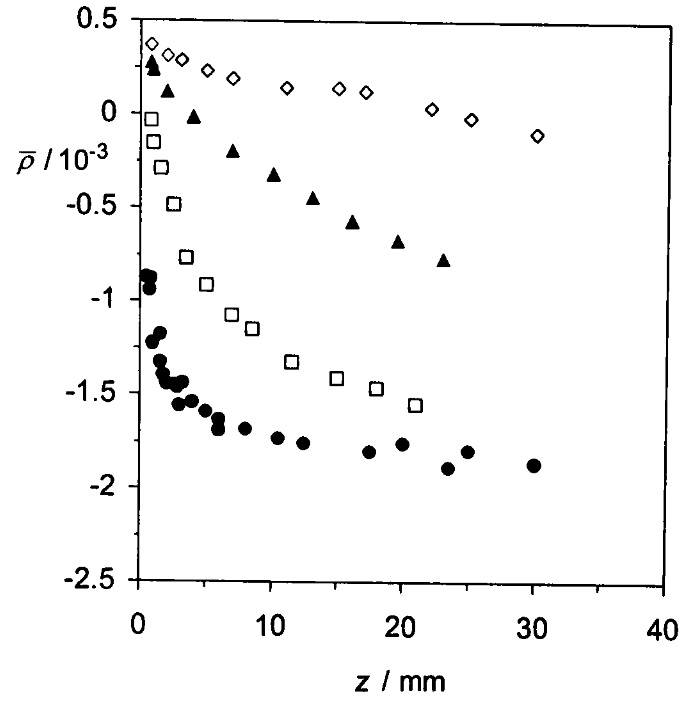

Figure E.11: Coefficient of ellipticity, $\bar{p}(z)$, for varying bulk concentrations, c_b, of C_{16}TAB at Re = 1950 (R_0 = 0.79 mm). The data are for c_b = 0.5 mM (◇), 0.73 mM (▲), 1.8 mM (□), and 6.17 mM (•).

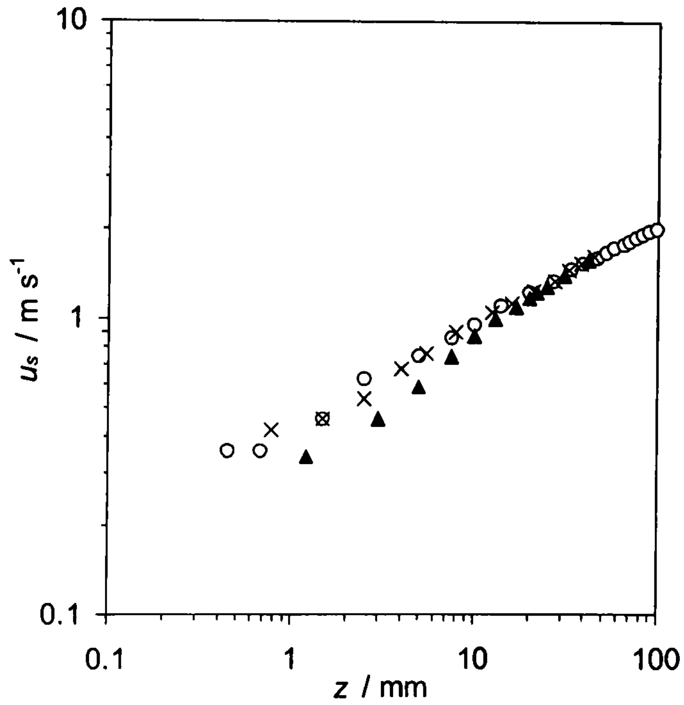

Figure E.12: Axial surface velocity, $u_s(z)$, for c_b = 4.0 mM C_{16}TAB (▲), c_b = 4.0 mM C_{16}TAB + NaBr (×), and water (o) at Re = 1950 (R_0 = 0.79 mm).

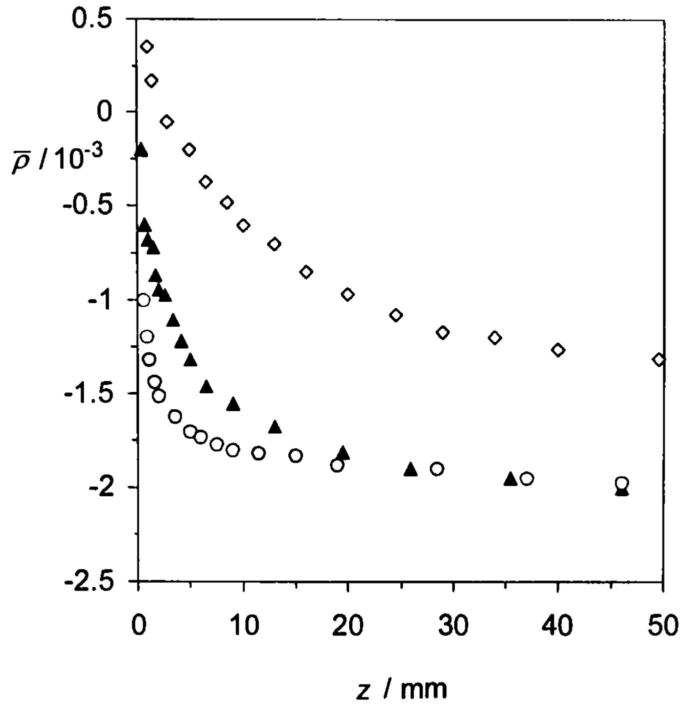

Figure E.13: Coefficient of ellipticity, $\bar{p}(z)$, for varying bulk concentrations, c_b, of C_{16}TAB at Re = 1950 (R_0 = 1.0 mm). The data are for c_b = 0.9 mM (◇), 1.8 mM (▲), and 3.0 mM (○).

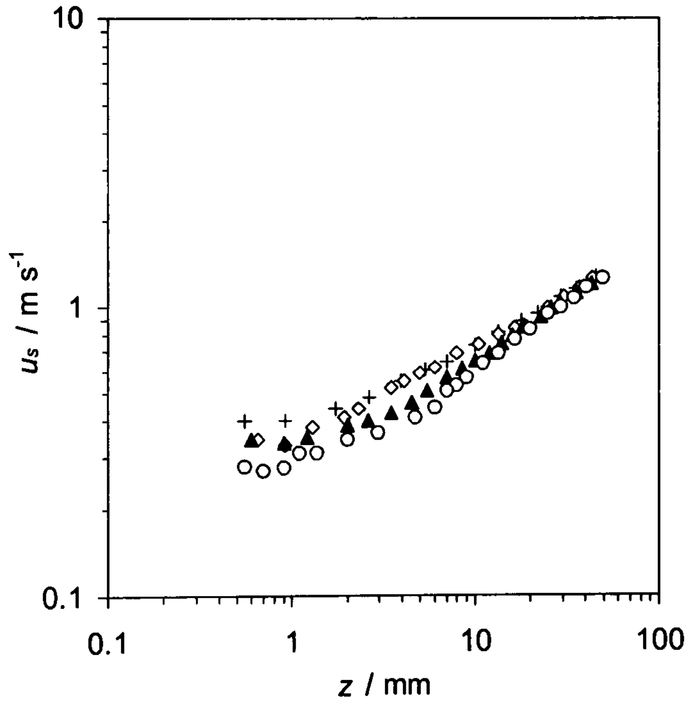

Figure E.14: Axial surface velocity, $u_s(z)$, for varying bulk concentrations, c_b, of C_{16}TAB at Re = 1950 (R_0 = 1.0 mm). The data are for c_b = 0.9 mM (◇), 1.8 mM (▲), 3.0 mM (○), and water (+).

E.4 C_{18}TAB

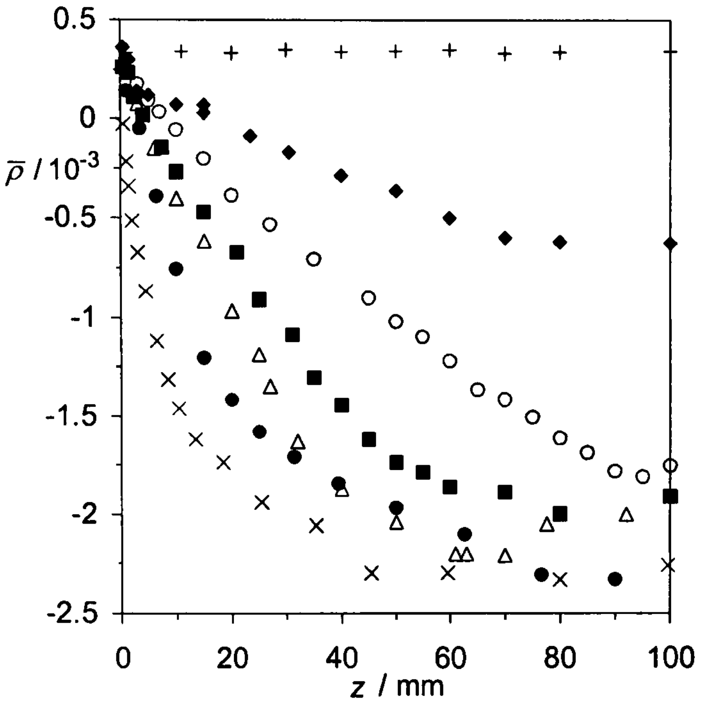

Figure E.15: Coefficient of ellipticity, $\overline{\rho}(z)$, for varying bulk concentrations, c_b, of C_{18}TAB at Re = 1280 (R_0 = 0.79 mm). The data are for c_b = 0.31 mM (♦), 1.0 mM (○), 2.15 mM (■), 5.0 mM (△), 7.5 mM (●, 40°C), 18.0 mM (×, 45°C), and water (+).

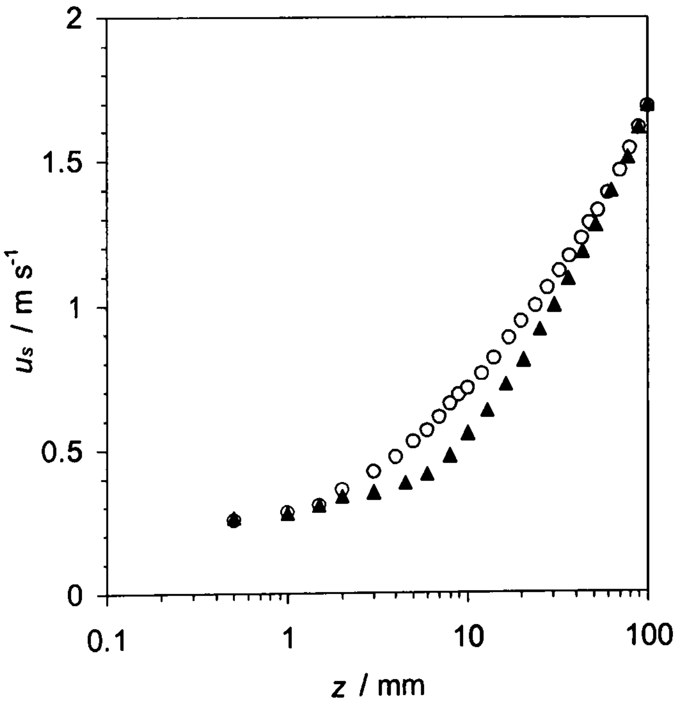

Figure E.16: Axial surface velocity, $u_s(z)$, for c_b = 18.0 mM C_{18}TAB (▲, 45°C) and water (○, 35°C) at Re = 1280 (R_0 = 0.79 mm).

E.5 $C_{10}E_8$

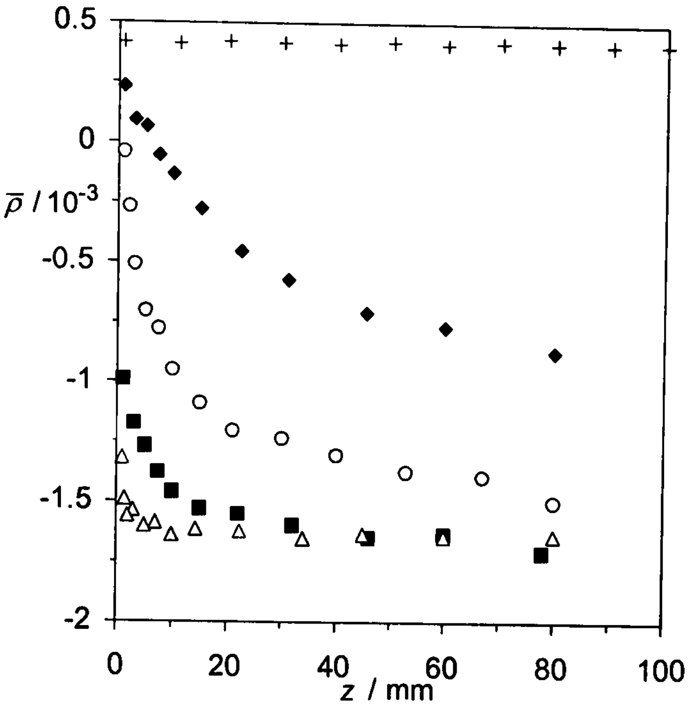

Figure E.17: Coefficient of ellipticity, $\bar{p}(z)$, for varying bulk concentrations, c_b, of $C_{10}E_8$ at Re = 1280 (R_0 = 0.79 mm). The data are for c_b = 0.5 mM (◆), 1.0 mM (○), 2.0 mM (■), 4.0 mM (△), and water (+).

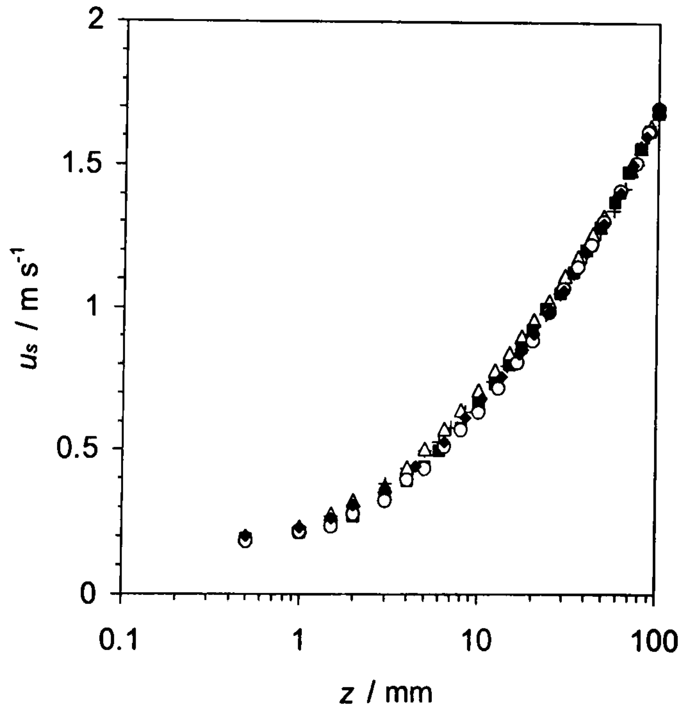

Figure E.18: Axial surface velocity, $u_s(z)$, for varying bulk concentrations, c_b, of $C_{10}E_8$ at Re = 1280 (R_0 = 0.79 mm). The data are for c_b = 0.5 mM (◆), 1.0 mM (○), 2.0 mM (■), 4.0 mM (△), and water (+).

E.6 $C_{12}E_8$

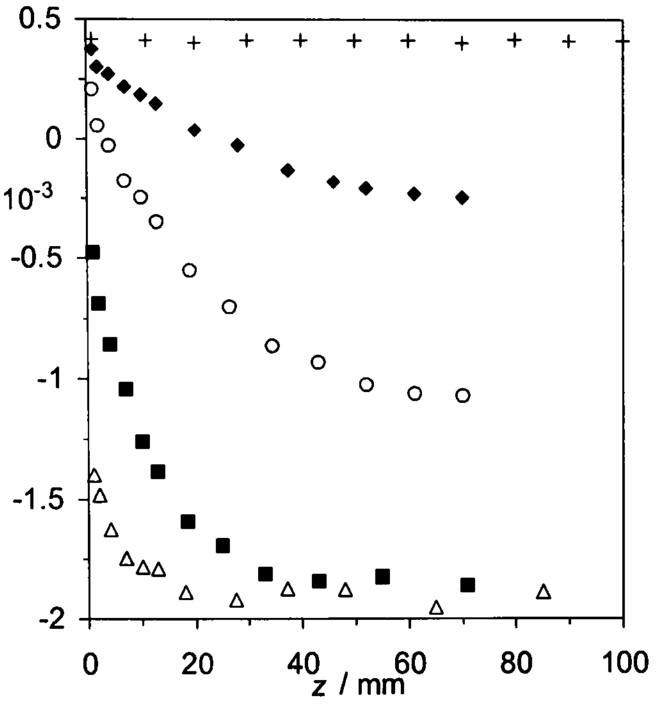

Figure E.19: Coefficient of ellipticity, $\bar{\rho}(z)$, for varying bulk concentrations, c_b, of $C_{12}E_8$ at Re = 1280 (R_0 = 0.79 mm). The data are for c_b = 0.5 mM (♦), 1.0 mM (○), 2.0 mM (■), 4.0 mM (△), and water (+).

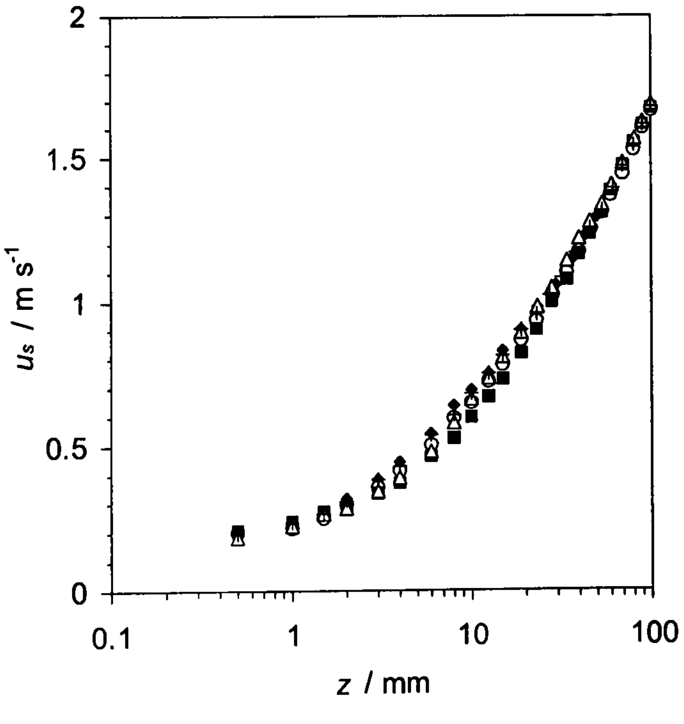

Figure E.20: Axial surface velocity, $u_s(z)$, for varying bulk concentrations, c_b, of $C_{12}E_8$ at Re = 1280 (R_0 = 0.79 mm). The data are for c_b = 0.5 mM (♦), 1.0 mM (○), 2.0 mM (■), 4.0 mM (△), and water (+).